Studies of glacier mass-balance processes and the climate response of glacier-fed rivers in the Himalaya

A thesis
submitted in partial fulfillment of the requirements
of the degree of

Doctor of Philosophy

by

Sourav Laha
ID: 20163452

DEPARTMENT OF EARTH AND CLIMATE SCIENCE

INDIAN INSTITUTE OF SCIENCE EDUCATION AND RESEARCH PUNE

March 30, 2022

Dedication

I dedicate my thesis to my father, *late Prabir Kumar Laha (July 1959 to Jan 2021)*. I hope that this achievement will complete the dream you had for me long back when you chose to give me the best education you could.

Certificate

Certified that the work incorporated in the thesis entitled *"Studies of glacier mass-balance processes and the climate response of glacier-fed rivers in the Himalaya"* submitted by *Sourav Laha* was carried out by the candidate, under my supervision. The work presented here or any part of it has not been included in any other thesis submitted previously for the award of any degree or diploma from any other University or institution.

Date: March 30, 2022

Dr. Argha Banerjee
Thesis Supervisor

Declaration

I declare that this written submission represents my ideas in my own words and where others' ideas have been included, I have adequately cited and referenced the original sources. I also declare that I have adhered to all principles of academic honesty and integrity and have not misrepresented or fabricated or falsified any idea/data/fact/source in my submission. I understand that violation of the above will be cause for disciplinary action by the Institute and can also evoke penal action from the sources which have thus not been properly cited or from whom proper permission has not been taken when needed.

Date: March 30, 2022

Sourav Laha
Roll Number: 20163452

Acknowledgments

I would like to take this as an opportunity to express my deepest gratitude to my thesis supervisor Dr. Argha Banerjee for suggesting these problems, giving me great motivation and inspiration and constant encouragement throughout my entire learning process and research experience. This thesis wouldn't be possible without his continuous support throughout my journey. His scientific insights and passion for glacio-hydrological research significantly influence my research.

I acknowledge the financial support from DST-INSPIRE (IF170526) to continue my research. I benefited from discussions with Prof. Ramachandran Shankar (IMSC, Chennai), Dr. Subimal Ghosh (IIT Bombay), Prof. Pradeep P Mujumdar (IISC Bangalore), Arijeet Dutta (IISER Pune), Anupam Samanta (IISER Pune), Vikram Singh Chandel (IIT Bombay), and Ela Chawla (IISC Bangalore). I acknowledge help from Gajendra Badwal, Surendra Badwal, Tokchand, Nepalese porters during the fieldwork at two Himalayan glaciers (Satopanth and Hamtah). Also, I am thankful to Earth and Climate Science department, IISER Pune for providing an excellent research environment.

Last but not least, a special thanks to my parents, Ms. Priya Das, and other family members for their endless patience, faith, and love throughout my whole journey.

Sourav Laha

Contents

Abstract

The climate change impact on the water security of the glacierised catchments of High Mountain Asia can potentially be amplified by the shrinkage of snow and ice reserve. However, uncertainties in quantitative descriptions of cryospheric processes, those of input data, and a serious lack of field observations compromise the predictability of Himalayan glaciers and glacier-fed rivers. In order to address some of the aspects of the broader issues, we choose specific problems related to the mass balance processes of glaciers and the climate response of glacier-fed rivers in the Himalaya. In the thesis, we develop modelling and field-based novel methods to quantify important processes related to the accumulation and ablation of ice on debris covered Himalayan glaciers. As changing glacier runoff is the key to understanding the future changes in Himalayan rivers, we analyse the climate response of the runoff of glacier-fed rivers. The major outcomes of the thesis are the following.

- Avalanching is a significant contributor to the accumulation of snow and ice on a large class of Himalayan glaciers. Field-based glaciological mass balance measurement ignores the avalanche contribution. No attempts have been made to quantify the net avalanche contribution to mass balance in the Himalaya. We first discuss diagnostic criteria to identify strongly avalanche-fed glaciers, and then develop an approximate method to quantify the magnitude of the avalanche contribution to the accumulation. Our simulations show that, in three well studied Himalayan glaciers, $\sim$95% of the total accumulation is controlled by avalanches. This study led to the first quantification of avalanches and

the associated biases in the glaciological mass balance of these glaciers. Also, point out the strong control of avalanches on the dynamics of these glaciers.

- Sub-seasonal ablation measurement by glaciological method involves tremendous human effort and often poses serious logistical challenges on debris-covered Himalayan glaciers. Measurement of vertical temperature profiles within debris allows estimation of point scale sub-debris ablation and is less labour-intensive than the glaciological method. Here, we developed novel techniques for estimating sub-seasonal ablation from vertical temperature profiles within the debris. Our analysis suggests that the accuracy of the ablation estimates from vertical temperature profiles is comparable to that of the glaciological method. Therefore, this measurement could be a convenient way of making accurate field measurements of local ablation rate over debris covered glaciers.

- The future changes in runoff from a catchment under a given climate forcing is determined by the corresponding climate sensitivity. Understanding the runoff sensitivity from the glaciersied Himalaya is important in the backdrop of potential climate-change impacts. Here, we analyse the sensitivities of river summer runoff to precipitation and temperature changes in two Himalayan catchments from the different climatic regimes. Our analysis suggests that summer runoff from the glacierised parts of the catchments is sensitive to temperature changes but is insensitive to precipitation changes. The behaviour of the summer runoff from the non-glacierised parts is exactly the opposite. Such precipitation-independent runoff from the glacierised parts stabilises the catchment runoff against precipitation variability to some degree. We also show that the impact of the future glacier loss on the inter-annual variability of summer runoff may be significant in these two catchments.

The outcomes from the thesis will contribute to improved predictability of

surface mass balance processes of Himalayan glaciers and that of the changing runoff of glacier-fed Himalayan rivers.

Chapter 1

Introduction

1.1 Importance of studying glaciers

The cryosphere is the part of earth system, which contain nearly 70% of the freshwater. It includes solid precipitation, snow, sea ice, icebergs, glaciers, ice caps, ice sheets, ice shelves, and frozen ground (permafrost). The cryosphere have important linkages and feedbacks with the atmosphere (e.g., Huybrechts et al, 2011) and hydrosphere (e.g., Schmittner et al, 2002), through its effects on surface energy and on moisture fluxes, by releasing large amounts of freshwater when snow or ice melts, and by locking up freshwater when they freeze. Different time scales are associated with different components of the cryosphere. Continental ice sheets (Greenland and Antarctica) undergo changes over timescales of up to millennia, which influence weather and climate (e.g., Chylek et al, 2004). Glaciers has relatively much smaller volumes and areas, which respond at typical timescales of years to centuries. Snow and sea ice are both of small volumes but large areas, with high seasonal variability. The permafrost interacts with the global climate on timescales from years to centuries (Turetsky et al, 2019). As the cryosphere exists near the melting point, it is highly sensitive to climate change. Therefore, scientists are trying to carefully predict the evolution of the cryosphere. Presently, glaciers and permafrost cover approximately $\sim 11\%$ of the earth's land surface (Lemke et al, 2007).

The ice mass stored in glaciers is very small compared to that in the polar ice sheets. Despite a tiny fraction (<1%) of the global cryosphere being stored in glaciers, they have drawn considerable attention from scientists. On a longer time scale ($\sim 10^6$ years), glaciers play an important role in mountain building and geomorphologic evolution of the landscape. Glacier is a good indicator for climate change (e.g., Oerlemans, 2005; Banerjee and Azam, 2016). For example, it preserves footprints of the past climate in their geomorphologic features like moraines (Benn and Evans, 2014). In a shorter time scale ($\sim 10^2 - 10^3$ years), changing glaciers have a profound impact on the global sea level (e.g., Meier et al, 2007; Church et al, 2013; Parkes and Marzeion, 2018; Kulp and Strauss, 2019). Changing glaciers also impact the regional water resources (e.g., Schaffer et al, 2019; Gao et al, 2020; Immerzeel et al, 2020) and affect the freshwater supply for drinking (Rasul and Molden, 2019), agricultural (Biemans et al, 2019), and industrial (Dhaubanjar et al, 2021) purposes. Understanding the present and future glacier mass loss is important to mitigate the water stress for the downstream populations (Marzeion et al, 2014; Hock et al, 2019). In more shorter time scale (in few hours), glacier related hazards like ice avalanche (Shugar et al, 2021), glacier lake outburst flood (Bhambri et al, 2016) create widespread destruction on human societies. Apart from that, studying and parameterizing the complex interactions and feedback processes between glaciers and other earth systems components, understanding the glacier-specific processes like mass-balance processes, ice flow, and hydrology in various glaciological settings are rich scientific points of interest.

1.2 What is a glacier?

Glacier is a mass of ice that form due to the accumulation of snowfall that does not melt entirely averaged over several years due to limited available energy and moves downslope due to gravity. Accumulated snow compacts and re-crystallizes over years and turns into ice that makes up glacier. Glacier ice persists over several decades to centuries, and undergoes deformation.

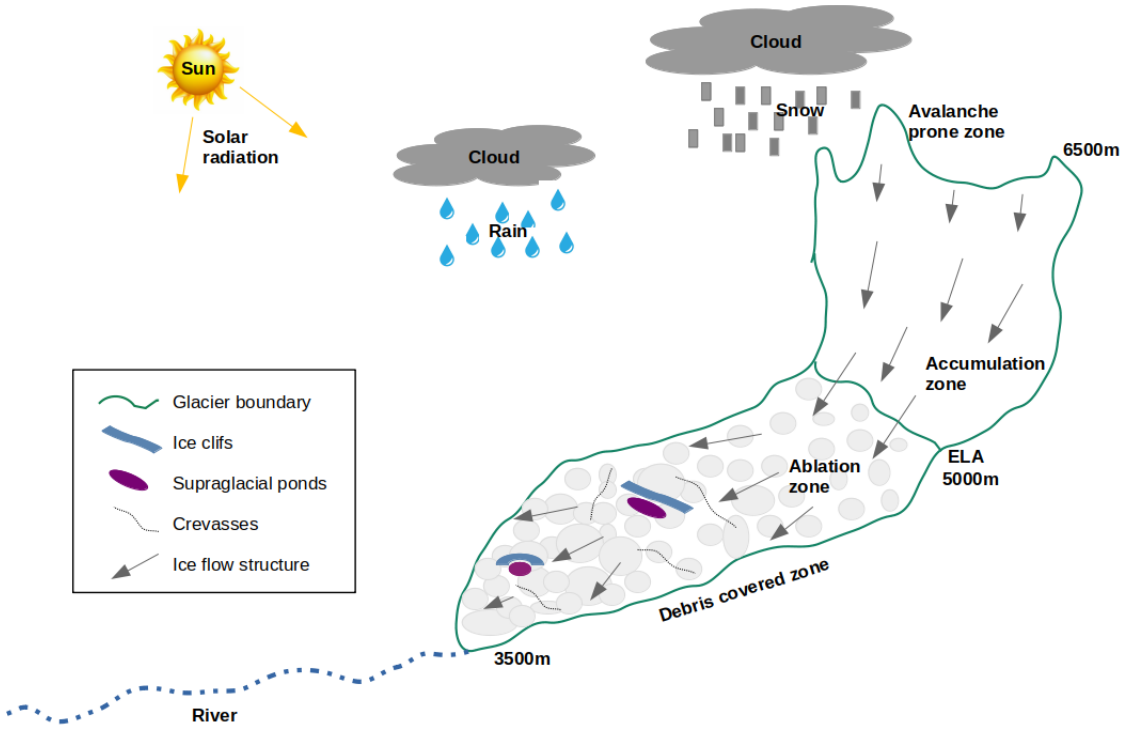

Figure 1.1: Schematic of a typical Himalayan glacier.

The accumulated snow and ice are transferred from the accumulation zone to the ablation zone (described in the sub-section) by the flow of a glacier (Fig. 1.1).

1.2.1 Zones in a glacier

Glacier area can be divided into two zones (Fig. 1.1). On the upper part of glacier, snowfall is generally higher and temperatures are cooler, therefore the annual accumulation exceeds the ablation there. This upper part is known as the 'accumulation zone'. The net gain of snow and ice added to glacier is called the 'accumulation'. On the lower part of glacier, temperatures are generally higher and the annual ablation exceeds the accumulation there. This lower part is known as the 'ablation zone'. The net melting of ice from glacier is called 'ablation'. The competition between the snow accumulation and the ice ablation determines the net mass balance of a glacier (Cuffey and Paterson, 2010). The accumulation zone and the ablation zone are separated by an 'equilibrium line', where the annual accumulation equals the annual ablation. The corresponding elevation of the equilibrium line is known as equilibrium line altitude or ELA, which is determined by the regional climate and topography (Cuffey and Paterson, 2010).

1.2.2 Glaciers and earth system

Glacier can be thought of as a 'system' with input, output, and interactions with the other components of the earth system like the atmosphere, ocean, rivers, and landscape (Benn and Evans, 2014). Ice mass enters the system in form of snowfall, and with time it turns into ice that flows downslope. As ice mass reaches the lower elevation, parts of it melt (Fig. 1.1) depending on the available energy. The erosional processes at the high-steep headwalls and sidewalls provide a significant amount of debris into the glacier by avalanches (Scherler et al, 2011a; Nagai et al, 2013; Banerjee and Wani, 2018) (Fig. 1.1), which is advected with glacier ice (Kirkbride and Deline, 2013; Wirbel et al, 2018). The meltwater from glacier leaves the system (Fig. 1.1) and con-

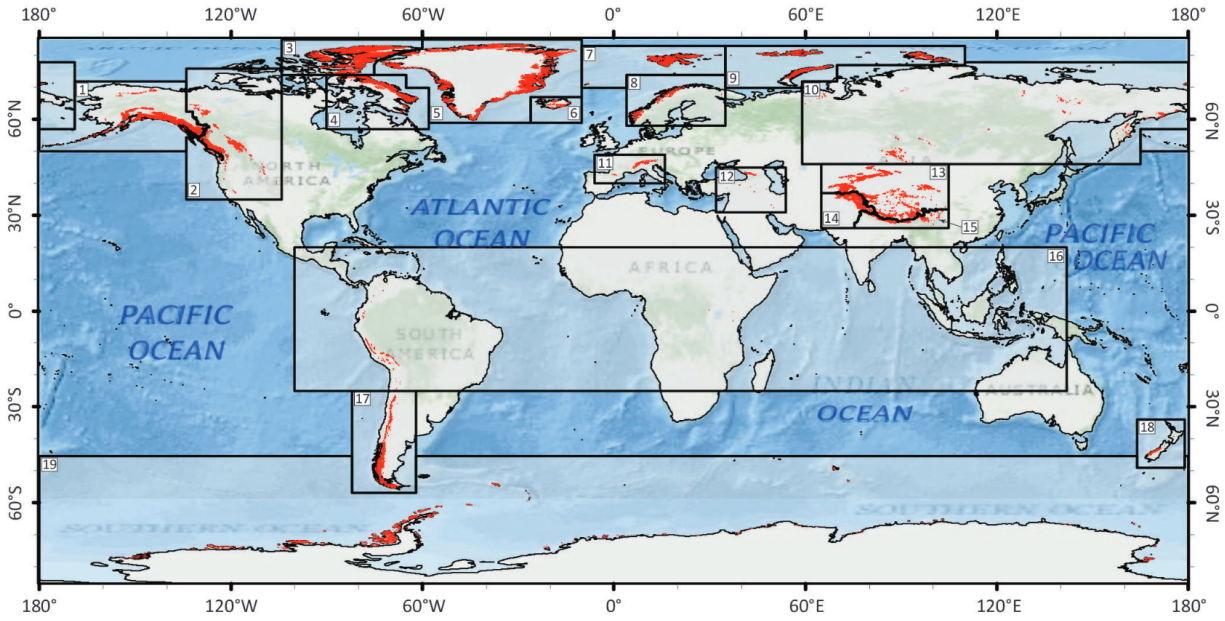

Figure 1.2: Glaciers over the world are shown in red color (Pfeffer et al, 2014), and the corresponding details of the region numbers are given in Fig. 1.3.

tributes to the riven runoff. The net mass loss from glaciers contributes to the global sea level.

As the snow accumulation and ice melting processes are sensitive to climate, glaciers are sensitive to climate variability. The glacier response time varies between years to decadel time scale (e.g., Jóhannesson et al, 1995). The deposited unsorted debris on the glacier and sediments from the glacier bedrock and headwall/sidewall erosion make different landforms like moraines. The processes of erosion and deposition make glacier valley, whose cross-sectional profile (e.g., 'U-shaped') is significantly different from corresponding river valley profiles (e.g., 'V-shaped') (Anderson and Anderson, 2010).

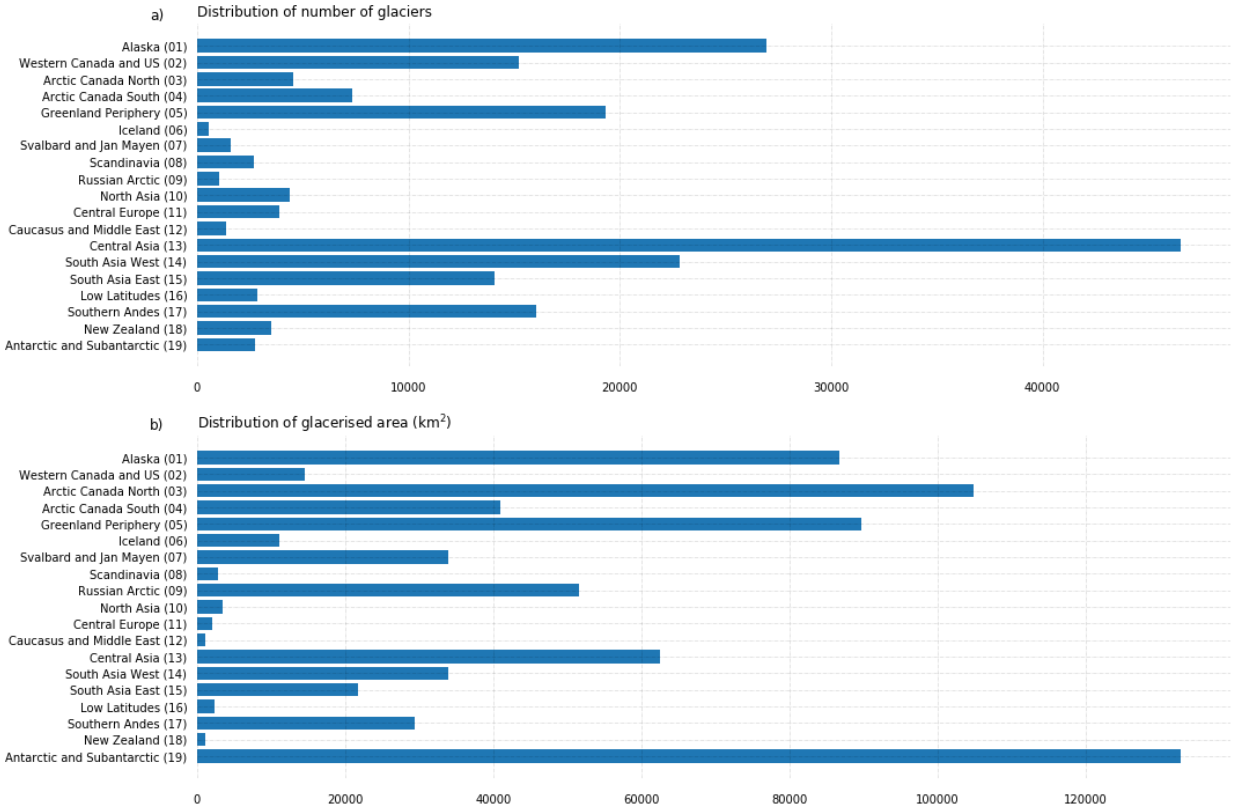

Figure 1.3: The distribution of the (a) number of glaciers, and (b) glacierised area over the world (Fig. 1.2) are shown here (Pfeffer et al, 2014).

1.2.3 Where do we find glaciers ?

There are about 216,000 glaciers that cover 706,000 km^2 of the earth surface area (Figs. 1.2 and 1.3) (RGI Consortium, 2017). Globally, glaciers are mostly found in the high latitude (e.g., Arctic), and in the high altitude (e.g., the Himalaya) depending on precipitation and temperature conditions (Fig. 1.3 and 1.3). Typically, glaciers exist and may even form in areas where,

- mean annual temperatures are below/close to the freezing point,
- significant amount of snowfall,
- limited melt energy allows snow to persist many years.

1.2.4 Types of glacier

Glaciers can be classified in several ways depending on their thermal regime, geometry, etc. The thermal distinctions are important in determining the degree to which a glacier can respond to the recent temperature warming. The temperature of the 'polar glacier' is well below the melting point of ice throughout the year. This type of glacier is generally found over the high latitudes (Fig. 1.2). In contrast, the temperature of 'temperate glacier' is at the melting point of ice. Therefore, these glaciers are more sensitive to climate change. If some parts of a glacier are cold and the renaming parts are temperate, then the glacier is called a 'polythermal glacier'. In terms of geometry, the 'valley glacier' covers a single valley compared to ice-caps which cover the tops of the peaks and drain down several valleys on the sides of the peak (Anderson and Anderson, 2010). Compared to ice-caps, ice-sheets are the continental glaciers with size $> 50 \times 10^3$ km^2.

1.3 Glacier energy balance

The energy balance at glacier surface can be expressed as (Cuffey and Paterson, 2010),

$$\begin{aligned} E_N = & \underbrace{(S\downarrow - S\uparrow)}_{\text{Net shortwave radiation}} + \underbrace{(L\downarrow - L\uparrow)}_{\text{Net longwave radiation}} + \underbrace{S}_{\text{Sensible heat flux}} \\ & + \underbrace{L}_{\text{Latent heat flux}} + \underbrace{E}_{\text{Evaporative heat flux}} + \underbrace{P_E}_{\text{Heat flux from precipitation}} \\ & + \underbrace{G}_{\text{Conductive of heat flux}} + \underbrace{R}_{\text{Heat flux from refreezing}} . \end{aligned} \tag{1.1}$$

Here, we follow the convention that energy fluxes (unit Wm^{-2}) towards glacier surface are positive. E_N is the net energy available for glacier melt. Positive E_N causes ice to melt, and negative E_N causes cooling. The ablation rate is calculated as $\frac{E_N}{\rho_w L_f}$, where ρ_w is the density of water and L_f is the latent heat of fusion.

1.3.1 Energy balance components

Shortwave radiation

Shortwave radiation is the energy produced by the sun with wavelength 0.39 to 0.76 μm (Oke, 2002). At the top of the atmosphere, the incident direct shortwave radiation is called the solar constant $S_0 = 1367\ \mathrm{Wm}^{-2}$ during day time, but zero during night. The incoming shortwave energy ($S\downarrow$) reaching the earth's surface is smaller than S_0, because some radiation scattered back to the space and some absorbed by the cloud, water vapor, and ozone in the atmosphere (Oke, 2002). The direct solar radiation at the surface depends on the zenith angle, which varies with latitude, time of the year, and time of the day (Oke, 2002). The glacier surfaces that face the sun get more direct radiation for ablation than surfaces that are obliquely oriented to the sun. In high mountain region, the shadows reduces the direct solar radiation during some times of the day and reduce ablation. Due to shading effect, small glaciers can survive beneath a steep mountain wall, while the other glacier in the surrounding valley disappeared (Cuffey and Paterson, 2010).

The amount of reflected shortwave energy ($S\uparrow$) from the surface depends on the surface albedo (α_s) by $S\uparrow = \alpha_s S\downarrow$. The net incoming shortwave radiation is $S_{\text{net}} = (1-\alpha_s)S\downarrow$. On a glacier, α_s vary between 0.2–0.85 depending on surface compositions (snow/ice/debris), amount of water and other impurities on the surface, surface roughness, and so on (Cuffey and Paterson, 2010). A typical net shortwave radiation energy value is $\sim$ 200 Wm^{-2} during the summer season (Azam et al, 2016) in Himalayan glaciers.

Longwave radiation

Assuming glacier surface to be black body, the amount of outgoing longwave radiation ($L\uparrow$) is given by Stefan–Boltzmann law, $L = \epsilon_s \sigma T_s^4$ (Oke, 2002), where ϵ_s, σ, and T_s are the emissivity, Stefan constant, and temperature of the body, respectively. For example, the wavelength of outgoing longwave radiation ($L\uparrow$) from glacier surface ranges from 4 to 30 μm (Oke, 2002). The glacier surface at 0°C, it emits longwave radiation of 311 Wm^{-2}. $L\downarrow$ mainly depends on the near-surface air temperature, and the temperature of the surrounding terrains. The Greenhouse gases (like water vapor) absorb and re-emit the longwave radiation from the atmosphere to glacier surface. Therefore the longwave can be significant during humid or overcast condition (Cuffey and Paterson, 2010). The net longwave radiation is usually negative when ice is melting, and its typical seasonal variation is about -70 to 50 Wm^{-2} (Azam et al, 2016) for typical Himalayan glacier.

Turbulent heat fluxes

Turbulent flux is the energy exchange associated with the evaporation/condensation at the boundary between glacier surface and the atmosphere (Oke, 2002). Wind mixes the air vertically by turbulent eddies. Turbulent heat fluxes are determined by wind speed, temperature, and moisture gradient between the air and the ice surface (Cuffey and Paterson, 2010). These fluxes are also affected by the exchange coefficient (C) between surface and atmosphere, which is a function of surface roughness and atmospheric stability (Oke, 2002). Sensible heat flux (S) and latent heat flux (L) can be expressed as

(Cuffey and Paterson, 2010),

$$S = \rho_a c_p C_S u(T_a - T_s) \quad (1.2)$$

$$L = \rho_a L_{v/s} C_L u(q_a - q_s). \quad (1.3)$$

Where ρ_a, c_p, u, and $L_{v/s}$ are the air density, specific heat capacity, wind speed, and latent heat of evaporation/sublimation, respectively. C_S and C_L are the exchange coefficients. Compared to radiative fluxes, turbulent flux contributions to the net balance is very small ($< 10\%$) (Cuffey and Paterson, 2010). However, in the sub-seasonal time scales due to cloudiness, high air temperature condition, etc, these flux contributions can be significant (e.g., Bonekamp et al, 2019).

Heat flux due to precipitation

The heat flux from precipitation (P_E) is estimated by $P_E = \rho_w c_p R(T_r - T_s)$, where R, T_r, and T_s are the rainfall rate, rain temperature, and surface temperature, respectively (Oke, 2002). For example, if there is a 10 mm of rainfall occurred at 10°C temperature on a melting surface, then it will contribute only 5 Wm^{-2} of energy. P_E is very small compared to other energy flux components, as discussed above. However, P_E may have indirect effects that can accelerate melting through effects on other components of the energy balance. For example, the albedo of snow decreases when it becomes wet, resulting in increased absorption of short wave radiation and thus more melt.(Cuffey and Paterson, 2010).

Conductive heat flux

The conductive heat flux (G) from the glacier surface into the glacier is calculated by Fourier's law of heat conduction, $G = K\frac{dT}{dz}$, where K is the thermal conductivity of snow or ice (2 W m^{-1} K^{-1}), z is the depth below the glacier surface, and $\frac{dT}{dz}$ is the thermal gradient (Cuffey and Paterson, 2010). In the Himalayan glaciers, the conductive heat flux mostly negligible ($< 10\%$) except during the summer monsoon when it was slightly positive and responsible for a small energy gain during the night in the upper layers

of the glacier, which resulted in melt when these layers are at melting point soon after sunrise (Azam et al, 2014).

Heat flux from refreezing

Refreezing of water (at temperature $< 0°C$) plays an important role in both energy- and mass-balance of a glacier, as this process releases latent heat (Cuffey and Paterson, 2010). This process can occur on snow or ice/firn in englacial or supraglacial locations. It depends on local temperature, pore-space, and water availability (Pfeffer et al, 1991). In a typical Himalayan glacier, refreezing can contribute $\sim$10–20 W m^{-2} of energy (e.g., Steiner et al, 2021).

1.4 Glacier mass balance

At any point on the surface a glacier, the specific mass balance (b) is defined as the change of ice mass per unit area over a year. Integral the annual specific mass balance over whole glacier obtains the net mass balance (B) (Cuffey and Paterson, 2010). Usually, mass balance studies calculate the ice mass changes over one hydrological year (starts from October for a typical Himalayan glacier) (Azam et al, 2014). If $B = 0$ averaged over many years, then glacier is in a steady state. If $B > 0$ ($B < 0$) then glacier advances (shrinks).

1.4.1 Accumulation and ablation processes

The accumulation processes are direct snowfall, wind-blown snow, refreezing of percolating meltwater into the snowpacks, and snow/ice avalanches from steep slopes of the headwall/sidewall. The fresh accumulated snow has a density of 50–70 kg m^{-3}, which transforms into firn (or wetted snow) with a density of 400–830 kg m^{-3} after it lasts for a melt season and undergoes changes in crystal morphology and structure (Cuffey and Paterson, 2010). Further compaction of firn occurs due to the interconnecting pore volume

decreases, air passage becomes smaller, and the crystal size becomes larger. The formation of glacier ice (density 830–923 kg m^{-3}) from the fresh snow can take from several years to decades or even more, depending on the regional temperature, frequency of melt season, and so on (Cuffey and Paterson, 2010).

The ablation processes are melting, evaporation, and sublimation. Ice melting at glacier surface is determined by the energy balance at the interface between glacier surface and the atmosphere (Sec. 1.3). The near surface air temperature is one of the significant factors that controls the melt at the lower altitudes (Ohmura, 2001). Although, the other meteorological factors like radiations, wind speed, humidity, clouds, and surface characteristics play an important role in the ablation processes (Cuffey and Paterson, 2010). In some glaciers, the presence of debris materials on glacier surface can modify the ice ablation rates (e.g., Naito et al, 2000; Kirkbride, 2011; Banerjee and Shankar, 2013).

1.4.2 Mass balance profile

Despite various complex accumulation and ablation processes on a glacier, the observed glacier mass balance profiles from different parts of the world typically follow a simple linear trend with elevation (Oerlemans, 2010). On the lower ablation zone, the linear mass balance profiles got distorted in the debris covered glaciers due to the insulating effect of the debris (e.g., Laha et al, 2017). Mass balance gradient of a glacier is defined as the rate of change of specific mass balance with altitude ($\beta = \frac{db(z)}{dz}$) (Cuffey and Paterson, 2010), it depends on the local climate (e.g., precipitation, temperature, and radiations) (Oerlemans and Hoogendoorn, 1989). A higher β is associated with higher ice velocity, which corresponds to the faster response of the glacier to climate change (Oerlemans, 2001).

1.4.3 Measurements of glacier mass balance

Glacier mass balance is obtained using in-situ measurements, remote sensing data, or proxy-based methods (Hubbard and Glasser, 2005; Cogley, 2017).

Glaciological method

The glaciological method is the in-situ measurements of point scale glacier mass balance. This method employs stakes over the ablation zone and snowpits over the accumulation zone of glacier (Østrem and Brugman, 1991). The annual accumulation can be identified using snowpits by visual inspection of the dirt layers, corresponding to last year's summer surface. The snowpit measurements are done at the end of the accumulation season, and the stakes measurements are done during the ablation season (Kaser et al, 2003). On the ablation zone, stakes are installed by drilling into glacier surface. The height of the stakes above glacier surface is monitored at regular time intervals (typically 15 days). The stake measurements provide the amount of ice masses added or removed at glacier surface (e.g., Azam et al, 2012; Shah et al, 2019). The net mass balance of a glacier is computed using the regressing plot of specific mass balance as a function of elevation $b(z)$ and glacier area-elevation distribution (hypsometry) $A(z)$. Then, the net mass balance of glacier is (Cuffey and Paterson, 2010),

$$B = \frac{\int b(z)A(z)dz}{\int A(z)dz}. \tag{1.4}$$

More details of the glaciological mass balance measurement techniques are described in Kaser et al (2003). Typical uncertainty of ± 0.3–0.5 m w.e.yr^{-1} (e.g., Azam et al, 2012)) in the glaciological mass balance technique may arise due to ice/snow density, the core length, stake height measurements, liquid water content of the snow, snow height, or the interpolation error due to finite number of point data (Thibert et al, 2008).

Geodetic method

The geodetic method of estimating glacier mass balance compares the surface elevation from two digital elevation model (DEM) and estimate the volumet-

ric change of glacier ice mass. The total ice volume change is determined by,

$$\Delta V = r^2 \sum_{k=1}^{K} \Delta h_k. \quad (1.5)$$

Here, r is the pixel size (in m) on a regularly spaced grid, K total number of pixels over the glacierised area, and Δh_k is the elevation change in each pixel (Zemp et al, 2013). The comparison of two DEMs is generally spans over 5–10 years intervals to minimize the associated uncertainties. Then, applying the density of snow/ice from different parts of the glaciers, the volume change is converted into mass change (Huss, 2013). Typical density of ice is assumed to be 850 kg m^{-3} (Shean et al, 2020), and uncertainty associated with the volume change to mass change is about 6% (Cogley, 2009; Huss, 2013). Another source of uncertainty is the boundary of the glaciers, which is applicable in both the glaciological and geodetic methods of estimating glacier mass balance. Glacier boundaries are taken from glacier inventories (e.g., Randolph Glacier Inventory) (Pfeffer et al, 2014). Shean et al (2020) shows that glacier area uncertainty is about 10% for a larger region of concern, while it can be more than 10% for individual glaciers.

The geodetic method of estimating regional glacier mass balance is one of the most common method, which is widely applied over the globe (e.g., Berthier et al, 2007; Bolch et al, 2011; Brun et al, 2017; Shean et al, 2020). Temporal resolution of the geodetic mass balance is limited due availability of satellite data. However, compared to the glaciological method, the geodetic method can cover a large glacierised region which is useful to understand the regional variability of glacier mass balance. The glaciological mass balance measurements can have biases, that can be calibrated using the geodetic method (e.g., Thibert et al, 2008; Zemp et al, 2013).

Hydrological method

Glacier mass balance can be estimated using the water balance of the corresponding glacier catchment (e.g., Hagg et al, 2004),

$$B = P \pm \Delta S_g - R - E^*. \quad (1.6)$$

Here P, ΔS_g, R, and E^* are the precipitation, storage change, glacier runoff at the terminus, and evaporation/sublimation, respectively, over the glacier. The hydrological method of estimating glacier mass balance requires accurate measurements of all the components on the right hand side of the Eq. (1.6). Estimating evaporation/sublimation needs meteorological parameters (air temperature, wind speed, etc). The precipitation measurements at some point on the glacier may not be the same as the other parts of the glacier. Precipitation in the high mountain catchment is one of the major sources of uncertainty. The detailed in-situ measurements are limited, also the observed data availability is relatively scarce (Immerzeel et al, 2012).

GRACE and ICESat satellite data

The GRACE (Gravity Recovery and Climate Experiment satellite) estimates the changes in the gravity field, used to compute the mass changes on the glacier (Breili and Rolstad, 2009). The GRACE satellite data are used in many studies to estimate the regional glacier mass balance (e.g., Matsuo and Heki, 2010; Jacob et al, 2012; Yi et al, 2014). Several limitations are associated with the GRACE-based regional glacier mass balance estimates. For example, changes in the gravity field can occur due to changes in the surface and sub-surface hydrology rather than glacier elevation change (Ramillien et al, 2008; Longuevergne et al, 2013). This problem arises particularly where the frequency of glacier lake increases (e.g., Nie et al, 2017). Therefore, the significant uncertainties associated GRACE's glacier mass loss estimates limit its applicability to estimate regional variability of glacier mass balance. The GRACE data can assess the changes in terrestrial water storage rather than glacier mass changes.

The ICESat (Ice, Cloud, and land Elevation Satellite) is a laser altimeter. The ICESat estimates of surface elevation are compared with the reference DEM to compute the surface elevation change, which converted into the volume change and subsequently the mass change. The precision of ICESat measurement decrease with increasing slope (Kääb et al, 2012). Also, the accuracy of ICESat based method depends on the quality of the reference DEM

(e.g., Treichler and Kääb, 2016). Multiple studies that exist over the Hindu-Kush Karakoram Himalaya, which estimates the glacier ice thickness changes using ICESat data (Gardner et al, 2013; Kääb et al, 2012; Neckel et al, 2014; Kääb et al, 2015). The ICESat data is preferable than the GRACE data, as GRACE has relatively large inherent uncertainties as discussed above.

1.5 Flow of glacier

Glacier ice can deform under applied stresses and flow. Ice effectively behaves like a non-linear viscous fluid with viscosity $\sim 10^{16}$ times larger than water (Glen, 1952). The processes associated with glacier ice flow are internal deformation, basal sliding, and/or subglacial-bed deformation. Glacier flow depends on the balance between the driving force, the downslope component of the gravitational acceleration, and the resistive drag force at the glacier bed and the glacier's margins. In most mountain glaciers, the flow velocity is a few tens to hundreds of meters per year (Scherler et al, 2008).

Internal deformation of glacier ice is the relative movement within or between ice crystals. The deformation within the crystal is mainly due to the presence of the crystal defect and that between the crystals, which involves recrystallization processes. internal deformation can be described as a plane shear flow for a large glacier (length and width $\gg$ mean ice thickness). Here, the shear stress (τ) is related to the rate of deformation ($\dot{\epsilon}$) by Glen's law i.e. $\dot{\epsilon} = A\tau^n$ (Glen, 1952), where A is the flow parameter which increases exponentially with the temperature, and n is usually taken as 3 (Cuffey and Paterson, 2010).

Sliding is also responsible for the mass transport in temperate glaciers. It is the slip between the glacier ice and its bedrock. The relation between the sliding velocity (v_s) and the shear stress at the base (τ_b) can be approximated by Weertman law, $v_s = c\frac{\tau_b^m}{\rho g h - p}$ (Weertman, 1957). Here p is the basal water pressure, the constants m and c depend on the characteristics of the glacier bed, and h is the ice thickness. The sliding speed increases when p approaches pressure due to overburden ice.

Vertically averaged ice velocity can be related to the ice thickness by the constitutive relation derived under shallow ice approximation (Oerlemans, 2001),

$$u = \left(\rho g h(-s + \frac{\partial h}{\partial x})\right)^3 \left(\frac{f_s}{h} + f_d h\right). \quad (1.7)$$

Here ρ, g, and s are the density of ice, acceleration due to gravity, and the slope at the point x, respectively. f_d, f_s are the constants that are associated with the deformation and the sliding component of the flow, respectively.

Glacier ice can melt under the overburden pressure, resulting a thin water film at the interface between the ice and glacier bed. The presence of water film can enhance the ice flow. The presence of water film at the base saturates the bed sediment, which reduces the strength of the material so that it can deform. This sub-glacial deformation needs soft sediment or weak rock at the base (Cuffey and Paterson, 2010). The ice flow creates interesting features like crevasses due to shear stresses in the ice linked with velocity variation across glacier surface. These crevasses can have depths up to several tens of meters (Colgan et al, 2016).

1.6 Climate response of glacier

Glacier tries to adjust its geometry, flow, surface elevation, terminus position, etc, in response to the climate variability towards a new equilibrium state (Cuffey and Paterson, 2010). If the climate remains steady, glacier reaches a steady state. The glacier starts advancing (retreating) due to cooling (warming) in the climate. The climate 'response time' of a glacier is defined by the transition time a glacier takes to complete most of its adjustments from one steady-state to another steady-state (Cuffey and Paterson, 2010).

Assuming linear response of glacier mass balance response to annual precipitation and summer air temperature change, we can write,

$$\delta b = s_P \delta P + s_T \delta T. \quad (1.8)$$

Here δ denotes the anomaly for a given year. The precipitation sensitivity of mass balance is defined by $s_P = \frac{\partial \delta b}{\partial P}$, and the temperature sensitivity is

defined by $s_T = \frac{\partial \delta b}{\partial T}$. Although, there is a possibility of having bilinear interaction term $\delta P \delta T$ in the Eq. (1.8). In literature, the precipitation sensitivity of glacier mass balance is generally defined as mass balance change due to a 10% change in the precipitation (Mölg et al, 2012).

1.7 Modelling of glacier

1.7.1 Modelling of glacier mass balance

The specific glacier mass balance ($b(z,t)$), at elevation z can be expressed as,

$$b(z,t) = Ac(z,t) - M(z,t) - S(z,t). \tag{1.9}$$

Here, Ac, M, and S are the accumulation, melt, and sublimation, respectively. The accumulation (Ac) is computed by (e.g., Azam et al, 2014),

$$Ac(z,t) = P(z,t) : T \leq T_{th} \tag{1.10}$$

$$0 : T > T_{th}. \tag{1.11}$$

Here, P and T are the amount of precipitation (unit m) and 2 m air temperature, respectively, at a given elevation band. T_{th} is the partitioning temperature between rainfall and snowfall.

Using the observed meteorological parameters, melt (M) can be estimated by the energy balance model (Eq. (1.1)). The melt estimation from the physically based energy balance model requires a lot of point scale field measurements of meteorological parameters, which are limited over the high mountain regions. Therefore, empirical relations between melt and near surface (2 m) air temperature is generally used to obtain melt on the glacier. It is well established that there is a strong correlation between melt and air temperature (e.g., Braithwaite and Olesen, 1989; Ohmura, 2001; Pratap et al, 2019). The physical basis of the dependence of melt on the air temperature mainly comes from the significant role of incoming longwave radiation on the energy budget (Ohmura, 2001). Assuming an empirical relation between air temperature and melt, Zingg (1951) proposed a temperature index or

degree-day model for estimating glacier snow or ice melt using the following equation,

$$M = DDF \sum_{i=1}^{n} T^{+} \Delta t : T > T_M \tag{1.12}$$

$$0 : T \leq T_M. \tag{1.13}$$

Here DDF is the degree-day factor, expressed in unit mm d^{-1} $^{\circ}C^{-1}$. n is the number of the time intervals. T^{+} is the total positive temperature during the time interval Δt. T_M is the threshold temperature for melt. This model has since applied to glaciers from different parts of the world (e.g., Hock, 2003; Wu and Wang, 2011; Azam et al, 2014; Pratap et al, 2019).

The sublimation can be estimated using the Eq. (1.3), it is one of the important mass balance processes (e.g., Winkler et al, 2009; MacDonald and Pomeroy, 2010; Stigter et al, 2018). The sublimation is strong at a very cold temperatures. Although, in the warm conditions, dry air and strong wind speed can increase the amount of sublimation.

1.7.2 Modelling of glacier dynamics

0-d glacier model

At time $t = 0$, let's consider a glacier with uniform width W_0, length L_0, and specific mass balance b_0, respectively. Over time t, the length change is L_1, the specific mass balance became $b_0 + b_1$, and the width became W_1. We assume that the ablation rate near the terminus a_0 remains constant over time t. Then the total changes in volume (for small changes) can be written as,

$$\frac{dV}{dt} = W_0 L_0 b_1 - W_1 a_0 L_1. \tag{1.14}$$

Assuming negligible width change, $\frac{dV}{dt}$ can be written as,

$$\frac{dV}{dt} = W_1 h_0 \frac{dL_1}{dt}. \tag{1.15}$$

Here, h_0 is the mean ice thickness. Now, equating the Eqs. (1.14) and (1.15), and rearranging gives a linear equation of the glacier length response as

follows (Cuffey and Paterson, 2010),

$$\frac{dL_1(t)}{dt} + \frac{L_1(t)}{\tau} = b_1 \frac{W_0}{W_1} \frac{L_0}{h_0}. \tag{1.16}$$

Here, $\tau = \frac{h_0}{a_0}$ is defined as the glacier response time. If the mass balance perturbation remains constant with time for $t > 0$, the solution of the Eq. (1.16) becomes,

$$L_1(t) = L_0 \frac{b_1}{a_0} \frac{\bar{W}}{W_t} [1 - \exp(-\frac{t}{\tau})]. \tag{1.17}$$

The values of τ range from 15–60 years for a typical valley glacier (Cuffey and Paterson, 2010).

1-d glacier model

The 1-d glacier flow model describes the time evolution of the glacier ice thickness $h(x, t)$ along the central flowline, therefore it is called the 'flowline model' (Oerlemans, 2001; Banerjee and Shankar, 2013). Here x is the distance along the central flowline, measured from the headwall of glacier. If glacier has any tributaries, the corresponding flowline merges to the main central flowline. In the flowline model, the time evolution of $h(x, t)$ is described as (Oerlemans, 2001),

$$\frac{\partial h}{\partial t} = -\frac{1}{W(x)} \frac{\partial (hWu)}{\partial x} + b(x). \tag{1.18}$$

Here $W(x)$ is the cross-sectional area of glacier at point x, $b(x)$ is the specific mass balance at point x. u is the depth-averaged ice velocity, which is the sum of the velocity due to internal deformation and sliding (Oerlemans, 2001). Suppose we have an initial ice thickness profile, along with a time dependent mass balance profile. In that case, solving the flowline model (Eq. (1.18)) along with the velocity can give the ice thickness profile ($h(x, t)$) at any subsequent time t, given glacier bedrock geometry and width distribution.

1.8 Hydrology of glacier and glacierised catchment

1.8.1 Hydrology of glacier

Hydrology of glacier is the study of meltwater storage and flows within a glacier (Cuffey and Paterson, 2010). The meltwater is mostly generated at the glacier surface, with significant diurnal variability in response to air temperature and radiation changes (e.g., Cauvy-Fraunié et al, 2013). The meltwater hydrograph is superimposed on a slowly varying baseflow discharge. Part of meltwater is stored in the snowpack, ice, englacial water pocket, supraglacial lakes, etc ,and rest of it flows towards glacier terminus and leaves glacier. Water can flow through the channels on glacier surface (supraglacial), within glacier ice through fractures/conduits (englacial), and at the ice-bedrock interface (subglacial) (Irvine-Fynn et al, 2017). The time scale of releasing the stored meltwater varies from diurnal scale to years, or even more depending on the type of the storage (Jansson et al, 2003).

At the beginning of the melt season, glacier runoff is slow and inefficient as it flows through the snow, which attenuates and is delayed. Also, the internal drainage network is mostly closed during that time. With the progression of the melt season, the internal drainage network redevelops and increases drainage efficiency. The meltwater decline at the end of the melt season, and the drainage network begins to close (Irvine-Fynn et al, 2017; Miles et al, 2019).

1.8.2 Hydrological characteristics of glacierised catchment

As glaciers are sensitive to air temperature, river runoff from glacierised catchments follows the air temperature variability at different time scales with a delay (Stenborg, 1970). On a regional scale, glacier meltwater can sustain during the end of summer, when the seasonal snow cover melts completely. Glacier meltwater also buffers during dry periods and maintains a

river runoff up to a certain level (Pritchard, 2019). The catchments with moderate glacierised fraction typically have lower inter-annual runoff variability than precipitation dominated or fully glacierised catchments (Chen and Ohmura, 1990). It is mainly due to the storage and release of water into and from glacier system (van Tiel et al, 2020).

On a longer time scale (decadal to centuries), the catchment glacier runoff varies in response to the changes in the volume and area of glacier ice due to climate change. As the air temperature continues to rise, glacier ice storage is depleted. As a result, glacier runoff increases towards a 'peak water' (Huss and Hock, 2018; Hock et al, 2019), followed by a decline in runoff in future warming. Globally, many mountain regions have already passed or are approaching 'peak water' in the coming decades (Huss and Hock, 2018; Nie et al, 2021).

1.9 Glacier induced hazards

Any glacier related processes directly affecting human life and infrastructure are known as glacial hazards (Reynolds, 1992). For example, glacier lake outburst flood (GLOF) is one of the most catastrophic processes in the high mountain regions (Roberts, 2005; Bhambri et al, 2016), which occurred due to a failure of the moraine-dammed lake. Retreating glaciers can form and/or expand such lakes, and these processes are expected to continue in the coming decades (Hock et al, 2019; Veh et al, 2020). Also, the ice avalanches from small hanging glaciers can create a devastating flood that can potentially destroy the downstream infrastructures (Shugar et al, 2021).

In this thesis, we have only focused on glaciers and the climate response of glacier-fed rivers over the Himalaya. Therefore, in the following sections, we have discussed the glacio-hydrological understanding over the Himalaya, which leads to a few open research problems addressed in this thesis.

1.10 Himalayan glaciers

The Hindu-Kush Himalaya is the largest reservoir of snow and ice outside the Polar regions; therefore, it is called the 'Third Pole' (Qiu, 2008). The Himalaya has extreme topography and heterogeneous climate. It consists of 87863 glaciers, which cover 121694 km^2 of total area (RGI Consortium, 2017) (Fig. 1.4). About 10% of the glacierised area of the Himalaya is covered by debris (Herreid and Pellicciotti, 2020). The regional distribution of the glaciers over the Himalaya is shown in Fig. 1.3 and 1.4. The central part consists of the largest glacier concentration over the Himalaya (Fig. 1.4). Regionally median elevation of glaciers varies between 5060–5700 m.a.s.l over the Himalaya. The mean ELA of Himalayan glacier is 5237 m a.s.l., which has a large regional variability. Also, the median elevations are a good proxy for the first-order guess of the ELA for a typical Himalayan glacier (Fig. 1.5).

1.10.1 Regional climate

The sources of the moisture over the Himalaya are brought from the Arabian sea, the Mediterranean region by the Westerlies, and the Bay of Bengal by the Indian summer monsoon (Bookhagen and Burbank, 2010). The Indian summer monsoon brings the ocean moisture over the Indian sub-continent, leading to intense precipitation during June–Sept particularly over the central, eastern, and some parts of the western Himalaya, where annual precipitation can reach up to 3 m (Bookhagen and Burbank, 2010; Maussion et al, 2014). Precipitation is due to the westerlies wind occurring mostly on the west part of the Himalaya during the winter, mostly in form of snow, with annual precipitation of about 1–2 m (Barlow et al, 2005; Bookhagen and Burbank, 2010; Maussion et al, 2014). Also, there is a strong north-south gradient in the precipitation due to the orographic effect over the Himalaya (Shrestha et al, 1999). Although the orographic effect increases the amount of precipitation with elevation (Barry et al, 1992), there is a significant spatial (Andermann et al, 2011) and temporal (Collier and Immerzeel, 2015) variability in the precipitation gradient observed over the Himalaya.

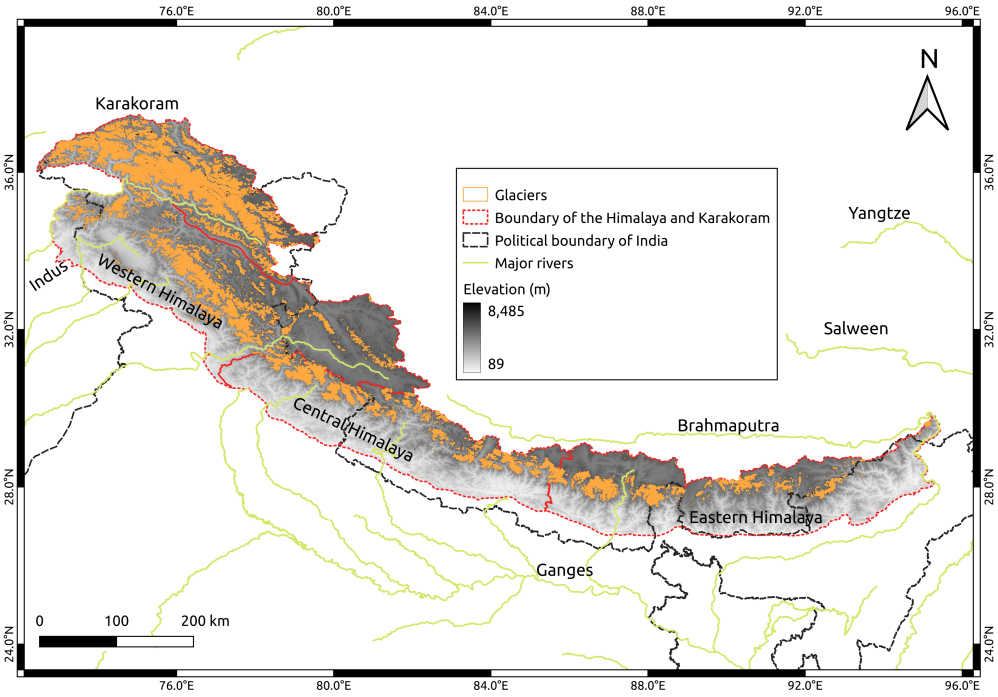

Figure 1.4: Distribution of glaciers over the Himalaya and Karakoram regions. The background elevation map was taken from 30 m resolution ASTER GDEM (version 3). The glacier boundaries were taken from RGI 6.0 (RGI Consortium, 2017). The political boundary of India is as per the Survey of India. The river network was taken from the GRDC dataset.

As glaciers over the eastern and central parts get summer-long snow accumulation due to monsoonal precipitation (Ageta and Higuchi, 1984), these glaciers are called 'summer accumulation type' glaciers. In the further west parts, the glaciers over the Karakoram, Pamir regions are called 'winter accumulation type' glaciers (Maussion et al, 2014).

1.10.2 Presence of debris covered glaciers

In most of Himalayan glaciers, the erosional processes at the high-steep headwalls and sidewalls provide a significant amount of debris into the glacier's accumulation zone by avalanches (Scherler et al, 2011a; Nagai et al, 2013; Banerjee and Wani, 2018) (Fig. 1.1). The deposited debris at the accumulation zone is transported englacially and emerged at the ablation zone of the glacier (Small et al, 1979; Kirkbride and Deline, 2013; Wirbel et al, 2018). This processes make a debris mantel which spread over the gently slopped lower part of the ablation zone (Quincey et al, 2009a; Scherler et al, 2011b). The debris thickness gradually increases towards glacier terminus up to a few meters (Nicholson et al, 2018; Shah et al, 2019).

The supraglacial debris strongly influence the surface energy balance on glacier. It is well established that supraglacial debris cover thicker than a few centimeters (>3 cm) insulates the underlying ice from the solar radiation (Östrem, 1959; Fujii, 1997; Mattson et al, 1993). The presence of thick debris cover reduces the available energy for glacier ice, which leads to changes in glacier mass balance profile (Naito et al, 2000; Banerjee and Shankar, 2013; Rowan et al, 2015; Anderson and Anderson, 2016; Ferguson and Vieli, 2021). Therefore, the specific mass balance profile of debris covered part is not linear compared to the clean ice part (e.g., Laha et al, 2017).

Here, we analysed the distribution of the fraction of debris cover area to the total ablation area of the glaciers over the Himalaya-Karakoram (HK) regions using an available dataset (Herreid and Pellicciotti, 2020). We found that the median of this distribution was 0.6 (Fig. 1.5). With that, we adopted a definition that glacier with debris covered area more than 60% of the total ablation area, we call it debris covered glacier. We found that 52% of the

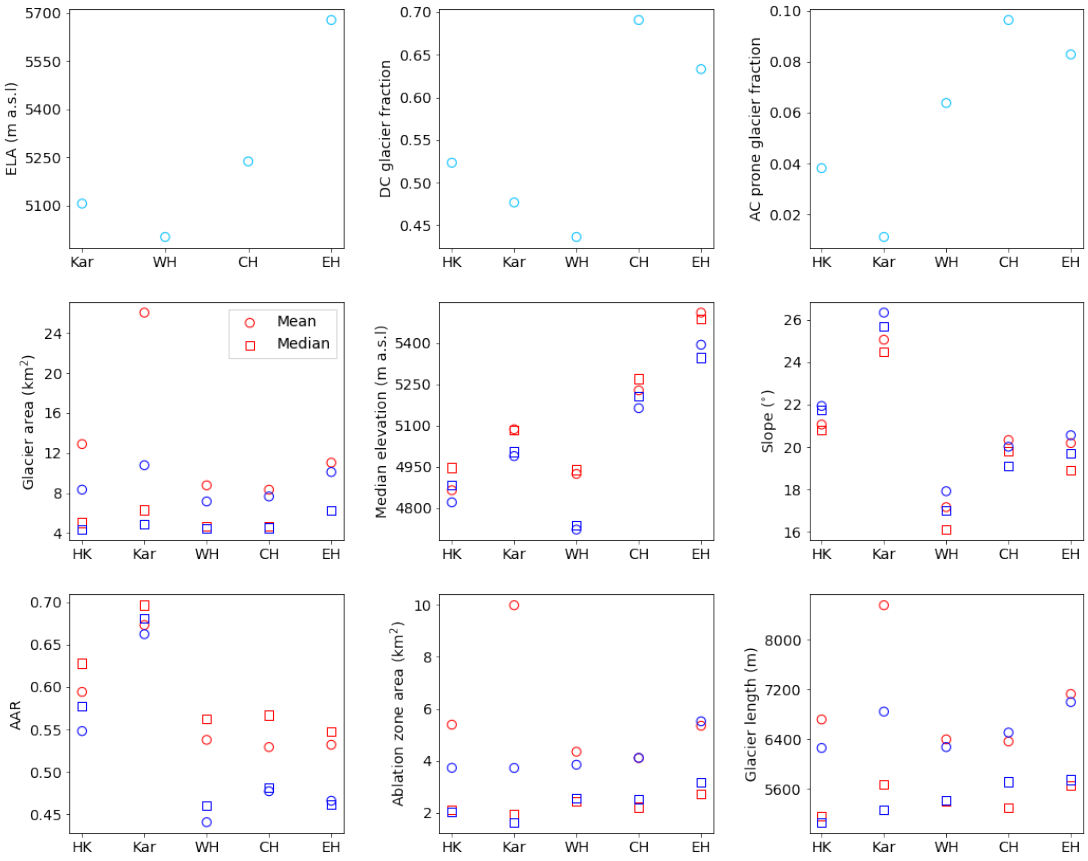

Figure 1.5: Mean (open circle) and median (open square) of the different properties of Himalaya-Karakoram glaciers are plotted here. The red color indicates all the glaciers in a region, and the blue color indicates the debris covered glaciers. The debris covered data was taken from Herreid and Pellicciotti (2020), and the region boundary was taken from Kraaijenbrink et al (2017). The notations 'AC', 'CH', 'EH', 'WH', 'Kar', 'HK' denotes avalanche, central Himalaya, eastern Himalaya, western Himalaya, Karakoram, and Himalaya-Karakoram, respectively. The ELA lines were available from Herreid and Pellicciotti (2020), with that, I used ASTER-30 m DEM to compute the mean ELA for a given region.

Himalayan glaciers have debris covering more than 60% of the total ablation area (Fig. 1.5). The typical median elevations and AAR values are relatively lower for debris covered glaciers than other glaciers.

1.10.3 Point scale energy balance studies

Point scale energy balance has been done in only a few glaciers over the Himalaya. These glaciers are AX010 (Kayastha et al, 1999), Chhota Shigri (Azam et al, 2014), Guxiang No. 3 (Wang and Deng, 1982), Parlung No. 4 (Zhu et al, 2015), Lirung (Sakai et al, 2002). Most of them are belong to the monsoon dominated central and eastern parts of the Himalaya. Only a few studies are available from the Karakoram region (Bonekamp et al, 2019).

The typical value of the albedo for fresh snow to debris covered ice varies from 0.98 to 0.3, as observed in the above studies over the Himalaya. The net shortwave energy typically ranges from 20 W m^{-2} (winter) to 200 W m^{-2} (summer monsoon) over the studied Himalayan glaciers. Glacier melt is mainly driven by the net shortwave radiation in the western part or Karakoram region, where the cloud cover is less during the melt season than in the central/eastern part of the Himalaya. In the Karakoram region, the surface albedo plays a dominant role in melt variability throughout the year (Bonekamp et al, 2019).

There is a typical seasonal variation of net longwave radiation is about -70 to 50 Wm^{-2} as observed over Himalayan glaciers. In the central and eastern part of the Himalaya, the melting is primarily dominated by the net longwave radiation due to the presence of both high- and low-level clouds during the melt season (Bonekamp et al, 2019). The melt rates are strongly correlated with the near-surface air temperature and melt (Ohmura, 2001). Therefore, the degree-day model is commonly used for melt estimation (Hock, 2003).

In a typical Himalayan glacier, the net radiation varies between -100 to 300 W m^{-2}. The sensible heat flux typically has maximum value in the summer-monsoon ($\sim$ 31 W m^{-2}). Latent heat flux is generally negative during post-monsoon and winter with typical values -40 to -30 W m^{-2} and positive during the summer monsoon ($\sim$ 10 Wm^{-2}).

1.10.4 Glacier scale mass balance studies

Glaciological mass balance studies

Very few glaciers over the Himalaya were monitored during the 19-th century due to the lack of national glacier monitoring programs. A Nepalese group started the first glaciological mass balance measurements on AX010, Yala, and Rikha Samba glaciers (Ageta et al, 1980; Fujita et al, 1998, 2001). After that, the Geological Survey of India (GSI) started monitoring the Gara glacier in 1974 (Raina et al, 1977). These mass balance data were mostly less than 10 years long. Presently, most of the glaciological mass balance measurements over the Himalaya are from India (covering western as well as parts of the central and eastern Himalaya) and Nepal (Azam et al, 2018).

Although it is assumed that the individual glacier mass balance would represent the corresponding region, glaciers are mostly selected for mass balance study based on logistical constrain. The glaciological mass balance measurements have been carried out in a total of 24 glaciers over the Himalaya, and most of them show negative mass balance. The glaciological mass balance ranges from -0.03 ± 0.28 to -1.43 m w.e yr^{-1}, with a mean value of -0.58 m w.e yr^{-1} from 1975–2015 (Azam et al, 2018). Typical glaciological mass balance uncertainty in the Himalayan glacier is about ± 0.3 (Mera glacier) to ± 0.4 (Chhota Shigri glacier) m w.e.yr^{-1} (Wagnon et al, 2013; Azam et al, 2012).

The seasonal snow accumulation measurements at high elevations are complicated due to wind drift, sublimation, and access difficulties. The ice core or shallow firn core is one of the important methods of evaluating snow accumulation rates, but these data are sparse or very limited over the Himalaya (Kaspari et al, 2008; Duan et al, 2015). Only a few ice-core data are available from the Himalaya (Thompson et al, 2000; Kaspari et al, 2008; Aizen et al, 2006, 2009). The typical accumulation rate on Himalayan glaciers is up to a meter water equivalent per year or more than that (Kaspari et al, 2008). Locally the accumulation rates are strongly influenced by wind speed and avalanche activities.

Only a few field-based records of ELA exist over the Himalaya; these are

from the Chhota Shigri glacier (Wagnon et al, 2007, 2013) and a few glaciers from Nepal (Acharya and Kayastha, 2019). However, long-term records are limited due to accessibility issues on the Himalayan glaciers and funding availability to carry out field expeditions. The typical range of mass-balance gradient is 0.003-0.01 m.w.e. yr^{-1} m^{-1}, although there is significant spatial variation over the Himalaya (Azam et al, 2018). On clean glaciers, the mass-balance gradient is a function of elevation; in contrast, the mass balance gradient in debris covered glaciers depends on the debris thickness distribution (e.g., Shah et al, 2019).

Problems associated with the glaciological mass balance measurements

The glaciological method of estimating glacier mass balance needs a lot of human effort and is often quite challenging. Also, debris in the ablation zone poses a logistical challenge in accessing glacier. For example, due to the difficulties in drilling on debris covered glaciers, the debris thickness measurements are mostly in the range of 30–50 cm where the stakes were installed (e.g., Nakawo and Young, 1981; Kayastha et al, 2000; Mihalcea et al, 2006; Haidong et al, 2006; Hagg et al, 2008). The glaciological mass balance measurements generally choose a relatively small and clean glaciers for a regional representative (e.g., Kaser et al, 2003). As a result, there are around 24 glaciers over the Himalaya, where glaciological measurements have been carried out or continued, and most of them are clean glaciers (Azam et al, 2018).

Lack of accumulation measurements due to inaccessible terrain in the accumulation zone of a typical Himalayan glacier (e.g., Vincent et al, 2013a), may bias the glaciological mass balance estimates (Fujita and Nuimura, 2011; Laha et al, 2017). The point scale precipitation (or particularly rainfall) measurement at the glacier base camp is generally used to extrapolate (with some precipitation gradient) over the glacier to get the snowfall accumulation (e.g., Ageta and Higuchi, 1984). Different statistical relations are used to estimate the probability that the precipitation falls as snow. These relations use a

threshold air temperature (T_{th}), below which the probability of snowfall is 1 and above that the probability is 0. T_{th} depends on the relative humidity and atmospheric pressure (Jennings et al, 2018). On a typical Himalayan glacier with a steep headwall, avalanches can transfer a large amount of snow on the glacier surface. In a high relief environment, avalanches are expected to have dominant control on the glacier accumulation process, which is very hard to measure (Benn and Lehmkuhl, 2000). Therefore, total accumulation estimation sometimes may have biases due to avalanches (Vincent et al, 2013a; Laha et al, 2017). Despite the importance of the avalanche, there is a serious lack of direct methods of estimating the avalanche contribution to the total accumulation of glaciers (Laha et al, 2017).

Ablation modelling over debris cover glaciers

Östrem (1959) introduced the concept of the enhanced ablation under thinner ($<$ 3–5 cm) debris and reduced ablation for thicker ($>$ 5 cm) debris. The critical debris thickness was defined as 3–5 cm (Östrem, 1959; Mattson et al, 1993). As the debris thickness has significant control on ice ablation, many studies tried to better constrain the Ostrem, (1959)'s curve by field measurements, experiments, and the energy balance modelling approaches.

A physically-based energy balance model requires a lot of in-situ meteorological measurements, which is the major limitation of this method, as these data are relatively scarce in the Himalaya. To date, ice ablation on the debris covered glaciers is generally obtained using simple degree-day models (Hock, 2003), modified degree-day models (Carenzo et al, 2016; Vincent and Six, 2013; Pellicciotti et al, 2005; Mihalcea et al, 2006), and/or a few physically-based models (Nakawo and Rana, 1999; Fujita and Sakai, 2014).

Conway and Rasmussen (2000) pioneered a relatively easy way of estimating the ice ablation on debris covered glaciers by measuring the vertical temperature profiles within the debris layer and assuming the debris layer as a homogeneous thermal conductor. This method has been applied to several debris covered glaciers over the Himalaya (Haidong et al, 2006; Nicholson and Benn, 2013; Chand et al, 2018; Rowan et al, 2020) and outside the Himalaya

(Nicholson and Benn, 2006). One of the major limitations of this method is that, the debris thermal properties may not be homogeneous in general, where the water/moisture content (Nicholson and Benn, 2013; Collier et al, 2014; Giese et al, 2020), porosity (Hinkel et al, 2001), etc, within debris can play an important role, can change the effective thermal properties. Therefore, a method of analysing vertical temperature profiles data that can take care of the vertical inhomogeneity of the debris thermal properties would be useful in this context.

1.10.5 Regional mass balance studies

Over the Himalaya-Karakoram, the mean geodetic mass balance was -0.21 ± 0.05 m w.e yr^{-1} during 2003–2008 (Kääb et al, 2012). Gardner et al. (2013) estimate the glacier mass loss rate -0.24 ± 0.11 m w.e yr^{-1} from ICESat satellite data, -0.16 ± 0.17 m w.e yr^{-1} from GRACE observations, and -0.72 ± 0.22 m w.e yr^{-1} by extrapolating glaciological observations over the Himalaya-Karakoram during 2003–2009. Brun et al. (2016) improved the geodetic mass balance estimation over whole high mountain Asia and estimated mean mass loss of -0.18 ± 0.04 m w.e yr^{-1} during 2000–2016, with relatively stable Karakoram glaciers (e.g., Fig. 1.6). They attribute the Himalaya has a negative mass balance of -0.33 ± 0.20 to -0.42 ± 0.20 m w.e yr^{-1}, and the Karakoram had zero mass balance (-0.03 ± 0.07 m w.e yr^{-1}). To date, systematic geodetic mass balance data is available from Shean et al. (2020) and Hugonnet et al (2021). It shows the mean mass balance over the Himalaya-Karakoram from 2000–2018 is -0.19 ± 0.03 m w.e yr^{-1}, a relatively stable Karakoram (Fig. 1.6). Large-scale studies show that, despite the insulating effect of debris, the thinning of debris covered ice is not significantly different from the thinning of clean ice, and sometimes the thinning from debris covered part exceeds the clean ice thinning (e.g., Kääb et al, 2012; Brun et al, 2017, 2019).

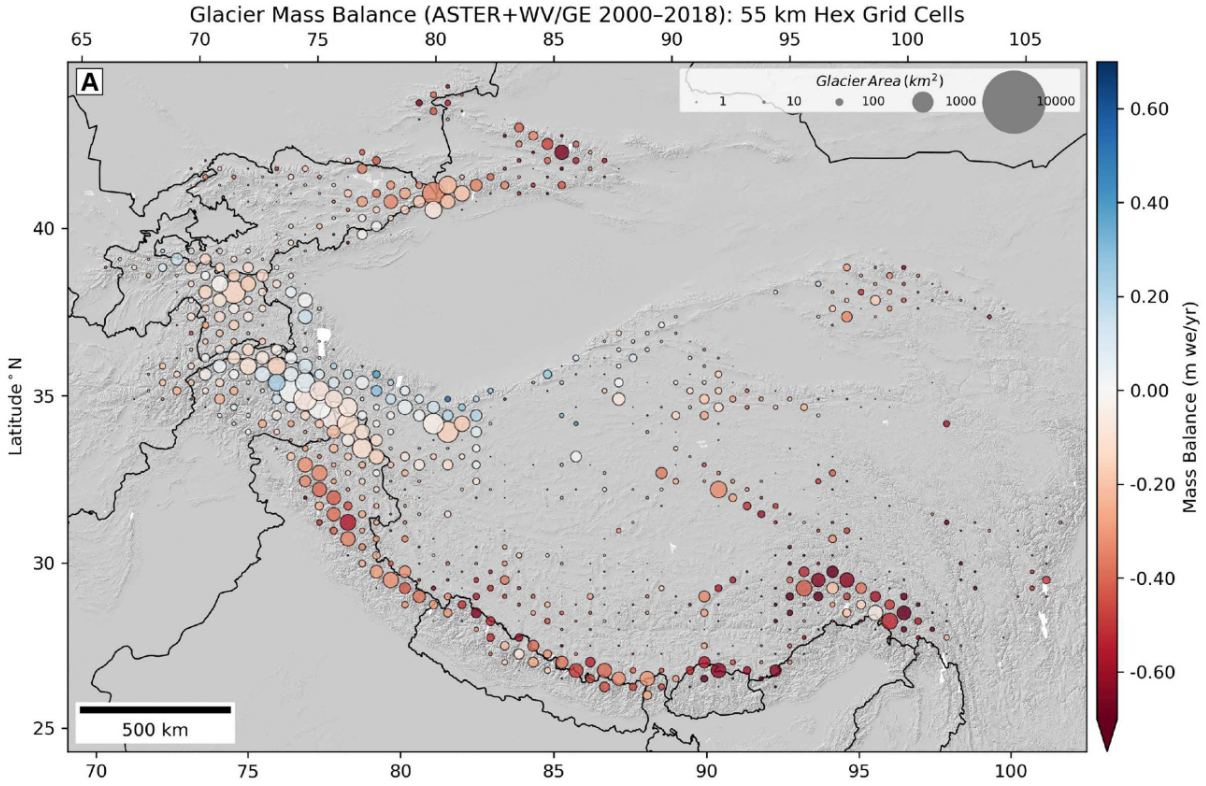

Figure 1.6: The specific glacier mass balance during 2000–2018 over the Himalaya-Karakoram regions (aggregated over 55 km grid cells) (Shean et al, 2020).

1.10.6 Inhomogeneous mass loss pattern

The spatial variability of the glacier mass balance over the Himalaya (Fig. 1.6) is mainly controlled by the regional climate forcing and corresponding glacier sensitivity to that climate forcing (Fujita and Nuimura, 2011; Sakai and Fujita, 2017; Brun et al, 2017; Shean et al, 2020). In general, the spatial variability of climate forcing comes through the near-surface air temperature, precipitation (and its seasonality), and insolation effect. The local scale spatial variability of mass balance (Fig. 1.6) is associated with the variable glacier geometries, presence of debris cover, mean ice thickness, supraglacial lakes/ice-cliffs, and so on (Fujita and Nuimura, 2011; Brun et al, 2019; Wang et al, 2019; Shean et al, 2020).

Most of the regions in the eastern Himalaya (particularly in the Everest region) (Fig. 1.6) show large negative mass balances, which is mainly due to the reduced precipitation or weakening the summer-monsoon there (Maurer et al, 2019; Shean et al, 2020). However, in the monsoon dominated central and eastern Himalaya, glaciers with high accumulation rates are more sensitive to temperature change than the amount of accumulation changes (Rupper and Roe, 2008). The large scale studies show less than a 10% rise in the annual mean rainfall and a small increase of winter snowfall over the Himalaya (e.g., Maurer et al, 2019). The near-zero mass balance over the Karakoram (Fig. 1.6) is known as the 'Karakoram anomaly', consistent with other studies (e.g Gardelle et al, 2012, 2013; Rankl et al, 2016). This situation is attributed to the increased winter snowfall (e.g., Archer and Fowler, 2004; Brun et al, 2017; Kumar et al, 2019; Shean et al, 2020) and the decrease in the mean summer temperature (e.g., Fowler and Archer, 2006) since 1960 (Bashir et al, 2017; Forsythe et al, 2017).

1.10.7 Importance of glaciers in basin scale runoff

The Himalaya is known as the 'water tower' of Asia (Xu et al, 2009; Immerzeel et al, 2020; Armstrong et al, 2020). Most of the important rivers in Asia originate from the Himalayan region; some of the western rivers (e.g., Indus) mostly depend on glacier melt due to weaker monsoon contribution (Azam

et al, 2021; Kulkarni et al, 2021). Any changes in glaciers directly affect the meltwater runoff and the seasonality of the river flow (Huss and Hock, 2018). The corresponding changes in river runoff may affect the water availability for the downstream population (Kaser et al, 2010; Ali et al, 2018; Biemans et al, 2019; Kulkarni et al, 2021). In addition, retreating glaciers increase the frequency of the moraine dammed lakes (Harrison et al, 2018), which are the potential natural hazards (Rounce et al, 2016). Preparedness to mitigate such challenges would require a detailed understanding of different hydrological processes over the Himalaya and accurate prediction of the future glacier changes in the region.

The basin scale runoff of the glacierised catchment mainly consists of rainfall, snowmelt, baseflow, and glacier melt (Lutz et al, 2014). The contribution of the glacier meltwater to the river runoff has a substantial spatial variability over the Himalaya, mainly driven by the glacier fraction, glacier volume, accumulation/ablation periods, atmospheric circulation, and the magnitude of other contributing components in the catchments (Gao et al, 2010; Lutz et al, 2014; Radić and Hock, 2014; Lutz et al, 2016). The glacier melt contribution is more important in the arid, and semi-arid westerlies controlled the west part of the Himalaya, e.g., Tarim (42%) (Gao et al, 2010), Upper Indus (33%) (Lutz et al, 2016) basins. Glacier melt contribution is relatively less significant in the monsoon dominated central or eastern part of the Himalaya, e.g., upper Ganges (12%), upper Brahmaputra (16%) (Lutz et al, 2014) basins. The glacier melt contribution decreases with decreasing altitudes, particularly in monsoon dominated regions. For example, precipitation contribution became dominant with the river flows in lowlands (e.g., Racoviteanu et al, 2013). But, how exactly glacier meltwater contribution depends on the glacierised fraction of the basins is still an open question.

Glacier melt is highly sensitive to the temperature (e.g., Azam and Srivastava, 2020), and the melt mostly occurs during the summer season (June–September) over the Himalaya. Due to recent warming, the temperature-controlled glacier melt shows a positive trend in some highly glacierised basins in the west Himalaya (Gao et al, 2010; Mukhopadhyay and Khan, 2014; Hasson et al, 2017). In the central/eastern Himalaya, some of the basins expe-

rienced a recent decrease in runoff due to a decline in precipitation (Chen et al, 2017; Anand et al, 2018). The overall climate response in the basin scale runoff over the Himalaya is highly variable and complex (Leclercq and Oerlemans, 2012; Sorg et al, 2012; Li et a, 2016; Ragettli et al, 2016; Huss and Hock, 2018). In particular, the individual glacier related process like the avalanching, presence of debris on the glacier limits the glacier scale understanding (e.g., Zhang et al, 2016). In the changing climate, the sensitivity of basin-scale river runoff to the meteorological forcing like temperature, precipitation could be a useful tool to understand the climate response of the river runoff over the Himalaya.

The annual glacier runoff is projected to rise and then decline by the end of the century as most of the glaciers are shrinking, but the timing of the 'peak water' (Huss and Hock, 2018) varies over the basins (Nie et al, 2021). The peak water timing depends on the total ice volume and glacierised fraction of the basin. The peak water timing is expected to appear by 2050 in some central and eastern Himalayan basins (Lutz et al, 2014; Huss and Hock, 2018; Luo et al, 2018; Rounce et al, 2020) according to the RCP4.5 scenario, and this prediction varies depending on the different RCP scenario (Nie et al, 2021). Understanding the present state of the basin-scale runoff over the Himalaya typically suffers from large uncertainties mainly due to the scarcity of glacio-hydro-meteorological measurements from the high-altitude areas (Wijngaard et al, 2017), spatial fragmentation of studies, non-uniformity of the method used, difficulties in accessing hydrology datasets that exist, biases in the available climate data (Wortmann et al, 2018). As discussed above, the uncertainties in the present state make the future predictions more uncertain.

1.11 Active research areas in the context of Himalayan glaciers

A significant fraction of the ablation zone of the Himalayan glacier is often covered by a thick layer of debris (Kraaijenbrink et al, 2018; Scherler et al, 2018; Herreid and Pellicciotti, 2020), which insulate the ice and complicates

the glacier-climate interactions. Highly debris covered glaciers typically have high and steep headwalls and sidewalls, where avalanches are frequent. These avalanches bring a lot of snow and debris to the glacier. The quantification of such avalanche contribution to the mass balance is missing because the field measurements of such avalanches are very difficult due to inaccessible avalanche cones. Therefore, modelling avalanches would be useful. The modelling of ablation on the debris covered glaciers typically used degree-day based models, which are oversimplified and may not capture the actual physical processes there. Direct glaciological mass balance studies are very limited over debris covered Himalayan glaciers due to logistical issues (Shah et al, 2019). Any relatively easy field-based technique to estimate the ablation on the debris covered part would be beneficial. These problems indicate that the mass balance processes over debris covered Himalayan glaciers need more focus.

Glaciers can maintain a relatively constant water supply during hot/dry years from the ice and snow reservoirs. So, if glaciers vanish, the frequency of extreme climate events (e.g., floods and droughts) is likely to increase. However, despite a lot of attention, quantification of the snow/ice reservoir contribution to the river runoff suffers from large uncertainties. One of the major reasons is the lack of in-situ measurements on glaciers, despite extensive glacier coverage over the Himalaya. On top of that, different methodologies like isotopic studies, water balance studies, and hydrological models add more complexity because of their various inherent uncertainties. The climate sensitivity of the runoff from high Himalayan catchments remains poorly constrained in the literature. Accurate estimates of the climate sensitivities of runoff can also be used to benchmark complex hydrological models (e.g., Dooge et al, 1999; Vano et al, 2014).

The high Himalayan catchments have the key properties to generate high runoff due to higher orographic rainfall and delayed release of water by storing in glaciers and snow. The key input data are the precipitation and air temperature to model the runoff, which are generally taken from gridded or reanalysis datasets. These datasets (particularly precipitation data) can have significant biases over the high Himalayan region due to existing complex to-

pography and the limited availability of in-situ meteorological measurements. Particularly, there is a serious lack of in-situ snowfall measurements over the Himalaya. One way forward for these issue is to setup more meteorological stations over the Himalaya and calibrate the gridded and/or reanalysis datasets. All the above understanding may help to reduce the existing significant uncertainties in the future prediction of the Himalayan glaciers and river runoff from the glacierised catchments.

Also, many high-altitude hydroelectric power stations are located over the Himalaya. The glacier related hazards like GLOFs, ice avalanches, etc, have the potential to damage the high Himalayan infrastructures. Recent studies show that the frequency of glacier-related hazards like GLOFs are likely to increase as glaciers shrink. To prevent damages, it requires a good understanding of glacier hazards related processes and identifying risky areas. This understanding will help to choose the locations of future hydro-electric stations, and the government can make aware of the existing stations.

1.12 Research objective of the present thesis

The objective of the thesis is to understand the important processes related to glacier mass balance and the climate response of glacier-fed rivers over the Himalaya. Here, we develop novel modelling and field-based methods to quantify important processes related to the accumulation and ablation of ice on debris covered Himalayan glaciers. We also analyse the climate sensitivity of the runoff of glacier-fed rivers to understand future runoff changes and their variability. The three specific problems addressed in this thesis are given below.

- While avalanching is a potentially significant contributor to the accumulation of a large fraction of debris covered glaciers over the Himalaya, it was ignored in field-based glaciological mass balance measurements. Here, we used 1-d glacier model simulations to quantify the avalanche contribution to the total accumulation for a few well-studied Himalayan glaciers.

- In many Himalayan glaciers, the supraglacial debris controls the supply of melt energy to the ice surface. We measured the vertical temperature profiles within the debris layer at 16 locations on the Satopanth glacier (the central Himalaya), Uttarakhand, India. We develop novel methods of analysing such data. The accuracy of the methods are tested using numerical experiments and in-situ measurements of sub-debris ice ablation rates.

- Analysis of the climate sensitivity of runoff is a tool to understand the climate response of runoff from the glacier-fed rivers, and it is poorly constrained for Himalayan rivers. Here we computed the climate sensitivity of river runoff in two Himalayan catchments. The estimated sensitivities are used to predict the future river runoff changes and their variability.

The above problems will contribute to improved predictability of mass balance processes of Himalayan glaciers, and that of the changing runoff of glacier-fed Himalayan rivers. The details of the individual problems are discussed in the subsequent chapters.

1.13 Organization of the present thesis

In this thesis, the glacio-hydrological research was carried out over the Himalaya. The thesis organization follows a general understanding of the glacio-hydrology over the Himalaya from basin scales to individual glacier scales. Chapter 1 above provides a review of the current state of understanding, leading to the research problems addressed in this thesis. The main research consists of three chapters, each based on an identified problem, followed by a chapter of conclusions and future outlook. This research has been published or under review in peer-reviewed scientific journals. Although there is no difference in the core scientific ideas and results, the layout of a chapter and that of the corresponding published/under-review articles may not match perfectly.

Chapter 2

Importance of avalanches to the total accumulation of debris covered glaciers

2.1 Introduction

Avalanches are the mechanical failure of snowpacks accumulated on a steep slope; it is a highly localised and stochastic accumulation of snow or ice, which is common in high mountains (Schweizer et al, 2003) like the Himalaya. The frequency, magnitude, and seasonality of avalanches depend on the snow type, thickness, and stratigraphy (Schweizer, 1999). Also, changing climate can trigger avalanche activity by changing the snowfall pattern (Ballesteros et al, 2018).

Generally, avalanche-fed glacier typically has high slopes in the ice catchment area. The headwall slope $> 30^{\circ}$ and connected to the accumulation zone are considered as the potential avalanche-prone zone of a glacier (Hughes, 2008). A study of 287 glaciers from Himalaya and Karakoram shows that 18% of those glaciers satisfy the above criteria for dominant avalanche-fed (Scherler et al, 2011a), and a high percentage of the ablation area of these glaciers are debris covered. This type of glaciers is very common in the Himalaya (Benn et al, 2003; Scherler et al, 2011a; Nagai et al, 2013). For

example, around 10% of glaciers in the central and eastern Himalaya are highly avalanche-fed (Fig. 1.5).

Avalanche carried a significant amount of snow and deposited it on the glacier surface. The glaciological measurements of this snow accumulation are very difficult due the hazardous avalanche cones along the valley walls (Fig. 2.1) of the glacier. Therefore, in-situ mass balance measurements missed the avalanche-induced snow accumulation, which may bias the estimates. Also, it is important to quantify the avalanche contribution to understand the long-term glacier response to climate change. Although the importance of avalanches is noticed by several studies (Benn and Lehmkuhl, 2000; Benn et al, 2003; Scherler et al, 2011a; Nagai et al, 2013), there is a lack in the quantification of such avalanche contribution as far as Himalayan glaciers are concerned.

Several models are developed to study the avalanche quantification by snow redistribution due to the gravitational process (Gruber, 2007; Bernhardt and Schulz, 2010). This kind of model needs snowfall data as one of the major input. Reanalysis or gridded precipitation data are generally used to get the snowfall. But there is a lack of field measurements of snowfall from the Himalaya (Viste and Sorteberg, 2015) to validate the reanalysis or gridded data, limiting the applicability of these models. However, these methods would not be capture the avalanche contribution to the mass balance of reconstituted glaciers (Benn et al, 2003). Therefore, the development of a method to quantify the avalanches would be helpful to reduce the inherent uncertainties in the glaciological mass balance estimates from these glaciers.

Motivated by that, we hypothesise that the significant avalanche accumulation exerts control on the observed shrinkage pattern in these Himalayan glaciers. If that is true, then the shrinkage pattern can be utilised to quantify the avalanche contribution. Here, we discuss diagnostic criteria for the identification of strong avalanche-fed glaciers. Then, we developed a novel method that provides a first-order quantification of the avalanches using numerical flowline model simulation. Here, we apply our method for Satopanth Glacier (30.73°N, 79.32°E) and Dunagiri Glacier (30.54°N, 79.89°E; also known as

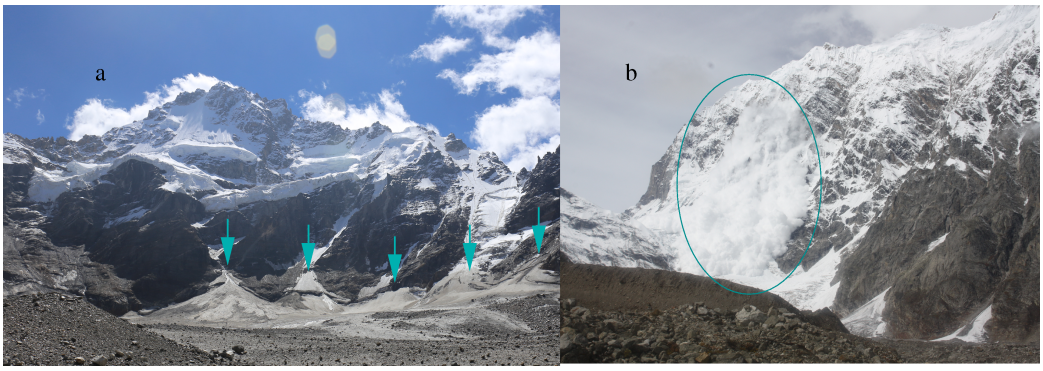

Figure 2.1: (a) The headwall of Hamtah glacier shows large avalanche cones. (b) A massive avalanche rolled down from the Choukhamba massif (7138 m) at the headwall of Satopanth glacier.

Dronagiri) in the central Himalaya, and Hamtah Glacier (32.22°N, 77.38°E) in the Western Himalaya (Table 2.1), where strong avalanche activity is suspected. We also performed a control simulation with the Chhota Shigri Glacier (32.28°N, 77.58°E), located ∼12 km to the west of Hamtah Glacier in the western Himalaya, where avalanches are not expected, and there we check the consistency of our method.

2.2 Identification of strongly avalanche-fed glaciers

2.2.1 Literature

Strongly avalanche-fed glacier typically has relatively smaller accumulation areas with steep slopes, and the steady-state AAR values are much lower (Benn and Lehmkuhl, 2000). Another study (Scherler et al, 2011a) shows that the glaciers with smaller AAR are correlated with other proxies for strong avalanches, like high slopes in the ice-catchment areas and a high percentage of ice-free catchment above the snowline. It is observed that any glacier with AAR<0.2 but doesn't show any fast retreat may be a strong avalanche-fed.

The avalanche release zone is typically defined as the area in the glacier

headwall with a slope $> 30^{\circ}$ and connected with the accumulation zone (Hughes, 2008). The ratio (R) of the total avalanche-release area to the total area of a glacier is used as an indicator of the strong avalanche-fed glacier (Hughes, 2008). However, extensive debris cover often associated with strong avalanche activity suppresses ablation leading to a larger glacier area (Banerjee and Shankar, 2013). This effect reduces the sensitivity of the ratio R to the presence of avalanche contribution in debris-covered glaciers (Table 2.1).

2.2.2 A new indicator for strong avalanche-fed glaciers

We propose a new indicator (R') for a strong avalanche-fed glacier. R' is a ratio defined as,

$$R' = \frac{\text{Area of avalanche release zone}}{\text{Total accumulation area}}. \quad (2.1)$$

This may work better for the debris covered glaciers since the total accumulation due to the direct solid precipitation (avalanching) is proportional to the area of the accumulation zone (avalanche-release zone) irrespective of the presence of a debris cover. The values of R' for the studied glaciers are discussed in Table 2.1.

2.3 Study area

We selected four well-studied Himalayan glaciers (Table 2.1) for this study (Fig. 2.2), where glaciological data are available. Out of these four glaciers, three of them (Satopanth, Hamtah, and Dunagiri) are suspected to be strongly avalanche-fed, and one (Chhota Shigri) is avalanche-free (Fig. 2.2).

The suspected avalanche-fed glaciers have AAR well below 0.2 and high debris cover fraction (Table 2.1). We have estimated the ratio R to be 0.8, 0.8, 0.7, and 0.3 for Satopanth, Dunagiri, Hamtah, and Chhota Shigri, respectively. The corresponding values of R' are 4.4, 6.1, 4.8, and 0.6, respectively. For the potential avalanche-fed glaciers, R' values are an order of magnitude larger than the glaciers with no avalanches (Table 2.1). We also checked for

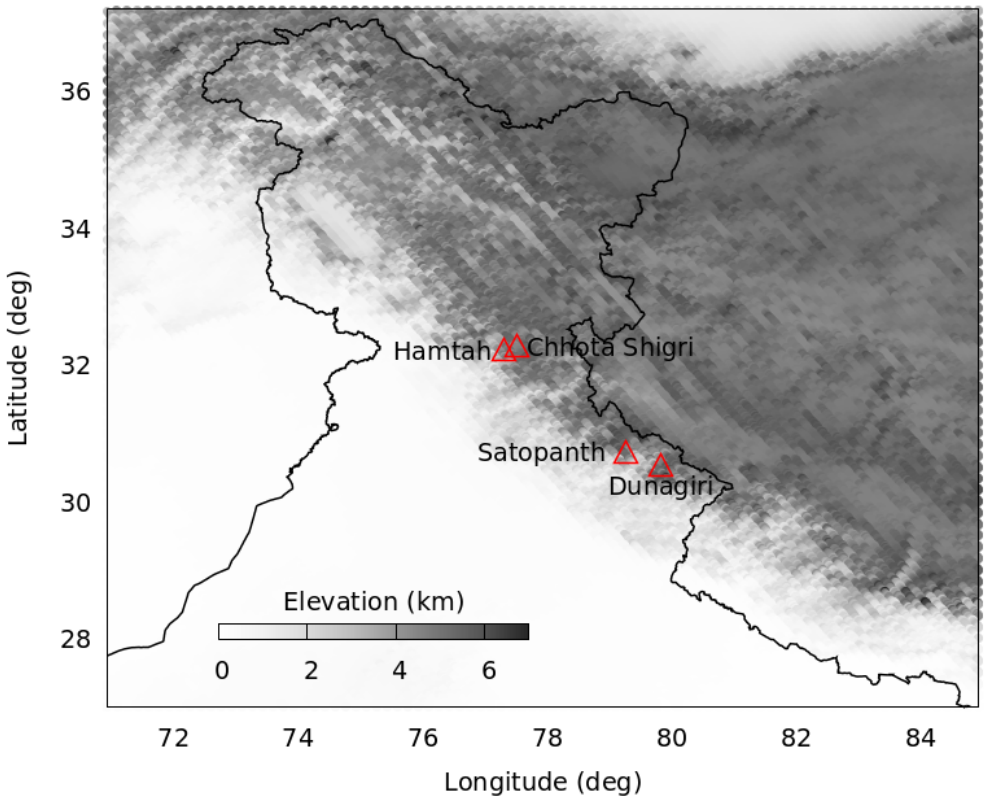

Figure 2.2: The location of the four studied glaciers is shown by open red triangles. The solid black line is the political boundary of India. The background color is the grey-scale elevation map (Amante et al, 2009).

another Himalayan glacier Dokriani (area 7 km^2, AAR 0.66, and debris-cover fraction 0.10), where the ratio R' was 0.9. All the values listed in Table 2.1, indicate strong avalanche contributions on Hamtah, Satopanth, and Dunagiri glaciers. In contrast, Dokriani and Chhota Shigri Glaciers may not receive any such significant avalanche contribution.

The glaciological mass balance from Hamtah (-1.45 m w.e. yr^{-1}) and Duangiri (-1.0 m w.e. yr^{-1}) shows the most values balance out of the set of 15 available glaciers in-situ mass balance data (Vincent et al, 2013) compared to their regional geodetic mass balance, which was in the range of -0.33 to -0.65 m w.e. yr^{-1} (Vincent et al, 2013). In Hamtah and Dunagiri glaciers, the details of the accumulation measurement e.g., pit locations, total number of pits, etc, are not available. The mass balance of Satopanth Glacier shows a negative value of -2.0 m w.e. yr^{-1}, where the accumulation is not measured directly and is obtained by extrapolation. The measurement of accumulation is somewhat difficult in extensively debris covered glaciers because of the related hazards due to its morphology. Despite the inherent uncertainties in the accumulation measurement in highly debris covered glaciers, such a large negative mass balance (Table 2.1) and the above-mentioned morphological characteristics indicate a strong avalanche activity on these glaciers that may have remained unaccounted for in the glaciological mass balance estimates.

The details of the individual glaciers (Table 2.1) used in this study are discussed below.

Satopanth Glacier

Satopanth Glacier (30.73°N, 79.32°E, central Himalaya) is in the Garhwal region of India (Fig. 2.2). It is around 14 km long with a total area of 19 km^2, which spans over 3900–6200 m a.s.l (Shah et al, 2019); almost 56% of the total area of the glacier is covered by supraglacial debris. The reported retreat rate was 5.6 ± 0.7 m yr^{-1} during 1957–2013 and a thinning rate of 0.18 ± 0.22 m yr^{-1} during 1962–2013 (Nainwal et al, 2016) used in this study. Our group initiated the mass balance measurements in 2014, the results are reported in Shah et al (2019). Here, we used the mass balance year Octo-

ber 2014 to October 2015 data derived from 40 stakes distributed over an elevation range of 3950–4625 m a.s.l on the glacier (Fig. 2.3a). Two best-fit elevation-dependent linear mass balance profiles are extracted from the stake data, one for the debris covered and another one for the debris-free ice, respectively. For the inaccessible debris free part at the higher reaches of the glacier where no stake data is available, the mass balance values are extrapolated using the above linear profile with an upper cut-off of 1.5 m w.e. yr^{-1} applied to the accumulation values. To compute the mass balance in each elevation band, we use the sum of the two mass balance values weighted by the corresponding debris-covered and debris free ice fraction at that elevation band (Fig. 2.4). The equilibrium line altitude (ELA) of 4910 m obtained from the extrapolation of the linear mass balance profile for the debris free ice compares well with the independent estimate of 4840 m a.s.l from the highest position of the end of summer transient snowline elevation as observed in cloud-free Landsat scenes from the year 2013 and 2016.

Hamtah Glacier

Hamtah Glacier (32.22°N, 77.38°E, western Himalaya) is located in the Lahul Spiti region district of Himachal Pradesh, India (Fig. 2.2). The glacier is 6 km long with a total area of 3.7 km^2 which spans over 4000–5000 m a.s.l (Shukla et al, 2015) (Fig. 2.3b), almost 68% of the total area of the glacier is covered by supraglacial debris. The reported long-term retreat rate of the glacier was 25.5 m yr^{-1} during 1963–2010 (Pandey et al, 2011). The retreat rate had come down to 13 m yr^{-1} during 1989–2010 (Pandey et al, 2011). The glaciological mass balance of the glacier was -1.45 m w.e. yr^{-1} during 2000-2009, measured by the Geological Survey of India (GSI) (Shukla et al, 2015). The mass-balance profile used in the simulation is a linear approximation of the available data for the mass balance year 2008–2009 (Fig. 2.4).

Dunagiri Glacier

Dunagiri Glacier (30.54°N, 79.89°E, central Himalaya) is located in the Chamoli district, Uttarakhand, India (Fig. 2.2). The glacier is around 4.2 km long with

a total area of 2.4 km^2 which spans over an elevation range of 4200–5100 m a.s.l (Kumar et al, 2017) (Fig. 2.3c). 85% of the total glacier area is covered by supraglacial debris. The long-term retreat rate of the glacier was reported 9 ± 0.6 m yr^{-1} during 1962–2013. Field data on the surface velocities and mass balance profile are available for the period 1984–1990 (Srivastava and Swaroop, 1992). We use the data of 1986–1987 as the corresponding mass balance (-1.0 m w.e. yr^{-1}) is similar to the mean mass balance for the whole observation period (Fig. 2.4). The mass balance profile used (Fig. 2.4) is a piece-wise linear approximation of the data.

Chhota Shigri Glacier

Chhota Shigri Glacier (32.28°N, 77.58°E, western Himalaya) is located in the Lahul Spiti district of Himachal Pradesh, India (Fig. 2.2). The glacier is around 9 km long with a total surface area of 15.7 km^2 which spans over an elevation range of 4050–6263 m a.s.l (Azam et al, 2014). This glacier is mostly debris-free, with approximately 4% of the total surface area is debris-covered (Vincent et al, 2013a). The morphology of Chhota Shigri Glacier (Table 2.1) indicates that the glacier may not get a significant avalanche contribution. The glacier had a long-term retreat rate of 25 m yr^{-1} during 1972–2006 (Ramanathan et al, 2011). The glaciological mass balance of the glacier was -0.57 ± 0.40 m w.e yr^{-1} during the period of 2002–2012 (Azam et al, 2014). The observed mean ELA was 5075 m a.s.l during 2002–2012 (Azam et al, 2012). The glacier had geodetic mass balance of -0.17 ± 0.09 m w.e yr^{-1} during 1988–2010 (Vincent et al, 2013a).

In all the studied glaciers, the mean surface velocity was obtained from the reported remote sensing data from 2000–2007 (Scherler et al, 2011a). The surface elevation data along the central flowline was obtained from Shuttle Radar Topographic Mission (SRTM1) DEM (Farr et al, 2007).

Table 2.1: Observed glacier properties.

Glacier name	Area (A) (km^2)	Accumulation-area ratio (α)	Debris-covered fraction	Avalanche-release zone (C) (km^2)	R $\left(\frac{C}{A}\right)$	R' $\left(\frac{C}{\alpha A}\right)$	Retreat rate (period) (m a^{-1})	Glaciological mass balance (m w.e. a^{-1})
Satopanth	19.0	0.18	0.56	15.2	0.8	4.4	5.6±0.7 (1957-2013)	-2.0 (2015)
Dunagiri	2.4	0.13	0.85	1.9	0.8	6.1	9.0±0.6 (1963-2013)	-1.0 (1984-1990)
Hamtah	3.7	0.14	0.68	2.5	0.7	4.8	25.5 (1963-2010)	-1.45 (2000-2009)
Chhota Shigri	15.7	0.46	0.04	4.3	0.3	0.6	25 (1972-2006)	-0.57 (2002-2012)

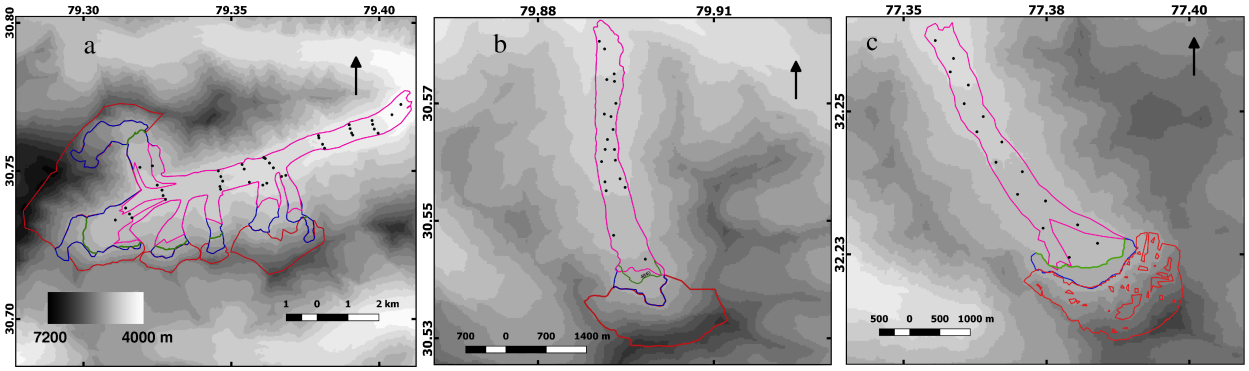

Figure 2.3: Maps showing glacier boundary (blue), the extent debris cover (pink), potential avalanche release zone (red) for (a) Satopanth Glacier, (b) Dunagiri Glacier, and (c) Hamtah Glacier. The background is the 200 m grey-scale contour map of SRTM1 DEM. The corresponding ELAs are shown as green lines. Approximate stake locations are shown as black dots.

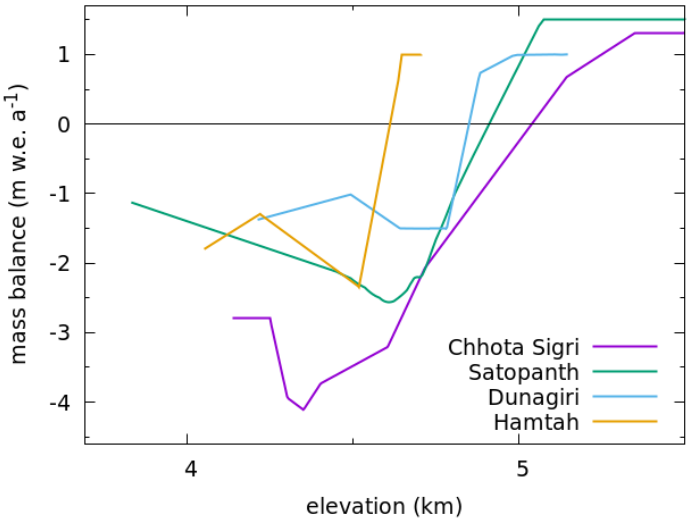

Figure 2.4: The mass balance profiles for the four studied glaciers.

2.4 Method of estimating the avalanche contribution

Our basic assumption is that the glaciological mass balance typically have a significant negative bias for any strongly avalanche-fed glacier. Then, the glaciological mass balance would be inconsistent with the observed state and the recent history of the glacier. For example, if the glacier is in a steady state, the observed steady-state length would be much larger than the length consistent with the mass balance. For a retreating glacier, both the long-term retreat rate and the thinning rate may be much smaller than the observed values. It may be noted that since avalanche-fed glaciers are also typically debris covered, they may take a characteristically long time to show any length retreat even as they lose mass through the thinning of a stagnant tongue after a sharp warming takes place (Banerjee and Shankar, 2013). For such stagnant glaciers, it is important to compare the thinning rates. To observe the discrepancies mentioned above, multi-decadal to century-scale data on thinning and/or retreat are required due to the long response time of such extensively debris covered glaciers.

Given the above assumption, the avalanche contribution can be estimated by simulating the recent evolution of the glacier. The ice thickness profile can specify any instantaneous transient state of a glacier in general for a given bedrock. To arrive at the right transient state, we start with a steady state length much larger than the present transient state and force it with a suitable negative mass balance until a state with reasonable length, velocity, and surface profiles is obtained. To ensure that our results are not dependent on the choice of initial steady state, we use more than one initial steady state. Once an approximation of any initial state is constructed, the glacier evolution can subsequently be simulated with the observed mass balance. If this results in a model state that is shrinking much faster than the observed loss rates, it signals the presence of a missing accumulation contribution for the glacier.

To estimate the actual magnitude of such a missing term, an arbitrary

constant accumulation term is added and is adjusted until the simulated rate of recent thinning and retreat match the observed values. While there may be a complex spatio-temporal pattern of avalanche accumulation on the real glacier, that need not be prescribed in detail for a reasonable fit to the observed glacier-averaged shrinkage rates as long as the net avalanche accumulation is captured correctly. This is due to the strongly diffusive nature of ice flow, which smooths out any observable effects of such variability on the glacier dynamics. This also implies that our method would only allow estimation of long-term mean values of the magnitude of the avalanche contribution, as the diffusive ice-dynamics filter out the details of the short wavelength and high-frequency spatio-temporal variability of the contribution.

2.4.1 The model

To implement the above discussed procedure, here we used 1-d flowline model (see Sec. 1.7.2 for details) of glacier dynamics to simulate the avalanche, where the time evolution of the ice thickness profile and the expression of ice-velocity is given by,

$$\frac{\partial h}{\partial t} = -\frac{1}{W(x)}\frac{\partial (hWu)}{\partial x} + b(x), \tag{2.2}$$

$$u = \left(\rho g h(-s + \frac{\partial h}{\partial x})\right)^3 \left(\frac{f_s}{h} + f_d h\right). \tag{2.3}$$

Here, the ice-density (ρ) is set to 900 kg m^{-3} and acceleration due to gravity (g) to 9.8 m s^{-2}. The sliding (f_s) and deformation (f_d) parameters are typically used as tuning parameters in the model (Adhikari and Huybrechts, 2009). Typical values of f_s and f_d are 5.7×10^{-20} Pa^{-3}m^{2}s^{-1} and 1.9×10^{-24} Pa^{-3}s^{-1}, respectively (Oerlemans, 2001). However, the range of f_s and f_d used for modelling of the Himalayan glaciers are 0.19×10^{-20}–1.75×10^{-20} Pa^{-3}s^{-1} and 1.7×10^{-25}–5.3×10^{-25} Pa^{-3}s^{-1}, respectively (Adhikari and Huybrechts, 2009; Venkatesh et al, 2012; Banerjee and Shankar, 2013; Banerjee and Azam, 2016). Given the glacier bedrock geometry, width distribution (hypsometry), mass balance profile, and an initial guess of ice thickness pro-

file along the central flowline, the Eq. (2.2) can be used to find the ice thickness ($h(x,t)$) for all subsequent time t. If the mass balance remains constant, the glacier reaches a unique steady state after a characteristic time, independent of the initial guess of ice thickness profile.

The method requires the glaciological mass balance, the velocity/thickness profile, long-term retreat and/or thinning rate, and hypsometric data as input for the selected glacier. The flowline model (Eqs. (2.2) and (2.3)) simulations are used to estimate the total accumulation of the selected glacier that is consistent with all other available glaciological data related to glacier dynamics and glacier geometry. Then, the difference between the modeled and glaciological mass balances is assumed to be due to avalanche contributions. We cannot rule out various other possible sources of this residual accumulation contribution, e.g., any potential systematic bias in the accumulation measurement due to chosen stake/pit locations or the effect of wind-driven inhomogeneous redistribution of snow and so on. However, we provide other circumstantial evidence from the knowledge of the catchment morphology, etc, to argue that the estimated missing contribution should be dominantly coming from avalanche activity.

2.4.2 Model implementation

We start with the surface elevation profile along the central flowline and the mass balance profile of the glacier concerned. We pick a piece-wise linear bedrock with two to three segments depending on the surface elevation profile. We assign a width for each grid point on the bedrock so that the bedrock has the same area-elevation distribution as the present glacier. We then simulate the glacier with a range of values of avalanche contribution uniformly added up to 1 km from the top of the glacier, such that corresponding steady state lengths are longer than the present glacier length. Subsequently, we simulate the glacier as the avalanche term reduces at a constant rate and store the intermediate transient states. The experiment is repeated for several values of the above rate of reduction. Then we plot data for all the intermediate states along with the corresponding observed data, and search

for the right set of states so that the initial glacier surface-elevation and/or velocity profiles, glacier length, approximately match the observed data that is available for that glacier. The chosen transient state initial state is then evolved with the avalanche term fixed at its initial value. At this stage, we also tune the constant flow parameters f_s and f_d within reasonable limits to the surface-velocity and thickness profile, retreat rate, and net balance of the simulated state so that a reasonable match with the corresponding observed data is achieved (see Fig. 2.5–2.7). If a good match is not found at this stage, we change the bedrock profile and repeat the whole procedure. While the actual glacier geometry might be more complex and there could be complications of tributaries etc., in the end our initial configuration has a similar length, area-elevation distribution, and a similar central-line velocity profile compared to the real glacier. This should ensure a similar dynamical behaviour in both the simulated and the real glaciers. We refer to the above numerical procedure as an experiment (1). We run this experiment for up to 50 years or more, depending on the available data.

Given the approximate nature of our method and the uncertainty implicit in the input data, we tune the parameters by trial and error to produce a reasonable match with the observed data to the eye. In view of the large uncertainties of the data used, we decided not to apply a systematic fitting procedure here and limited ourselves to exploring the sensitivity of our results to various tunable model parameters and the choice of the initial state. These details are described in Sec 2.5.

Subsequently, we perform another control experiment, experiment (2), to test the robustness of the above avalanches estimating method. We choose a glacier, Chhota Shigri, where no such avalanches are there. Here, the initial transient profile, as obtained above, is forced only with the glaciological mass balance profile, with the constant avalanche term turned off, to see if it is consistent with observed recent dynamics of the glacier.

2.4.3 Model sensitivity

To check the sensitivity of the above model, we repeated the above experiments with different values of the tunable parameters like f_s, f_d, s, and considered the effect of a 10% uncertainty of the observed retreat rate. Other possible sources of uncertainty that are harder to take into account are the effects of actual bedrock shape, tributary geometry, the shape of the mass-balance profile used, and so on. To check the dependence on the mass balance profile, we apply constant shifts to the profile by about 10% of the mass balance.

2.5 Results and discussions

Here, we discuss the results obtained from the above flowline model runs for each identified potential avalanche-fed glaciers. The corresponding observed and modeled surface profile and velocity profiles are shown in Fig. 2.5–2.7. The results are also summarised in Table 2.2.

2.5.1 Estimated avalanches

Satopanth Glacier

The simulated recent state of Satopanth Glacier has a mass balance of -2.0 m w.e. a^{-1} if only the glaciological estimate is considered. However, in the experiment (1), a net avalanche contribution of 1.8 m w.e. a^{-1} is needed to produce a mean retreat rate of 7.5 m a^{-1} and a net thinning of the lower ablation zone by 0.18 m w.e. a^{-1} during 1960 to 2010, which are similar to the corresponding observed values. Without any additional avalanche term (experiment (2)), the glacier thins fast with rates of 2.0 m w.e. a^{-1} during 1960 to 2010. Moreover, the ice-flow velocity at the upper ablation zone vanishes quickly, leading to a complete detachment of the lower part (Fig. 2.6a). Any such detachment or strong slowdown has not been observed in the field. For example, our recent measurements of surface flow velocities during 2014–2015 on the upper stakes indicate healthy velocities of more than

50 m a^{-1}. Therefore, the present retreating state is not that far away from a steady state and is getting nourished by an avalanche contribution with an estimated magnitude of the order of 1.8 m w.e. a^{-1}. This contribution added to the glaciological mass balance yields a residual of -0.2 m w.e. a^{-1}, which is a revised estimate for the recent mass balance. A possible geodetic mass balance measurement can be used to verify this claim. Remarkably, the frontal retreat rate remains the same in both the experiments; this is not unexpected as due to a long response time and low ice-flow velocities near the terminus, the retreat rate is chiefly controlled by the local ice thickness profile in the lowermost part of the glacier.

Duangiri Glacier

In Dunagiri glacier, where the recent glaciological mass balance is -1.0 m w.e. a^{-1}, an avalanche contribution of 0.7 m w.e. a^{-1} is necessary to obtain a realistic retreat rate of 12.5 m a^{-1} over the past 50 years (Fig. 2.6b). Without the avalanche term, this glacier displays a thinning rate of -1.0 m w.e. a^{-1}, and flow velocity reduces rapidly across the ablation zone. The future runs again suggest a complete detachment of the ablation zone from the headwall within 20 years (Fig. 2.6b). Though velocity data is not available for the current decade to crosscheck, a slowdown by a factor of 5 or more in the upper ablation zone over the past 20 years and a complete detachment of the ablation zone over the next 20 years seem unlikely. Therefore, it is likely that the mass balance of the glacier over the past 50 years is about -0.3 m w.e. a^{-1}, the residual obtained by adding the avalanche contribution to glaciological mass balance.

Hamtah Glacier

In Hamtah glacier, we estimate an avalanche contribution of 1.0 m w.e. a^{-1}, by requiring that the state has the right elevation (2000) and velocity profile ($\sim$2003), and shows reasonable retreat rates. Our modeled retreat rates for the period 1963–2013 is 22 m a^{-1} (Fig. 2.6c), which compares favorably with the observed long-term retreat (Pandey et al, 2011). We do not attempt to fit

Table 2.2: Model parameter and results.

Glacier name	$10^{-20} \times f_s$ (See Eq. (2.3)) ($Pa^{-3}m^2s^{-1}$)	$10^{-25} \times f_d$ (See Eq. (2.3)) ($Pa^{-3}s^{-1}$)	Modelled mass balance (Δm_1) (m w.e. a^{-1})	Avalanche contribution (Δm_2) (m w.e. a^{-1})	Residual $\Delta m_1 + \Delta m_2$ (m w.e. a^{-1})	Retreat rate (period) (m a^{-1})
Satopanth	4.9	1.4	-2.0	1.8±0.5	-0.2±0.5	7.5 (1953-2013)
Dunagiri	1.0	1.1	-1.0	0.7±0.2	-0.3±0.2	12.5 (1960-2010)
Hamtah	3.4	1.3	-1.5	1.0±0.3	-0.5±0.3	20.5 (1960-2010)
Chhota Shigri	1.6	1.3	-0.6	0	-0.6	22.6 (1990-2010)

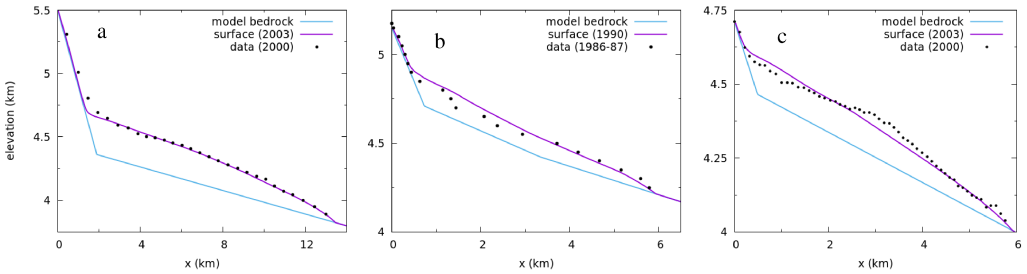

Figure 2.5: The comparison of the observed and modeled surface elevation profiles for the recent states of a) Satopanth, b) Dunagiri, and c) Hamtah glaciers.

the recent slowdown of the retreat discussed previously, as we are interested in the long-term mean behaviour of the glacier. This modeled state has a residual mass balance of -0.5 m w.e. a^{-1} once the avalanche term is included. According to experiment (2), without such significant avalanche feeding, the initial glacier state from 1963 would have slowed down dramatically, with the ablation area getting completely detached by now (Fig. 2.6c).

Chhota Shigri Glacier

In Chhota Shigri Glacier, where no significant avalanche contribution is expected as discussed before, we have modeled the glacier without any avalanche term and reproduced the observed dynamics of the glacier with just the glaciological mass-balance profile (Fig. 2.7) (Azam et al, 2014). In this case, we start with a longer steady state (ELA $\sim$ 4900m) and apply a step rise of ELA by 150 m. Then an intermediate state is chosen such that it has the right length, retreat rate, thickness, and velocity profile. The modeled glacier has an ELA of 5040 m, consistent with the observed mean ELA of 5075 m during 2002 to 2010 (Azam et al, 2012). The simulated glacier shows a retreat of 22.6 m a^{-1} from 1990 to 2010, with a mass balance of -0.6 m w.e. a^{-1}. This modeled retreat rate is comparable with the observed retreat rate of 25 m a^{-1} from 1972 to 2006 (Ramanathan et al, 2011). On the other hand, the geodetic mass balance of -0.17 ± 0.09 m w.e. a^{-1} during 1988–2010 is somewhat smaller than the modeled value. However, the reported glaciolog-

ical mass balance of -0.57 ± 0.40 m w.e. a^{-1} during 2002–2012 (Azam et al, 2014) and geodetic mass balance of -0.5 ± 0.3 m w.e. a^{-1} during 2000–2012 (Vijay and Braun, 2016) match the modeled value. The surface-elevation profile and velocity profiles match is also reasonable (Fig. 2.7). The result of this control experiment for a glacier where avalanches are expected to be insignificant, provides strong support for the general validity of our method.

2.5.2 Model sensitivity

In the model glaciers, the flow is dominated by slip. Therefore, the uncertainty of the values of f_d does not affect our result. On the other hand, changing f_s by about 10% disturbs the match between observed and modeled velocity and thickness profile. However, the match can be restored by changing s on the lower part of the bedrock by about 2%. These adjustments of f_s and s changes the estimated avalanche contribution by about 10%, depending on the glacier and the actual values of the parameter. Allowing an uncertainty of retreat rates of the order of 10%, leads to an uncertainty of the estimated avalanche contribution that is less than 10%. The 10% shift in the mass-balance profile leads to a variation of our avalanche estimate by about 12%. Therefore, we expect an uncertainty of at least about 30% in the estimated avalanche contributions. However, a larger mass-balance uncertainty would lead to a correspondingly higher uncertainty of the avalanche-strength estimate. Thus the long-term avalanche contributions to accumulation on Satopanth, Dunagiri, and Hamtah glacier are estimated to be 1.8±0.5, 0.7±0.2, and 1.0±0.3 m w.e. a^{-1} respectively.

2.5.3 Validation of estimated avalanches

Validation with geodetic mass balance

The glaciological mass balance for the two Central Himalayan glaciers, Satopanth and Dunagiri glaciers, are -2.0 m w.e. a^{-1} during 2014–15 and -1.0 m w.e. a^{-1} during 1984–1990, respectively. The other suspected avalanche-fed Western Himalayan glacier modeled here, Hamtah Glacier, has a mass balance of

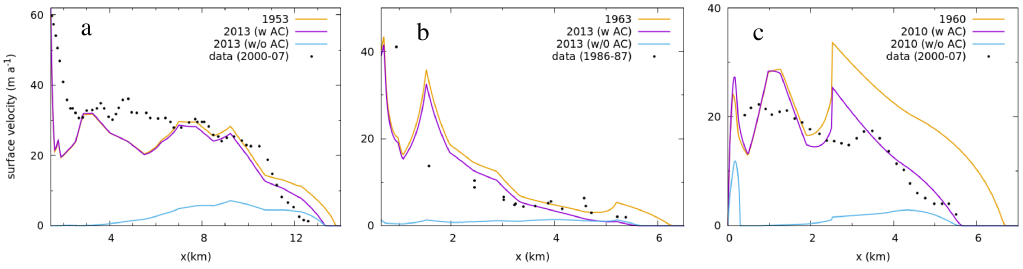

Figure 2.6: The modeled velocity profile (solid line) for a) Satopanth, b) Dunagiri, and c) Hamtah glaciers for the initial and recent states are shown for the runs with and without added avalanche contribution (AC). The dots denote available velocity data.

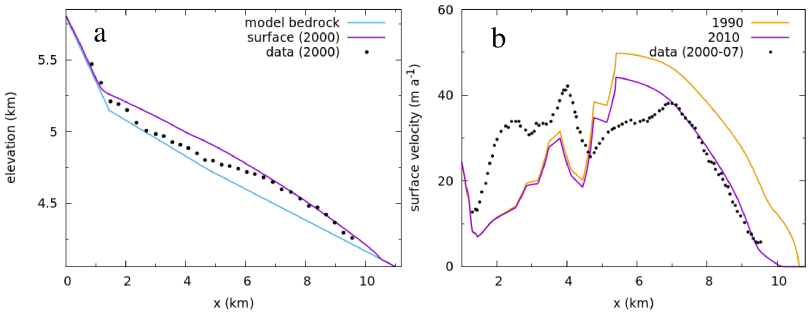

Figure 2.7: a) Comparison of the observed and modeled surface elevation profiles for the recent states of Chhota Shigri Glacier. b) The modeled velocity profile (solid line) for the initial and recent states are shown. The dots denote the observed velocities for the corresponding recent state.

-1.45 m w.e. a^{-1} during 2000–2009 (Shukla et al, 2015). In fact, these are three of the most negative mass balance values observed in the region (Vincent et al, 2013a). These values are considerably more negative than the estimated region-wide mean mass balance of -0.5 m w.e. a^{-1} in the Himalaya (Cogley, 2011). This is consistent with the possibility that significant accumulation contribution due to a putative avalanche activity in these glaciers might have been missed.

Unlike the glaciological method, the geodetic method captures glacier-wide changes, whether or not avalanche contributions are present. Therefore, if our method of estimating avalanche contribution is correct, then our estimated avalanche contribution for these three glaciers, when added to the glaciological mass balance, should lead to residuals that are similar to the corresponding geodetic mass balance. Indeed, the residual mass balance of -0.2 m w.e. a^{-1}, -0.3 m w.e. a^{-1}, and -0.5 m w.e. a^{-1} on Satopanth, Dunagiri, and Hamtah glaciers, respectively, are similar to the existing independent geodetic mass-balance estimates. For example, regional-scale geodetic mass-balance estimates from the Western and Central Himalayan glaciers point to a mass loss of 0.33–0.65 m w.e. a^{-1} over the past one to four decades (Bolch et al, 2011; Kääb et al, 2012; Vincent et al, 2013a; Gardelle et al, 2013; Vijay and Braun, 2016). Also, on Hamtah glacier, the geodetic mass balance during 2000-2011 is -0.45 ± 0.16 m w.e. a^{-1} (Vincent et al, 2013a). This consistency of the residual mass-balance values for the three glaciers computed here, with the known geodetic mass-balance measurements, indicates the reliability of our method of estimating avalanche contribution. In contrast, on Chhota Shigri Glacier, where no significant avalanche activity is unlikely, all the three estimates, namely, the modeled, geodetic, and glaciological mass balances, are mutually consistent.

Validation with regional precipitation

A naive expectation regarding the magnitude of the suspected avalanche accumulation is that it should be similar to or less than the total precipitation over the whole avalanche-contributing zone. We compute the ratio of the

estimated avalanche accumulation to the product of mean Tropical rainfall measuring mission (TRMM) precipitation and the area of the avalanche-release zone for all the three glaciers. However, the possible uncertainty associated with TRMM precipitation data from the high Himalaya and a potential intensification of precipitation through strong orographic effects due to the high headwalls would mean that these values are only ball-park estimates. We find that the calculated ratios are about 1.3 ± 0.4, 0.6 ± 0.2, and 1.8 ± 0.5 for Satopanth, Dunagiri, and Hamtah glaciers, respectively. While these values indicate that our estimates are broadly consistent with the potential avalanche accumulation as estimated from the local TRMM precipitation rate, they are somewhat larger for Hamtah and Satopanth glaciers. Despite of the possible uncertainties in the computed ratio, this discrepancy suggests a potential bias in our estimates of the avalanche strength using a simplified flowline model. For example, in Satopanth Glacier, a few tributaries join the main trunk glacier in the middle ablation zone (Fig. 2.3a). While modeling the glacier, we have approximated this geometry by that of a simple glacier that shares an identical hypsometry, ignoring the actual tributary configurations. That could be a possible source of bias for this glacier. However, Hamtah does not have any such complications. We shall investigate these issues further and attempt possible refinements of the flowline model to include the tributaries explicitly in the future.

2.6 Summary

We have discussed the importance of avalanche derived accumulation on a large class of Himalayan glaciers and the diagnostic criteria to identify such glaciers. Using standard glaciological mass-balance techniques, measurement of this avalanche contribution to the mass balance is extremely difficult. Motivated by that, we have described a simplified numerical flowline model-based method that allows a first-order estimation of avalanche contribution. The method utilises the available long-term data on glacier dynamics and determines a missing mass-balance term necessary to make the recent

multi-decadal dynamics consistent with the glaciological mass balance. Our simplified models for three Himalayan glaciers, namely, Satopanth, Dunagiri, and Hamtah glaciers, demonstrate that the above mentioned avalanche-accumulation contribution dominates the accumulation and exerts overwhelming control over the dynamics of a significant number of Himalayan glaciers. This demands further work on more sophisticated theoretical tools and, more importantly, direct field-measurement techniques to quantify the avalanche activity and their long-term trends in the region. Our control experiment with Chhota Shigri Glacier is consistent with no significant avalanche contribution, asserting the robustness of the method in estimating avalanche contribution to mass balance.

Chapter 3

Conductive heat flux through supraglacial debris layer

3.1 Introduction

The influence of supraglacial debris on ablation depends on debris thickness and thermal properties (Mattson et al, 1993; Mihalcea et al, 2006; Reid et al, 2012; Fyffe et al, 2020). The variability of the debris thickness and its thermal properties mainly controls the sub-debris ablation both within and between the glaciers over the Himalaya (Brock et al., 2010; Nicholson and Benn, 2013; Rounce et al, 2015; Nicholson et al, 2018; Chand et al, 2018; Shah et al, 2019). The debris thickness typically has a large spatio-temporal variation over a glacier (Mihalcea et al, 2008; Nicholson et al, 2018; Shah et al, 2019). The factors that control the variability of debris thermal properties are the spatial distribution of the debris sources (Banerjee and Wani, 2018), supraglacial transport rate (Kirkbride, 2000), local lithology, and particle size distribution (Juene et al, 2014). Debris thermal properties may also have seasonal variation (Nicholson and Benn, 2013). For example, monsoon precipitation could affect debris thermal diffusivity (κ) by changing the water content within the debris layer. A higher water content within pore spaces increases the effective conductivity of the debris layer as water is a better conductor of heat than the air that it replaces (Hinkel et al, 2001; Nicholson

and Benn, 2013). The behaviour of κ is more complex as the volumetric heat capacity goes up with water filling the pore spaces (Hinkel et al, 2001). Porosity is also likely to be varying across locations or with depth. In general, these effects will add to the inhomogeneity of κ within the debris layer. Such a large spatio-temporal variation of κ, as well as debris thickness is a cause of concern in glacier-wide energy-balance models (Reid et al, 2012) and sub-debris ablation estimations (Zhang et al, 2011; Nicholson and Benn, 2013; Chand et al, 2018).

Ablation model on debris covered glaciers are typically modified degree-day models (Carenzo et al, 2016; Vincent and Six, 2013; Pellicciotti et al, 2005; Mihalcea et al, 2006) or physically-based models that assume a steady linear temperature profile within the debris layer (Nakawo and Rana, 1999; Fujita and Sakai, 2014) have been employed on debris-covered glaciers. Physically-based models informed by and tested against extensive observations are expected to have better transferability in both space and time (MacDougall et al, 2013). Several detailed energy balance and/or mass-balance models for various glaciers, with explicit procedures for computing conductive heat transfer through supraglacial debris, have been published to date (Nakawo and Rana, 1999; Reid and Brock, 2014; Nicholson and Benn, 2006; Fyffe et al, 2014; Collier et al, 2014). However, point-scale energy balance estimation requires detailed measurement of a relatively large number of observables like various energy fluxes and meteorological parameters. Moreover, glacier-wide extrapolation of results introduces additional uncertainty due to the noisy distribution of debris layer properties as discussed above. A further complication is that measurements of the thermal properties of the debris layer and its variability, which are crucial ingredients for such models, are relatively scarce in the Himalaya (Conway and Rasmussen, 2000; Haidong et al, 2006; Nicholson and Benn, 2013; Rounce et al, 2015; Chand et al, 2018; Rowan et al, 2020).

To obtain the debris thermal diffusivities and sub-debris ablation, the time series of vertical temperature profiles are typically used (Conway and Rasmussen, 2000; Nicholson and Benn, 2013; Chand et al, 2018; Rowan et al, 2020). Conway and Rasmussen (2000) pioneered a relatively easy method

of obtaining sub-debris ablation from debris temperature data at Khumbu Glacier, Nepal Himalaya. This method assumes one-dimensional heat conduction through a homogeneous debris layer. Henceforth, we refer to this method as the CR method. To date, this method has been applied several debris covered glaciers in the Himalaya (Haidong et al, 2006; Nicholson and Benn, 2013; Chand et al, 2018; Rowan et al, 2020) and also outside the Himalaya (Nicholson and Benn, 2006). The limitations of this method of sub-debris ablation estimate due to discretisation errors arising out from vertical spacing between the temperature sensors, as well as those due to any vertical inhomogeneity in the thermal diffusivity, were not explored in the available literature. Moreover, the implications of the underlying assumption of this method that, the debris layer can be approximated as a one-dimensional homogeneous purely conductive medium may not have been explored fully in the literature. It is expected that the lateral variation of the debris-layer thermal properties (Suzuki et al, 2007), that of the debris layer thickness (Mihalcea et al, 2008), and that of the temperature distribution at the surface (Kraaijenbrink et al, 2018) may lead to substantial lateral heat flow that cannot be captured fully in an one-dimensional model. In addition, ignoring the non-conductive processes, e.g., latent heat fluxes, may bias the ablation estimates (Giese et al, 2020).

A different method was employed at 25 locations on Miage Glacier in the Italian Alps (Brock et al., 2010), determining thermal conductivity from simultaneous measurement of ablation and the temperature difference between the debris surface and debris-ice interface. However, the assumption of a linear mean temperature profile may not hold, for example, due to possible vertical variation of thermal properties. Similarly, thermal conductivity was determined on Baltoro glacier, Karakoram (Mihalcea et al, 2006), but the temperature gradients and ablation were measured at a different location. Since ablation at stakes of very close proximity was observed to vary up to a factor of three (Mihalcea et al, 2006), the inherent uncertainty in this method may be significant. Moreover, the possibility of seasonal variation of thermal properties was not addressed in the above contributions. Remotely-sensed thermal band images have also been used to estimate the thermal

resistance of supraglacial debris cover, allowing calculation of sub-debris ablation rates. Again, this method assumes a linear vertical temperature profile (Nakawo and Young, 1982; Nakawo and Rana, 1999; Fujita and Sakai, 2014), moreover applied to an instantaneous surface-temperature map. The utility of such remote sensing methods in getting the thermal properties of the debris layer requires to be tested against extensive field data. Given the expected inhomogeneity of debris layer properties at all spatial scales, the thermal properties can vary with debris thickness, depth, and water content. Also, there could be temporal variability at seasonal to sub-seasonal time scale. This is an important area of research in a glacierised region like the Himalaya.

The glaciological method of monitoring a network of ablation stakes installed across a glacier surface is used to measure the ablation rate on debris-covered glaciers and is generally considered the most accurate method for doing so (Cogley, 2011). The glaciological method is labour-intensive (Kaser et al, 2003). From our direct experience (Shah et al, 2019), the logistical challenges and human resource requirements for performing sub-seasonal glaciological mass balance measurement on a debris-covered Himalayan glacier are considerable. This exercise requires bimonthly field visits to obtain only ablation and surface-displacement data. In addition, the processes and properties operating in the debris layer between measurements is a black box. The physical properties of the debris layer are often measured at the time that ablation stakes are installed, but that does not afford insight into the processes that produce ablation between measurements.

The CR method of estimating sub-debris ablation is more efficient than the glaciological method and has co-benefits that the glaciological method does not. By the CR method, continuous sub-seasonal (up to daily time resolution) time series of ablation can be obtained with a fraction of the physical labour required to obtain the same by the glaciological method, because the data capture is automated. Also, installing temperature sensors in a debris pit is logistically very easy as no drilling is required than installing a stake on the debris covered glacier. Effective thermal diffusivity time series provides insight into the thermal properties of the debris layer and processes therein,

and those data can be used to help develop physically-based models and constrain parameter uncertainty. Furthermore, the temperature time series can be used for additional purposes, such as validating physical representations in models.

Reducing the labour associated with on-site data acquisition and increasing the co-benefits of sub-debris ablation monitoring systems could substantially advance understanding of glacier change in HKKH. However, while the potential of the CR method is established, sources of error in predicted ablation are not yet well constrained. With the above motivation, this study aimed to increase the utility of the method introduced by Conway and Rasmussen (2000) as a tool for monitoring debris-covered glacier change by testing the key assumptions it is based on, quantifying prediction error, and testing a novel computational approach to estimating parameter values. Here, we measured the vertical temperature profiles of debris from 16 locations on Satopanth Glacier (central Himalaya, India) during the ablation season of 2016 and 2017. The analyses focused on: a) identifying an optimal sensor spacing to minimise discretisation errors, b) the effect of vertical inhomogeneity on prediction error. Using synthetic experiments, the accuracy of different methods in estimating the parameter values was evaluated. Then, the accuracy of predictions of sub-debris ablation made using the different methods was assessed using extensive in-situ glaciological ablation data (Shah et al, 2019).

3.2 Study area and field data

We had selected relatively large debris covered Satopanth glacier (30.73°N, 79.32°E) from Garhwal region of India, central Himalaya (Fig. 3.1). The glacier is around 14 km long with an area of ∼19 km^2, and supraglacial debris covers ∼60% of the glacier area (Shah et al, 2019). The glacier spans over an elevation range of 3900 m a.s.l to 6200 m a.s.l. Geologically Satopanth Glacier falls under the Higher Himalayan Crystalline Zone, where the typical rocktypes are calc-silicate, predominantly schist with lesser amounts of

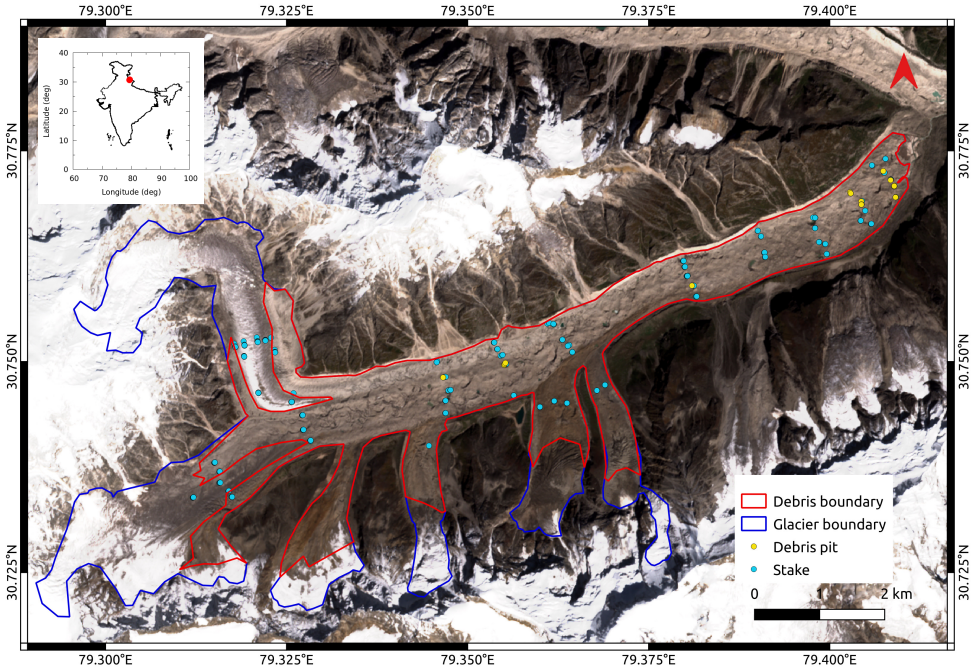

Figure 3.1: A map of Satopanth Glacier showing the debris pits (solid yellow circle) and ablation stakes (solid sky-blue circles) on the glacier surface, used in this study. The blue and red solid lines denote the boundaries of the glacier and the debris-covered area, respectively. The inset map is the political boundary of India (solid black line) as per the Survey of India, with a solid red circle indicating the location of Satopanth Glacier.

biotite-gneiss, and granite with tourmaline (Valdiya et al, 1999; Nainwal et al, 2008). The glacier valley has high and steep walls, from which a large volume of snow and loose debris are transported onto the glacier by frequent avalanches and rockfalls. These avalanches are the major source of the total accumulation of the glacier (Laha et al, 2017). The supraglacial debris covers start around 4500–4700 m a.s.l elevation and thicken along downglacier, where the greatest debris thickness was found ∼1.27 m near the terminus (Shah et al, 2019). The distribution of debris is uneven, and debris thickness varies between 0.05–1.27 m with a monotonic increase along downglacier where the slope is relatively gentle (∼ 7°). It was observed that the debris thickness locally could change by order of magnitude (Shah et al, 2019). The ablation zone of the glacier consists of supraglacial ponds and ice cliffs of various size, which are prevalent characteristics of such low sloping and large debris covered glaciers (Sakai and Fujita, 2010).

3.2.1 Debris temperature measurement

Debris temperature profiles were obtained from a pit dug into debris at 11 locations from the lower ablation zone (elevation range 3800–4000 m a.s.l) and 5 locations from the upper-middle ablation zone (elevation range 4100–4400 m a.s.l) of Satopanth glacier (Fig. 3.1,3.2). The field measurements were carried out during the ablation season 2016 and 2017. There were no ice-cliffs and/or ponds near (within ∼50 m) any debris pit. Debris temperatures were recorded at 15–60 min intervals by HOBO Onset TMC6-HD Water/Soil thermistors (accuracy 0.2°C) at 3 to 8 depths within the debris layer, connected to HOBO Onset U12-4 External Channel Data Loggers at the debris surface (Fig. 3.3). The thermistors were inserted into the walls of each pit and the pits back-filled. The duration of these temperature records varies from 7 days to more than a year, depending on the location, with some data gaps. The details of the debris temperature measurement from each pit are given in Table 3.1. One example of a year-long temperature record (with some gaps) from a debris pit with sensors at three different depths is shown in Fig. 3.4. The debris thickness of these pits varies between 0.22–0.77 m.

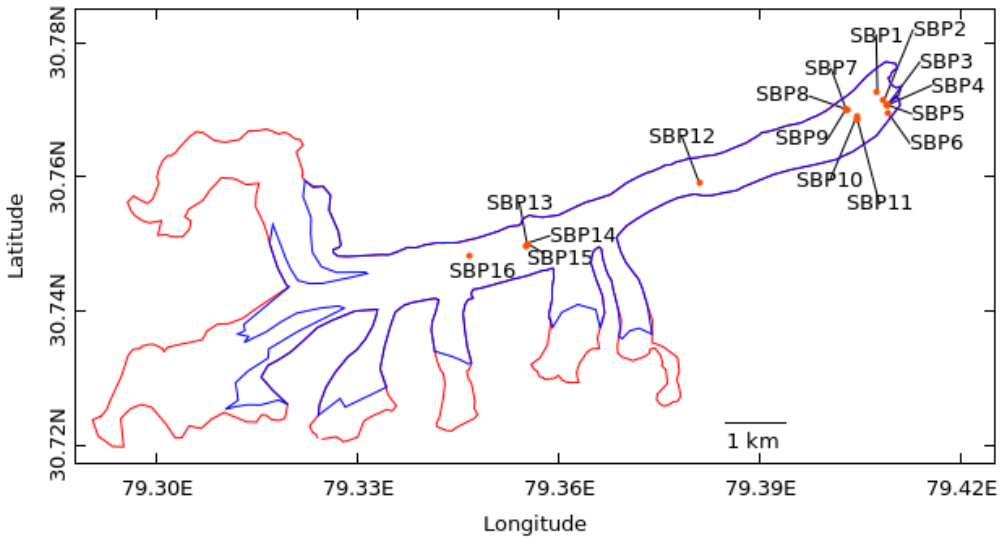

Figure 3.2: Location of the 16 pits on Satopanth Glacier (Table 3.1) was shown by red circle, labeled with pit name. The solid red line is the glacier boundary, and the blue line is the extent of debris.

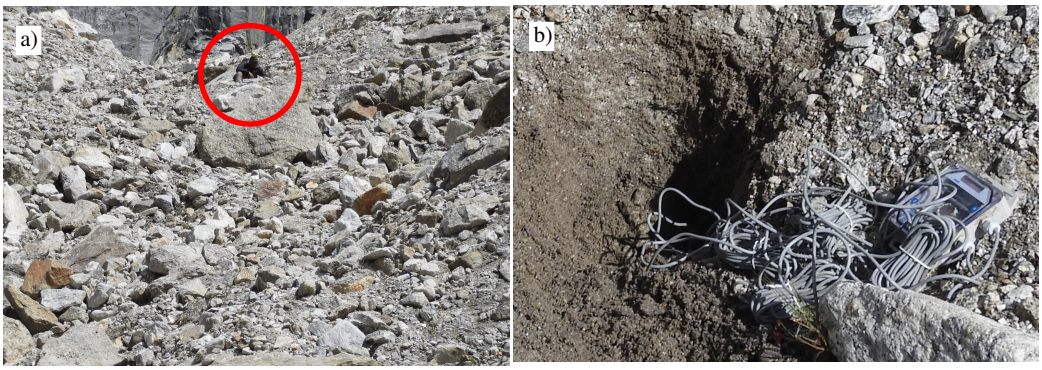

Figure 3.3: a) Surrounding area of an example pit (SBP5) as shown here. A red circle indicated a person sitting near the pit. b) Pit SBP5 dug on Satopanth Glacier for temperature measurement. The temperature sensors were inserted on the pit wall, which was connected to the data logger on the surface.

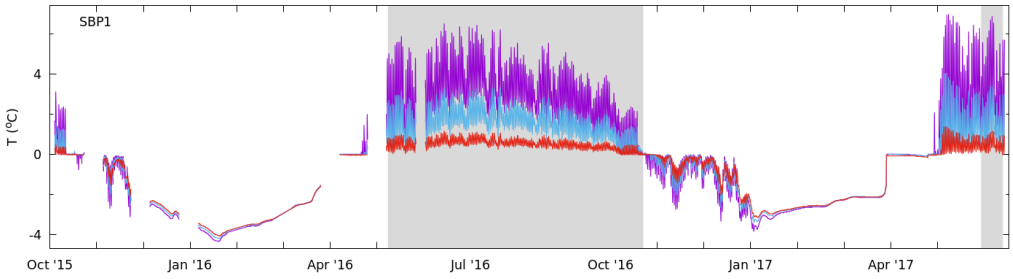

Figure 3.4: The temperature time series recorded at a depth of 4 (solid red line), 16 (solid blue line), and 28 cm (solid purple line) at pit SBP1 (see Table 3.1 for details). The light gray shading denotes the data used for ablation estimation, based on the availability of ablation stake data that it was compared with.

In each pit, we skipped the temperature data for 2–3 days (depending on debris thickness) to equilibrate the temperature profiles as the temperature got perturbed during the sensor installation procedure.

Vertical temperature profile data from each pit were split into a set of several records with duration varied between 7–15 days, according to the availability of the observed melt data to facilitate the sub-debris ablation comparison. Therefore, we had 64 temperature records from 16 pits for the rest of the analysis. We computed the thermal diffusivities from each temperature record using different methods (discussed later) and used that to compute the sub-debris melt rate and compared it with observed glaciological method.

3.2.2 Glaciological method of ablation measurements

Mass balance in the ablation zone of Satopanth glacier has been monitored since summer 2014 by the glaciological method with a network of bamboo stakes ($\sim$ 83) spanning an elevation range of 3900 m a.s.l to 4700 m a.s.l (Shah et al, 2019). The debris thickness at the stake locations varied from 0.05 m to 1.27 m. The ablation values at the stakes were recorded once in each 15 days or so with some gaps. A detailed description of these ablation data was reported in Shah et al (2019). We had taken the ablation data for the melt season of 2016 and 2017 (Shah et al, 2019), which were used to validate the ablation estimate from temperature profile data. Shah et al (2019) showed that sub-debris ablation on Satopanth Glacier is more sensitive to debris thickness than elevation.

3.3 Theory of one-dimensional vertical heat conduction through a debris layer

On debris-free glaciers, energy consumed in ablation is transferred directly to the ice, primarily through direct solar radiation and the turbulent sensible heat flux. When the ice is covered by debris, that energy is used instead

Table 3.1: Details of the debris temperature measurements at Satopanth glacier are given here. Pits with data gaps are marked with a '*'.

Pit name	Lat (°N)	Lon (°E)	Elevation (m)	Measurement period (DD/MM/YYYY)	Time step (min)	Debris thickness (cm)	Sensor depths (cm)
SBP1*	30.77249	79.40726	3892	13/10/2015–13/06/2017	60	33	4, 16, 28
SBP2*	30.77154	79.40842	3875	08/10/2015–07/06/2016	60	53	2, 17, 34
SBP3	30.77078	79.40891	3886	13/06/2017–21/06/2017	15	55	31, 37, 43, 49
SBP4	30.77078	79.40891	3886	13/06/2017–21/06/2017	15	51	27, 33, 39, 45
SBP5	30.77078	79.40891	3886	13/06/2017–21/06/2017	15	52	34, 40, 46
SBP6*	30.76946	79.40907	3900	09/10/2015–07/06/2016	60	77	14, 23, 32, 41, 50, 59, 68
SBP7	30.77009	79.40282	3942	01/07/2017–30/09/2017	15	40	16, 22, 28, 34
SBP8	30.77009	79.40282	3942	01/07/2017–30/09/2017	15	38	14, 20, 26, 32
SBP9	30.77009	79.40282	3942	01/07/2017–30/09/2017	15	45	21, 27, 33
SBP10	30.76901	79.40436	3946	21/06/2017–01/07/2017	15	30	6, 12, 18, 24
SBP11	30.76901	79.40436	3946	21/06/2017–01/07/2017	15	31	9, 15, 21, 27
SBP12	30.75902	79.38098	4141	02/10/2017–31/12/2017	15	50	26, 32, 38
SBP13*	30.75218	79.353691	4320	14/06/2016–29/05/2017	30	50	2, 10, 22, 38
SBP14*	30.75218	79.353691	4320	14/06/2016–29/05/2017	30	40	1, 5, 15, 30
SBP15*	30.75218	79.353691	4320	14/06/2016–29/05/2017	30	40	1, 8, 18, 32
SBP16	30.74813	79.34661	4381	10/10/2017–31/12/2017	30	22	6, 10, 14, 18

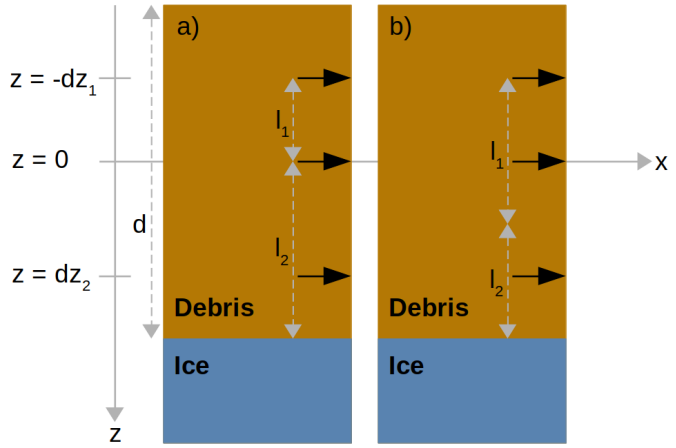

Figure 3.5: Schematic diagram of a debris pit with debris thickness d. The vertical positions of the temperature sensors ($z = -dz_1$, $z = 0$, and $z = dz_2$) are indicated with solid black arrows. (a) and (b) shows the layer thickness l_1 (l_2) for the top (bottom) layer as used in the $\mathrm{CR_i}$, and $\mathrm{MC_i}$ methods, respectively.

to heat the surface of the debris layer. Sub-debris ablation occurs due to the consequent heat conduction through the layer to the debris-ice interface. Therefore, it is possible to estimate the ablation rate by estimating the conductive heat flux through the debris layer.

Supraglacial debris is manifestly an inhomogeneous medium, and the interface between the debris and the atmosphere is uneven. Consequently, there could be temperature gradients and heat flow in the horizontal direction (Evatt et al, 2015). However, past work (Conway and Rasmussen, 2000) suggests that horizontal heat fluxes are not large relative to the vertical heat flux, and hence the one-dimensional heat equation seems to be sufficient to represent the flux of heat used in ice ablation. However, it is possible to incorporate the effects of lateral heat fluxes, to some degree, by including a source term in the one-dimensional heat equation.

The conceptual mathematical model we use is the one-dimensional heat equation in a vertically inhomogeneous medium with an inhomogeneous heat source or sink

$$\partial_t T(z,t) = \frac{1}{\tilde{C}(z)} \partial_z \left(K(z)\, \partial_z T(z,t) \right) + s(z). \tag{3.1}$$

Here, $T(z,t)$ is the debris temperature at depth z and time t (Fig. 3.5). $\tilde{C}(z) \equiv \rho_d(z) C(z)(1-\phi(z))$, where $\rho_d(z)$, $C(z)$ and, $\phi(z)$ are the density, heat capacity and the porosity of the debris respectively, at depth z. $K(z)$ is the thermal conductivity of the debris. $s(z)$ is an external source (sink) of heat that can arise from various processes like latent heat of condensation/evaporation, convective heat transport, and horizontal transport of heat. $s(z)$ estimates the accuracy of the one-dimensional model.

Due to limited field data of debris temperature, we simplify the model defined in Eq. (3.2) by assuming: (a) $\tilde{C}(z)$ is homogeneous, namely independent of z, (b) $K(z)$ and $s(z)$ are piece-wise constant in z. Namely, we assume that it is reasonable to model the debris as a layered medium, the thermal properties of each layer being characterized by a constant $\tilde{C}$ and varying K and s. Then Eqn (3.2) simplifies to,

$$\partial_t T(z,t) = \partial_z^2 (\kappa(z) T(z,t)) + s(z). \tag{3.2}$$

Where $\kappa(z) = \frac{K(z)}{\rho_d C(1-\phi)}$ is the thermal diffusivity of the layer. The boundary conditions between the intermediate layers are specified by the continuity of the heat flux across the interface. Only the thermal diffusivity can be inferred from this model and not the thermal conductivity. Hence to estimate sub-debris ablation rates, we assume ρ_d, C, and ϕ to be 2700 kg m^{-3}, 750 J kg^{-1}K^{-1}, and 0.3, respectively (Conway and Rasmussen, 2000).

The sub-debris ablation rate is calculated using the estimated values of κ by the following equation,

$$M = \frac{\rho_d C(1-\phi)}{L_f \rho_w} \kappa \frac{dT}{dz}. \tag{3.3}$$

Here $\frac{dT}{dz}$ is the vertical temperature gradient. The latent heat of fusion is $L_f = 3.34 \times 10^5$ J kg^{-1} and water density $\rho_w = 1000$ kg m^{-3}.

3.4 Methods of analysing vertical temperature profiles using one-dimensional heat equation

We discuss the existing CR method and three new methods of estimating κ and s, and hence sub-debris ablation rates. We outline the synthetic experiments we used to assess the accuracy of the values of κ estimated using the four methods. Then, we explain the procedures used to estimate sub-debris ablation rates on Satopanth Glacier, using measured temperature data and the four analytical methods. The methods used to evaluate the accuracy of estimated ablation rates using glaciological ablation data are detailed, along with the estimation of uncertainties.

In this work, since we are mainly interested in estimating the sub-debris ablation rates, we concentrate on the lower part of the debris layer, namely only on the data from the bottom three sensors in every pit (Table 3.1). Thus the computational domain of our model is from the depth of the third deepest sensor in each pit to the debris-ice interface. Another reason for this choice is that we observe that the data from the deeper sensors are less noisy than the data from the shallower ones. This is presumably because that the penetration depth of the heat flux at a certain frequency decreases with the frequency, and hence consequences of the high frequency forcing at the surface get filtered out in the deeper sensors.

The standard method of estimating sub-debris ablation from debris temperature data assumes vertically homogeneous thermal diffusivity (Conway and Rasmussen, 2000). Since we are only modelling a restricted region of the debris (from the depth $-dz_1$ to ice-debris interface as illustrated in Fig 3.5), we concentrate on the simplest cases of a one-layer model (homogeneous medium) and a two-layer model. The definition of layers is also hypothetical and somewhat depends on the models. The advantage of the two-layered model is, it adds vertical inhomogeneity in the model up to some extent.

In the one-layer model (denoted by subscript 'h'), κ and s are the two model parameters. The top boundary condition is the temperature data

from the top sensor at depth $-dz_1$, and the bottom boundary at the debris-ice interface was assumed to be at $0°C$ (Fig. 3.5).

In the two-layer model (denoted by subscript 'i'), the extent of the layers is discussed in the next section (schematics of the layers are given in Fig. 3.5). $\kappa_{1,2}$ and $s_{1,2}$ are the four model parameters. As above, the top boundary condition is the temperature data from the top sensor at depth $-dz_1$ and the bottom boundary at the debris-ice interface with the temperature at 0°C. The boundary condition at the interface between two layers is the continuous heat flux.

Here we discuss below the two different inversion techniques, (a) finite difference, and (b) Bayesian, to estimate κ and hence sub-debris ablation rate from debris temperature data.

3.4.1 Finite difference method

Assuming that, the temperature time series at three depths ($z = -dz_1$, $z = 0$, and $z = dz_2$ as shown in Fig. 3.5) are available, using Taylor series expansion, the second-derivative term in the right-hand side of Eq. (3.2) can be approximated as follows,

$$\partial_z^2 T(0,t) \approx \frac{\frac{T(-dz_1,t)-T(0,t)}{dz_1} - \frac{T(0,t)-T(dz_2,t)}{dz_2}}{\frac{dz_1+dz_2}{2}} + \frac{dz_1 - dz_2}{3}\partial_z^3 T(0,t) + O(dz^3) + ... \quad (3.4)$$

Here, the lowest order error term is linear in $(dz_1 - dz_2)$ when $dz_1 \neq dz_2$, and $O(dz^3)$ otherwise. This suggests that in this finite-difference scheme the errors are generally larger in case of non-uniform sensor spacing (i.e., $dz_1 \neq dz_2$). It is a property of discretisation scheme along with the oscillatory nature of the signal.

Homogeneous CR method ($\mathbf{CR_h}$)

Given the discrete time series of temperature measured at the three sensors (as shown in Fig. 3.5), this method (Zhang and Osterkamp, 1995; Conway

and Rasmussen, 2000) employs the following finite-difference approximations to evaluate the derivative terms in Eq. (3.2) assuming higher-order correction terms (Eq. (3.4)) to be zero,

$$\partial_t T(0,t) \approx \frac{T(0,t+\Delta t) - T(0,t)}{\Delta t} \tag{3.5}$$

$$\partial_z^2 T(0,t) \approx \frac{\frac{T(-dz_1,t)-T(0,t)}{dz_1} - \frac{T(0,t)-T(dz_2,t)}{dz_2}}{\frac{dz_1+dz_2}{2}}. \tag{3.6}$$

Henceforth, we refer to this method as the $\mathrm{CR_h}$ method, where the subscript 'h' refers to the assumption of the homogeneous debris layer. We used the above method to analyse the temperature data from the three bottom-most sensors for each record, ignoring the upper sensors installed in a few pits (Table 3.1). Temperature data from upper sensors are typically more noisy, possibly due to convective processes, moisture exchange, etc (Collier et al, 2014; Giese et al, 2020). The time step (Δt) varied from 15 min to 1 hr, depending on the pits (Table 3.1).

It follows from Eq. (3.2) that the values of $\partial_t T$ and $\partial_z^2 T$ computed using Eqs. (3.5) and (3.6) should be linearly related up to the measurement uncertainties and discretisation errors. The slope and intercept of the best-fit straight line to these data points are used to obtain κ and s (Conway and Rasmussen, 2000). The standard error of the corresponding linear fits was considered as the uncertainty in κ and s. However, any time-varying source term due to the latent heat flux, $s(t)$, may cause deviations from the expected linear behaviour, which is discussed in more detail later.

Inhomogeneous CR method ($\mathrm{CR_i}$)

The $\mathrm{CR_h}$ method outlined above makes the simplifying assumption of a vertically homogeneous debris layer, whereas the thermal properties are likely to have vertical variations (Evatt et al, 2015; Nicholson and Benn, 2013). To account for the effects of vertical variations of debris thermal diffusivity in a simple way, we propose the following modification of the discretisation scheme used in the $\mathrm{CR_h}$ method (Eq. (3.6)) within a simple two-layered model.

$$\frac{T(0,t+\Delta t)-T(0,t)}{\Delta t} \approx \frac{\left(\kappa_1 \frac{T(-dz_1,t)-T(0,t)}{dz_1} - \kappa_2 \frac{T(0,t)-T(dz_2,t)}{dz_2}\right)}{\left(\frac{dz_1+dz_2}{2}\right)} + s, \tag{3.7}$$

where κ_1, κ_2 are the thermal diffusivities of the top and bottom layers with thickness dz_1 and dz_2, respectively (Fig 3.5a). We computed the terms in Eq. (3.7) using observed temperature data and used a three-parameter linear regression to obtain the best-fit values of κ_1, κ_2, and s. To minimise the number of fitting parameters, $\rho, C, \phi,$ and s have been assumed to have no variation with depth. The uncertainty in κ was computes similarly as described in the $\mathrm{CR_h}$ method.

3.4.2 Bayesian method

The Bayesian approach to infer the values of κ and s, which we collectively denote as m, from the observed temperature profiles, which we denote by y, is based on Bayes's theorem. The theorem states that the probability of the parameters being m, given the observations y, is given by

$$p(m|y) = \frac{p(y|m)p(m)}{p(y)}, \tag{3.8}$$

where $p(y|m)$ is the probability of observing y, given that the parameters are m. We estimated this probability using our forward model as detailed below. $p(m)$ is the apriori probability of the parameters being m. We assume $p(m)$ to be a uniform distribution over a specified range of the parameters. $p(y)$ is an unimportant normalization constant (Gelman et al, 2014). We describe our implementation of this method for the one-layer case ($\mathrm{MC_h}$) and the two-layer case ($\mathrm{MC_i}$) below.

Homogeneous Bayesian method ($\mathrm{MC_h}$)

The vertical heat conduction through a homogeneous layer between the upper sensor and the debris-ice interface was simulated by solving Eqn. (3.2) numerically with an explicit Forward-in-Time-Central-in-Space finite-difference

scheme (Slingerland and Kump, 2011). The upper boundary condition was fixed using the observed temperature at $z = -dz_1$ (Fig. 3.5). The bottom boundary at the debris-ice interface was assumed to be at 0°C. The spatial and temporal grid sizes were 0.01 m and 1.0 s, respectively. As the observed temperature data had an hourly to sub-hourly temporal resolution (Table 3.1), linearly interpolated values of the temperature data from the top sensor were used to set the upper boundary condition. The temperature data for the first day of the simulation were repeated seven times for model spin-up. The modeled temperatures (T^{mod}) at $z = 0$ and $z = dz_2$ were used to compute the sum of squared errors (δ^2) relative to the observed temperatures (T^{obs}) as follows.

$$\delta^2 = \frac{1}{N}\sum_t \left[(T^{obs}(0,t) - T^{mod}(0,t))^2 + (T^{obs}(dz_2,t) - T^{mod}(dz_2,t))^2\right] \quad (3.9)$$

where t denotes the time step, and N is a normalization factor that counts the total number of data points being fitted.

We assumed that $p(y|m) \sim \exp(-\delta^2)$ and that $p(m)$ is a uniform distribution over a given range of the parameters. The corresponding ranges for the parameters κ and s were 0.01 to 10 mm^2s^{-1}, and -6×10^{-4} to 6×10^{-4} Ks^{-1}, respectively. We searched the two-dimensional space of the parameters (κ, s) using a Monte Carlo procedure to minimise δ^2 (Eq. (3.9)). The steps involved in this stochastic minimisation procedure are as follows.

- Simulation started with randomly chosen model parameters (κ, s) for the debris layer within the mentioned range.
- Random corrections $\kappa + \epsilon\Delta\kappa$ and $s + \epsilon\Delta s$ were proposed for the model parameters (κ, s), and temperature profiles were simulated with the new set of parameters. Here, ϵ was a uniform random number in the range -1 to 1, and $\Delta\kappa$ and Δs were fixed step sizes.
- The proposed parameters were then accepted with metropolis probability (Gelman and others, 2013) of $\text{Max}[1, e^{-\Delta\delta^2}]$, where $\Delta\delta^2$ is the difference between the δ^2 computed for the initial and the proposed

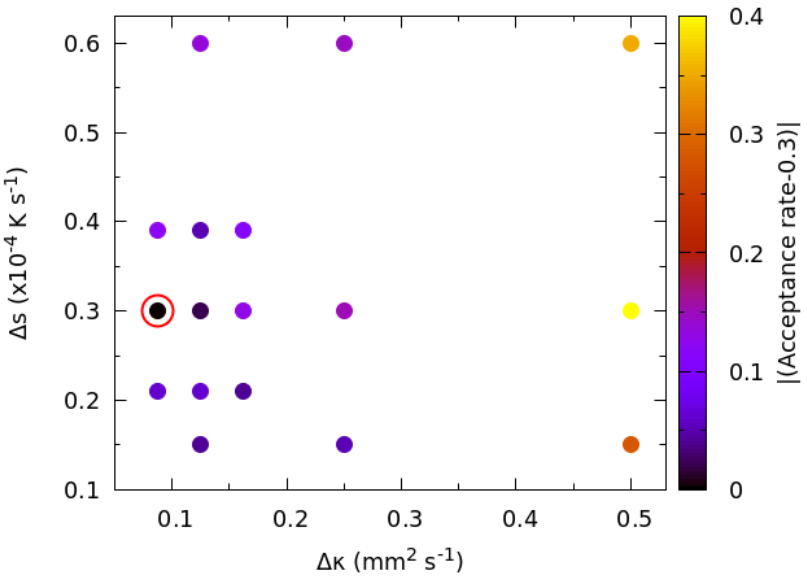

Figure 3.6: An example of the grid search procedure in the Bayesian method to find the pair of step sizes ($\Delta\kappa$ and Δs) which correspond to the mean acceptance rate closest to 30%. Here, the pair $\Delta\kappa$ and Δs plotted for an arbitrary pit SBP4 (Table 3.1), and the selected pair was denoted by the open red circle.

models. Whenever the proposed set of parameters was accepted, the initial set of parameter values (κ, s) was replaced by corresponding proposed values.

This procedure was repeated to perform a random walk in the parameter space for up to 5000 iterations. Efficient sampling of the parameter space requires an acceptance rate of approximately between 20–50% for the Monte Carlo approach (Gelman and others, 2013).

To achieve a reasonable acceptance rate, the step sizes $\Delta\kappa$ and Δs were tuned. First, we ran the MC for 5000 iterations for 9 pairs of ($\Delta\kappa$,Δs), with $\Delta\kappa$ (Δs) being 0.05, 0.025, and 0.0125 times the allowed range of κ (s) values. The mean acceptance rate over the last 2000 iterations in each of these runs was used to locate the ($\Delta\kappa$,Δs) pair value that gave an acceptance rate closest to 30%. Then, we zoomed around the neighborhood of the selected

pair within a region ±30% of the selected values (Fig. 3.6), and 9 pairs of ($\Delta\kappa$,Δs) values were chosen to repeat the whole procedure. The pair that gave an acceptance rate closest to 30% among the 18 trial pairs of ($\Delta\kappa$,Δs) was chosen (Fig. 3.6). This procedure was performed separately for each of the records.

With the chosen step sizes ($\Delta\kappa$,Δs), we ran the Monte Carlo for 10000 iterations. To check the convergence of the model parameters, we ran five independent Monte Carlo simulations, each time with a different random initial model and with a different sequence of pseudo-random numbers. We checked the auto-correlations of the time series and inspected the distribution of sampled parameters to ensure efficient sampling. Finally, we used the set of all accepted states from the last 5000 iterations of each of these five independent runs for our final calculations. Out of all the selected states, the maximum-likelihood state, i.e., the model with a minimum value of δ^2, was used to compute the best-fit temperature profile and thermal diffusivities. For each of the temperature records analysed, the ensemble of accepted states was utilised for computing the corresponding uncertainties of the best-fit parameters.

Inhomogeneous Bayesian method ($\mathbf{MC_i}$)

This method used two layers, with the boundary being equidistant from the sensors at $z = 0$ and $z = dz_2$ (Fig. 3.5b). Here, the forward model was solved imposing the continuity of the temperature and the heat flux at the interface between the two layers. In this case, m consisted of four parameters, κ_1, κ_2, s_1, and s_2, where subscripts 1 and 2 refer to the top and bottom layers, respectively. Apart from these differences, the same procedures and the apriori distributions used in the $\mathrm{MC_h}$ were used for the $\mathrm{MC_i}$.

3.4.3 Uncertainty in thermal diffusivity due to temperature measurement error

The uncertainties in the estimated values of κ due to the measurement errors in the debris temperature profiles were computed using a separate set of Monte Carlo simulations for both the finite-difference and Bayesian methods. We added a zero-mean random Gaussian noise to the temperature time series and the depths of the temperature sensors. The temperature noise had a standard deviation of 0.2°C, which was the specified accuracy of the thermistors. The standard deviation of the noise in the position of the temperature sensors was assumed to be 2 cm. The data with added noise were used as inputs to the four methods to obtain debris thermal diffusivities and ablation rates. This procedure was repeated 100 times for each method, and 100 copies of the noisy data set were used to compute the uncertainties of the best fit values of κ and s.

The above analysis was done for two randomly chosen pits, SBP4 and SBP7. We found that uncertainties in both κ and s were similar for the two data sets. Further, we checked that the uncertainties in each parameter (κ and s) did not change significantly if we increased the number of noisy data set from 100 to 150. The mean percentage error in both κ and s obtained from these computations was assumed to be the same for all the debris pits. Finally, the uncertainties in both κ and s due to measurement errors estimated by the above procedure (σ_0) were combined with the fit uncertainties (σ_1) from each method discussed above, to compute total uncertainties ($\sqrt{\sigma_0^2 + \sigma_1^2}$).

3.4.4 Synthetic experiments to check the accuracy of the methods

We took the top sensor data from an arbitrarily chosen pit SBP6 (Table 3.1) to fix the upper boundary temperature and ran a forward model simulation of the heat diffusion equation (Eq. (3.2)) under various circumstances as described below. Hourly temperature data at two bottom sensors were gen-

erated using the forward model simulations. The synthetic data were used as input to the methods (as discussed above) to recover κ. For simplicity, we assumed ρ, C, and ϕ to be the same constant throughout all experiments.

Experiment 1

We analysed the effect of varying the separation between sensors (dz), which controls the corresponding discretization errors, on the performance of the methods. Here, we kept the position of the top sensor fixed, and used the same κ for both layers with all sources (s) set to zero. Only the position of the two bottom sensors was varied. Synthetic data were generated for two different dz values of 5 cm and 20 cm, respectively (Table 3.2).

Experiment 2

Experiment 2 was designed to check the effect of the inhomogeneities in s values. Here both the layers had the same κ value, 1 mm^2 s^{-1}, and dz was set to 5 cm. Two different values of source terms $s_1 = 10^{-4}$ Ks^{-1} , and $s_1 = 2{\times}10^{-4}$ Ks^{-1}, were used for the two layers and synthetic data generated (Table 3.2).

Experiment 3

This experiment was designed to check the effect of various values of dz_1 and dz_2. Here, we ran a forward model simulation of the heat diffusion equation (Eq. (3.2)), for a given constant κ (1 mm^2 s^{-1}) and various values of dz_1 and dz_2. For two-layered models ($\mathrm{CR_i}$ and $\mathrm{MC_i}$), we computed the effective thermal diffusivity (κ_{eff}) by

$$\frac{d}{\kappa_{\mathrm{eff}}} = \frac{l_1}{\kappa_1} + \frac{l_2}{\kappa_2}, \tag{3.10}$$

where l_1 and l_2 are the thickness of the top and bottom layers, respectively. κ_1 and κ_2 are the thermal diffusivity of the top and bottom layers of the corresponding models.

In each method, the recovered κ_{eff} values for different sets of dz_1 and dz_2 were used to analyse the effect of relative separation between sensors on the

accuracy of the corresponding method. We restricted the range of dz_2/dz_1 to 1–5.7, which was in line with the typical values used in the literature (Conway and Rasmussen, 2000; Nicholson and Benn, 2006; Brock et al., 2010; Nicholson and Benn, 2013; Reid et al, 2012; Rounce et al, 2015; Chand et al, 2018; Rowan et al, 2020). In our field measurements, the dz_2/dz_1 varied in the range 1–1.5 (Table 3.1).

For independent verification of the trend of κ_{eff} with dz_2/dz_1 as obtained in synthetic experiment 1, we plotted the estimated κ_{eff} for all the four methods as a function of dz_2/dz_1. To further validate the above trend, we used the available debris temperature data from Khumbu glacier, eastern Himalaya, Nepal (Rowan et al, 2020). We considered the pits where debris temperatures was measured at more than seven different depths during the summer season (Rowan et al, 2020). We split the temperature profile data from each pit into a 15-day window for consistency with our methodology. For each temperature record, we applied the CR_h method to estimate the κ for different dz_2/dz_1 by selecting three different sensor depths.

Experiment 4

This experiment was designed to check the performance of the methods in the case of a vertically inhomogeneous distribution of κ. Here, we kept $dz_2/dz_1 = 1$ and $s = 0$. We used two horizontally homogeneous layers with different κ (κ_1 for the top layer and κ_2 for the bottom layer) to generate the temperature data at two bottom sensors in the forward model simulation. The boundary between the two layers was equidistant from the two sensors with depths 0 and dz_2 (Fig. 3.5).

Then, the κ_{eff} obtained from the forward model simulation was compared with the κ_{eff} from all the methods to check the accuracy of the methods in recovering κ. This process was repeated for different sets of κ_1 and κ_2 in the forward model simulations.

We also took the top sensor data from another arbitrarily chosen pit SBP3 (Table 3.1) and repeated all the synthetic experiments to ensure our results were not specific to the record/pit analysed.

Additionally, to ascertain the performance of the methods for different diurnal temperature amplitudes, we had repeated the above three experiments by changing the diurnal temperature amplitude of the top sensor in the forward model simulation by a factor of 5.

3.4.5 Sub-debris ablation estimation

Using the debris temperature profile data, we estimated κ from four different methods (Section 4.1). Given the estimated values of κ, sub-debris ablation rates were estimated using Eqn (3.3). The values ρ_d, C, and ϕ (Eqn (3.3)) were assumed to have 10% uncertainties (Conway and Rasmussen, 2000; Nicholson and Benn, 2013). In both CR_h and CR_i methods, the value of $\frac{dT}{dz}$ was obtained by a linear fit to the mean temperature at all three sensors (Conway and Rasmussen, 2000), whereas in MC_h and MC_i methods, $\frac{dT}{dz}$ was obtained by a linear fit to the mean simulated temperatures at each of the grid points from depth dz_2 to the debris-ice interface (Fig. 3.5). In CR_i and MC_i methods, the thermal diffusivity estimated for the bottom-most layer in the simulation, κ_2, was used to compute the sub-debris ablation rates.

The estimated sub-debris ablation rates obtained from the temperature profiles were compared to the glaciological method using stakes. To make the comparison, we needed the observed ablation rate for the given debris thickness of each of the pits. Because of random local variations of debris thickness, we generally did not have ablation stakes installed with exactly the same debris thickness as that of the nearest pit. Following Shah et al (2019), we considered all the data points of the sub-debris ablation available across the debris-covered ablation zone for each of the periods and interpolated the observed ablation rates as a function of debris thickness (Shah et al, 2019) to estimate the glaciological ablation rates corresponding to the debris thickness of the pits. The number of available stakes for any given period varied between 12 to 65. For each of the glaciological ablation rate values, the corresponding uncertainty was computed by the procedure described in Shah et al (2019), and the following paragraph provides a brief discussion on that.

A zero-mean random Gaussian noise with a standard deviation of 2 cm was added to each glaciological ablation data to mimic the measurement noise. Then, we fitted the ablation data with added noise to the form given in Shah et al (2019). The quoted uncertainties in the glaciological ablation rates were estimated from the mean prediction band (90% confidence level) of the fitted function. This procedure was repeated for 100 times. Each time, we also added random Gaussian noise to the debris thickness of any pit while estimating the glaciological ablation rates to the corresponding debris thickness. The standard deviation of this noise was assumed to be 3 cm, which was due to the roughness at the debris surface. In three specific pits (SBP1, SBP2, and SBP6 in Table 3.1), due to a heap of rocks on the top of the surface, we added a random value between 5 cm to 15 cm to the debris thickness value used in the simulation. This procedure was also repeated for 100 times. Then, we were left with a total of 10^4 estimates of observed ablation rates for each temperature record, which was used to estimate the mean observed glaciological ablation rate and its uncertainty.

3.5 Results and discussions

3.5.1 Lessons from synthetic experiments

Effect of discretization on the accuracy of the methods

For $dz = 5$ cm, the estimated κ values from all the methods reproduced the forward model κ-values ($\kappa_1 = \kappa_2 = 1.0$ mm^{2}s^{-1}), except that κ_2 was underestimated in $\mathrm{MC_i}$ method by 10% (Table 3.2). In this experiment, forward models were run with $s = 0$, and both the CR and MC method estimates for source value matched that. However, $\mathrm{CR_i}$ method yielded a small positive s value of 0.01×10^{-4} Ks^{-1}.

For $dz = 20$ cm, the best-fit κ-values in both $\mathrm{CR_h}$ and $\mathrm{CR_i}$ method underestimated the forward model values ($\kappa_1 = \kappa_2 = 1.0$ mm^{2}s^{-1}) by up to 20% (Table 3.2). In contrast, κ_1 and κ_2 were retrieved accurately in both the MC methods. s values estimated by the CR and MC methods matched the

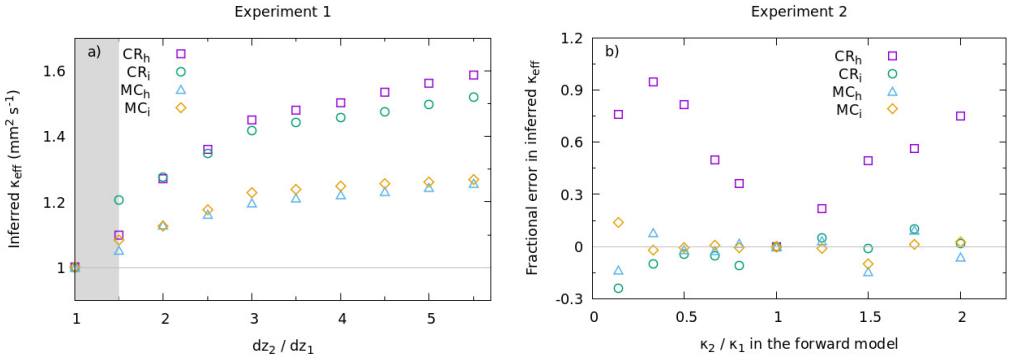

Figure 3.7: a) In synthetic experiment 3, the inferred κ_{eff} values from the four methods were plotted for different values of (dz_2/dz_1) (see the text for details). The black horizontal line denotes the value of κ_{eff} (1 mm^2 s^{-1}) used in the synthetic experiments. The vertical gray band was the range (see the text for details) of (dz_2/dz_1) in the field data (Table 3.1) of debris temperature used in this study. b) In synthetic experiment 4, the fractional errors in inferred κ_{eff} relative to the forward model values were plotted against (κ_2/κ_1) used in the forward model. Here we kept $(dz_2/dz_1) = 1$.

known forward-model value of $s = 0$ Ks^{-1}, while in the CR$_{\text{i}}$ method, again a small negative s value of -0.03×10^{-4} Ks^{-1} was obtained.

Inhomogeneity of heat sources and the accuracy of the methods

Experiment 2 analysed the effect of the inhomogeneities of the s values on the performance of the methods. The fitted s values in both CR$_{\text{h}}$ and CR$_{\text{i}}$ method (0.87×10^{-4} Ks^{-1} and 1.24×10^{-4} Ks^{-1} respectively) failed to reproduce the effective s (1.5×10^{-4} Ks^{-1}) in the forward model simulation (Table 3.2). The MC$_{\text{h}}$ estimates of s was 0.80×10^{-4} Ks^{-1}. Whereas s_1 and s_2 in the MC$_{\text{i}}$ method have 60% and 81% departure from the forward model value. So all of the methods failed to reproduce s values. For this experiment, the forward model used the same κ values of 1×10^{-6} m^{2}s^{-1} for both layers. That was also not captured by any of the methods.

Table 3.2: Details of the synthetic data generated by the forward model and relative performance of the methods. The units of κ is $\mathrm{mm^2 s^{-1}}$ and s is $\times 10^{-4}$ $\mathrm{K s^{-1}}$. The result from $\mathrm{MC_h}$ method was similar to that of from $\mathrm{MC_h}$ method.

Sensor depths (cm)	Debris thickness (cm)	Δz (cm)	Forward model				$\mathrm{CR_h}$ method		$\mathrm{CR_i}$ method			$\mathrm{MC_i}$ method			
			κ_1	κ_2	s_1	s_2	κ	s	κ_1	κ_2	s	κ_1	κ_2	s_1	s_1
Experiment 1 : Discretisation error															
35,40,45	50	5	1.0	1.0	0	0	1.0 ±0.01	0.0	1.0 ±0.01	1.0 ±0.01	0.01 ±0.01	1.0 ±0.02	0.9 ±0.03	0.0 ±0.00	0.0 ±0.02
5,25,45	50	20	1.0	1.0	0	0	0.9 ±0.05	0.0	0.9 ±0.04	0.8 ±0.07	−0.03 ±0.02	1.0 ±0.03	1.0 ±0.01	0.0 ±0.00	0.0 ±0.04
Experiment 2 : Inhomogeneities in sources															
35,40,45	50	5	1.0	1.0	1.0	2.0	0.88 ±0.07	0.87 ±0.07	1.01 ±0.01	1.07 ±0.01	1.24 ±0.02	1.5 ±0.02	1.3 ±0.04	1.6 ±0.00	2.8 ±0.01

Effect of sensors spacing on the accuracy of the methods

The results from experiment 3 established that all the methods reproduced the known κ_{eff} accurately for $dz_2/dz_1 = 1$ (Fig. 3.7a). As the ratio increases $dz_2/dz_1 > 1$, we found a systematic bias in the recovered κ_{eff}, which increased with increasing dz_2/dz_1 values for four methods (Fig. 3.7a).

Effect of inhomogeneity on the accuracy of the methods

Results from synthetic experiment 4 established that the accuracy of recovered κ_{eff} in the methods depends on the magnitude of the ratio (κ_2/κ_1), which denotes the inhomogeneity of the two-layer used (Fig. 3.7b). The root means squared error (RMSE) between forward model κ_{eff} with that from the CR_h, CR_i, MC_h, and MC_i methods were 0.62, 0.08, 0.07, and 0.03 $\text{mm}^2\ \text{s}^{-1}$, respectively. In general, the MC_i method outperformed in recovering κ_{eff}, which yielded the smallest RMSE compared to the other three methods. In comparison, the performance of the CR_i and MC_h methods was comparable to the MC_i. The commonly used standard finite-difference method (CR_h) performed worst in this experiment. These results highlight the importance of using the MC_i or CR_i method to estimate sub-debris melt that considers the effect of inhomogeneity in the debris layer.

We verified that the results of synthetic experiments remained the same when the above exercise was repeated by taking top sensor data from another arbitrarily chosen pit SBP4. We had also looked for possible effects of diurnal temperature amplitude on the accuracy of the methods. It was seen that it did not change the above results discussed above.

3.5.2 Trends of effective thermal diffusivities from actual pit data

We plotted the estimated κ_{eff} values from the pit data using the four methods as a function of dz_2/dz_1. As Fig. 3.8(a–d) shows, biases in κ_{eff} for $dz_2/dz_1 > 1$ associated with all four methods. The trend of increasing κ_{eff} with increasing $(dz_2/dz_1) > 1$ from pit data is consistent with the results from synthetic

Table 3.3: Comparison of estimated κ_{eff} from this study with the values from the literature, within and outside the Himalaya. Here, the range of κ_{eff} obtained from the pits at Khumbu Glacier is marked with a '*'.

Source	Glacier (country)	Method	Range of κ_{ef}
	Within Himalaya		
This study	Satopanth (India)	CR_h	0.10±0.10–2
		CR_i	0.30±0.10–3
		MC_h	0.30±0.15–3
		MC_i	0.42±0.10–3
?	Khumbu (Nepal)	CR_h	0.6±0.1–0.9
?	Ngozumpa (Nepal)	CR_h	0.7±0.1–0.9
Chand et al (2018)	Lirung (Nepal)	CR_h	0.2±0.0–2.0
Rounce et al (2015)	Imja-Lhotse Shar (Nepal)	CR_h	0.3±0.1–1.2
Rowan et al (2020)	Khumbu (Nepal)	CR_h	0.7±0.1
		CR_h	0.1±0.2–11.4
	Ngozumpa (Nepal)	CR_h	1.0±0.1
	Imja-Lhotse Shar (Nepal)	CR_h	1.4±0.1
	Outside Himalaya		
?	Larsbreen (Svalbard)	CR_h	0.3±0.1–1.2
	Belvedere (Italy)	CR_h	0.4±0.1–1.4
Anderson et al (2021)	Kennicott (Alaska)	CR_h	0.7–3.1
Brock et al. (2010)	Miage (Italy)	Brock et al. (2010)	0.5–1.0
Reid et al (2012)	Haut Glacier d'Arolla (Switzerland)	Brock et al. (2010)	0.7

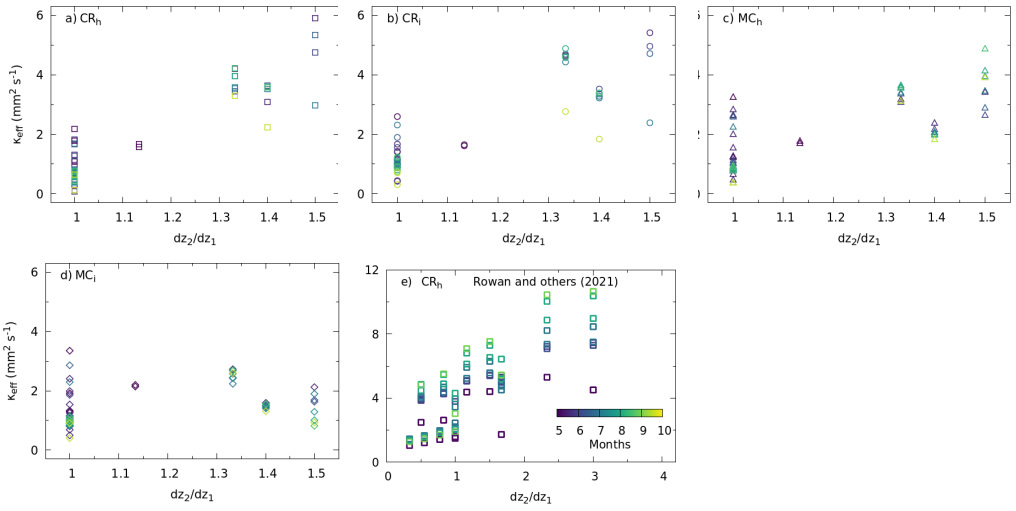

Figure 3.8: a)–d) Estimated values of κ_{eff} from the four methods are plotted as a function of dz_2/dz_1 for all the records. The colors of the symbols denote the month of the temperature measurement. e) The CR_h method estimates of κ_{eff} plotted for different dz_2/dz_1 in a pit (KH1) from Khumbu Glacier during the ablation season of 2014 (Rowan et al, 2020)

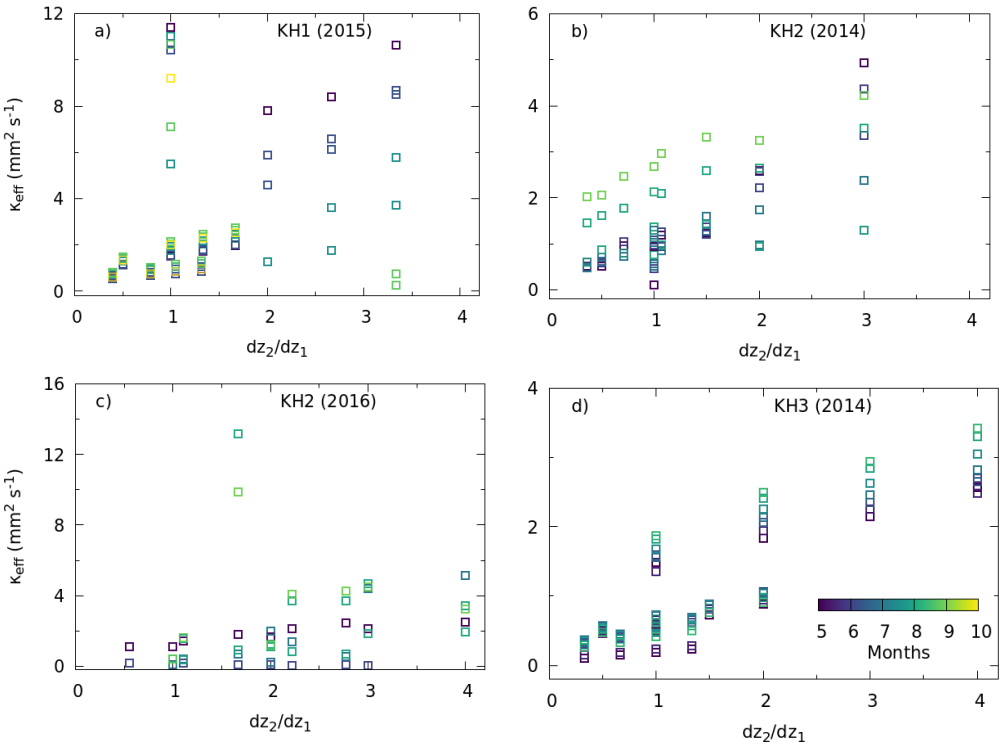

Figure 3.9: CR_h estimates of κ plotted for different dz_2/dz_1 from Khumbu Glacier during the ablation season of 2014–2016 for different pits (Rowan and others, 2021)

experiment 1, despite the limitations of the methods (discussed later). This confirms the robustness of the finding from synthetic experiment 1. A similar trend of increasing κ_{eff} with increasing $dz_2/dz_1 > 1$ was also observed in the data from Khumbu glacier, which was analysed using CR_h method (Fig. 3.8f and 3.9). Although Rowan et al (2020) pointed out that, except for the pit KH1, debris temperature data were highly affected by the presence of non-conductive processes. The true values of κ_{eff} at Satopanth and Khumbu glaciers were unknown, so the accuracy of κ_{eff} estimated for those sites cannot be assessed explicitly. However, the trends of κ_{eff} from actual pit data provide additional evidence supporting the results obtained in synthetic experiment 3.

While the dependence of the biases in recovered κ_{eff} on dz_2/dz_1 can be theoretically expected from Eq. (3.4), the sign of the bias can not be determined without knowledge of $\partial_z^3 T(0,t)$. With only three sensors used to analyse debris temperature profiles, one could not determine the sign of $\partial_z^3 T(0,t)$ using finite difference methods. However, if we consider the known analytical solution for the case of an infinite slab with sinusoidal temperature variation applied on the upper boundary (Anderson and Anderson, 2010), it is seen that $\partial_z^3 T(0,t)$ is positive for all t. This is consistent with the sign of the bias found here in synthetic experiment 3 (Fig. 3.7a). Given that the trend is the same in the theory, synthetic experiment, and observationally-derived values, these results support the conclusion that the accuracy of κ_{eff} decreases with increasing dz_2/dz_1.

3.5.3 Distribution of thermal diffusivities

Based on the results obtained above, hereinafter we only considered the set of temperature records where $dz_1 = dz_2$. This criteria leaves 38 temperature records out of 64. During the field experiment, we found that the debris thickness in four records from the pit SBP1 (for ablation season 2016) had changed after installation, which may be due to debris movement. These were discarded, leaving 34 records. In CR_h and CR_i methods, four records (of the 34) resulted in unphysical negative values of κ_{eff}; therefore, these were

also discarded. So, in the rest of the paper, we discuss only 34 records with respect to the Bayesian method (MC_h and MC_i) and 30 records with respect to the finite-difference method (CR_h and CR_i).

CR_h method : For the selected records, the mean (standard deviation) estimated κ from the CR_h method was 0.8 (0.4) mm^2s^{-1}. The κ values were in the range 0.1–2.1 mm^2s^{-1}. This implies a mean (standard deviation) thermal conductivity of 1.1 (0.6) $Wm^{-1}K^{-1}$. For this method, the R^2 of the fits for the selected records varied between 0.43–0.93.

CR_i method : In the CR_i method, the mean (standard deviation) estimated κ_1 and κ_2 were 1.0 (0.4) and 1.4(0.6) mm^2s^{-1}, respectively, for the selected records. The values of κ_1 and κ_2 were in the range 0.2–2.4 and 0.6–3.1 mm^2s^{-1}, respectively. This implies a mean (standard deviation) thermal conductivity of the top and bottom layer were 1.4 (0.6) and 2.0(0.8) $Wm^{-1}K^{-1}$, respectively. R^2 of the fits for the selected records varied between 0.41–0.98.

MC_h method : In the MC_h method, the mean (standard deviation) estimated κ was 1.2 (0.7) mm^2s^{-1} for the selected records. The values of κ were in the range 0.4–3.3 mm^2s^{-1}. This implies a mean (standard deviation) thermal conductivity of 1.7 (1.0) $Wm^{-1}K^{-1}$. For this method, the δ^2 of the fits for the selected records varied between 0.005–0.08, and the Monte Carlo acceptance rate varies from 22% to 43%.

MC_i method : In the MC_i method, the mean (standard deviation) estimated κ_1 and κ_2 were 1.2 (0.6) and 2.0 (1.0) mm^2s^{-1}, respectively, for the selected records. The values of κ_1 and κ_2 were in the range 0.3–3.2 and 0.7–4.3 mm^2s^{-1}, respectively. This implies a mean (standard deviation) thermal conductivity of the top and bottom layer were 1.7 (0.8) and 2.8(1.4) $Wm^{-1}K^{-1}$, respectively. For this method, the δ^2 of the fits for the selected records varied between 0.0005–0.01, and the Monte Carlo acceptance rate varies from 22% to 43%.

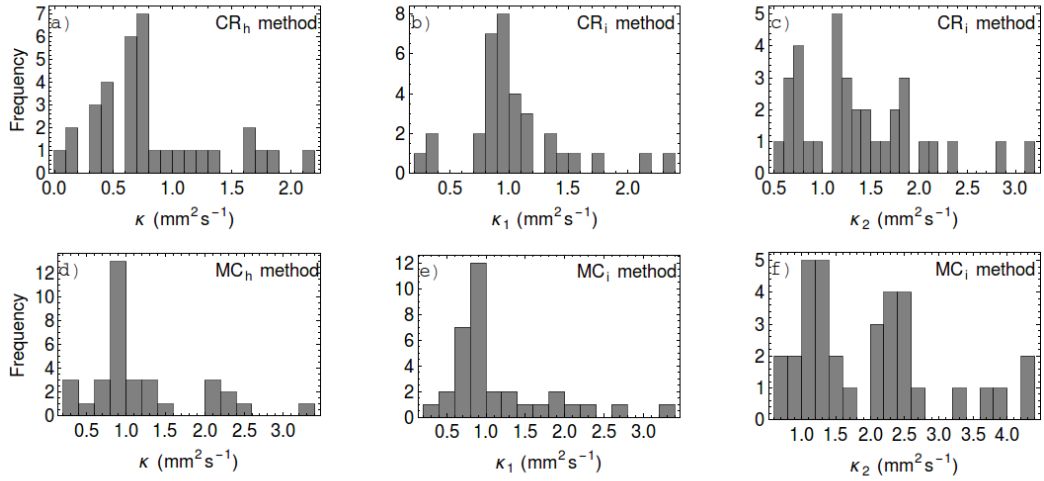

Figure 3.10: Histogram of estimated κ for selected records from all four methods are shown here.

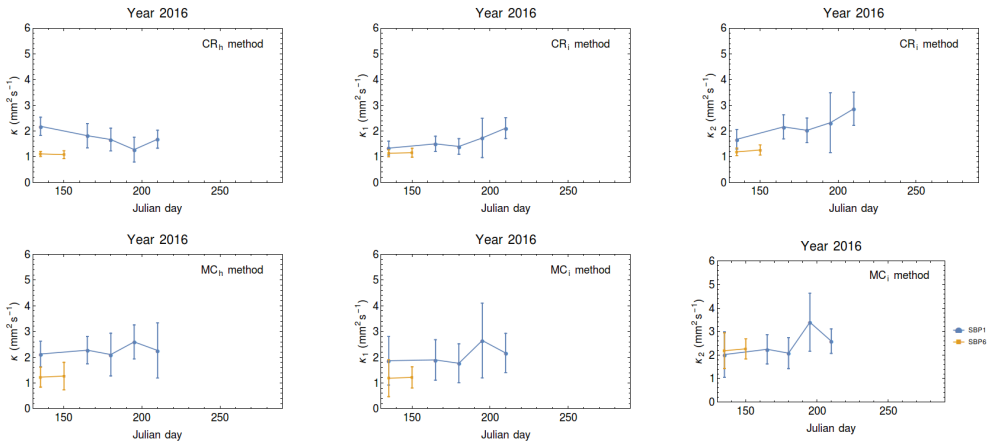

Figure 3.11: Temporal distribution of estimated κ for all four methods during the ablation season 2016. Different colors and symbols denoted different pits.

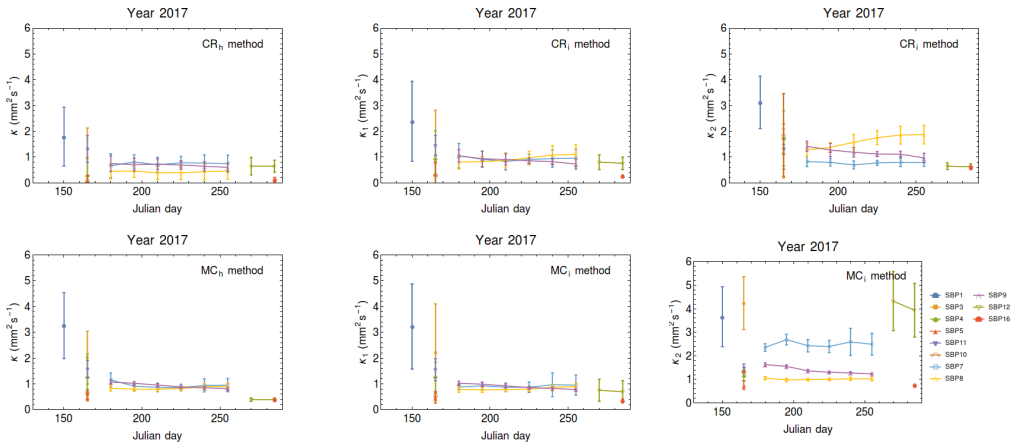

Figure 3.12: Temporal distribution of estimated κ for all four methods during the ablation season 2017. Different colors and symbols denoted different pits.

In the MC_i method, the mean, standard deviation, and range of κ_1 (κ_2) were 1.2 (2.0), 0.6 (1.0), 0.3–0.32 (0.7–4.3) mm^{2}s^{-1}, respectively. In the other three methods, the corresponding values and fit qualities in Table 3.4. The uncertainty in the fitted κ values reported in previous studies ranged from 10% to 34% (Conway and Rasmussen, 2000; Nicholson and Benn, 2013; Rounce et al, 2015; Chand et al, 2018). In this study, all the four deployed methods had a median uncertainty of 11%. The magnitude of the difference between the values of κ estimated for each layer using the two inhomogeneous methods (CR_i and MC_i) was similar (Table 3.4). The range of κ_{eff} was similar for all the methods, with somewhat larger values compared to the previous reports from glaciers in and outside the Himalaya (Table 3.3). However, the corresponding median κ_{eff} in all the methods was similar to that reported in the literature. We speculate that the larger thermal diffusivity values in a few pits at Satopanth Glacier may be related to possible changes in moisture content, latent heat fluxes, ϕ, C, or ρ_d during the study period. However, to ascertain that additional in-situ measurements of K, C, ϕ, ρ_d, moisture content, horizontal and vertical heat fluxes are needed, which will be taken up in the future.

Table 3.4: Details of the thermal properties and heat source/sink terms obtained using the four different methods for the selected pits where $dz_2 = dz_1$, and the goodness-of-fit metrics corresponding to each method.

	CR_h method	CR_i method	MC_h method	MC_i method
Mean (standard deviation) of κ (mm^2s^{-1})	0.8 (0.4)	κ_1: 1.0 (0.4)	1.2 (0.7)	κ_1: 1.2 (0.6)
		κ_2: 1.4 (0.6)		κ_2: 2.0 (1.0)
Range of κ (mm^2s^{-1})	0.1–2.1	κ_1 : 0.2–2.4	0.4–3.3	κ_1: 0.3–3.2
		κ_2: 0.6–3.1		κ_2: 0.7–4.3
Mean (standard deviation) of K ($W\ m^{-1}K^{-1}$)	1.1 (0.6)	K_1: 1.4 (0.6)	1.7 (1.0)	K_1: 1.7 (0.8)
		K_2: 2.0 (0.8)		K_2: 2.8 (1.4)
Mean (standard deviation) of s ($\times 10^{-4}$ Ks^{-1})	-0.4 (0.7)	0.1 (0.3)	-0.1 (0.6)	s_1: -0.3 (2.3)
				s_2: -0.6 (2.5)
Range of s ($\times 10^{-4}$ Ks^{-1})	-1.7 to 0.8	-0.9 to 0.3	-2.0 to 0.4	s_1: -5.0 to 5.0
				s_2: -4.7 to 5.0
Range of R^2 of the fits	0.43–0.93	0.41–0.98		
Range of δ^2 (Eqn. (3.9)) of the fits			0.005–0.08	0.0005–0.01
Monte Carlo acceptance rates			22%–43%	22%–43%

Spatial variability of thermal diffusivities

We found significant spatial variability in κ within the uncertainty using all the methods (Figs. 3.11 and 3.12). The mean (standard deviation) of κ_{eff} was estimated using the CR_i and MC_i methods, and that from the literature were 1.3 (0.8), 1.5 (0.9), and 0.9 (0.5) $\text{mm}^2\ \text{s}^{-1}$, respectively. So, there was a greater within-glacier variability of κ_{eff} at Satopanth Glacier than reported in the literature. This spread in κ, as well as the vertical inhomogeneity, are important because they imply that debris thickness estimates made using remote-sensing data using the average value of κ may be more uncertain than they have been reported to be (Mihalcea et al, 2008; Foster et al, 2012; Schauwecker et al, 2015). The same may be true of the predictions of the sub-debris ablation or meltwater runoff that have been made using energy-balance models (Nicholson and Benn, 2006; Reid and Brock, 2014; Lejeune et al, 2013) or glacio-hydrological models (Fujita and Sakai, 2014; Hagg et al, 2018; Zhang et al, 2019), where a spatially uniform thermal diffusivity has been assumed. The results presented here may help improve the estimates of the prediction uncertainties in future studies.

Temporal variability of thermal diffusivities

A seasonal trend was evident in the estimates made using data records of at least a few months in length, in which κ increases after the onset of the monsoon (Figs. 3.11 and 3.12). We found the same result using the data from Khumbu Glacier (Rowan et al, 2020) (Figs. 3.8f and 3.9). However, the observed seasonal amplitude was smaller than the estimated uncertainties in all the above cases. This implies that the seasonal variability in κ is not likely to be a significant uncertainty source in of debris thickness or ablation models.

3.5.4 Distribution of heat sources

The range of s values obtained in CR_h, CR_i, and MC_h methods were -1.7×10^{-4} to 0.8×10^{-4}, -0.9×10^{-4} to 0.3×10^{-4}, and -2.0×10^{-4} to 0.4×10^{-4}

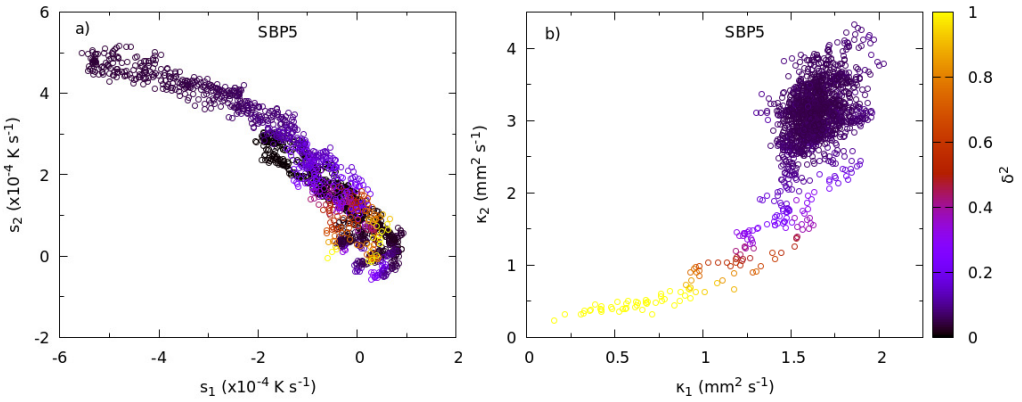

Figure 3.13: For an arbitrarily chosen pit SBP5 (Table 3.1), a) s_1-s_2, and b) κ_1-κ_2 values of all the accepted models from the last 5000 iterations of MC_i method was plotted where the corresponding δ^2 of the fits colored each point. The models are not covering the whole s_1-s_2 plane, instead these two parameters were anti-correlated with all points roughly on $s_1+s_2 \sim 0$ line. Also, the δ^2 did not change significantly along this line compared to that from the κ_1-κ_2 plane.

Ks^{-1}, respectively. The mean (standard deviation) of s values in there three methods were -0.4×10^{-4} (0.7×10^{-4} Ks^{-1}), 0.1×10^{-4} (0.3×10^{-4}), and -0.1×10^{-4} (0.6×10^{-4}) Ks^{-1}, respectively.

s_1 and s_2 values from both layers in the $\mathrm{MC_i}$ method were in the range of $-5.0{\times}10^{-4}$ to $5.0{\times}10^{-4}$ Ks^{-1} and $-4.7{\times}10^{-4}$ to $5.0{\times}10^{-4}$ Ks^{-1}, respectively. The corresponding mean (standard deviation) were $-0.3{\times}10^{-4}$ ($-2.3{\times}10^{-4}$) Ks^{-1} and $-0.6{\times}10^{-4}$ ($-2.5{\times}10^{-4}$) Ks^{-1}, respectively, which was larger than s estimated from finite difference methods. The range of s_1 and s_2 obtained in the $\mathrm{MC_i}$ method was close to the range of s used in the corresponding model setup. One can see in Fig. 3.13a, the δ^2 of the fits did not minimizes in the s_1 and s_2 plane compared to the κ_1 and κ_2 plane (Fig. 3.13b). Also, we observed that the values of s_1 and s_2 were anti-correlated, with all the points roughly on the line of $s_1 + s_2 \sim 0$. Similar δ^2 of the fits can be obtained just by changing the sign of s_1 and s_2 values. This indicates that the MC_i method is not sensitive enough to estimate the vertical inhomogeneities in s.

To understand if the thermal impact of the obtained s values were significant, we compared the net heat contributed by the sources with corresponding melt energy flux. Averaging over all the selected records for the $\mathrm{CR_i}$ method, we found that the net estimated heating of the layers due to sources was not significant relative to the uncertainty (6 ± 9 Wm^{-2}), whereas the mean conductive flux of 36 ± 6 Wm^{-2} supplied to the ice layer below. A similar result was found in the case of $\mathrm{CR_h}$ and $\mathrm{MC_h}$ methods.

The above findings suggest that, on average, the debris layer can be well approximated by a one-dimensional model (Eqn. (3.2)) and horizontally homogeneous conductor, where internal sources (e.g., those due to latent heat or lateral inhomogeneity) play a relatively minor role, within uncertainty. The same feature was evident from the data from Khumbu glacier (Rowan et al, 2020), where the net estimated heating of the layers due to sources varied from 4 ± 12 to 16 ± 17 Wm^{-2}. Therefore, it may be worth exploring if the above result is a general feature of debris-covered glaciers in the Himalaya or elsewhere.

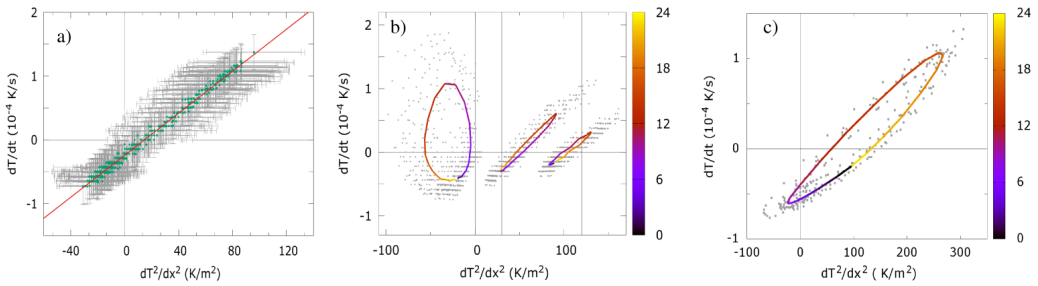

Figure 3.14: a) A linear fit (solid red line) to $\partial_t T$ data as a function of measured $\partial_z^2 T$ (green dots) from pit SBP3 during pre-monsoon, 2016. b) Data from three different depths in the same pit during the pre-monsoon season, 2016 (grey dots). Closer to the surface, the mean diurnal variation (solid colored line, color denotes hour of the day) shows an elliptical pattern. c) An similar elliptical behaviour was obtained in a numerical experiment in the absence of any sources due to finite discretisation errors (see text for details).

3.5.5 Effect of time-varying heat sources on the discretisation procedure of the $\mathrm{CR_h}$ method

A time-dependent heat source ($s(t)$) can cause deviation from a simple linear relation between $\partial_t T$ and $\partial_z^2 T$ in the $\mathrm{CR_h}$ method. Exchange of latent heat during evaporation/condensation of liquid water in the debris and/or melting/refreezing within the debris layer is a potential source ($s(t)$). Its magnitude may depend on the moisture availability, a changing local temperatures within the layer, or a variable turbulent exchange with the atmosphere. These factors are expected to vary on a seasonal to daily time scales, introducing non-linearities in the relationship between $\partial_t T$ and $\partial_z^2 T$, and creating difficulties in the estimation of κ. However, if κ is known, the same non-linearity can be used to estimate the time-varying source strength $s(t)$, provided the signals are larger than the sum of measurement errors and discretisation errors.

Indeed, the plots of $\partial_t T$ and $\partial_z^2 T$ show a large scatter near the surface (Fig. 3.14b). Similar trends have been observed elsewhere and attributed to

non-conductive heat transfer modes near the debris surface (Nicholson and Benn, 2013). However, a closer look at the data reveals that the scattered points describe an elliptical curve that traversed with a period of 24 hours. If the mean daily behaviour over several weeks is plotted, this pattern becomes quite clear (Fig. 3.14b), and the magnitude of the effect seems to attenuate with sensor depth (Fig. 3.14b). This points to a strong source term with a characteristic diurnal cycle. However, as explained below, these signals are spurious and are caused by the discretisation errors inherent in the finite-difference method used.

The solution for subsurface temperature variation given hypothetical vertical heat conduction within a homogeneous semi-infinite conductor with a sinusoidal temperature variation at the surface is as follows (Anderson and Anderson, 2010),

$$T(z,t) \;=\; T_0 + \Delta T \exp(-\frac{z}{z_0}) \sin(\omega t - \frac{z}{z_0}). \tag{3.11}$$

Here, ω is the angular frequency, $z_0 = \sqrt{\pi\kappa/\omega}$ is a characteristic length scale. This solution describes a temperature profile that oscillates in space and time. The oscillation amplitude is damped exponentially with depth, and has a phase lag that increases linearly with depth. For heat conduction through supraglacial debris, the presence of a 0°C ice-debris interface complicates the actual solution. However, similar behaviour is expected at least in the limit of $z << z_0$ and $z << d$, which is near the debris surface.

To accurately compute the spatial derivatives of such an oscillatory function by finite-difference methods, the spatial steps in Eq. (3.2) must be smaller than the characteristic length scale z_0 i.e. $\Delta z << z_0$. For a diurnal surface temperature variation and a typical κ value of 1 mm^2 s^{-1} , $z_0 \sim 20$ cm. Therefore with $\Delta z \sim 10$ cm, the finite difference errors are large. At depths $z > z_0$, where the oscillation amplitude (ΔT) is small compared to the mean (T_0), finite difference errors become less important.

The form of the above solution (Eq. (3.11)) suggests that both $\partial_t T$ and $\partial_z^2 T$ vary as $\sin(\omega t + \phi)$, leading to a parametric linear relationship between them as t varies. On the other hand, the discretised versions (Eqs. (3.5) and (3.6)) $\partial_z^2 T$ pick up a phase difference, δ, that depends on $\Delta z/z_0$ and is

Table 3.5: Statistical measures used to compare the ablation rate estimates from four different methods with the glaciological data considering only the selected temperature records (see Sec. 3.5.6 for details).

	CR_h method	CR_i method	MC_h method	MC_i method
RMSE (cm w.e. day^{-1})	0.48	0.32	0.36	0.30
R^2_{adj}	0.06	0.30	0.30	0.43
Mean bias (cm w.e. day^{-1})	0.34	-0.03	0.16	-0.10
Relative bias	39%	-4%	19%	-11%

negligible only if $\Delta z << z_0$. Thus, we have to consider points $(\sin(\omega t + \phi), sin(\omega t + \phi + \delta))$, which parameterise an ellipse in general as t varies and create periodic elliptical scatter such as that we observe in our near-surface data.

To verify this conjecture, we obtained a numerical solution of the heat diffusion equation for a homogeneous debris layer that is forced by a diurnal sinusoidal surface temperature variation with $s = 0$. The simulated temperature profiles are then used to construct a discrete temperature time series at depths similar to those in our experiments and analysed using the method of Conway and Rusmusssen (2000). The result of this test (Fig. 3.14c) shows an apparent elliptical variation solely due to finite-difference errors. This subtlety has been overlooked in the literature to the best of our knowledge. It is likely that much of the scatter seen at the near-surface data is due to such discretisation errors. Non-conductive effects (e.g., the latent-heat flux and convective heat exchange) that have been invoked to explain this scatter are likely to be much smaller in magnitude.

3.5.6 Sub-debris ablation rate estimates

Considering the selected pits with $dz_2 = dz_1$ used for the analysis, the glaciological ablation rates varied between 0.2–1.3 cm w.e. day^{-1} (Fig. 3.15). The debris thickness in these pits ranged from 22 to 77 cm. In general, for any

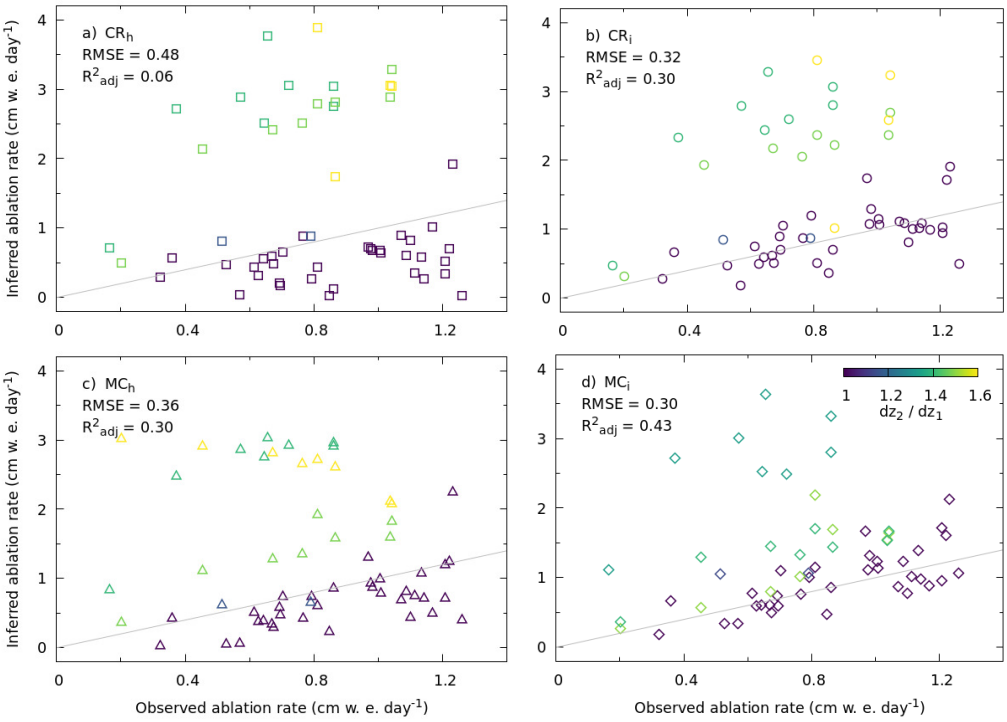

Figure 3.15: Comparison of ablation rate estimates from the CR_h (a), CR_i (b), MC_h (c), MC_i (d) methods, with that obtained from the observed glaciological method using ablation stakes. Each point is colored by dz_2/dz_1 of the corresponding pit. The asserted RMSE and R^2_{adj} were estimated using the selected temperature records with $dz_2/dz_1 = 1$ (see text for details). The solid grey line is a guide to the eye that denotes a perfect match.

given period, higher ablation rates were found at pits with thinner debris and vice versa, which is consistent with the results from Shah et al (2019) and other studies (e.g., Winter-Billington and others, 2020). The CR_h, CR_i, MC_h, and MC_i estimates of ablation rates varied between 0.02–1.9, 0.2–1.9, 0.04–2.3, and 0.2–2.1 cm w.e. day^{-1}, respectively.

The comparisons between the observed glaciological ablation rates with those obtained using the debris temperature profiles (Fig. 3.15) yielded RMSE's of 0.48, 0.32, 0.36, and 0.30 cm w.e. day^{-1} using the CR_h, CR_i, MC_h, and MC_i methods, respectively (Table 3.5). The number of fitted parameters in these four methods was 2, 3, 2, and 4, respectively; therefore, we also used the adjusted R^2 (R^2_{adj}) as a measure of the goodness-of-fit of the models. The R^2_{adj} values were 0.06, 0.30, 0.30, and 0.43, respectively, for the CR_h, CR_i, MC_h, and MC_i methods (Table 3.5). This suggested that the MC_i method most accurately reproduced the observed ablation rates, and the least accurate estimates were found using the CR_h method, which is commonly used in the literature.

The values of RMSE showed that the models performed adequately, with errors in the order of a few cm, and accumulating to 36 to 58 cm w.e. over a four-month ablation season (e.g., Fig. 3.17). The R^2_{adj} values were not as compelling; the value of 0.06 for the CR_h method was particularly low, but even the value of 0.43 calculated for the MC_i method was not as high as might be expected. This is due to the penalties applied in the calculation of R^2_{adj} for the predictor variables that do not significantly increase the goodness-of-fit of the model. As stated above, the source term, s, did not contribute significantly to ablation rates; therefore, the R^2_{adj} of the regression models were penalised for including s as a predictor variable.

Figure 3.17 provides an example of the cumulative ablation predicted for an individual pit. Similar plots for the remaining pits can be found in Fig. 3.18. It can be seen that the accuracy of sub-seasonal ablation estimates improved when the inhomogeneous methods (CR_i and MC_i) were applied to individual pits. The MC_i method was in near-perfect agreement with the measurements for the first three months.

The mean biases (relative biases) between the CR_h, CR_i, MC_h, and MC_i

method estimates of ablation rates and the observed ablation rates were 0.34 (39%), −0.03 (−4%), 0.16 (19%), and −0.10 (−11%) cm w.e. day^{-1}, respectively (Table 3.5). The mean biases were higher in the homogeneous methods (CR_h and MC_h) relative to those in the inhomogeneous methods (CR_i, MC_i) (Figs. 3.15 and 3.17). The CR_i method had the least, while the CR_h method was the most biased.

Figure 3.15 shows that ablation rates estimated using data where the thermistors were unevenly spaced through the debris layer were significantly less accurate than those made with data where $dz_1 = dz_2$. This was consistent with the result of synthetic experiment 3 (see Sec. 3.5.1), which showed that the accuracy of estimates of κ_{eff} decreased with increasingly uneven sensor spacing.

The uncertainties associated with ablation rates obtained by the glaciological method were 0.1–0.7 cm w.e. day^{-1} (Fig. 3.16) (Shah et al, 2019). By comparison, the uncertainties in estimated ablation rates that were made using the MC_i method ranged from 0.04 to 0.72 cm w.e. day^{-1} (Fig. 3.16). The uncertainties in the estimated ablation rates from the other three methods were comparable to that of the MC_i method, but, as discussed above, these methods were less accurate.

The above findings imply that vertical temperature profile measurements can be used to estimate sub-debris ablation (Fig. 3.15) and its sub-seasonal variability (e.g., Fig. 3.17) with accuracies comparable to that of the glaciological method in the thickly debris-covered parts of the glacier. The automated temperature sensors provide continuous data, which can be used to obtain the seasonal to sub-seasonal ablation rates with a fraction of physical labour that is required to obtain the same by the glaciological method. Therefore, this method may be particularly suitable for relatively inaccessible debris-covered HKKH glaciers, where in-situ ablation monitoring is sparse and is logistically challenging. The findings suggest that the assumption of a purely conductive, vertical heat transport within the debris layer provides a reasonably accurate description of the sub-debris heat fluxes over the debris-covered ablation zone. The departures from such an idealised model do not lead to errors in the sub-debris ablation estimates that are significant given

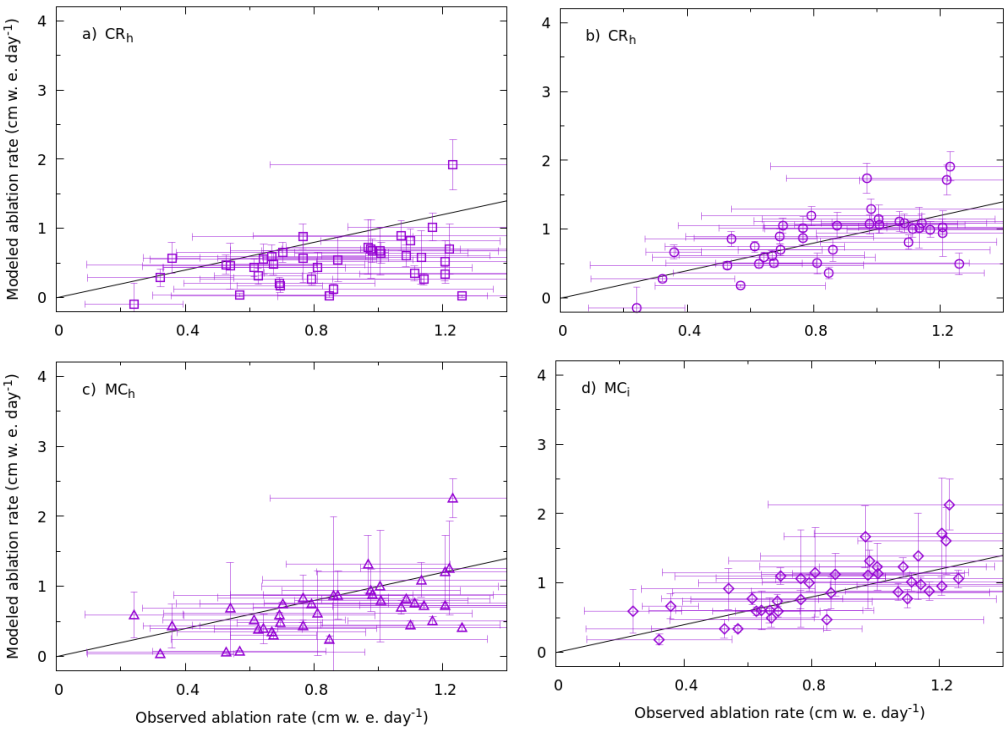

Figure 3.16: Comparison of ablation rate estimates from CR_h (a), CR_i (b), MC_h (c), MC_i (d) methods, and that obtained from the glaciological method using ablation stakes. Here we plotted only the selected records (see text for more details) with the corresponding estimated uncertainties. The solid gray line is a guide to the eye that denotes a perfect match.

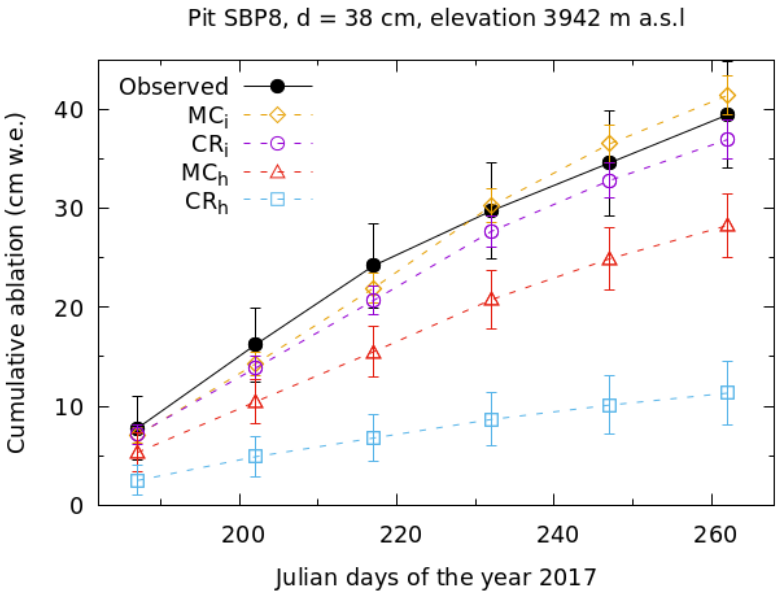

Figure 3.17: Observed and modelled ablation for pit SBP8 during the ablation season of 2017.

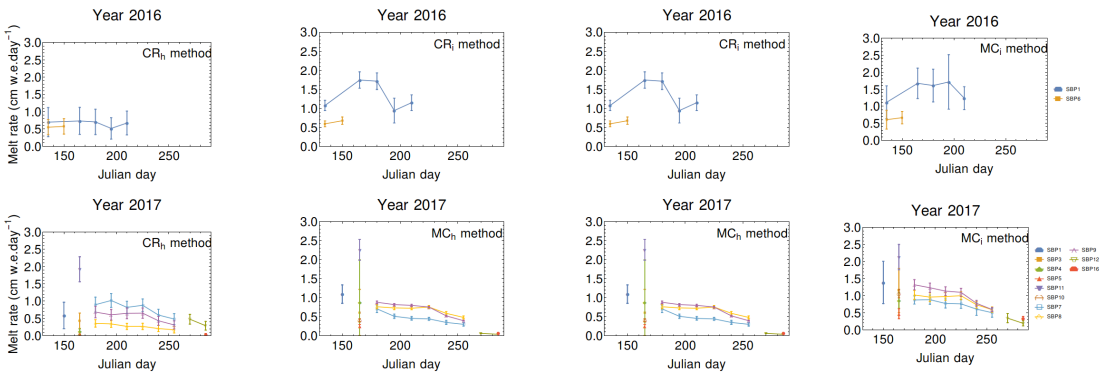

Figure 3.18: Seasonal ablation rates obtained from all four methods were plotted with the corresponding estimated uncertainty for ablation seasons 2016 and 2017. Different colors and symbols denoted different pits.

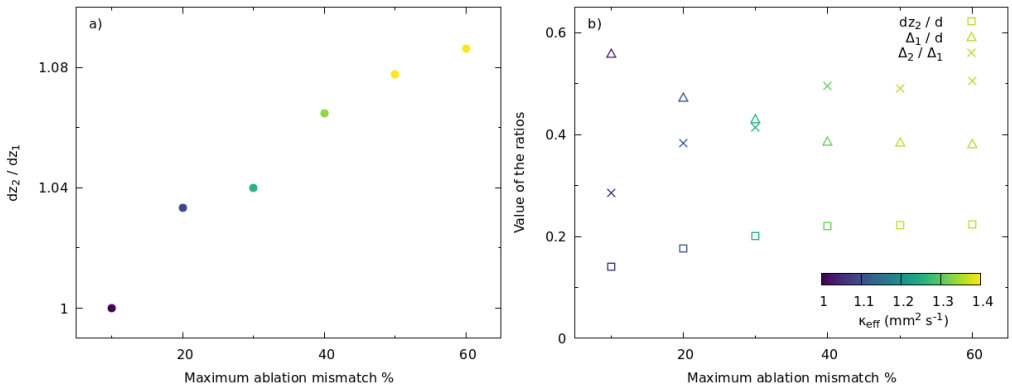

Figure 3.19: a) In the MC_i method, we plotted the maximum ablation mismatch percentages (Fig. 3.15d) and the corresponding mean dz_2/dz_1. b) The mean values of the ratios dz_2/d, Δ_1/d, and Δ_2/Δ_1 were plotted for different maximum ablation mismatch percentages (see Sec. 3.5.6 for more details). Each point was colored by the corresponding mean κ_{eff}.

the level of uncertainty typically present in the corresponding glaciological estimates.

Effect of the experimental set-up on the accuracy of sub-debris ablation estimation

Based on the above results, an irregular sensor spacing leads to biased estimates of thermal diffusivity as well as sub-debris ablation rates. In the idealised settings of synthetic experiment 3, we found 10% bias in dz_2/dz_1 leads to <5% biases in both κ_{eff} as well as κ_2 in the MC_i or CR_i methods (Fig. 3.7a). In reality, those biases could be different due to complexities arising from the inhomogeneities in the debris layer, debris thickness, the elevation of the pits, different surface temperatures, and so on. That is why we used a comparison of sub-debris ablation with the glaciological observations to check the effect of different parameters related to the experimental setup on the accuracy of sub-debris ablation estimation (Fig. 3.19).

We considered the set of temperature records where the MC_i method reproduced the observed glaciological ablation rates within a 20% error. The

corresponding RMSE between observed and inferred ablation rate was 0.12 cm w.e. day^{-1}. Denoting the separation between the debris surface to the top sensor and that between the bottom sensor to the ice surface by Δ_1 and Δ_2, respectively, the experimental set up for this set was characterised by, $dz_2/dz_1 = 1 \pm 0.03$, $0.14 < dz_2/d < 0.18$, $0.47 < \Delta_1/d < 0.56$, and $0.29 < \Delta_2/\Delta_1 < 0.39$. Beyond these ranges, both the effective thermal diffusivity and the ablation mismatch increased systematically (Fig. 3.19).

3.5.7 Recommendations for experimental design

Based on the above discussion, we recommend the following protocol for an accurate estimation of sub-debris ablation using vertical debris-temperature profiles.

- Place three temperature sensors within the debris layer.
- Maintain an equal spacing between the successive sensors with a tolerance of 3%.
- Set the sensor spacing to be $\sim \frac{1}{5}$-th of the debris thickness at the location.
- The top sensor is to be placed approximately at the middle of the debris layer.
- Discard the debris temperature data for the first three days after the installation to allow thermal transients to disappear.
- Analyse the debris temperature profiles using a finite-difference method that incorporates the vertical inhomogeneity of the debris layer, preferably the $\mathrm{MC_i}$ method introduced here.

3.6 Summary

We have presented an analysis of the accuracy of thermal diffusivity and sub-debris ablation estimates made using in-situ temperature measurements

within the supraglacial debris on Satopanth Glacier from 2016 to 2017 ablation seasons. We have compared four different methods of analysing the debris temperature profiles. The methods are based on one-dimensional heat conduction through a single-layered or a two-layered conductor. The accuracy of the methods was evaluated using idealised synthetic experiments and by direct comparison with the glaciological ablation observations at Satopanth Glacier. We assessed the effects of the vertical spacing of the temperature sensors within the debris layer and vertically inhomogeneous thermal properties. Our analysis suggests,

- Independent of the method used to analyse the vertical temperature profile, the most accurate thermal diffusivity and sub-debris ablation estimates are obtained from data collected at vertically equispaced temperature sensors. A non-uniform sensor spacing leads to systematic biases in the estimated thermal diffusivity and sub-debris ablation, which increases with the ratio of the sensor spacing.

- The methods of analysing thermal profile data that assume a two-layered conductor provide more accurate estimates of thermal diffusivity of the debris layer and that of sub-debris ablation.

- Temperature profiles measured with vertically equispaced sensors and analysed with a two-layered conductor model can obtain sub-debris ablation with an accuracy comparable to the glaciological method.

Chapter 4

Climate response of river runoff from high Himalayan catchments

4.1 Introduction

High Mountain Asia (HMA) is known as the 'water tower' for densely populated river basins like Indus, Ganges, and Brahmaputra (Immerzeel et al, 2020) due to a intense orthographic precipitation and a massive cryospheric reserve of fresh water (Xu et al, 2009). Snow and glacier fed Himalayn rivers are important in terms of industrial uses (Rasul, 2014), household water (Bandyopadhyay, 2013), seasonal agricultural water demand (Biemans et al, 2019), etc. They are also critical for socio-economic and geopolitical stability of the region (Simons et al, 2020). The presence of glaciers in a catchment significantly influences the seasonality, the variability, and the long-term changes of its runoff (Hock et al, 2005). Melt water from glaciers stabilises the river runoff from the HMA and it buffers against drought during the driest years to some extent (Pritchard, 2019). However, the dynamical snow and ice reserve makes the Himalayan rivers, some of the most vulnerable ones to climate change impact (Immerzeel et al, 2020). For example, possible conversion of summer snowfall into rain (Smith and Bookhagen, 2018),

coupled with a high sensitivity of glacier mass balance to snowfall change due to the albedo feedback (Kumar et al, 2019), may lead to a significant loss glacier cover by 2100, even for the more conservative warming scenarios (Kraaijenbrink et al, 2017).

Therefore, it is important to analyse the potential hydrological changes at regional to catchment scales. This problem has motivated several glacio-hydrological model studies of the Himalayan basins and catchments (see Azam et al (2021) for a review). A number of studies assessed the potential changes in the water cycle and the river runoff from HMA due to a changing climate from catchment scale to basin scale (Sorg et al, 2012; Li et a, 2016; Ragettli et al, 2016; Huss and Hock, 2018). All these studies point out to overall decline in the river runoff by 2100 due to decline in the ice-reserve and somewhat increasing water uptake. This 'peak water' is a typical characteristic of the long-term response glaciersied catchments to sustained warming (Hock et al, 2005). These models often differ from each other in the level of descriptions of glacial processes, e.g., no explicit treatment of the glaciers (Pokhrel et al, 2014), a static (Nepal, 2016) or dynamic (Kraaijenbrink et al, 2017) glacier cover, a simple temperature-index (Chandel and Ghosh, 2021) or detailed energy-balance based ice-melt model (Fujita and Sakai, 2014), and so on. Even a single model, when tuned with different available baseline climate data products, predicts a wide range of future hydrological changes (Koppes et al., 2015). In addition, the available future climate projections used to drive the glacio-hydrological models have a large spread (Sanjay et al, 2017). All of the above factors contribute to a wide range of predictions for the future changes in the runoff of Himalayan catchments (e.g. Nie et al, 2021).

Assessing climate sensitivity of the runoff of Himalayan catchments may prove useful in reconciling the range of predictions available in the literature. Climate sensitivity of runoff is defined as the change in runoff due to a unit perturbation in a forcing variable, e.g., precipitation or temperature (Zheng et al, 2009). The climate sensitivities estimated from different models, which are forced by different projected climate forcing, can therefore be compared (Vano and Lettenmaier, 2012). A climate sensitivity analysis may also reveal

key differences and similarities in the climate response of runoff generated from the different parts of a catchment that are dominated by either snow melt or glacier melt or rainfall (Fujita and Sakai, 2014). It may also bring out the similarities and the differences among catchments across the Himalayan arc with their distinct climate settings, and thus, provide a better handle on the runoff response in the ungauged catchments in this data-sparse region (Azam et al, 2021).

In the literature, climate-sensitivities have been used to estimate long-term runoff changes due to temperature and precipitation forcing in both glacierised (Chen and Ohmura, 1990) and non-glacierised catchments (Dooge et al, 1999; Zheng et al, 2009; Vano and Lettenmaier, 2012). In the Himalaya, climate sensitivity of glacier mass balance proved useful to explain the observed spatial pattern of glacier thinning (Sakai and Fujita, 2017; Kumar et al, 2019), or to identify an inherent bias in scaling-based glacier evolution models which are often used in glacio-hydrological studies (Banerjee et al, 2020). Despite its potential utility, detailed studies of the climate sensitivity of the runoff of Himalayan glacierised catchments are rare (Fujita and Sakai, 2014; Azam and Srivastava, 2020). Climate sensitivities of runoff can be obtained simply by regressing the observed variability of runoff to those of its meteorological drivers (e.g. Zheng et al, 2009). When observations are not available, model simulations can be used for the same (Vano and Lettenmaier, 2012).

This motivates the present study of climate sensitivities of runoff of two contrasting glacierised Himalayan catchments: winter-precipitation dominated Chandra (the western Himalaya), and summer-precipitation dominated upper Dudhkoshi (the eastern Himalaya). Here, we use the Variable Infiltration Capacity (VIC) model (Liang et al, 1996) augmented with a glacier-melt module, to simulate runoff over the period 1980–2018. The glaciers are assumed to be static during the simulation period. With the limited available field data of runoff, we calibrated a minimum number of model parameters to avoid overfitting issues. The inter-annual variability of the simulated summer runoff was used to compute the runoff sensitivity to annual precipitation and summer temperature. The simulated runoff is

used to estimate and validate the sensitivities of summer runoff to annual precipitation and summer temperature. The sensitivities of the runoff of the glacierised and non-glacierised parts of the catchments are also analysed. These sensitivities are then used to understand the multidecadal changes in the mean and the variability of summer runoff of the two catchments, as the glaciers shrink in a warming climate.

A general limitation of the linear sensitivity analaysis is that the mean background state of the catchment concerned is assumed to remain the same. With shrinking Himalayan glaciers, this may seem to limit the applicability of the linear response model to these catchments. However, It is expected that glacier loss may be much larger by 2050 or 2100 (Kraaijenbrink et al, 2017). To take care of the changing glaciers, we discuss an alternative method to compute future runoff changes by computing the respective sensitivities of runoff generated from the glacierised and nonglaciersied parts separately. The estimated sensitivities are used to compute the future runoff changes by 2050, and compared with the existing model studies. We also attempt to explain the glacier-compensation effect, and to estimate the timing and magnitude of 'peak water' using the climate-sensitivities.

4.2 Study area

We considered two catchments, Chandra from the western Himalaya and upper Dudhkoshi from the eastern Himalaya (Figs. 4.1a and 4.2a–b). These two catchments belong to two contrasting climatic regimes. The western Himalayan catchment is winter snow dominated, while the eastern Himalayan catchment is summer rain dominated. Other than that, the two catchments are similar in terms of the specific summer runoff, glacierised fraction, and recent glacier area and mass loss (Table 4.1).

4.2.1 Chandra catchment

The Chandra catchment is in Lahaul-Spiti district, Himachal Pradesh, India (Figs. 4.1a and 4.2a). The catchment covers an area of 2440 km^2 , of which

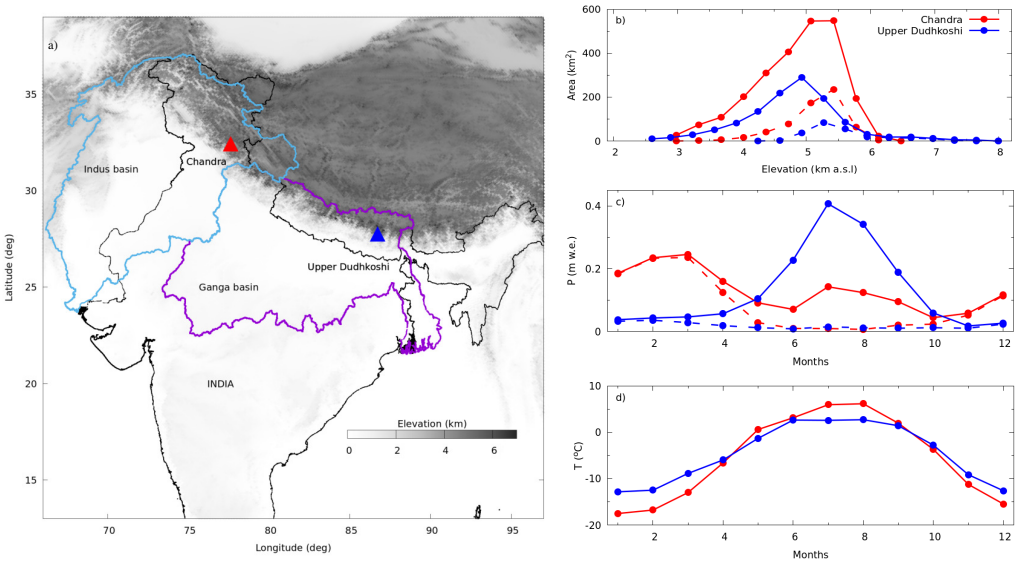

Figure 4.1: a) The location of Chandra (red solid triangle) and upper Dudhkoshi (blue solid triangle) catchments on a grey-scale elevation map (Amante et al, 2009). In the rest of the plots red (blue) colors refer to Chandra (upper Dudhkoshi) catchment. The solid magenta (sky-blue) polygon shows Ganga (Indus) basin. b) Area-elevation distribution of the catchments (solid lines + solid symbols), and that of the glacierised parts (dashed lines + solid symbols). c) Mean monthly precipitation (solid lines + solid symbols), along with the monthly snowfall (dashed lines + solid symbols). d) Mean monthly temperature profiles (solid lines + solid symbols).

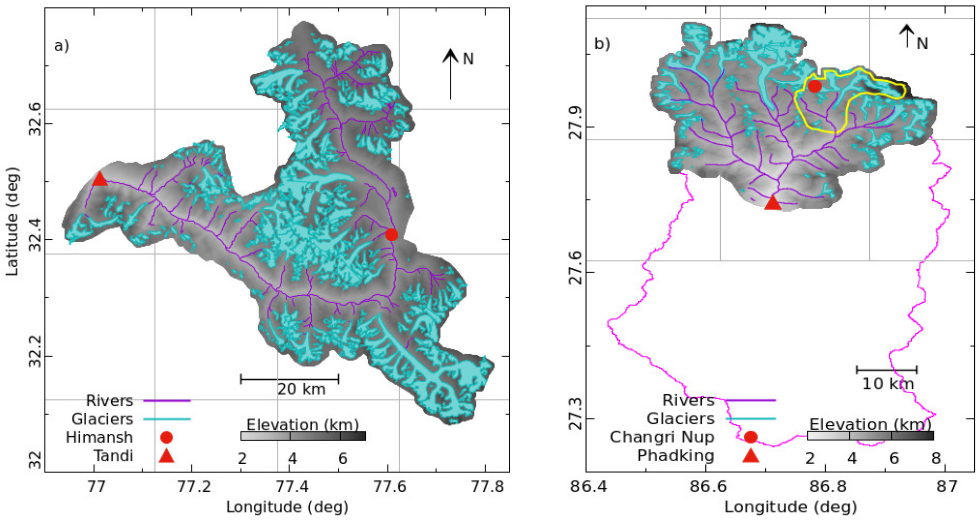

Figure 4.2: Maps of (a) Chandra and (b) upper Dudhkoshi catchments showing glaciers (Cyan polygons) and streams (purple lines). The red solid circles (triangles) are the meteorological (hydrological) stations. The ERA5 grid boxes are shown with solid gray lines in the background. Solid magenta and yellow polygons show Dudhkoshi and Periche catchments.

25% is glacierised. It spans an elevation range 2850–6500 m a.s.l with catchment outlet at Tandi (32.548°N, 76.975°E). Most of the precipitation here occurs during the winter months due to the western disturbances (Bookhagen and Burbank, 2010) and the influence of Indian summer monsoon is relatively weak (Fig. 4.1c). The mean annual precipitation and temperature in the catchment are 1.61 m yr^{-1} , and -5.5°C (from bias-corrected reanalysis data as described later).The ratio of summer to winter precipitation is 0.5, where summer refers to the high-discharge period of May to September (Azam et al, 2019). The same definition of summer is used in the rest of this paper. The ratio of solid to liquid precipitation is also 0.5. Over the last two decades, the reported rates of glaciers mass loss varies from -0.13±0.11 m w.e. yr^{-1} to -0.56±0.38 m w.e. yr^{-1}(Gardelle et al, 2012; Vincent et al, 2013a; Vijay and Braun, 2016; Brun et al, 2017; Maurer et al, 2019; Shean et al, 2020) and losing area at the rate of (0.11–0.55)% $decade^{-1}$ (Pandey et al, 2013; Mukherjee et al, 2018).

4.2.2 Upper Dudhkoshi catchment

The upper Dudhkoshi catchment considered here is in Solukhumbu district of Nepal (Figs. 4.1a and 4.2b). The catchment covers an area of 1190 km^2, and spans an elevation range 2600–7900 m a.s.l.. 20% of the catchment is glaciersied. The catchment outlet is at Phadking (27.745°N, 86.713°E). Due to a dominant influence of Indian summer monsoon, more than 80% of the precipitation in this catchment happens during the summer months (Fig. 4.1c). Accordingly, the ratio of solid to liquid precipitation is relatively low (~ 0.1). The mean annual precipitation is 1.53 m yr^{-1}, and mean annual temperature is -4.7°C (from bias corrected reanalysis data described later). The reported rates of glaciers mass loss over the last two decades varied from -0.26 ± 0.13 to -0.52 ± 0.22 m w.e. yr^{-1} (Bolch et al, 2011; Gardelle et al, 2012; Nuimura et al, 2012; Brun et al, 2017; King et al, 2017; Maurer et al, 2019), and the corresponding estimates of the rate of area loss lies in the range 0.12 to 0.42% $decade^{-1}$ (Bolch et al, 2011; Thakuri et al, 2014; King et al, 2017).

Table 4.1: A summary of the characteristics of Chandra and upper Dudhkoshi catchments. The meteorological variables are bias-corrected reanalysis data averaged over the catchments (Hersbach et al, 2020), the hydrological data are from model simulations (the present study). The glacier mass-balance and area-loss estimates are from the existing literature (Table 4.4).

Catchment	Chandra	Upper Dudhkoshi
Area (km^2)	2440	1190
Outlet	Tandi	Phadking
Elevation range (m a.s.l)	2850–6500	2600–7900
Glacierised fraction	0.25	0.20
Annual temperature (°C)	−5.5	−4.7
Annual precipitation (mm yr^{-1})	1610	1531
Summer precipitation / winter precipitation	0.5	6.8
Liquid precipitation/ solid precipitation	0.5	9.7
Glacier area loss (% $decade^{-1}$)	1.1–5.5 [a]	1.2–4.2 [b]
Glacier mass balance (m w.e. yr^{-1})	-0.13 ± 0.11 to -0.56 ± 0.38 [c]	-0.26 ± 0.13 to -0.52 ± 0.22 [d]
Annual runoff (m yr^{-1})	1.25	0.99
Summer runoff/annual runoff	0.86	0.81

[a] (Pandey et al, 2013; Mukherjee et al, 2018)

[b] (Bolch et al, 2011; Thakuri et al, 2014; King et al, 2017)

[c] (Gardelle et al, 2012; Vincent et al, 2013a; Vijay and Braun, 2016; Brun et al, 2017; Maurer et al, 2019; Shean et al, 2020)

[d] (Bolch et al, 2011; Gardelle et al, 2012; Nuimura et al, 2012; Brun et al, 2017; King et al, 2017; Maurer et al, 2019; Shean et al, 2020)

4.3 Data and methods

We simulated the runoff of the above two catchments over the period 1980–2018 using VIC model (Liang et al, 1996), augmented with a temperature-index based glacier-melt module (Hock, 2003) and forced with bias-corrected reanalysis data (Hersbach et al, 2020). The model was calibrated with the help of available summer runoff and geodetic glacier mass balance from both the catchments. The simulated runoff was utilised to obtain the sensitivities of summer runoff to summer temperature and annual precipitation changes. Note that throughout the paper, the annual quantities correspond to the hydrologic year from 1st October of a calendar year to 30th September of the next, and summer season refers to the period from 1st May to 30th September (e.g., Azam et al, 2019). This study focused on the climate sensitivities of summer runoff, which was $81-86\%$ of the annual runoff in these catchments (Table **??**). Also, during the summer season, Himalayan glaciers contribute significantly to the total catchment runoff (e.g., Azam et al, 2021). Below we first present our climate-sensitivity based theoretical approach, followed by methodological details related to the input data, the model, and the analyses performed.

4.3.1 Hydro-meteorological and glaciological data

Observations

Observed hourly runoff of Chandra river at Tandi (32.55°N, 76.97°E, 2850 m a.s.l.) from 26th June, 2016 to 30th Oct, 2018 was available for three summer seasons with some data gaps (Fig. 4.9b) (Singh et al (2020); Table 4.2). Hourly 2m air temperature, precipitation, and incoming shortwave radiation were measured at the Himansh station (32.409°N, 77.609°E, 4080 m a.s.l.) in the catchment between 18th October, 2015 to 5th October, 2018 with some data gaps (Singh et al (2020), Table 4.2).

Hourly runoff from upper Dudhkoshi catchment was observed at Phadking (27.74°N, 86.71°E, 2600 m a.s.l.) between 7th April, 2010 and 16th April, 2017 (Fig. 4.9a) (Chevallier et al, 2017). Available hourly air tempera-

Table 4.2: Details of the hydrometeorological observations used in this study. As no radiation data available from Phadking station in upper Dudhkoshi catchment, we used the incoming shortwave radiation data from near by Changri Nup station. All hydro-meteorological data of upper Dudhkoshi catchment are accessible from this link http://www.papredata.org/.

Parameters (station name)	Sensor	Accuracy (Range)	Data availability
Chandra catchment (Pratap et al, 2019; Singh et al, 2020)			
Runoff (Tandi)	YSI radar	± 2 mm	26Th June, 2016 to 30th Oct, 2018 (with gaps)
Precipitation (Himansh)	OTT Pluvio precipitation bucket	± 0.05 mm	18th Oct, 2015 to 5th Oct, 2018 (with gaps)
2m air temperature (Himansh)	Campbell HC2S3	±0.1°C (−50 to + 60 °C)	18th Oct, 2015 to 5th Oct, 2018 (with gaps)
Incoming shortwave radiation (Himansh)	Kipp and Zonen four component net radiometer	< 5%–day total (305–2800 nm, 0–2000 Wm^{-2})	18th Oct, 2015 to 5th Oct, 2018 (with gaps)
Upper Dudhkoshi catchment (Chevallier et al, 2017; Sherpa et al, 2017)			
Runoff (Phadking)	Campbell sensor (details not available)		7th April 2010 to 16th April 2017
Precipitation (Phadking)	Campbell sensor (details not available)		7th April 2010 to 23th April 2017 (with gaps)
2m air temperature (Phadking)	Campbell sensor (details not available)		7th April 2010 to 23th April 2017 (with gaps)
2m air temperature (Changri Nup)	Vaisala HMP45C	±0.2°C	1st Nov, 2010 to 30th Nov, 2014
Incoming shortwave radiation (Changri Nup)	Kipp and Zonen CNR4	±3%–day total (0.305–2.8 μm)	1st Nov, 2010 to 30th Nov, 2014

ture and precipitation data at Phadking from 7th April, 2010 to 23th April, 2017 (with some data gaps) (Chevallier et al, 2017) were used. The daily incoming shortwave radiation data for the period 1st November, 2010 to 30th November, 2014 at nearby Changri Nup station (27.983°N, 86.783°E, 5400 m a.s.l.) in the same catchment were used (Sherpa et al (2017); Table 4.2).

We considered 8 available geodetic mass-balance observations that spanned a decade or more, for each of the catchments (Table 4.4). Randolph Glacier Inventory (RGI 6.0) (Arendt et al, 2017) was used for the glacier boundaries that corresponded to the glacier extent in 2002.

4.3.2 Reanalysis data and bias correction

We used hourly 2-m air temperature, precipitation, and wind-speed from fifth-generation European Center for Medium-Range Weather Forecasts Atmospheric Reanalysis of the global climate (ERA5) from 1980 to 2018 (Hersbach et al, 2020) to force the VIC model at a spatial resolution of $0.25° \times 0.25°$. Following the existing hydrological studies of various high Himalayan catchments (Soncini et al, 2016; Azam and Srivastava, 2020), the temperature data were bias-corrected. The available observed air-temperature data at the Himansh station (Chandra catchment), and at Phadking (Dudhkoshi Catchment) were used to compute the mean monthly temperature biases (Fig. 4.4), assumed to be constant for the whole catchment and over the whole simulation period. Note that the observed air temperature at a given station is likely to be well correlated with that at other locations in the catchments. For example, the variability of 15-day mean temperature of the ERA5 grid box containing the outlets of upper Dudhkoshi and Chandra catchments, explained 85 and 79% of that of the corresponding grid boxes farthest from the outlets.

To compute temperature at any given elevation within a grid box, mean monthly lapse rates (Fig. 4.3) were used. In Chandra catchment, the lapse rates were computed at the grid box containing Himansh station using ERA5 temperature from the four near-neighbour grid boxes. The corresponding annual lapse rate of 4.7 ± 1.2 °C km^{-1} was consistent with previously observed

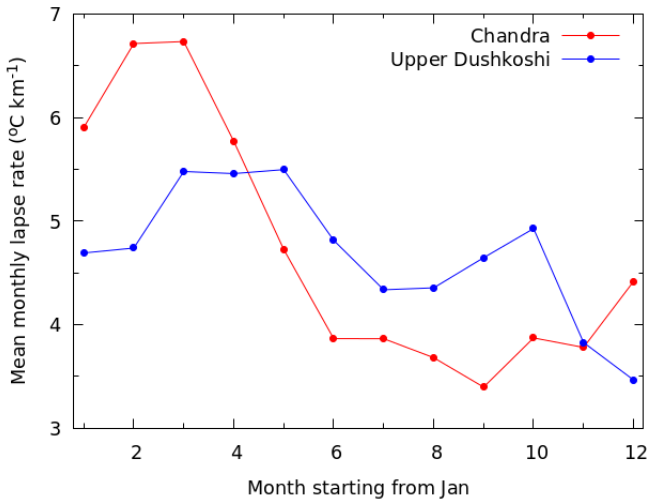

Figure 4.3: The mean monthly temperature lapse rates for Chandra (red symbols + line) and upper Dudhkoshi (blue symbols + line) catchments.

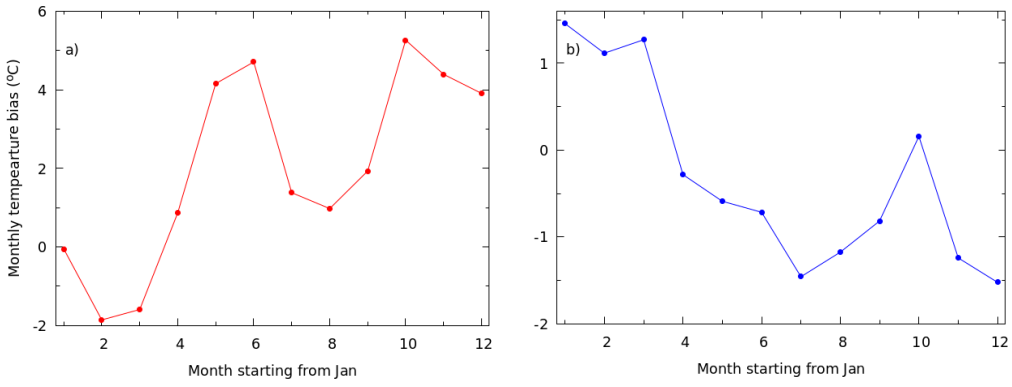

Figure 4.4: Mean monthly bias in ERA5 2m air temperature for (a) Chandra, and (b) upper Dudhkoshi catchments with respect to the corresponding stations (Himansh and Phadking, respectively).

values of 4.4–6.4 °C km^{-1} (Azam et al, 2019; Pratap et al, 2019). In upper Dudhkoshi catchment, the monthly lapse rates derived from ERA5 were significantly larger than those observed between Phadking and Changri Nup stations over the period 2013–2016, so we used the observed lapse rates. The corresponding mean annual lapse rate of 4.6±0.6 °C km^{-1} in this catchment was the same as that previously reported (Pokhrel et al, 2014).

ERA5 precipitation data was corrected by scaling with a catchment-specific constant α_P for each of the catchments following the existing studies from the region (Huss and Hock, 2015; Bhattacharya et al, 2019; Azam and Srivastava, 2020). The scale factor, which ensured water balance over the catchments, was calibrated using the observed runoff and glacier mass-balance employing a Bayesian procedure (described later in the text). In some of the existing studies in the region, an elevation-dependent precipitation scaling has also been employed (e.g., Azam et al, 2019). However, as an elevation-dependent correction may potentially introduce additional uncertainties (e.g., Johnson and Rupper, 2020), we preferred a constant α_p keeping the number of calibration parameters to a minimum. Note that the precipitation biases over the rugged Himalayan catchments (∼1000 km^2) cannot be corrected using data from a single station because of a high spatial variability and a small correlation length associated with precipitation (Singh and Kumar, 1997).

We scaled the incoming shortwave radiation obtained from VIC model by a catchment-specific constant to match the corresponding mean values observed at Himansh (Chandra catchment) and Changri Nup (upper Dudhkoshi catchment) stations (Fig. 4.6).

4.3.3 Model setup

We divided each studied catchment into two parts, the glacierised and non-glacierised ones. On the non-glacierised part, we ran another VIC model (Liang et al, 1996) to compute the surface runoff, baseflow, and evapotranspiration at hourly time steps (Fig. 4.5). On the glacierised part, a VIC model was used to get the snow melt and a temperature-index model (Hock,

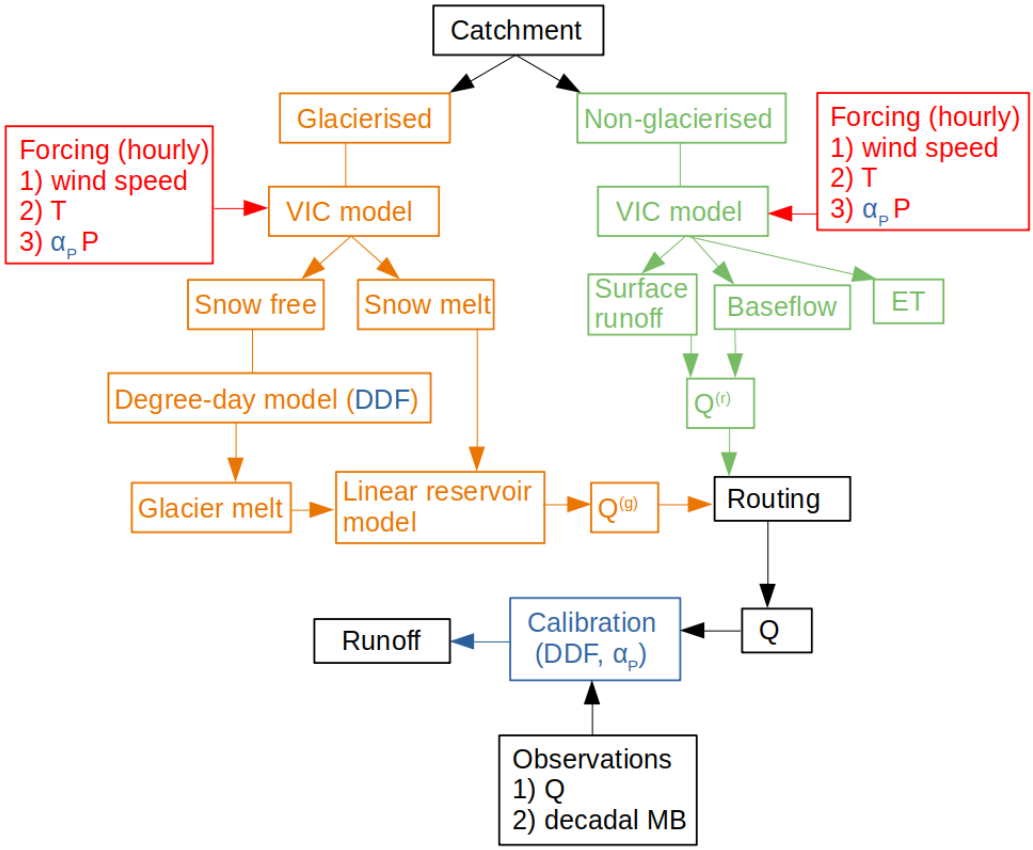

Figure 4.5: Flow chart of the model setup (see Sect. 4.3.3 for details).

2003) to obtain the glacier melt (Fig. 4.5). The additional glacier module was needed as VIC model does not have the capability to compute glacier melt (Liang et al, 1996). A similar approach to represent glacier melt was used in existing VIC model studies in the region (Zhang et al., 2013; Zhao et al, 2015; Chandel and Ghosh, 2021). Hourly hydrological fluxes of the non-glacierised and glacierised parts within each gridbox were combined and routed (Lohmann et al, 1998) to obtain the total runoff at the catchment outlet. Further details of the model implementations, calibration, parameter sensitivity, and uncertainty analysis are presented below.

Hydrological model

VIC (version 4.2.d, accessible from https://vic.readthedocs.io/en/master/; Liang et al (1996)) is a semi-distributed macro-scale hydrological model, which simulates the fluxes of water and energy for a grid-based representation of a catchment (Liang et al, 1996). The model uses physically-based parameterisation of different hydrological processes. In this model, water can enter a gridbox only from the atmosphere, and once water from each gridbox reaches the river channel, it can not flow back into the gridbox. The above assumptions allow each gridbox to be simulated independently, but limit the applicability of the model to a larger grid size (>>1 km). The VIC model considers sub-grid heterogeneity in surface topography, land-cover, and subsurface soil properties. Different vegetation classes are represented by tiles covering a fraction of the gridbox, and an area-weighted sum over the tiles obtains various hydrological fluxes for each gridbox. VIC model partitions the input precipitation at each gridbox into rain and snow based on a threshold temperature T_{th}. The VIC model uses a two-layered snowpack, computing all the associated energy fluxes to estimate the snow melt at a given elevation via an energy-balance approach. The surface-albedo parameterisation includes the effects of snowfall and aging of snow (Andreadis et al, 2009). Parameterisations of snow-sublimation and refreezing of meltwater within the snowpack are also included in the model (Andreadis et al, 2009). Evapotranspiration is computed by Penman-Monteith equation (Liang et al, 1996) as the sum of canopy evaporation, bare soil evaporation, and transpiration for each vegetation class. VIC allows multiple subsurface soil layers, and here we used three of them. The partitioning between surface runoff and infiltration into the top layer is done using a variable infiltration curve (Liang et al, 1996) controlled by the parameter b_{inf}. The infiltrated water goes to the middle layer, and subsequently to the bottom layer, driven by gravity. The bottom layer produces the baseflow based on its moisture content with a maximum allowed baseflow of Ds_{max}. At low soil moisture (below a fraction Ws of the maximum allowed soil moisture), the baseflow is linear in soil moisture. It remains so up to a fraction Ds of Ds_{max}. If soil moisture content, or equiv-

alently the baseflow, is above the respective thresholds (determined by Ws or Ds), a non-linear ARNO recession curve determines baseflow (Liang et al, 1996). The chosen values of the 5 VIC model parameters discussed above are given in Table 4.3.

We ran VIC model at a spatial resolution of 0.25° × 0.25° and time resolution of an hour. Chandra (upper Dudhkoshi) catchment covered parts of 11 (6) ERA5 grid boxes (Figs. 4.2a–4.2b), with fractional grid cover in the range 2.5–92% (2–68%). The model was set up using static input parameters like soil properties (Nachtergaele et al, 2010), land use (Friedl and Sulla, 2019), vegetation information (Rodell et al, 2004) and elevation distributions for each individual gridbox (obtained from 30 m resolution Shuttle Radar Topography Mission digital elevation model (Farr et al, 2007)). We used 10 elevation bands for each gridbox. Depending on the elevation range within a gridbox, the size of the bands varied in the range 100–300 m. A minimal set of meteorological forcing parameters, namely, bias-corrected air temperature, scaled precipitation, and wind speed obtained from ERA5 reanalysis data (Hersbach et al, 2020) were used to force the model. For model spin-up, we extended the meteorological input data back by repeating the data from 1980 to 1984. Subsequently, simulations were run over the period of 1980–2018. We scaled the incoming shortwave radiation obtained from VIC model to match the corresponding mean value observed at Himansh (Chandra) and Changri Nup (upper Dushkoshi) stations (Fig. 4.6).

Glacier model

On the glacierised part of each catchment, a separate VIC model simulation computed the snow melt and snow-covered fraction of each elevation band (Fig. 4.5). A temperature-index model (Hock, 2003) with catchment-specific degree-day factors (DDF), obtained the ice melt over the corresponding snow-free areas. The glacier melt module was forced with the bias-corrected ERA5 air temperature that were corrected further for the elevation of the band using the mean monthly lapse rates (Fig. 4.3). The DDF values for each of the catchments were calibrated against the observed glacier mass balance and

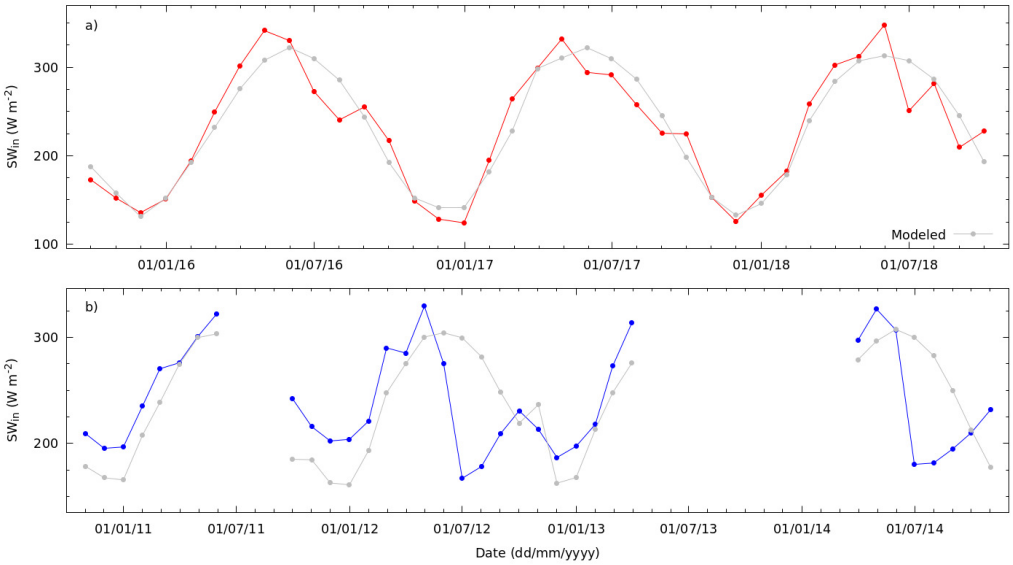

Figure 4.6: The incoming shortwave radiation (SW_{in}) estimated by VIC model was scaled so that it matched that observed at Himansh (Chandra catchment) and Changri Nup (upper Dudhkoshi catchment). In this plot, monthly modelled (gray lines and symbols) and observed (red lines and symbols for Chandra and blue lines ans symbols for upper Dudhkoshi catchments) are shown. In Chandra (upper Dudhkoshi) catchment the correction factor used was 2.1 (0.71). In upper Dudhkoshi catchment the modelled SW_{in} did not capture the observed drop in SW_{in} due to the presence of monsoon clouds, but overall the modelled and observed data matched well.

Table 4.3: Values of VIC model parameters, glacier runoff and routing model parameters used in the simulation are listed below.

Parameter	Range	Value used here
VIC model parameters (https://vic.readthedocs.io/en/master/)		
Ds	0.1–0.5	0.35
Ds_{max} (mm day^{-1})	10–20	15
Ws	0.4–1.0	0.7
b_{inf}	0.001–0.100	0.050
T_{th} (°C)	−1.0–1.0	0.0
Glacier runoff (Hannah and Gurnell, 2001)		
K_{fast} (hr)	1–24	12
K_{slow} (hr)	500–2000	1200
Routing model (Lohmann et al, 1998)		
UH^F_{max} (hr)	0.5–4.0	2
UH^F_{pow} (hr)	2–6	4
Bf (hr)	1000–3000	2000
Ks (hr)	100–1000	550

catchment runoff using a Bayesian method. The snow melt, ice melt, and rainfall on the glaciers were routed through two linear reservoirs (Hannah and Gurnell, 2001) with reservoir constants K_{fast} and K_{slow}, to obtain the glacier runoff (e.g., Radić and Hock, 2014). Glacier mass balance of the catchments were computed by subtracting the total ice and snow melt from the total snowfall over the glacierised parts. The present glacier module did not consider snow redistribution within or between the glacierised and the non-glacierised parts of the catchment via avalanching (Laha et al, 2017) or wind redistribution. The effect of supraglacial debris layer on melting was ignored (Kraaijenbrink et al, 2017) for the sake of simplicity. Also, we did not consider any baseflow contribution from the glacierised parts.

We assumed a static glacier cover here as the observed percentage loss of glacier area over the simulation period was small (1–5 % decade^{-1}) for both the catchments (Table 4.1). Biases due to such a static-glacier approximation were found to be small for another glacierised Himalayan catchment over the same period (Azam and Srivastava, 2020) justifying our approach. However, a dynamic description of glaciers within the glacio-hydrological model is essential for predicting the long-term changes in runoff due to potentially large changes in glacier extent over the coming decades (e.g., Kraaijenbrink et al, 2017).

Routing model

The surface runoff and baseflow from non-glacierised parts, and the glacier runoff for each grid boxes were routed (Lohmann et al, 1998) to get the total runoff at the catchment outlet. The flow from each gridbox was partitioned into the fast and slow components using hydrographs parameterised with Bf and Ks, UH^F_{max}, and UH^F_{pow} (Lohmann et al, 1998). The total hourly runoff produced from each grid box was routed downstream in the direction of steepest descent using a linearised Saint-Venant equation (Lohmann et al, 1998). The steps of the routing model are discussed below.

- The snowmelt fluxes of VIC model from the glacierised part of a grid was taken as an input of a 'slow' linear reservoir with time scale K_{slow}

(Hannah and Gurnell, 2001) (Table 4.3).

- The ice melt fluxes of the the temperature-index model along with the the rainfall from the glacierised part of a grid was taken as an input of a 'fast' linear reservoir with time scale K_{fast} (Table 4.3).

- The outputs of the slow and fast linear reservoirs are added in parallel and considered as the glacier runoff (Hannah and Gurnell, 2001).

- Total runoff from the non-glacierised part of a grid was determined by the unit hydrograph (UH) method followed by the algorithm of Lohmann et al. (1998).

- We assume the form of UH for 'fast' flow to be $t^{UH^F_{pow}} \exp(-\frac{t}{UH^F_{max}})$ (Table 4.3), where UH^F_{max} is the decay time-scale and UH^F_{pow} is an integer exponent. The UH for 'slow' flow was determined by another two time scale Bf and Ks (Table 4.3, (Lohmann et al, 1998)).

- Total runoff from non-glacierised part was convoluted by the corresponding UH.

- The runoff from glacierised and non-glacierised part of a grid were added to get the total runoff for river routing.

- Hourly river routing is done by the linearised Saint-Venant equation (Lohmann et al, 1998)).

- We used a conceptual river network for moving water from one grid to another.

- River routing module consists of two more parameters one is diffusivity another is advective velocity, which were taken to its standard values (Lohmann et al, 1998)).

Model calibration

With the limited set of observations available for the studied catchment, calibrating a large number of tunable parameters in the model may not necessar-

ily lead to a better representation of the relevant processes (Jost et al, 2012), and may encounter the issue of over-fitting. Moreover, it may also suffer from equifinality (Beven and Freer, 2001; Jost et al, 2012), where more than one parameter combinations reproduce the observed runoff. These issues are likely to compromise the ability of the calibrated model to capture the responses of the glacierised and the non-glacierised parts of the catchments. Therefore, here we calibrated only two model parameters: 1) precipitation scale factor α_P, and 2) DDF of ice. These two parameters are crucial for determining the catchment-wide water balance and the glacier mass balance. For the rest of the VIC model parameters, we used the central values of the recommended range (Table 4.3). Note that, these uncalibrated VIC model parameters values were similar to that of the corresponding calibrated values used in some of the studies from the region (e.g., Zhang et al., 2013; Zhao et al, 2015; Bhattacharya et al, 2019; Chandel and Ghosh, 2021). This suggested that the VIC model parameters used here to describe the two Himalayan catchments were representative ones. These model parameter values are listed in Table 4.3.

To calibrate for the parameters α_P and DDF, we used the following Bayesian method (e.g., Tarantola et al, 2005). For given a set of available observations d and a set of model parameters θ, the posterior probability of the model parameters given the observations was,

$$p(\theta|d) \propto p(d|\theta)p(\theta). \tag{4.1}$$

Here $p(\theta)$ was the prior distribution of the model parameters α_P and DDF. A uniform prior distribution over a range covering the corresponding values reported over the High Mountain Asia was assumed: 0.7–2.5 for α_P (Huss and Hock, 2015; Bhattacharya et al, 2019; Azam and Srivastava, 2020), and 2–16 mm $^{\circ}C^{-1}$ day^{-1} for DDF (Singh et al., 2000; Nepal, 2016; Azam et al, 2019). The conditional probability $p(d|\theta)$ of the observations d given the model parameter θ was assumed to be,

$$p(d|\theta) \sim e^{-\frac{\sum_i (Q_i^{mod} - Q_i^{obs})^2}{2\sigma_Q}} \times e^{-\frac{1}{2}\frac{\sum_j (b_j^{mod} - \mathrm{b}_j^{obs})^2}{2\sigma_b}}. \tag{4.2}$$

Here the superscript *obs* and *mod* denoted the observed and modelled values,

respectively. The total summer runoff for the i-th year was Q_i, and the summation was over all the years with observed runoff data. The uncertainty σ_Q in summer runoff was taken to be $\sim$10% of the mean summer runoff, which is conservative estimate given the existing estimates 5% reported for other Himalayan rivers (e.g., Singh et al., 2005). The j-th observed regional geodetic glacier mass balance for each catchment was denoted by b_j. This summation was over 8 such observations (Bolch et al, 2011; Gardelle et al, 2012; Nuimura et al, 2012; Vincent et al, 2013a; Vijay and Braun, 2016; Brun et al, 2017; King et al, 2017; Mukherjee et al, 2018; Maurer et al, 2019; Shean et al, 2020) for each of the catchment as listed in the supplementary Table 4.4. The corresponding median uncertainties was 0.13 m w.e yr^{-1} (Table 4.4). An empirical factor of $\frac{1}{2}$ in the exponent associated with the squared deviations of mass-balance in Eq. (4.2) ensured that the two exponential weights were of similar magnitude for the most-probable models. For each of the catchments, the two-dimensional parameter space was scanned with step sizes of 0.2 for α_P, and 0.5 mm °C^{-1} day^{-1} for DDF. This yielded an ensemble of $11 \times 29 = 319$ different model outputs for each of the catchments. For each of these models associated weight $p(\theta|d)$ was computed using Eq. (4.1).

Model validation, parameter sensitivity, and uncertainty

The results from the most-probable model, the one corresponding to the maximum $p(d|\theta)$ were used for estimating summer runoff and its components, and glacier mass balance. The weighted ensemble of all the 319 models was used to obtain the corresponding 2σ uncertainties.

To assess the model performance, the simulated mean summer runoff, decadal glacier mass balance, and glacier melt contribution were compared with the corresponding modelled and observed values previously reported in the region. As discussed before, the observed runoff was available for only 3 to 7 years and all of it was utilised for the above calibration. As an additional check, for upper Dudhkoshi catchment the calibration procedure was repeated using data from a set of four consecutive years, while the remaining three year's data were utilised for validation. This experiment was repeated

4 times, for different choices of the set of four consecutive years.

Following earlier studies (e.g., He et al, 2015), the parameter sensitivity of the results of the most-probable model was estimated with the help of additional 22 simulations where one of the 11 glacio-hydrological model parameters (Table 4.3) was perturbed by ±25% of the range of corresponding recommended values. The sensitivity of summer runoff to these 11 parameters were computed at the corresponding optimal values of DDF and α_P. Perturbing the parameters one by one in the 11-d parameter space is similar to computing the multidimensional gradient in this space to understand the model sensitivity. To confirm the results of the above parameter sensitivity analysis, additional 80 simulations were ran where a randomly chosen pair of parameters were simultaneously perturbed.

4.3.4 Climate sensitivity of runoff

The climate sensitivity of specific summer runoff Q (m yr^{-1}) is defined as the change in runoff due to a unit perturbation in a meteorological forcing parameter (e.g., Zheng et al, 2009). Here, we considered the sensitivity of Q due to changes in annual precipitation P (m yr^{-1}) and mean summer temperature T (°C). We did not consider the annual or winter temperature as it is the summer temperature that controls glacier melt (e.g., Pratap et al, 2019).

Climate sensitivities and summer runoff anomalies

The sensitivities of summer runoff relate (e.g., Zheng et al, 2009) the anomalies of summer runoff δQ (m yr^{-1}), annual precipitation δP (m), and summer air-temperature δT (°C) as follows.

$$\delta Q = s_P \delta P + s_T \delta T. \tag{4.3}$$

Here, precipitation sensitivity is denoted by $s_P \doteq \frac{\partial Q}{\partial P} = \frac{\partial \delta Q}{\partial P}$ (m yr^{-1} m^{-1}), and temperature sensitivity is denoted by $s_T \doteq \frac{\partial Q}{\partial T} = \frac{\partial \delta Q}{\partial T}$ (m yr^{-1} °C^{-1}). In Eq. (4.3), a possible bilinear interaction term proportional to $\delta T \delta P$ (Lang, 1986) was not considered. We confirmed this correction term, when included

in the regression for the catchment studied, was not significant ($p < 0.05$). The inherent assumption in Eq. (4.3) is that the runoff response is linear due to changes in annual precipitation and summer temperature. Therefore, even if δP and δT are correlated, then also we can write the Eq. (4.3). However, δP and δT are found mostly uncorrelated on the glaciers over the world (Banerjee, 2022).

We also considered the runoff from glacierised part of the catchments $Q^{(g)} \doteq Q_0^{(g)} + \delta Q^{(g)}$, and that from the non-glacierised part of the catchments $Q^{(r)} \doteq Q_0^{(r)} + \delta Q^{(r)}$. Here, the notations Q_0 and δQ denote the long-term mean and the anomaly for a given year, respectively. The corresponding sensitivities were defined in a similar way and led to the relations,

$$\delta Q^{(g)} = s_P^{(g)} \delta P + s_T^{(g)} \delta T, \tag{4.4}$$

$$\delta Q^{(r)} = s_P^{(r)} \delta P + s_T^{(r)} \delta T. \tag{4.5}$$

Given the instantaneous glacier fraction x, the quantities defined for the glacierised and non-glacierised part of the catchments are related to those defined for the whole catchment as,

$$\delta Q = x \delta Q^{(g)} + (1 - x) \delta Q^{(r)}, \tag{4.6}$$

$$s_T = x s_T^{(g)} + (1 - x) s_T^{(r)}, \tag{4.7}$$

$$s_P = x s_P^{(g)} + (1 - x) s_P^{(r)}. \tag{4.8}$$

We also considered the linear sensitivities for the monthly catchment runoff during the summer (May to September) as defined below.

$$\delta Q_m = s_{P_m} \delta P_m + s_{T_m} \delta T_m, \tag{4.9}$$

where δQ_m is the monthly runoff anomaly of the m-th month , δP_m is the cumulative precipitation anomaly up to month m starting from beginning of the hydrological year. δT_m is the air temperature anomaly for the month m. The monthly precipitation and temperature sensitivities are denoted by s_{P_m} and s_{T_m}, respectively. Note that while the temperature sensitivities of monthly runoff were defined with respect to the monthly mean temperature anomaly, for the corresponding sensitivity to monthly precipitation was defined using

the cumulative precipitation up to that month in a given hydrological year. This was done to accommodate the effects of the temporary storage of solid precipitation in the seasonal snow and glacial ice reservoirs.

Variability of summer runoff

The climate sensitivities defined above allow determination of the interannual variability of summer runoff given those of P and T,

$$\sigma_Q = \sqrt{s_T^2 \sigma_T^2 + s_P^2 \sigma_P^2}, \tag{4.10}$$

where σ_Q, σ_P, and σ_T are standard deviations of Q, P, and T, respectively. An implicit assumption here is that δP and δT are uncorrelated over the simulation period, which we verified to be true at $p < 0.05$ level for both the catchments.

Long-term changes in mean summer runoff

The climate sensitivities defined above can be used to predict the multi-decadal changes in summer runoff (ΔQ) for given changes in annual precipitation (ΔP) and mean summer temperature (ΔT). For a change in glacier fraction Δx from the initial value of x_0 (i.e., $x \doteq x_0 + \Delta x$), the following linear-response equation can be constructed ignoring the terms that were higher order in Δ.

$$\begin{aligned} \Delta Q &= x(s_P^{(g)} \Delta P + s_T^{(g)} \Delta T) + (1 - x)(s_P^{(r)} \Delta P + s_T^{(r)} \Delta T) \\ &\quad + \Delta x (Q_0^{(g)} - Q_0^{(r)}). \end{aligned} \tag{4.11}$$

A similar linear-response approach was used to analyse glacier-compensation effect (Chen and Ohmura, 1990) without explicitly referring to climate sensitivity. As ERA5 annual precipitation showed low/little spatial variability within the two catchments (Fig. 4.7), we ignored the spatial variation of the generated runoff within the off-glacier or glacierised areas in formulating Eq. (4.11). The implicit assumptions in the above formulation were: 1) the climate sensitivities of runoff from glacierised and non-glacierised parts do not change appreciably over a few decades, and 2) the contribution of the

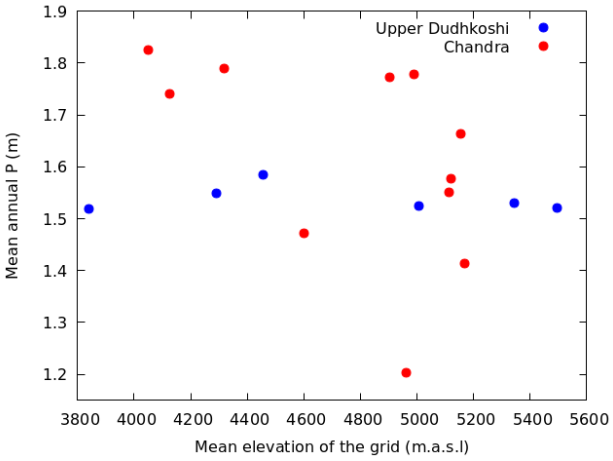

Figure 4.7: In Chandra and upper Dudhkoshi catchments, the mean annual precipitation of individual gridboxes are plotted against mean elevation of the corresponding gridbox.

deglacierised area to the changes in summer runoff is well represented by the difference between the mean runoff of the glacierised and non-glacierised parts. Note that climate-sensitivity based predictions for future changes in runoff are reliable as long as the predicted changes lie within the range of the recent interannual variability of P, T and Q. Beyond this range, uncontrolled extrapolation errors may creep in.

4.3.5 Estimation of climate sensitivities of summer runoff

In order to estimate the sensitivities s_T and s_P (Eq. (4.3)), we regressed simulated time series of δQ for the catchments during 1997–2018 with the corresponding time series of δT and δP. The standard error of the fits obtained the corresponding uncertainties. The sensitivities estimated from the simulated δQ time series over 1997–2018 were validated using that during 1980–1996 by computing the corresponding Nash-Sutcliffe efficiency (NSE) and root mean squared error (RMSE). The climate sensitivities of glacierised and non-glacierised parts (Eqs. (4.4) and (4.5)) and the corresponding uncertainties were estimated in the same way as above using the anomalies $\delta Q^{(g)}$

and $\delta Q^{(r)}$, along with δP and δT.

Apart from the sensitivities of summer runoff, we also computed the precipitation and temperature sensitivities of glacier mass balance using the corresponding simulated interannual variability over the period of 1980–2018. The precipitation sensitivity of glacier mass balance was defined to be the mass-balance change due to a 10% change in precipitation following the convention used in the literature (e.g., Wang et al, 2019).

The future changes in summer runoff and its variability

Equation (4.11) was applied over the part of the Chandra catchment that was glacierised at 2000 (such that $x_0 = 1$) to estimate the changes in summer runoff of glaciers by 2050 (Huss and Hock, 2018). The corresponding projected changes in T (Kraaijenbrink et al, 2017), x (Huss and Hock, 2018) in the Indus basin were used for this calculation (Fig. 4.20), and the results were compared with the existing basin-wide model estimates (Huss and Hock, 2018). The projected precipitation changes in this basin were not significant within the uncertainties (Kraaijenbrink et al, 2017), and were ignored here.

We computed σ_P and σ_T during 1980–1996 and 1997–2018 from the forcing data, and used Eq. (4.10) to predict the corresponding σ_Q. These predictions were validated using the corresponding σ_Q obtained directly from the simulated summer runoff time series. We used the same equation to understand the future changes in σ_Q in the studied catchments due to shrinking glaciers. We also analysed the variation of σ_Q for a set of hypothetical catchments with the same σ_P, σ_T, but having different x. Note that an empirical non-monotonic dependence of the coefficient of variation of runoff across catchments on the corresponding fractional glacier cover with a minimum at a moderate glacier cover is well known and has been termed as 'glacier-compensation effect' (Chen and Ohmura, 1990).

Long-term changes in summer runoff

Equation (4.11) was used to investigate the multi-decadal changes in the summer runoff, assuming glacier-loss scenarios in Chandra and upper Dudhkoshi

catchments to be the same as those projected for Indus and Ganga basin under RCP 2.6 climate scenario (Huss and Hock, 2018). The corresponding temperature projections were obtained from available estimates for the western and eastern Himalaya, respectively (Kraaijenbrink et al, 2017). The related precipitation changes, which were not significant within the uncertainties for both the regions (Kraaijenbrink et al, 2017), were ignored here. Consequently, the terms with ΔP in Eq. (4.11) did not contribute to the estimated changes.

Under a sustained warming, glacier runoff is expected to show a peak over a multidecadal scale due to the excess meltwater contribution from the shrinking glacier reserve, which is followed by a decline in the runoff as the ice reserve depletes (Huss and Hock, 2018). Following (Huss and Hock, 2018), we defined 'peak water' as the maximum change in runoff of the area that was glacierised at 2000 AD, and used Eq. (4.11) to predict the timing and the magnitude of the 'peak water' in the studied catchments. While the glacier boundaries (Arendt et al, 2017) belonged to 2002, the small changes in glacier area between 2000 and 2002 was ignored for this calculation due to an observed slow rate of glacier area change (Table 4.2). Our estimates of the magnitude and the timing of the peak water for these catchments were compared with the corresponding area-weighted estimates obtained from available $0.5° \times 0.5°$ gridded predictions (Huss and Hock, 2018).

4.4 Results and discussions

4.4.1 The calibrated models

The Bayesian calibration method fitted the observed glacier mass balance and the summer runoff data simultaneously, that yield unique best-fit models for both the catchments (Figs. 4.8a–4.8b). Thus, the present calibration strategy resolved the equifinality problem that is usually encountered while calibrating glacio-hydrological models using only discharge data (e.g., Azam and Srivastava, 2020). The most-probable DDF values were 5.0 and 7.5 mm day^{-1} $°\text{C}^{-1}$ for Chandra and upper Dudhkoshi catchments, respectively.

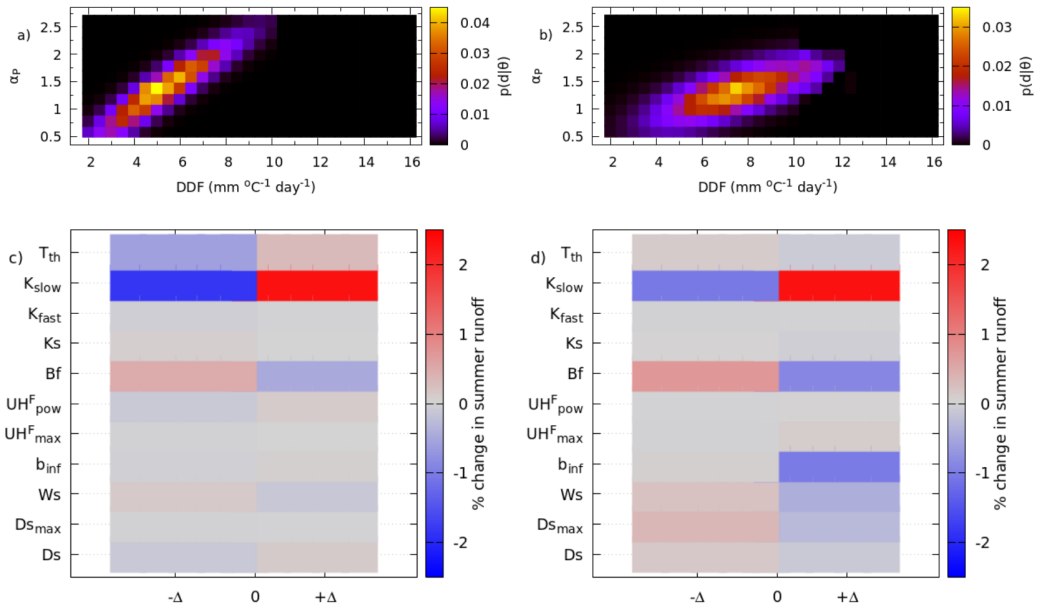

Figure 4.8: (a) and (b) shows the posterior probability distribution $p(d|\theta)$ of the model parameters (α_P, DDF) for Chandra and upper Dushkoshi catchment, respectively (see text for details). (c) and (d) shows the sensitivities of the simulated summer runoff to perturbations in 11 uncalibrated VIC the model parameters for Chandra and upper Dushkoshi catchment, respectively. Here, $\pm\Delta$ denotes the perturbation of parameters by $\pm 25\%$ of the corresponding prescribed range (see text for details and Table 4.3).

These DDF values were in the same ballpark range as previously used in studies in and around Chandra (Azam et al, 2019; Pratap et al, 2019) and Dudhkoshi catchments (Pokhrel et al, 2014; Khadka et al, 2014; Nepal, 2016). The best-fit α_P was 1.4 for both the catchments which was within the range of values 0.7–1.5 used in the existing studies in the Himalaya to correct various reanalysis products (Huss and Hock, 2015; Bhattacharya et al, 2019; Azam and Srivastava, 2020).

The calibrated models reproduced the observed summer runoff of the catchments reasonably well (Fig. 4.9) with RMSEs of 11 and 12% of the mean summer runoff, and NSEs of 0.88 and 0.80 for Chandra and upper Dudhkoshi catchments, respectively. These RMSE and NSE values were comparable to or smaller than those reported in the existing studies from the region (Nepal, 2016; Mimeau et al, 2018; Bhattacharya et al, 2019; Azam et al, 2019; Azam and Srivastava, 2020). Four additional calibration experiments for upper Dudhkoshi catchment, each one using a different set of 4 consecutive years of runoff data for calibration, obtained most-probable models with DDF (7.2±1.1 mm day^{-1} °C^{-1}), α_P (1.43 ± 0.03), NSEs (0.79–0.86), and RMSEs (10–14% of mean summer runoff) similar to those mentioned above.

4.4.2 Simulated runoff and its parameter sensitivity

The simulated mean summer runoff of Chandra and upper Dudhkoshi catchments over the period 1980–2018 were 1.08±0.03 and 0.81±0.02 m yr^{-1}, respectively (Fig. 4.10). The corresponding standard deviations were 0.14 and 0.10 m yr^{-1}. The mean summer runoff of the glacierised and the non-glacierised parts of Chandra catchment were 1.54 and 0.92 m yr^{-1}, respectively. The corresponding values for upper Dudhkoshi catchment were 1.59 and 0.61 m yr^{-1}. In these two catchments, more than 81% of the simulated annual runoff were during the summer season. In comparison, seven years of observation from upper Dudhkoshi catchment (Chevallier et al, 2017) showed a mean specific summer runoff of 0.86±0.05 m yr^{-1}, which was 83% of the mean annual runoff. Our simulations indicated that glacier runoff contributed 39±9% and 36±11% of the total summer runoff in upper Dudhkoshi

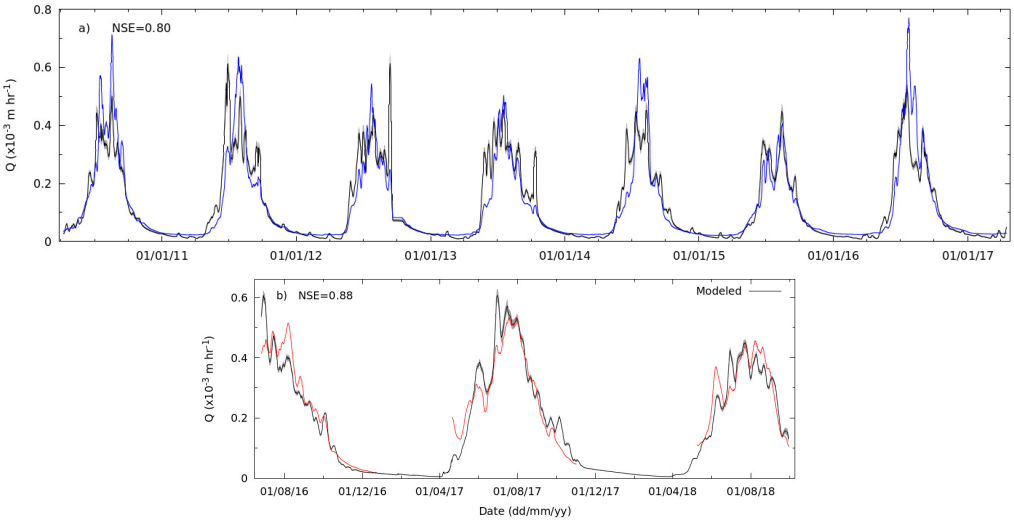

Figure 4.9: Modelled weekly runoff (black lines, with grey bands denoting 2-σ uncertainty) compared with the corresponding observations for (a) upper Dudhkoshi and (b) Chandra catchments (blue and red solid line, respectively).

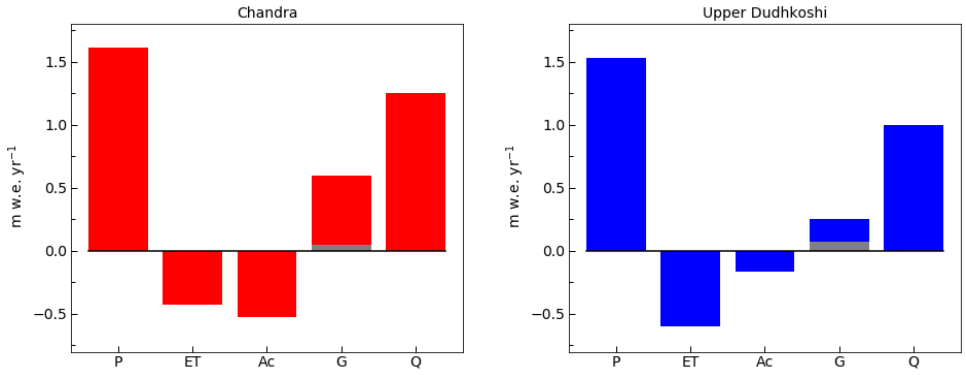

Figure 4.10: The components of annual hydrological balance equation $P - ET - Ac + Q^{(g)} = Q$ are shown for the two catchments. All the components are normalised by the total catchment area. P, ET, Ac, $Q^{(g)}$, and Q are the annual precipitation, evapotranspiration, glacier accumulation, the runoff from glacerised area, specific runoff from whole catchments, respectively. The imbalance contributions of the glaciers are also shown with grey bars.

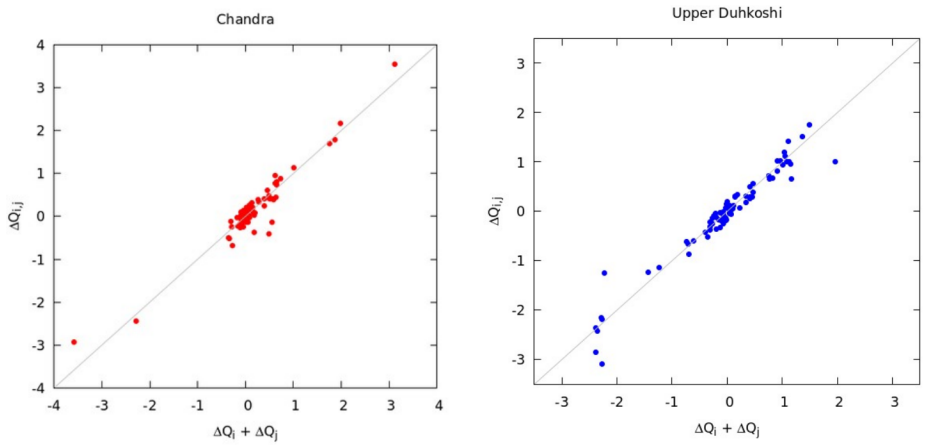

Figure 4.11: Percentage changes in runoff ($\Delta Q_{i,j}$) in 80 model runs, where two randomly chosen parameters out of the 11 VIC model parameters were perturbed simultaneously, are plotted against the sum of the runoff changes ($\Delta Q_i + \Delta Q_j$) from two corresponding experiments where only one of the two parameters were perturbed.

and Chandra catchments, with the glacier ice loss amounting to 9% and 4% of the respective total summer runoff (Fig. 4.10).

Existing model studies reported annual runoff of 1.6 m yr^{-1} during 2000–2010 (Nepal, 2016) and 0.96 m yr^{-1} during 1981–2015 (Chandel and Ghosh, 2021) for the whole Dudhkoshi catchment (Fig. 4.2b), and 0.95 m yr^{-1} during 2013–2015 (Mimeau et al, 2018) for Periche sub-catchment (Fig. 4.2b). The last two estimates compared well to those presented above. Existing estimates (Chandel and Ghosh, 2021) of summer runoff (0.87 m yr^{-1}) and glacier runoff (0.76 m yr^{-1}) of Dudhkoshi catchment were also consistent with our results. No such previous runoff estimates were available for Chandra catchment. The estimated glacier contributions to runoff obtained here were largely consistent with the existing model studies from the region (Nepal, 2016; Engelhardt et al, 2017; Mimeau et al, 2018; Azam et al, 2019; Chandel and Ghosh, 2021) when the differences in fractional glacier cover were taken into account (Table 4.5).

The parameter-sensitivity analysis revealed that the absolute changes in summer runoff were less than $\sim 1.5\%$ for all the parameters, except Bf and

K_{slow} (Figs. 4.8b–4.8d). Slightly higher summer-runoff sensitivities (1.8–2.5 %) for the two longer time scales Bf and K_{slow} became less than 1%, when the annual runoff was considered. The additional 80 simulations where two parameters were perturbed simultaneously, obtained runoff changes almost equal to the sum of those obtained in the corresponding pair of simulations with a single perturbed parameter (Fig. 4.11). A generally low parameter sensitivity of the summer runoff implied that the present summer runoff estimates were relatively robust to the uncertainties in these 11 glacio-hydrological model parameters (Table 4.3).

4.4.3 Simulated glacier mass balance and its climate sensitivity

The simulated glacier mass balance for Chandra and upper Dudhkoshi catchments over 1980–2018 were -0.18 ± 0.10 and -0.37 ± 0.04 m w.e. yr^{-1}. These estimates were comparable to the existing geodetic observations within the uncertainties (Fig. 4.12c; Table 4.4). The RMSE between modelled and observed mass balance of Chandra and upper Dudhkoshi catchments were 0.10 and 0.11 m w.e. yr^{-1}, respectively.

The sensitivity of the modelled glacier mass balance to temperature was -0.47 ± 0.09 and -0.27 ± 0.05 m yr^{-1} °C^{-1} for Chandra and upper Dudhkoshi catchments, respectively. The corresponding precipitation sensitivities for these catchments were 0.2 ± 0.04 and 0.05 ± 0.02 m yr^{-1} for a 10% change in precipitation. These sensitivities were significant at $p < 0.01$ level. The previously reported mass-balance sensitivities at a regional scale (Shea and Immerzeel, 2016; Sakai and Fujita, 2017; Tawde et al., 2017; Wang et al, 2019) and for individual glaciers from the western and central Himalaya (Azam et al, 2014; Wang et al, 2019; Sunako et al., 2019; Azam and Srivastava, 2020) spanned a wide range (Table 4.6). This possibly reflected the corresponding differences of the climate setting, geometry, and topography of the glaciers studied, along with underlying model assumptions, model calibration, input data sets, and so on. The mass-balance sensitivities obtained in the present study were well within the above range. A relatively higher summer tem-

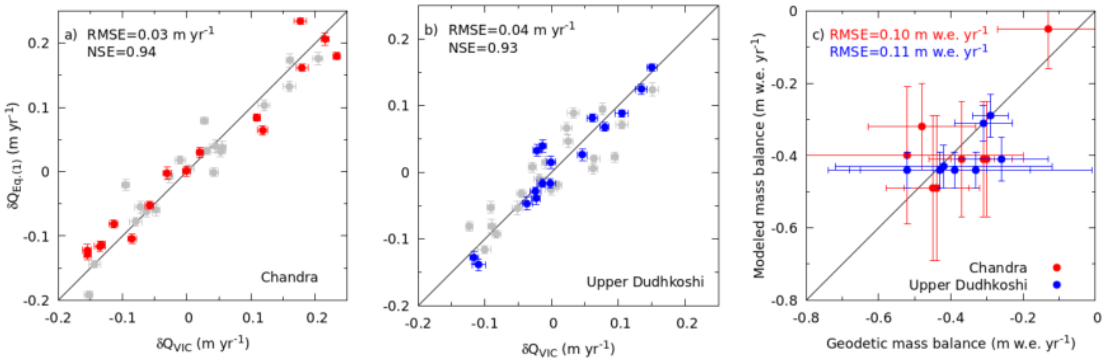

Figure 4.12: The summer runoff anomalies $\delta Q_{\text{Eq.(1)}}$ as computed using the Eq. (4.3) are compared with those from the VIC model simulations δQ_{VIC}, for (a) Chandra, and (b) upper Dudhkoshi catchments. The red (blue) solid circles are for Chandra (upper Dudhkoshi) catchment during the validation period 1980–1996. The gray solid circles denote data from the calibration period 1997–2018. (c) A comparison of the modelled glacier mass balance with the available regional-scale geodetic mass balance for Chandra (solid red circles) and upper Dudhkoshi (solid blue circles) catchments. The modeled values are over to the same period as that of the corresponding observed geodetic mass balance (Table 4.4). The solid gray line in each plot shows the 1:1 reference line.

perature sensitivity of the glaciers Chandra catchment compared to those of upper-Dudhkoshi was in apparent contradiction with an expected stronger influence of temperature forcing on summer-accumulation type glaciers due to a conversion between snow and rain (Fujita, 2008; Kumar et al, 2019). However, apart from the precipitation seasonality, mass-balance sensitivity also depends on factors like glacier hypsometry such that a relatively weaker temperature-sensitivity of glaciers in summer-monsoon fed Dudhkoshi compared to that in winter-snow fed Chandra cannot be ruled out. In fact, a similar trend of mass-balance sensitivities over these two regions were also found in a regional-scale energy-balance model study (Sakai and Fujita, 2017).

4.4.4 Climate sensitivities of catchment runoff

A linear fit of the summer runoff anomalies to those of summer temperature and annual precipitation (Eq. (4.3)) during 1997–2018 worked well for both Chandra (R^2=0.92) and upper Dudhkoshi (R^2=0.93) catchments. These fits obtained respective temperature sensitivities of summer runoff s_T of 0.12±0.01 and 0.12±0.03 m yr^{-1} °C^{-1} for Chandra and upper Dudhkoshi catchments, respectively. The corresponding best-fit s_P were 0.39±0.03 and 0.47±0.06 m yr^{-1} m^{-1}. These sensitivities were all significant at $p < 0.01$ level. The estimated sensitivities for the two catchments were the same within the limits of uncertainty, and the corresponding percentage changes in runoff were also similar (Table 4.7). This may be a surprising feature given the contrasting precipitation regimes of the catchments. This issue is discussed later in the text.

The sensitivities computed over the calibration period (1997–2018) reproduced the variability of summer runoff over the validation period (1980–1996) reasonably well (Figs. 4.12a–4.12b) with RMSE $<$ 0.04 m yr^{-1} and NSE $>$ 0.93. This also validated the use of Eq. (4.3) to predict the interannual variability of summer runoff in these two catchments. The sensitivities reported here were also in line with the previous estimates from the region (Fujita and Sakai, 2014; Pokhrel et al, 2014; Azam and Srivastava, 2020) or elsewhere (Engelhardt et al, 2015; He, 2021) (Table 4.8).

Table 4.4: A comparison of modelled glacier mass balance with the available regional geodetic mass balance for both the catchments. For the modelled mass balance values marked with *, the modelled mean were computed starting from the year 1980.

Period	Mean modelled mass balance (m w.e yr^{-1})	Observed geodetic mass balance (reference) (m w.e yr^{-1})
Chandra catchment		
1980–2018	−0.18±0.10	
1980–1992	0.29±0.18	
1993–2018	−0.42±0.14	
1975–2000	−0.05±0.11*	−0.13±0.14 (Maurer et al, 2019)
2001–2016	−0.32±0.12	−0.48±0.15 (Maurer et al, 2019)
2000–2012	−0.40±0.19	−0.52±0.32 (Vijay and Braun, 2016)
2000–2015	−0.41±0.16	−0.30±0.10 (Mukherjee et al, 2018)
2000–2016	−0.41±0.16	−0.37±0.09 (Brun et al, 2017)
		−0.31±0.08 (Shean et al, 2020)
1999–2011	−0.49±0.20	−0.45±0.13 (Gardelle et al, 2012)
		−0.44±0.09 (Vincent et al, 2013a)
Upper Dudhkoshi catchment		
1980–2018	−0.37±0.04	
1980–1992	−0.19±0.07	
1993–2018	−0.46±0.05	
1975–2000	−0.29±0.06*	−0.29±0.05 (Maurer et al, 2019)
1970–2007	−0.31±0.05*	−0.31±0.08 (Bolch et al, 2011)
2001–2016	−0.44±0.05	−0.39±0.06 (Maurer et al, 2019)
2000–2016	−0.44±0.05	−0.33±0.32 (Brun et al, 2017)
		−0.52±0.22 (King et al, 2017)
		−0.43± 0.25 (Shean et al, 2020)
1999–2011	−0.41±0.06	−0.26±0.13 (Gardelle et al, 2012)
1992–2008	−0.43±0.06	−0.42±0.30 (Nuimura et al, 2012)

Table 4.5: A comparison between the estimated glacier ice melt contribution to annual runoff from this study and that of from the available literature.

Study area	Glacerised fraction	Reference	% of glacier ice melt contribution to annual runoff
Chandra catchment	0.25	This study	31 ± 11
Chhota Shigri glacier	0.50	Azam et al. (2019)	18 ± 3
		Engelhardt et al. (2017)	33 ± 4
Upper Dudhkoshi catchment	0.20	This study	32 ± 9
Dudhkoshi catchment	0.13	Nepal (2016)	5
		Chandel and Ghosh (2021)	8
Periche catchment	0.43	Mimeau et al. (2018)	45

During 1980–2018, the simulated summer runoff in Chandra and upper Dudhkoshi catchments varied in the range 0.86–1.33 and 0.55–0.98 m yr^{-1}, respectively. The respective ranges of summer temperature were 2.0–5.3 and 1.2–2.3°C, and those of annual precipitation were 1.05–2.10 and 1.17–1.92 m yr^{-1}. As discussed before, the sensitivities estimated above are applicable within the above range of precipitation and temperature forcing. Note that in both the catchments, s_P was significantly smaller than 1 m yr^{-1} m^{-1}. This indicated an interannual change of the storage in the glaciers, and a change in evapotranspiration from the off-glacier area in response to the precipitation forcing.

Similarly, Eq. (4.9) described the monthly runoff variability reasonably well. The corresponding best-fit models obtained RMSE ranging between 0.01–0.02 m yr^{-1} and NSE in the range of 0.66–0.91 (Fig. 4.13) over the validation period. Only exception was that for Dudhkoshi catchment in the months of August (RMSE 0.04 m yr^{-1}, and NSE 0.26) and September (RMSE 0.02 m yr^{-1}, and NSE 0.31), where the fits were not good.

Table 4.6: A comparison of glacier mass balance sensitivities to temperature and precipitation from this study with those available in the literature.

Catchment	References	Glacier mass balance sensitivity to	
		Temperature (m yr^{-1} $°C^{-1}$)	Precipitation (m yr^{-1}, relative to 10% change in precipitation)
Regional values			
Chandra	This study	-0.47±0.09	0.2±0.04
Chandra	Tawde et al. (2017)	-0.16	0.09
4 western Himalayan glaciers	Wang et al. (2019)	-0.24 to -0.83	0.06 to 0.09
Indus basin	Shea and Immerzeel (2016)	-0.31 to -0.79	
Upper Dudhkoshi	This study	-0.27±0.05	0.05±0.02
Dudhkoshi	Sakai and Fujita (2017)	-0.17 to -0.36	
5 Eastern/central Himalayan glaciers	Wang et al. (2019)	-0.56 to -1.00	0.05 to 0.08
Ganga basin	Shea and Immerzeel (2016)	-0.29 to -0.76	
Western Himalayan glaciers			
Chhota Shigri glacier	Azam et al. (2014)	-0.52	0.16
Shaune Garang, Gor-Garang, Gara, Siachen	Wang et al. (2019)	-0.83, -0.71, -0.71, -0.24	0.06, 0.06, 0.06, 0.09
Central/eastern Himalayan glaciers			
AX010, Changmekhampu, Yala, Tipra	Wang et al. (2019)	-1.00, -0.66, -0.58, -0.56	0.08, 0.06, 0.05, 0.07
Trambau	Sunako et al. (2019)	-0.90	0.18
Dokriani	Azam and Srivastava (2020)	-1.11	0.24

The monthly temperature sensitivity s_{T_m} (Eq. (4.9)) varied between 11.5±1.7 to 33.9±2.8 $\times 10^{-3}$ m $^{\circ}C^{-1}$ yr^{-1} for Chandra, and 14.5±2.7 to 32.6±7.7 $\times 10^{-3}$ m $^{\circ}C^{-1}$ yr^{-1} for upper Dudhkoshi (see Table 4.9 for more details). In both the catchments, the maximum S_{T_m} was found in the month of June, consistent with a strong contribution to runoff from melting winter snow. In upper Dudhkoshi catchment, the monthly temperature sensitivities were not statistically significant for the month July to September (Table 4.9) the maximum monthly temperature sensitivities was found in the month of August, suggesting a more or less exclusive control of monsoon precipitation over runoff during these months.

The fitted monthly precipitation sensitivity s_{P_m} (Eq. (4.9)) varied between 0.02±0.00 to 0.15±0.03 m yr^{-1} m^{-1} for Chandra catchment, and 0.09±0.02 to 0.15±0.06 m yr^{-1} m^{-1} for upper Dudhkoshi catchment (Table 4.9). A relatively higher (lower) s_{P_m} during the summer months in upper Dudhkoshi (Chandra) was likely related to a dominant contribution of summer rain (meltwater) to the runoff in this catchment as discussed above. In both the catchments, the best-fit s_{P_m} was the lowest for the snowmelt-dominated month of May. The precipitation sensitivity of monthly discharge was the maximum during the months of June and July in Chandra. The seasonal snow in this catchment melted mostly during these two months (Fig. 4.14), leading to high monthly runoff variability depending on the sign and magnitude of the deviation of winter snowfall from its climatological mean. In contrast, in upper Dudhkoshi catchment, the contribution of summer rainfall to the runoff was dominant, the monthly runoff during June to August was more sensitive to precipitation anomalies (Table 4.9).

4.4.5 Response to a recent step change in climate

An analysis of the ERA5 data revealed a statistically significant (at $p < 0.01$ level) step-change in annual precipitation and summer temperature at 1992 in both Chandra and upper Dushkoshi catchments (Fig. 4.15a,b). The corresponding changes in mean annual precipitation in Chandra and upper Dudhkoshi catchments were 0.12 ± 0.07 and 0.09 ± 0.06 m yr^{-1}, respectively.

Table 4.7: Percentage sensitivity values for both the studied catchments are given below.

Sensitivity parameter	Chandra catchment	Upper dushkoshi catchment
Catchment summer runoff sensitivities		
s_T (% of Q change per °C warming)	11±1	14±4
s_P (% of Q change due to 10% change in P)	6±1	9±1
Glacier and off-glacier summer runoff sensitivities		
$s_T^{(g)}$ (% of Q change per °C warming)	37±2	58±7
$s_T^{(r)}$ (% of Q change per °C warming)	2±1	3±5
$s_P^{(g)}$ (% of Q change due to 10% change in P)	-2±1	0±0
$s_P^{(r)}$ (% of Q change due to 10% change in P)	9±1	9±1

Table 4.8: Comparison of our estimates of catchment runoff sensitivities with that of reported in the Himalaya and elsewhere.

Catchment name	s_T (% of Q change per °C warming)	s_P (% of Q change due to 10% change in P)	Reference
Engabreen	24	2	Engelhardt et al. (2015)
Ålfotbreen	17	6	Engelhardt et al. (2015)
Nigardsbreen	21	4	Engelhardt et al. (2015)
Storbreen	19	3.3	Engelhardt et al. (2015)
Ala-Archa	9	7	He (2021)
Dokriani	20	16	Azam and Srivastava (2020)
Dudhkoshi	5	10	Pokhrel et al. (2014)
Trambau	27	-0.6	Fujita and Sakai (2014)
Chandra	11±1	6±1	This study
Upper Dudhkoshi	14±4	9±1	This study

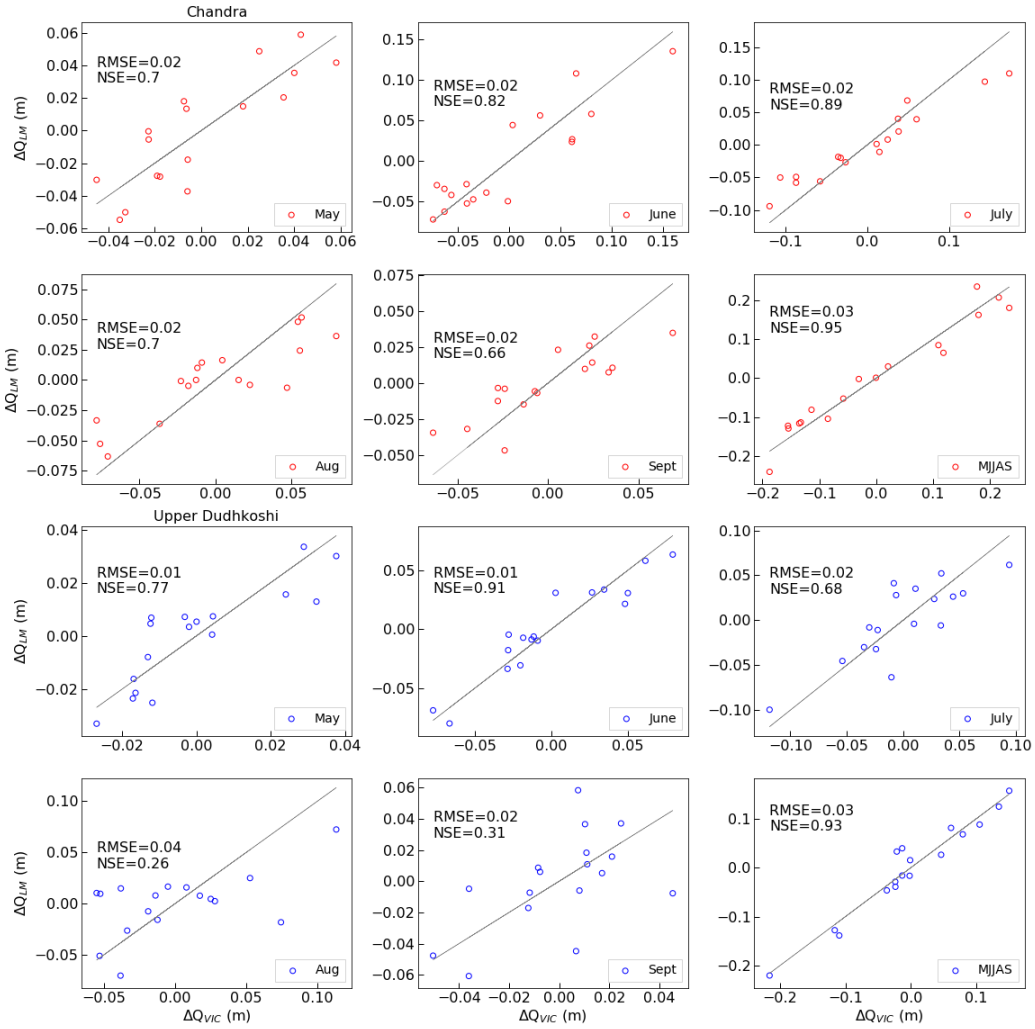

Figure 4.13: The performance of the linear sensitivity models, that were calibrated over 1997–2018, for individual summer months and full summer (May–September) for both Chandra (red open circles) and upper Dudhkoshi (blue open circles) catchments are validated over the period of 1980–1996. ΔQ_{LM} was the runoff anomaly computed from the linear model (Eq. (4.9)) and ΔQ_{VIC} was runoff anomaly computed from VIC model. The solid gray line is a guide to the eye denoting a perfect match.

Table 4.9: The precipitation and temperature sensitivities of monthly runoff (s_{T_m} and s_{P_m}) for both the catchments are tabulated. The sensitivity values marked with * are not significant at $p < 0.01$ level. See main text for the definitions of the sensitivity coefficients (Eq. (4.9)).

	s_{T_m} ($\times 10^{-3}$ m yr^{-1} °C^{-1})	s_{P_m} (m yr^{-1} m^{-1})
Chandra catchment		
May	26.0±3.0	0.01±0.02*
June	33.9±2.8	0.14±0.02
July	27.7±3.2	0.15±0.03
Aug	18.2±5.2	0.07±0.01
Sept	11.5±1.7	0.02±0.00
Upper Dudhkoshi catchment		
May	14.5±2.7	0.02±0.04*
June	32.6±7.7	0.10±0.05
July	20.7±22.3*	0.15±0.06
Aug	38.3±39.7*	0.11±0.05
Sept	10.2±10.9*	0.09±0.02

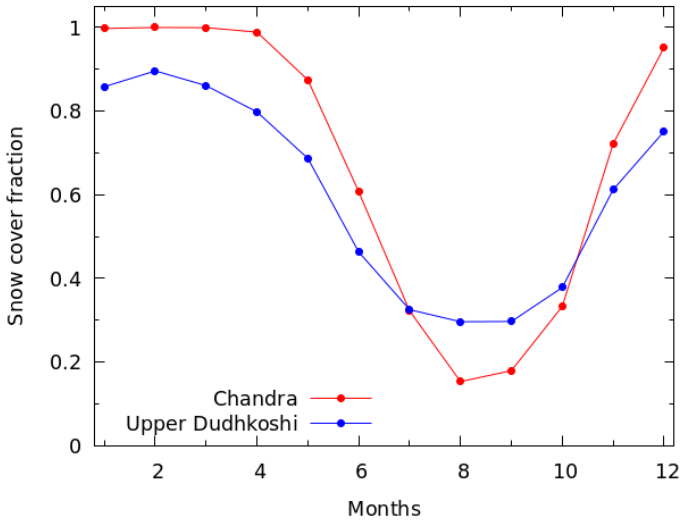

Figure 4.14: Mean monthly modeled snow-cover fraction of the both catchments Chandra (red color) and upper Dudhkoshi (blue color) are shown.

The respective changes in mean summer temperature were 0.84±0.32 °C and 0.51±0.11 °C (Table 4.10).

The above step-change in climate led to a corresponding significant response in the glacier mass balance (Fig. 4.15c) with increases in the mean mass loss by 0.71±0.23 and 0.27±0.10 m w.e. yr^{-1} in Chandra and upper Dudhkoshi catchments, respectively. These changes are in line with a recently reported step change in glacier mass balance across the Himalaya before and after 2000 (Maurer et al, 2019) (Table 4.4). However, our results indicated that the step change took place in 1992. A reconstruction of the mass balance of Chhota Shigri glacier from Chandra catchment (Azam et al, 2014), also showed an increase in the rate of glacier mass loss by 0.10±0.18 m w.e. yr^{-1} after 1992 (though it was not statistically significant). Overall, these results confirmed that the glacier module used here did a reasonable job of simulating the response of glacier mass balance to climate forcing.

According to VIC model results, the summer runoff increased in Chandra and upper Dudhkoshi catchments by 0.03±0.04 and 0.10±0.04 m yr^{-1} , respectively (Table 4.10), in response to the above step-change in climate after

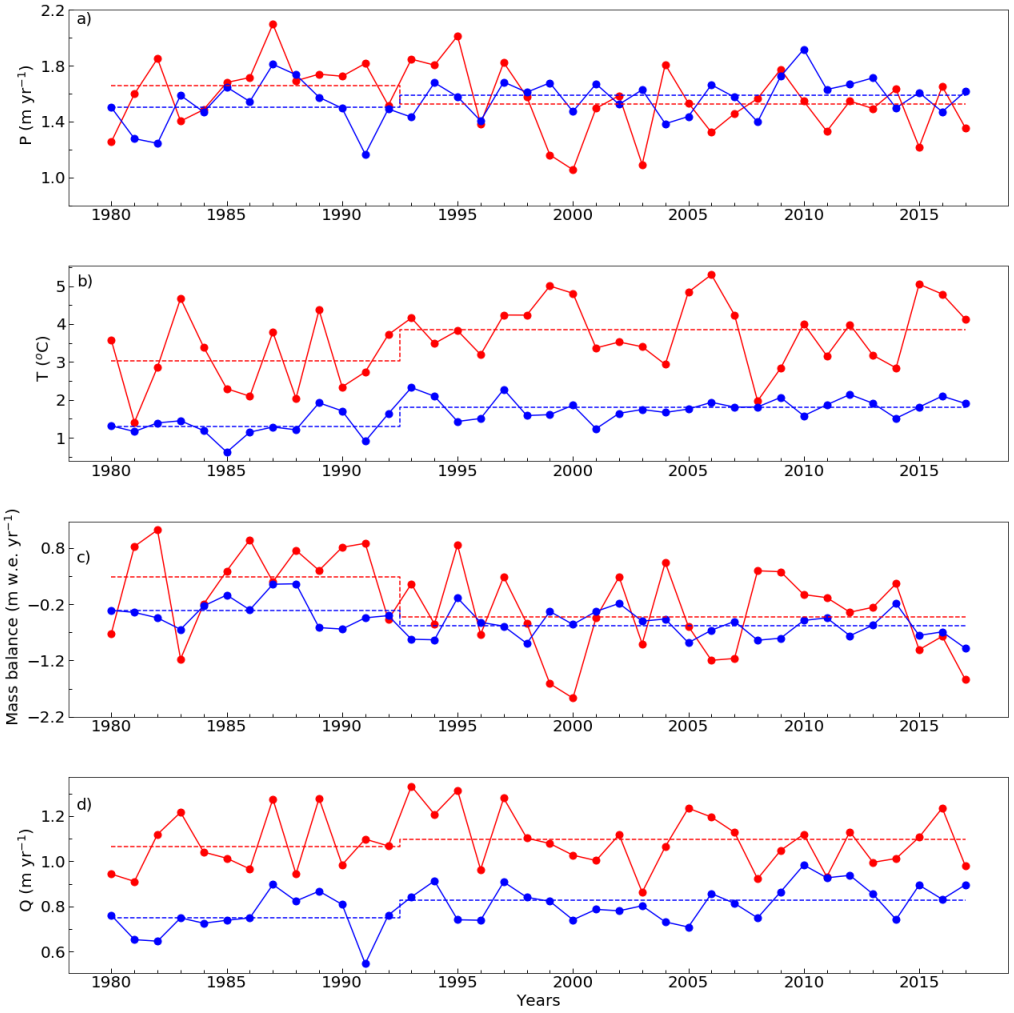

Figure 4.15: The time series of a) annual precipitation, b) mean summer temperature, c) annual glacier mass balance and d) total summer runoff plotted for Chandra catchment (red solid symbol and line) and Dudhkoshi catchment (blue solid symbol and line). The corresponding dotted lines show the mean values before and after 1992 (see text for further discussions).

Table 4.10: The magnitude of the step changes in annual precipitation (P), summer temperature (T_s) and the summer runoff (Q) for both catchments before and after 1992 are listed below.

	1980–1992			1993–2018		
	P (m yr^{-1})	T_s (°C)	Q (m yr^{-1})	P (m yr^{-1})	T_s (°C)	Q (m yr^{-1})
Chandra	1.46±0.18	3.02±0.94	0.97±0.11	1.34±0.21	3.86±0.82	1.00±0.11
Upper Dudhkoshi	1.69±0.20	1.30±0.33	0.92±0.12	1.78±0.09	1.81±0.26	1.02±0.09

1992. The predictions for the same response obtained using the best-fit linear form (Fig. 4.16) were 0.05±0.01 and 0.12±0.03 m yr^{-1} for these two catchments, respectively. This consistency between the linear model predictions and the corresponding VIC model results was a piece of evidence in favor of the reliability of the linear sensitivity model in computing the response of summer runoff to climate forcing.

4.4.6 Climate sensitivities of glacier runoff

The estimated temperature sensitivities of glacier runoff $s_T^{(g)}$ were 0.41±0.02 and 0.47±0.06 m yr^{-1} °C^{-1} for Chandra and upper Dudhkoshi catchments, respectively (significant at $p < 0.01$ level). The corresponding precipitation sensitivities $s_P^{(g)}$ were −0.12±0.08 and 0.00±0.02 m yr^{-1} m^{-1} (not significant at $p < 0.05$ level). A compilation of glacier runoff sensitivities (Table 4.11) indicated that the sensitivities reported by here were largely in line with those reported previously in the Himalaya (Fujita and Sakai, 2014; Chandel and Ghosh, 2021) and elsewhere (Anderson and Anderson, 2010; Soruco et al., 2015; Pramanik et al., 2018). Again, both the catchments had similar absolute values of $s_P^{(g)}$ and $s_T^{(g)}$ within the corresponding uncertainties. The corresponding percentage sensitivity values were rather similar, except a somewhat higher percentage change in glacier runoff due to unit temperature change in upper Dudhkoshi catchment (Table 4.7).

Interestingly, summer runoff of both winter-accumulation type glaciers in Chandra catchment and summer-accumulation type glaciers in upper Dudhkoshi

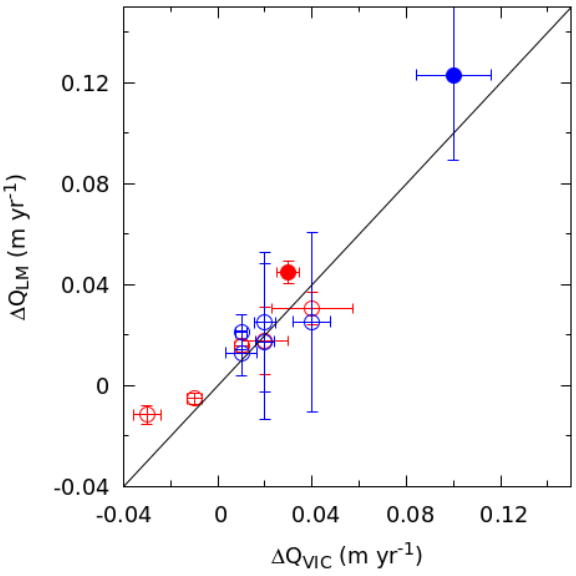

Figure 4.16: The response of of summer runoff to the step change in climate as computed using VIC model (ΔQ_{VIC}) and using linear sensitivity coefficients (ΔQ_{LM}) are compared. The solid circles denote the changes in total summer runoff and open circles denote changes in monthly summer runoff. Red (blue) symbols are denote data from Chandra (upper Dudhkoshi) catchment. The diagonal solid line denote a perfect match between the two models.

Table 4.11: Comparison of our estimates of climate sensitivity of glacier runoff with that of reported in the Himalaya and elsewhere.

Catchment name	$s_T^{(g)}$ (% of Q change per °C warming)	$s_P^{(g)}$ (% of Q change due to 10% change in P)	Reference
Midtre Lovenbreen	55	1	Pramanik et al. (2018)
Kongsvegen	71	3	Pramanik et al. (2018)
Kronebreen-Holtedahlfonna	55	4	Pramanik et al. (2018)
Brewster glacier	60	4	Anderson et al. (2010)
La Paz, Bolivia		6	Soruco et al. (2015)
Trambau	53	-7	Fujita and Sakai (2014)
Chandra	37 ± 2	-2 ± 1	This study
Upper Dudhkoshi	58 ± 7	0 ± 0	This study

catchment was approximately independent of the corresponding precipitation variability. This similarity between the two catchments with contrasting climate regimes led to the question whether glacier runoff is precipitation-insensitive in general. In a separate study by one of the present authors demonstrated that the above property is generally true, irrespective of the climate setting of the glacier or the values DDF parameters that describe the glacier (Banerjee, 2022).

In both the studied catchments, a positive precipitation anomaly did not translate into a higher summer runoff of the glaciers (Fig. 4.17). With increasing precipitation, the rainfall on glacier did not change, and snowmelt showed a very weak (Chandra) to no (upper Dudhkoshi) increase (Fig. 4.17). This implied that a higher precipitation contributed mostly to a positive storage change (snow accumulation) on the glaciers. In addition, a higher snowcover and/or an association between higher-than-normal precipitation and lower mean temperature (not statistically significant) caused a decline in glacier melt, and amplified the changes in glacier storage change (Fig. 4.17). These effects combined to yield a nearly precipitation-insensitive glacier runoff in both the catchments. In contrast, a higher glacier melt with increasing mean summer temperature caused a relatively high temperature sensitivity of $Q^{(g)}$ in both the catchments (Fig. 4.17). Here, the glaciers effectively acted as infinite reservoirs over an annual scale so that the meltwater volume was limited only by the available energy. A higher temperature implied a higher available energy, and thus a higher meltwater flux from the glaciers. These arguments were consistent with a high correlation ($r > 0.9, p < 0.05$) between the summer temperature and summer runoff of the glacierised parts for both the catchments (Fig. 4.17).

The negligible $s_P^{(g)}$ discussed above implied a stabilisation of the total runoff of the glacierised catchments against precipitation variability, as the runoff contribution from the glacierised fraction x was essentially independent of precipitation (Eq. 4.8). The magnitude of the precipitation sensitivity of catchment runoff s_P is thus expected to decrease with the glacier fraction x. This stabilising effect is consistent with a reported buffering of catchment runoff by glaciers during the extreme drought years across High Mountain

Asia (Pritchard, 2019).

4.4.7 Climate sensitivity of runoff of the non-glacierised parts

In the non-glacierised parts of Chandra and upper Dudhkoshi catchments, $s_T^{(r)}$ of 0.02±0.01 and 0.03±0.04 m yr^{-1} °C^{-1} and $s_P^{(r)}$ of 0.56±0.04 and 0.59±0.07 m yr^{-1} m^{-1} were obtained, respectively. These sensitivities were all significant at $p < 0.01$ level. Again, both the catchments had similar absolute values of $s_P^{(r)}$ and $s_T^{(r)}$ within the corresponding uncertainties, and the corresponding percentage sensitivity values were similar (Table 4.7).

Compared to the sensitivities of glacier runoff, the climate sensitivities of the runoff from the non-glacierised parts showed an exactly opposite trend. The summer runoff of the off-glacier areas were relatively insensitive to temperature anomalies, but sensitive to precipitation anomalies (Fig. 4.18). Because of the presence of seasonal snow cover over the non-glacierised parts, a temperature dependence of the summer runoff may be expected. However, the total amount of snowmelt during the summer was limited by the supply of seasonal snow, and not by the available energy. This led to a weak response of the total summer runoff from the non-glacierised parts to temperature forcing. This argument was supported by the fact that the summer runoff from the non-glacierised parts were uncorrelated with summer temperature and strongly correlated with summer precipitation ($r > 0.9, p < 0.05$). Our results suggest that the precipitation changes in these two catchments caused comparable changes in surface runoff, groundwater/baseflow, and evapotranspiration (Fig. 4.18). Consequently, about ∼2/3rd of the precipitation anomaly translated to that of the total runoff. Interestingly, evapotranspiration anomalies in the glacier-free parts of Chandra (upper Dudhkoshi) were controlled by the summer temperature (precipitation) (Fig. 4.18). This suggested a water-limited condition in the summer monsoon-fed upper Dudhkoshi catchment, and an energy-limited condition in the winter snow-fed Chandra catchment.

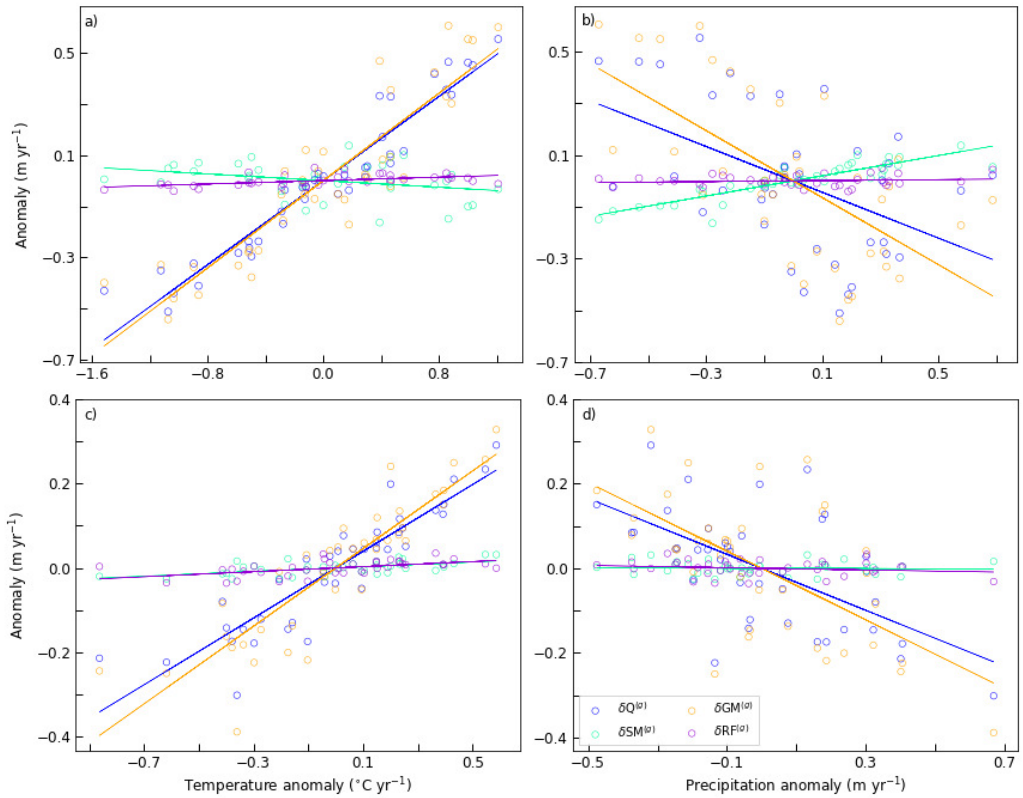

Figure 4.17: The anomalies of glacier runoff $\delta Q^{(g)}$, and its components, namely, snowmelt $\delta SM^{(g)}$, glacier ice melt $\delta GM^{(g)}$, and rainfall $\delta RF^{(g)}$ for the glacierised parts of the catchments are plotted as a unction of the corresponding temperature and precipitation anomalies: (a, b) for Chandra catchment, and (c, d) for upper Dudhkoshi catchment. The corresponding best-fit straight lines are also shown.

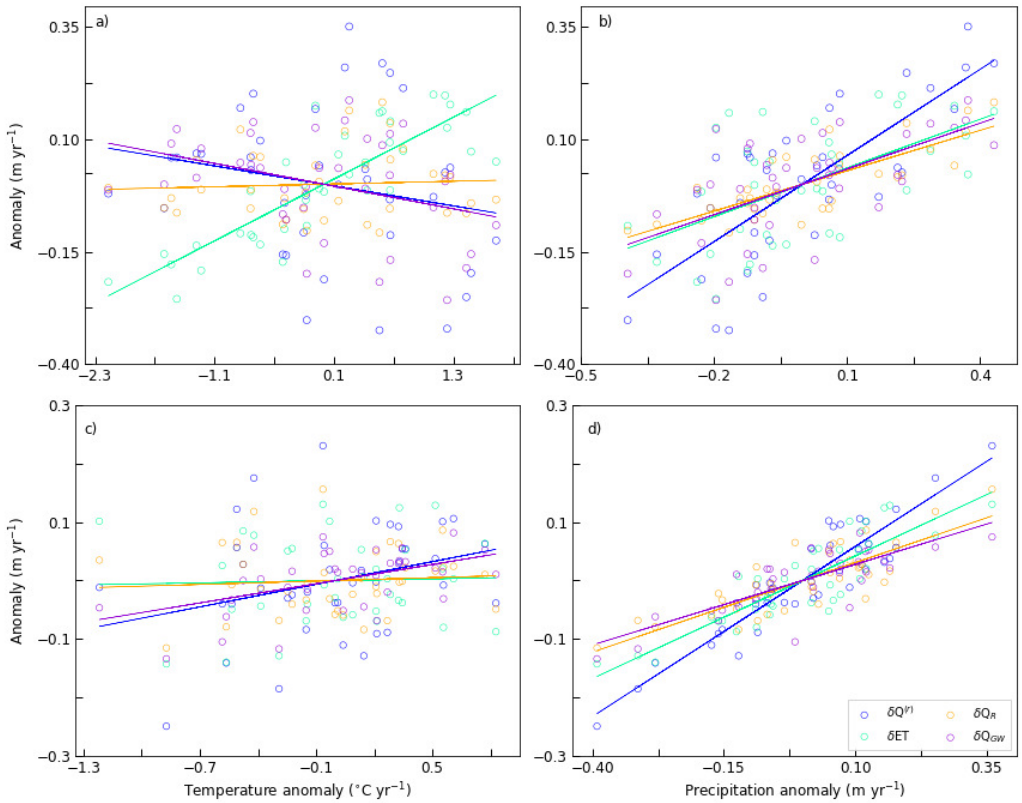

Figure 4.18: The anomalies of glacier off-runoff ($\delta Q^{(r)}$), and its components, surface runoff (δQ_R) and groundwater/baseflow (δQ_{GW}) are plotted here. The corresponding evapotranspiration (δET) anomalies are also shown. (a)–(b) are the plots for Chandra catchment, and (c)–(d) for upper Dudhkoshi catchment, respectively.

4.4.8 Implications of the estimated climate sensitivities

The above estimated climate sensitivities from glacierised and non-glacierised parts of the catchments suggested $s_P^{(g)} \approx 0$ and $s_T^{(r)} \approx 0$. Thus, Eqs. (4.3)–(4.11) can be simplified to the following approximate relations describing the response of the summer runoff to climate variability and change in these two catchments.

$$\begin{aligned}
\delta Q &\approx x s_T^{(g)} \delta T + (1-x) s_P^{(r)} \delta P, && (4.12)\\
\delta Q^{(g)} &\approx x s_T^{(g)} \delta T, && (4.13)\\
\delta Q^{(r)} &\approx (1-x) s_P^{(r)} \delta P, && (4.14)\\
\sigma_Q &\approx \sqrt{x^2 s_T^{(g)2} \sigma_T^2 + (1-x)^2 s_P^{(r)2} \sigma_P^2}, && (4.15)\\
\Delta Q &\approx x s_T^{(g)} \Delta T + (1-x) s_P^{(r)} \Delta P + \Delta x (Q_0^{(g)} - Q_0^{(r)}). && (4.16)
\end{aligned}$$

These simplified equation suggested that the key parameters that determined the climate response of these glacierised catchments to given climate forcing were $s_T^{(g)}$ and $s_P^{(r)}$. According to Eq. (4.12), the precipitation and temperature sensitivity of catchment runoff are essentially given by $(1-x)s_P^{(r)}$ and $xs_T^{(g)}$, respectively. As both the catchments had similar $s_P^{(r)}$, the corresponding s_P were also similar with a slightly smaller value in Chandra catchment due to a higher fractional glacier cover there. On the other hand, a slightly higher $s_T^{(g)}$ in upper Dudhkoshi catchment, together with a slightly lower glacier cover there, led to similar s_T in the two catchments. Below we discuss the implications of the above simplified linear-response formulae for the future changes in the mean summer runoff and its variability.

Climate-sensitivity, and changes in summer runoff and its variability

As discussed before, estimating the future changes mean summer runoff using Eq. (4.16) requires the changes in summer precipitation or temperature to be within the range of calibration. It turns out that under most of the projected scenarios, including the optimistic RCP 2.6 ones, the temperature

changes (Kraaijenbrink et al, 2017) in the two catchments by ∼2050 go beyond the calibration range. Therefore, we did not attempt to predict the future changes in summer runoff. Only for Chandra catchment, the projected mean temperature changes of 1.1°C by 2050 under RCP 2.6 scenario were within the calibration range, and obtained a glacier runoff change of 0.27±0.03 m yr^{-1}. This was comparable to the corresponding reported estimate of 0.25 m yr^{-1} for the entire Indus basin (Huss and Hock, 2018).

Over the calibration period 1997–2018, Chandra and upper Dudhkoshi catchments had σ_P of 0.22 and 0.15 m yr^{-1}, and σ_T of 0.89 and 0.34 °C, respectively. These values, together Eq. (4.15), predicted σ_Q of 0.13 and 0.08 m yr^{-1} for the two catchments, which equalled the corresponding values obtained directly from the simulated summer runoff (Fig. 4.19a). A corresponding close match was also obtained over the validation period of 1980-1996 (Fig. 4.19a).

Equation (4.15)) can also be used to predict the variation of $\sigma_Q$in these catchments due to the shrinkage glacier cover if σ_P and σ_T were to remain unchanged. The shape of hyperbolic $\sigma_Q(x)$ curve for both the catchments (Fig. 4.19b) indicated that major changes in runoff variability may not take place due to the expected glacier loss alone. However, possible changes in σ_P and σ_T may drive significant future changes of σ_Q in these two catchments, as underlined by the difference between the simulated σ_Q for the two catchments over the periods 1980–1996 and 1997–2018 (Fig. 4.19b).

Glacier-compensation curve

For a set of hypothetical catchments with different values of x, but similar $s_T^{(g)}$, $s_P^{(r)}$, σ_T and σ_P, Eq. (4.15) implies that σ_Q is a hyperbolic function of x (Fig. 4.19b). The runoff variability is high in the limit $x \to 0$ due to a precipitation sensitive off-glacier runoff with $\sigma_Q \approx (1-x)s_P^{(r)}\sigma_P$. In the opposite limit of $x \to 1$, σ_Q is again high due to a high temperature sensitivity of glacier runoff, with $\sigma_Q \approx x s_T^{(g)}\sigma_T$. These two competing effects yield a minimum in σ_Q at an intermediate value of x (Fig. 4.19b). This nonmonotonic behaviour of runoff variability with x is well known empirically (e.g., Chen

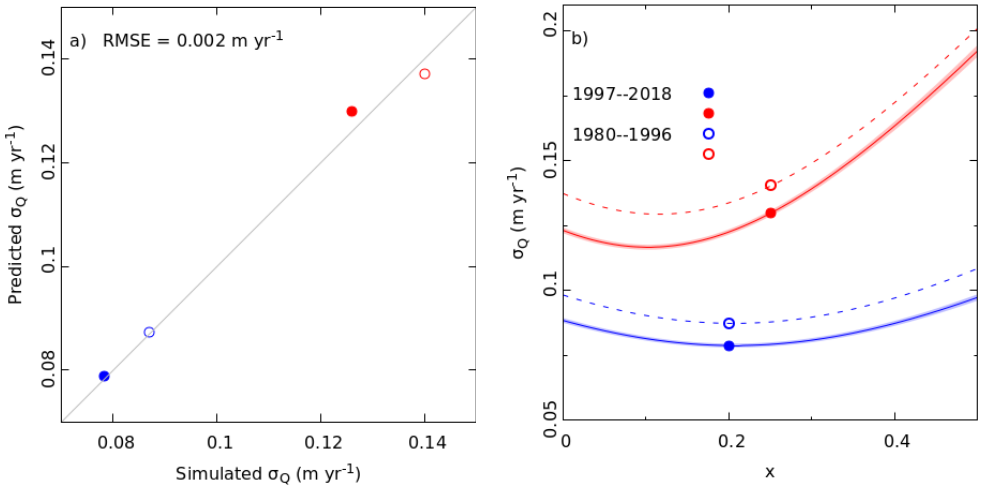

Figure 4.19: a) Predicted σ_Q using Eq. (4.15) are compared with the corresponding simulated values for both the catchments. The solid and open circles denote data for the periods 1997–2018 and 1980–1996, respectively. Data for Chandra and upper Dudhkoshi catchments are shown with red and blue symbols, respectively. b) The solid (dashed) lines show $\sigma_Q(x)$ obtained using σ_T and σ_T values from 1997–2018 (1980–1996).

and Ohmura, 1990), and is termed as glacier-compensation effect. The above theoretical explanation of the effect is consistent with a reported strong correlation between runoff and precipitation (temperature) in the limit of small (extensive) glacier cover (van Tiel et al, 2020). Note that while Eq. (4.15) suggests a hyperbolic glacier compensation curve, some of the existing studies used an empirical parabolic curve (e.g., Chen and Ohmura, 1990).

Chen and Ohmura (1990) suggested that the glacier-compensation curve can be utilised to estimate the change in σ_Q as glacier cover changes. However, recent model simulations indicated that a time-dependent glacier-compensation curve rules out such possibility (van Tiel et al, 2020). This is consistent with Eq. (4.15), which indicates that apart from a changing glacier cover, the compensation curve (and thus σ_Q) can shift when σ_P and/or σ_T changes with time.

Prediction of peak water

The predicted future changes of glacier runoff in Chandra catchments, which was obtained using Eq. (4.16), reproduced the peak-water effect successfully (Fig. 4.21). This calculation was done only for the optimistic RCP 2.6 scenario (Fig. 4.20) as the corresponding temperature change was within the range of annual temperature over the period 1980–2018 and the present estimates of climate sensitivities could be used safely. The estimated peak water was 12±8% of the present glacier runoff, and the estimated timing was 2033±7. In Chandra catchment, the estimated peak-water in glacier runoff is expected to cause a 0.05 m yr^{-1} to rise in catchment runoff. This change may not be detectable, given the recent interannual variability of catchment runoff $\sigma_Q = 0.14$ m yr^{-1}. Note that the above estimates are comparable to previously predicted a peak water of 14±3% on 2030±4 (Huss and Hock, 2018). It is encouraging that a simple climate-sensitivity based approach presented here could capture the peak-water effect in Chandra catchment as well as a state-of-the-art glacio-hydrological model (Huss and Hock, 2018). Note that for Chandra catchment, our simulated recent glacier runoff, the initial glacier cover, and geodetic mass balance used for calibration were sim-

ilar to the corresponding values used by Huss and Hock (2018) for the Indus basin.

In upper Dudhkoshi catchment, we estimated a peak water of 10±4% of the present glacier runoff, and the estimated timing was 2022±4 (Fig. 4.21b). This estimated peak water was significantly smaller and quicker compared to that of Huss and Hock (2018). This inconsistency may be related to possible extrapolation errors as, the projected temperature changes crossed the range of interannual variability by 2024. Moreover, there were several difference between the two models in this region, which may contribute to the above mismatch. The RGI 4 glacier inventory used by Huss and Hock (2018) had 25% higher glacier cover in Ganga basin compared to RGI 6 used here. Also the authors calibrated their model using a geodetic mass-balance record which was twice as negative as the median of the eight geodetic mass balance records used here. Also, the present estimates of glacier runoff in upper Dudhkoshi catchment was almost half of that reported by Huss and Hock (2018) for Ganga basin. The above differences likely led to a corresponding large difference in the modelled climate sensitivities of glacier runoff between the present study and that of Huss and Hock (2018) in this region.

4.4.9 Limitations of the study

The present study suffers from a general problem that affects all glacio-hydrological studies in the Himalaya which is a lack of long-term hydro-meteorological field data. We have used runoff time series generated with VIC model simulations that forced by ERA5 reanalysis data to circumvent the issue. The reanalysis data was bias corrected using the limited field data. In addition, a parsimonius calibration strategy of using only two tuning parameters, a precipitation scale factor and the degree-day factor, to fit both the weekly summer discharge and the decadal-scale glacier mass balance data minimised the possibility of over-fitting. The sensitivity to the chosen values of the model parameters that were not calibrated for, were within reasonable limits. The comparison with limited field data that were available showed that the model performance was reasonable in terms of the RMSE and NSE

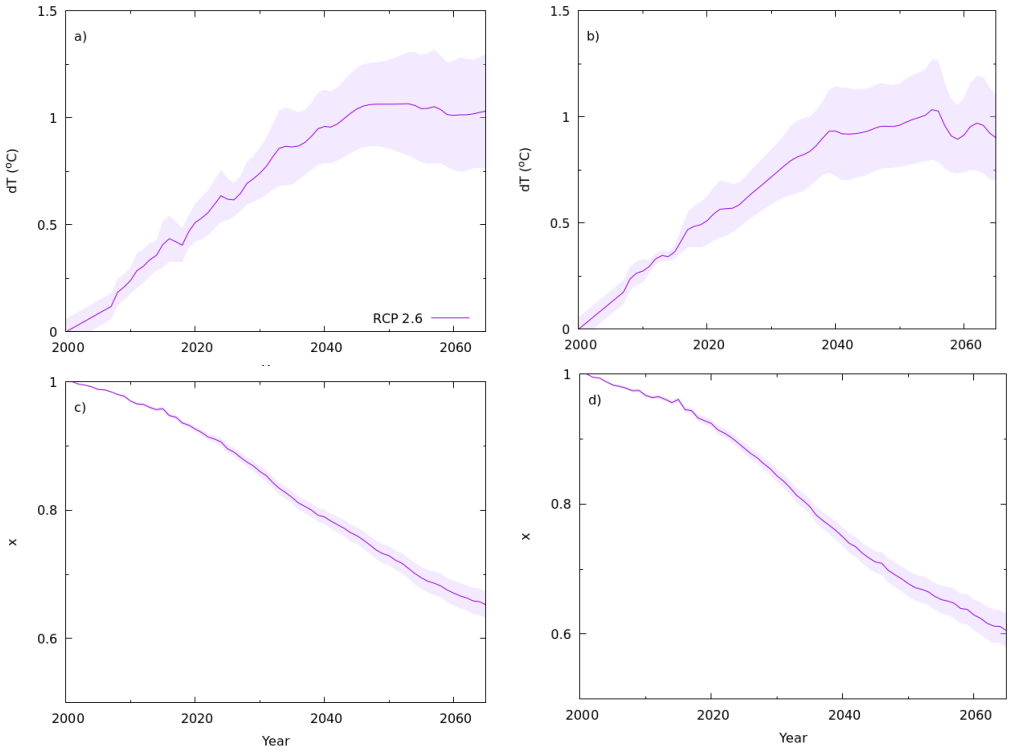

Figure 4.20: Projected temperature changes over the (a) western, and (b) eastern Himalaya predicted for RCP 2.6 climate scenario (Kraaijenbrink et al., 2017). Kraaijenbrink et al. (2017) provided temperature change data from 2005 onward. Here we extrapolated the data between 2000–2005 using the trend between 2005–2010. Fractional changes in glacier area for (a) Indus, and (b) Ganga basins predicted using RCP 2.6 scenario (Huss and Hock, 2018). In all the four plots, the band is showing the corresponding uncertainties associated with the future projection.

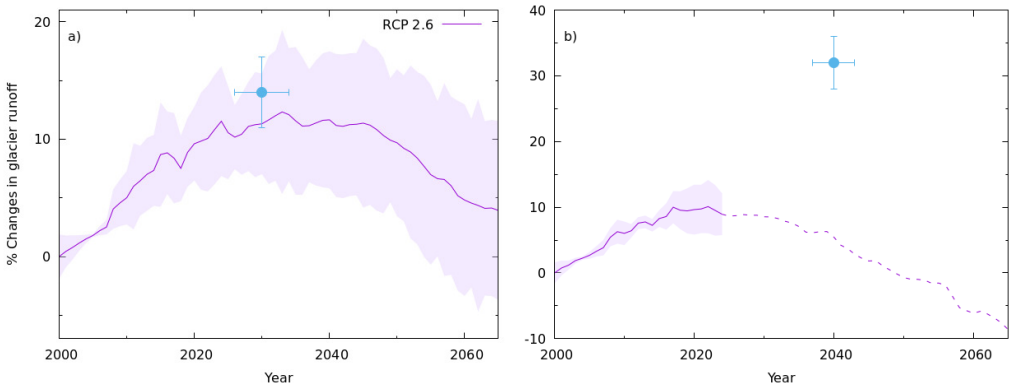

Figure 4.21: The 'peak water' due to future glacier changes predicted using Eq. (4.16) for (a) Chandra, and (b) upper Dudhkoshi catchments, respectively. The solid sky-blue dots represents the corresponding 'peak water' as reported in Huss and Hock (2018) for both the catchments. Dashed portion of the solid line in upper Dudhkoshi catchment indicate the corresponding temperature change beyond the calibration range of the catchment. See text for details.

values. The simulated discharge and glacier mass balance compared well with those from existing studies. In addition, we performed a set of additional calibration runs for upper Dudhkoshi where 4 years of observation were used for calibration, along with a 3 years-long validation period. These runs also supported the effectiveness of the tuning procedure. Note that the ice melt module used here assumed the glacier extent to be static. However, this is not a serious limitation as the observed changes in glacier fraction was within 0.01–0.04 over the simulation period as discussed before. Based on these points, it may be assumed the augmented VIC model used here represented the hydrology of these two Himalayan catchments reasonably well. Therefore, within the range of forcing over which the linear models were calibrated, the linear models are expected to provide reasonable description of the climate response of the catchments. Whenever future changes in glacier fraction is expected to be significant, corresponding estimates can be incorporated using the glacier-fraction dependent linear model introduced here.

In addition, the the present model we have not considered the effect of

debris present on the glacier surface (Shah et al, 2019) and some complicated mass-balance processes like avalanches (Laha et al, 2017). So, it would be useful to see if we incorporate the presence of debris, avalanche activity in the model, then if obtained sensitivity values remain the same of how much it will affect.

Keeping the above limitations in mind, it would be interesting to repeat the study in a data-rich glacierised catchment, and verify that the climate sensitivity and glacier fraction based simple linear model presented here performs at par with more complex process-based distributed glacio-hydrological models in predicting the multidecadal runoff response for a given climate scenario.

We emphasise that there is an inherent limitation of the climate sensitivity based approach used here. The predictions from such models cannot be extended to the longer time scale of a century or so as the corresponding changes in meteorological forcing and runoff may be beyond the range of interannual variability over which the model is calibrated. However, on a relatively shorter time scale of multiple decades, this model maybe quite useful. Also, over longer time scales the dynamic glacier geometry which was ignored in our simulation may lead to systemtic changes in $Q_0^{(g)}$ that cannot be captured in a linear response approach.

4.5 Summary

In this paper, we simulate the runoff of Chandra (western Himalaya) and upper Dudhkoshi (eastern Himalaya) catchments over 1980–2018, using the VIC model augmented with a temperature-index glacier-melt module. Calibrating two model parameters using a Bayesian method that simultaneously fits the available summer runoff and decadal-scale geodetic glacier mass balance, our simulation obtained a good match with both observations and the existing model results. The simulated climate sensitivities of summer runoff to temperature and precipitation forcing in the catchments reveal some interesting patterns. The precipitation sensitivities of the summer runoff of the

non-glacierised parts of the catchments are high, but those of the glacierised parts are negligible. In contrast, the temperature sensitivities of summer runoff of glaciers are high, but those of the non-glacierised parts are negligible. As a consequence, the temperature sensitivity of the glacier runoff and the precipitation sensitivity of the off-glacier runoff are critical determinants of the future changes of summer runoff and its variability in these two catchments. Despite the limitations like calibration with a limited dataset, the use of a simple temperature-index glacier module, the static-glacier assumption, ignoring the effects of supraglacial debris cover and avalanching, and so on, the present study brings out some interesting similarities in the climate sensitivities of two glacierised Himalayan catchments with contrasting climate regimes. Further studies of the climate sensitivities of a larger set of Himalayan glacierised catchments, with an improved model that relaxes some of the above assumptions, are needed to explore if the above properties, or at least some of them, are general in nature. It will also be important to extend the present analysis to runoff sensitivities at the sub-seasonal time scale.

Chapter 5

Conclusions and future outlook

Glaciers all over the globe are shrinking (Hugonnet et al, 2021) due to climate change. Shrinking glaciers have become a major concern for the high mountain Asia (e.g., Immerzeel et al, 2020; Armstrong et al, 2020), as it is one of the largest reservoirs of snow and ice outside Poles. Also it is the headwater of the several major Asian rivers (Pritchard, 2019; Immerzeel et al, 2020) with large downstream population. The availability of water for drinking (e.g., Dangi et al, 2018), seasonal agricultural use (e.g., Biemans et al, 2019), and hydropower generation and other industrial use (e.g., Ali et al, 2018) affected by shrinking glaciers. A lack of long-term glacio-hydro-meteorological data from the region (Miller et al, 2012; Azam et al, 2021), uncertainties in understanding different cryospheric processes, and uncertainties in the future climate projections (Joseph et al, 2018) compromise a satisfactory understanding of the future changes in the runoff from the Himalayan catchments. Therefore accurate understanding the response of the Himalayan glacier due to climate forcing and the climate response of glacier-fed rivers in the Himalaya is important.

However, the climate response of the Himalayan glaciers is complicated by the variability in the regional climate, complex local topography, not so well-understood processes like avalanching, the presence of debris cover on the glacier surface (Benn and Lehmkuhl, 2000; Scherler et al, 2011a). In particular, the processes related to mass balance on debris covered Himalayan

glaciers are important hurdles, that prevent accurate prediction of glacier response to climate change. The response of glacier mass balance due to climate forcing affects the meltwater contribution to the glacier-fed rivers. Therefore, understanding the climate response of glacier-fed rivers and the climate sensitivity of runoff from these catchments may provide useful clues. The future change in catchment runoff and its variability in the high Himalaya can be assessed in general using climate sensitivities,.

Motivated by the above issues, we focus on the mass balance processes of debris covered glaciers over the Himalaya at the beginning of the thesis. We develop modelling and field-based novel methods to quantify important processes related to the accumulation (chapter 2), and ablation (chapter 3) of ice on debris covered Himalayan glaciers. Later in the thesis, we focus on the climate response (chapter 4) of river runoff from glacierised catchments. The major conclusions drawn from the three studied problems and possible future directions are summerize below.

Estimation of avalanche strength

We have presented an approximate method to quantify the magnitude of the avalanche accumulation using a simplified numerical flowline model-based method (chapter 2). Our simulations for Hamtah, Satopanth, and Dunagiri Glaciers indicate that extensive avalanches from the vast headwalls contribute more than 95% of the total accumulation in these glaciers. Therefore, the avalanche contributions influence both the dynamics and the glacier extent over a longer time scale. Despite the large uncertainties in our estimates arising out of the assumptions and simplifications involved in our method and limitations due to a lack of detailed data, these results underline the necessity of quantification of the magnitude of the avalanche-derived accumulation on a large class of Himalayan glaciers (e.g., $\sim 10\%$ in central Himalaya (Fig. 1.5)). This is necessary to explain the present length, thinning, and retreat patterns of these glaciers. Given the above understanding, the future directions for quantifying avalanches and their effects are likely to be the following.

It is important to develop a scheme to relate the strength of avalanche

accumulation to climate change at the scale of the whole Himalaya. It will be interesting to investigate the role of avalanches in the large-scale glacier mass balance over the Himalaya, and its effects on the glacier dynamics. Also, avalanching quickly bring down snow from higher elevation to lower elevation, where it can melt faster. Therefore, it is interesting to see the effect of including avalanching in the glacio-hydrological models to simulate the basin-scale runoff. In this context, the existing methods of estimating gravitational redistribution of snow (e.g., Gruber, 2007; Bernhardt and Schulz, 2010), combined with methods similar to the one presented here, could be useful starting points. Therefore, studying avalanches requires progress in modelling tools and direct field observation techniques.

Modelling ice ablation on debris covered glaciers

We have presented an analysis of the accuracy of thermal diffusivity and sub-debris ablation estimates using in-situ measurements of temperature profiles of the supraglacial debris layer on Satopanth Glacier during the 2016 and 2017 ablation seasons (chapter 3). We compared four different methods of analysing the temperature profiles. The methods are based on one-dimensional heat conduction through a single-layer or a two-layer conductor. Our analysis suggests that a one-dimensional and purely conductive heat transport within the debris layer is accurate enough to describe surface melts over the debris-covered ablation zone. The departure from such an idealised model does not lead to significant errors given the level of uncertainty in corresponding glaciological estimates of sub-debris ablation rates. The consequence of the findings is that vertical temperature-profile measurement can be employed to estimate sub-seasonal ablation rates with reasonable accuracy. Measuring sub-seasonal ablation rates using vertical temperature profiles may be particularly suitable for relatively inaccessible debris-covered Himalayan glaciers where regular monitoring of a stake network is logistically challenging. Given the above understanding, the future directions for reducing inherent uncertainties of the methods and their effects are likely to be the following.

In this study, all the above methods provide effective values of κ and s for the debris layer based on debris-temperature measurements under certain model assumptions. However, in reality, both physical and thermal properties of debris-layer like K, C, ρ_d, ϕ, and moisture content have spatial and temporal variability. Therefore, detailed in-situ measurements of K, C, ρ_d, ϕ, moisture content, horizontal and vertical heat fluxes are needed to identify possible violations of model assumptions, and to quantify their effects on the accuracy of one-dimensional heat conduction based methods. The methods discussed in the thesis can be employed to different debris-covered glaciers to understand the seasonality of the ablation rate over the Himalaya with minimal human effort compared to the glaciological method. Then, it will be interesting to investigate the drivers of the observed seasonal pattern of the ablation rates over the Himalaya. Also, progress is needed on the large-scale remote-sensing based methods to estimate the thermal properties of debris.

Climate response of runoff from glacierised catchments

The response of catchment runoff to climate forcing is determined by its climate sensitivity. We investigate the sensitivity of summer runoff to precipitation and temperature changes in winter-snow dominated Chandra (western Himalaya), and summer-rain dominated upper Dudhkoshi (eastern Himalaya) catchments in order to understand the nature of the climate change impact on the mean summer runoff and its variability (chapter 4). The runoff over the period 1980–2018 is simulated with a semi-distribute hydrologic model, which is calibrated using available discharge and glacier mass loss data. An analysis of the interannual variability of the simulated summer runoff reveals that the runoff from the glacierised parts of the catchments is sensitive to temperature changes, but is insensitive to precipitation changes. The behavior of the summer runoff from the non-glacierised parts is exactly the opposite. Such precipitation-independent runoff from the glacierised parts stabilises the catchment runoff against precipitation variability to some degree. With shrinking glacier cover over the coming decades, the summer runoff from the two catchments is expected to become

more sensitive to the precipitation forcing and less sensitive to the temperature forcing. Because of these competing effects, the impact of the glacier loss on the interannual variability of summer runoff may not be significant compared to the variability due to future changes in climate forcing (e.g., temperature and precipitation). Knowledge of the climate sensitivities of runoff of the glacierised and the non-glacierised parts allows an estimation of future changes of catchment runoff and the amplitude and the timing of 'peak water' under any given climate scenario. However, the characteristic 'peak water' in the long-term mean summer runoff, which is caused by the excess meltwater released by the shrinking ice reserve, may not lead to a detectable signal over the background interannual variability of runoff in these two catchments.

Since the patterns of the climate sensitivities of the glacier runoff were similar for the two catchments despite their contrasting climate regime, it may be worth exploring if this is a general feature of the climate sensitivity of glacier runoff in the Himalaya or elsewhere.

Synthesis

The broader issue related to Himalayan glaciers and glacier-fed rivers is to accurately understand their climate response, which can provide better predictability. To address this problem, one needs to look at the important glacier-scale processes which control the mass balance of glaciers, also basin-scale runoff generation processes. The present thesis identifies a few important physical processes (e.g., avalanche, heat conduction through debris) that controls the mass balance of Himalayan glaciers, which can be included in the large-scale model to reduce the associated processes-based uncertainties. Also, the present thesis provides a better insight into the climate response of runoff generated from different parts of a glacierised Himalayan catchment, which can be used for future prediction of river runoff. We had shown that runoff from different parts of glacierised catchment has a similar climate response, which is independent of the climate regime of the corresponding

catchment. So, in a broader picture, the present thesis improves the understanding of the accumulation and ablation processes, and runoff generation from Himalayan glaciers.

Future outlook

A natural extension of the work discussed in the thesis is to attempt to scale up the local understanding related to glacier accumulation, ablation, and river runoff in glacier-fed rivers to the regional or global scale. For example, we have shown that avalanche is a significant contributor to the mass balance of a typical Himalayan glacier, and it is very common in the high mountain environment. On a glacierised catchment, avalanches can bring down a significant amount of snow from a higher elevation to a relatively lower elevation, where it can quickly melt and contribute to the river runoff. Therefore, it will be interesting to include the avalanche processes in the glacio-hydrological models, and investigate the corresponding effect on the runoff hydrograph. Algorithms are available to incorporate the avalanche process, e.g., gravitational redistribution of snow (Gruber, 2007; Bernhardt and Schulz, 2010). One of the major input for this kind of models is snowfall data, which is generally taken from the reanalysis and/or gridded datasets. In the high Himalaya, reanalysis and/or gridded dataset of precipitation can have a large bias. Also, there is a serious lack of in-situ snowfall measurements over the Himalaya. So, we need to install a lot of rain/snow gauges over the Himalaya to calibrate the gridded and/or reanalysis precipitation data.

The glacio-hydrological model discussed in chapter 4, doesn't include the glacier dynamics and the effect of debris cover. The high mountain hydrology is affected by glacier evolution. Despite its importance, many existing glacio-hydrological models over the Himalaya-Karakoram region ignore glacier dynamics (Azam et al, 2021). Ignoring glacier dynamics may lead to a large bias in the long-term glacier melt contributions. One way forward is to incorporate the dynamical ice-flow models, e.g., SIA (Banerjee et al, 2020),

and investigate its effect on the glacier melt contribution in the long run. The glacier model discussed in chapter 4 used a simple degree-day model (Hock, 2003), assuming all the glacier ice is clean. Similarly, we can use the degree-day model with separate degree-day factors for clean and debris covered ice, or we can use the debris thickness dependent model (Shah et al, 2019) to estimate the melt from debris covered part. In this context, the debris cover map can be used from Herreid and Pellicciotti (2020), and the debris thickness map from Rounce et al (2021).

Incorporating the above additional component in the glacio-hydrological model would help to reduce the existing present state uncertainty in the river runoff, as well as its future prediction. The outcome may provide a detailed understanding of the climate response of the glacierised part over the Himalaya.

Here, we list out few more important glacier specific issues related to the broader problem of glacier response to climate forcing that have not been studied in the thesis. To improve individual debris covered glacier scale understanding, we need to focus on the supraglacial lakes/ice-cliffs on the glacier surface. These supraglacial ponds/ice-cliffs are the hotspot of melting on any debris covered glaciers. Therefore, estimating glacier-wide ablation on the debris covered glacier needs to detailed study to quantify the local enhancement of melting by the supraglacial ponds/ice-cliffs. So, the surface energy balance of these lakes/ice-cliffs, along with a high-resolution map of these small glacier features (like supraglacial ponds/ice-cliffs) would be useful. In the context of ablation modelling on debris covered glaciers, we need to check the applicability of large-scale debris thickness dependent temperature index models. Here, a satellite-derived accurate debris thickness map would be very important (e.g., Rounce et al, 2021), and this data needs to be calibrated using a large number of in-situ measurements.

Also, studying glacier-related hazards is one of the important topics of research in order to mitigate the risk. It requires a quantitative understanding of processes related to the glacier hazards like GLOFs, ice avalanches from hanging glaciers, etc, in terms of both modelling and in-situ observations to identify the potentially dangerous glaciers or glacier lakes.

Chapter 6

Published and under-review articles

- Laha, S., Kumari, R., Singh, S., Mishra, A., Sharma, T., Banerjee, A., . . . Shankar, R. (2017). Evaluating the contribution of avalanching to the mass balance of Himalayan glaciers. Annals of Glaciology, 58(75pt2), 110-118. doi:10.1017/aog.2017.27

- Laha, S., Banerjee, A., Singh, A., Sharma, P., and Thamban, M.: The control of climate sensitivity on variability and change of summer runoff from two glacierised Himalayan catchments, Hydrol. Earth Syst. Sci. Discuss. [preprint], https://doi.org/10.5194/hess-2021-499, in review, 2021.

- Laha, S., Winter-Billington, A., Banerjee, A., Shankar, R., Nainwal, H.C., Koppes, M. (2021). Estimation of ice ablation on debris-covered Satopanth glacier, central Himalaya from vertical debris-temperature profiles. *Revised version of the manuscript is submitted in the Journal of Glaciology (JOG)*

Bibliography

Acharya, A., and Kayastha, R. B. (2019). Mass and energy balance estimation of Yala Glacier (2011–2017), Langtang Valley, Nepal. Water 11:6. doi: 10.3390/w11010006

Adhikari, S., and Huybrechts, P. (2009). Numerical modelling of historical front variations and the 21st-century evolution of glacier AX010, Nepal Himalaya. Annals of Glaciology, 50(52), 27-34.

Adhikari, T. R., Devkota, L. P. (2016). Climate change and hydrological responses in Himalayan basins, Nepal. In Climate Change, Glacier Response, and Vegetation Dynamics in the Himalaya (pp. 65-85). Springer, Cham.

Ageta Y, Ohata T, Tanaka Y, Ikegami K and Higuchi K (1980). Mass balance of glacier AX010 in Shorong Himal, east Nepal during the summer monsoon season. J. Jpn. Soc. Snow Ice 41(Special), 34–41

Ageta Y and Higuchi K (1984). Estimation of mass balance compo-nents of a summer-accumulation type glacier in the NepalHimalaya.Geogr. Ann. Ser. Phys. Geogr.,66, 249–255

Aizen, V. B., Aizen, E. M., and Melack, J. M. (1996). Precipitation, melt and runoff in the northern Tien Shan. Journal of Hydrology, 186(1-4), 229-251.

Aizen, V. B., et al. (2006). Climatic and atmospheric circulation pattern variability from ice-core isotope/geochemistry records (Altai, Tien Shan and Tibet). Annals of Glaciology, 43, 49–60.

Aizen, V. B., Mayewski, P. A., Aizen, E. M., Joswiak, D. R., Surazakov, A. B., Kaspari, S., ... and Finaev, A. (2009). Stable-isotope and trace element time series from Fedchenko glacier (Pamirs) snow/firn cores. Journal of Glaciology, 55(190), 275-291.

Akhtar, M., Ahmad, N., and Booij, M. J. (2008). The impact of climate change on the water resources of Hindukush–Karakorum–Himalaya region under different glacier coverage scenarios. Journal of hydrology, 355(1-4), 148-163.

Aktar, W., Sengupta, D., and Chowdhury, A. (2009). Impact of pesticides use in agriculture: their benefits and hazards. Interdisciplinary toxicology, 2(1), 1-12.

Ali, S. A., Aadhar, S., Shah, H. L., and Mishra, V. (2018). Projected increase in hydropower production in India under climate change. Scientific reports, 8(1), 1-12.

Amante, C. and B.W. Eakins, 2009. ETOPO1 1 Arc-Minute Global Relief Model: Procedures, Data Sources and Analysis. NOAA Technical Memorandum NESDIS NGDC-24. National Geophysical Data Center, NOAA. doi:10.7289/V5C8276M.

Anand, J., Gosain, A. K., Khosa, R., and Srinivasan, R. (2018). Regional scale hydrologic modeling for prediction of water balance, analysis of trends in streamflow and variations in streamflow: The case study of the Ganga River basin. Journal of Hydrology: Regional Studies, 16, 32-53.

Andermann, C., Longuevergne, L., Bonnet, S., Crave, A., Davy, P., and Gloaguen, R. (2012). Impact of transient groundwater storage on the discharge of himalayan rivers. Nature Geoscience, 5 (2), 127–132.

Andermann, C., Bonnet, S., & Gloaguen, R. (2011). Evaluation of precipitation data sets along the Himalayan front. Geochemistry, Geophysics, Geosystems 12(7).

Anderson, R. S., and Anderson, S. P. (2010). Geomorphology: the mechanics and chemistry of landscapes. Cambridge University Press.

Anderson, L. S., and Anderson, R. S. (2016). Modeling debris-covered glaciers: response to steady debris deposition. The Cryosphere, 10(3), 1105.

Anderson, L. S., Armstrong, W. H., Anderson, R. S., and Buri, P. (2021). Debris cover and the thinning of Kennicott Glacier, Alaska: in situ measurements, automated ice cliff delineation and distributed melt estimates. The Cryosphere, 15(1), 265-282. DOI: https://doi.org/10.5194/tc-10-1105-2016

Anderton, S., Latron, J., Gallart, F. (2002). Sensitivity analysis and multi-response, multi-criteria evaluation of a physically based distributed model. Hydrological Processes, 16(2), 333-353.

Andreadis, K. M., Storck, P., and Lettenmaier, D. P. (2009). Modeling snow accumulation and ablation processes in forested environments. Water resources research, 45(5).

Archer, D. R., and Fowler, H. J. (2004). Spatial and temporal variations in precipitation in the upper indus basin, global teleconnections and hydrological implications. Hydrol. Earth Syst. Sci. 8, 47–61. doi: 10.5194/hess-847-2004

Arendt, A., Bliss, A., Bolch, T., Cogley, J. G., Gardner, A., Hagen, J. O., ... and Zheltyhina, N. (2017). Randolph Glacier Inventory–A Dataset of Global Glacier Outlines: Version 6.0: Technical Report, Global Land Ice Measurements from Space. DOI: https://doi.org/10.7265/N5-RGI-60

Armstrong, R. L., Rittger, K., Brodzik, M. J., Racoviteanu, A., Barrett, A. P., Khalsa, S. J. S., ... and Armstrong, B. (2019). Runoff from glacier ice and seasonal snow in High Asia: separating melt water sources in river flow. Regional Environmental Change, 19(5), 1249-1261.

Arora, M., Rathore, D. S., Singh, R. D., Kumar, R., and Kumar, A. (2010). Estimation of melt contribution to total streamflow in River Bhagirathi and River DhauliGanga at Loharinag Pala and Tapovan Vishnugad project sites. Journal of Water Resource and Protection, 2(07), 636.

Azam, M. F., Wagnon, P., Ramanathan, A., Vincent, C., Sharma, P., Arnaud, Y., ... and Berthier, E. (2012). From balance to imbalance: a shift in the dynamic behaviour of Chhota Shigri glacier, western Himalaya, India. Journal of Glaciology, 58(208), 315-324.

Azam, M. F., Wagnon, P., Vincent, C., Ramanathan, A., Linda, A., Singh, V. B. (2014). Reconstruction of the annual mass balance of Chhota Shigri glacier, Western Himalaya, India, since 1969. Annals of Glaciology, 55(66), 69-80.

Azam MF and 10 others (2016). Meteorological conditions, seasonal and annual mass balances of Chhota Shigri Glacier, westernHimalaya, India.Ann. Glaciol.,57, 328–338

Azam, M. F., Wagnon, P., Berthier, E., Vincent, C., Fujita, K., and Kargel, J. S. (2018). Review of the status and mass changes of Himalayan-Karakoram glaciers. Journal of Glaciology, 64(243), 61-74.

Azam, M. F., Wagnon, P., Vincent, C., Ramanathan, A. L., Kumar, N.,Srivastava, S., ... Chevallier, P. (2019). Snow and ice melt contributions in a highly glacierized catchment of Chhota Shigri Glacier (India) over the last five decades. Journal of Hydrology, 574, 760-773.

Azam, M. F., and Srivastava, S. (2020). Mass balance and runoff modelling of partially debris-covered Dokriani Glacier in monsoon-dominated Himalaya using ERA5 data since 1979. Journal of Hydrology, 125432.

Azam, M. F., Kargel, J. S., Shea, J. M., Nepal, S., Haritashya, U. K., Srivastava, S., ... and Bahuguna, I. M. (2021). Glaciohydrology of the Himalaya-Karakoram. Science. DOI: 10.1126/science.abf3668

Bamber, J.L., R.L. Layberry and S.P. Gogineni, (2001). A new ice thickness and bed data set for the Greenland ice sheet, 1. Measurement, data reduction, and errors, J. Geophys. Res., 106, 33733–33780.

Bandyopadhyay, J. (2013). Securing the Himalayas as the water tower of Asia: an environmental perspective. Asia Policy, 16(1), 45-50.

Banerjee, A., and Shankar, R. (2013). On the response of Himalayan glaciers to climate change. Journal of Glaciology, 59(215), 480-490.

Banerjee, A., and Azam, M. F. (2016). Temperature reconstruction from glacier length fluctuations in the Himalaya. Annals of Glaciology, 57(71), 189-198.

Banerjee, A. (2017). Brief communication: Thinning of debris-covered and debris-free glaciers in a warming climate. The Cryosphere, 11(1), 133-138.

Banerjee, Argha, and Bilal Ahmad Wani.(2018). Exponentially decreasing erosion rates protect the high-elevation crests of the Himalaya. Earth and Planetary Science Letters 497 (2018): 22-28.

Banerjee, A., Patil, D., and Jadhav, A. (2020). Possible biases in scaling-based estimates of glacier change: a case study in the Himalaya. The Cryosphere, 14(9), 3235-3247.

Banerjee, A. (2022). A weak precipitation sensitivity of glacier runoff. Geophysical Research Letters, 49(5), e2021GL096989.

Ballesteros-Cánovas, J. A., Trappmann, D., Madrigal-González, J., Eckert, N., and Stoffel, M. (2018). Climate warming enhances snow avalanche risk in the Western Himalayas. Proceedings of the National Academy of Sciences, 115(13), 3410-3415.

Barlow, M., Matthew, W., Bradfield, L., and Heidi, C. (2005). Modulation of daily precipitation over southwest Asia by the Madden-Julian oscillation. Monthly Weather Review, 133(12),3579–3594.

Barry, R. G. (1992). Mountain weather and climate (2nd ed.). New York: Routledge.

Bartholomaus, T. C., Anderson, R. S., and Anderson, S. P. (2008). Response of glacier basal motion to transient water storage. Nature Geoscience, 1(1), 33-37.

Barnett, T. P., Adam, J. C., and Lettenmaier, D. P. (2005). Potential impacts of a warming climate on water availability in snow-dominated regions. Nature, 438(7066), 303.

Bashir, F., Zeng, X., Gupta, H., and Hazenberg, P. (2017). A hydrometeorological perspective on the karakoram anomaly using unique valley-based synoptic weather observations. Geophys. Res. Lett. 44, 10470–10478. doi: 10.1002/2017GL075284.

Benn DI and Lehmkuhl F (2000). Mass balance and equilibrium-line altitudes of glaciers in high-mountain environments. Quatern.Int., 65/66, 15–29.

Benn, D. I., Kirkbride, M. P., Owen, L. A., and Brazier, V. (2003). Glaciated valley landsystems. Glacial landsystems, 372-406.

Benn, D., and Owen, L. A. (2005). Equilibrium-line altitudes of the last glacial maximum for the Himalaya and Tibet: an assessment and evaluation of results. Quat. Int. 138-139, 55–58.

Benn, Douglas, and David JA Evans (2014). Glaciers and glaciation. Routledge.

Benn, D. I., Thompson, S., Gulley, J., Mertes, J., Luckman, A., and Nicholson, L. (2017). Structure and evolution of the drainage system of a Himalayan debris-covered glacier, and its relationship with patterns of mass loss. The Cryosphere, 11(5), 2247-2264.

Benn, D. I., Astrom, J., Zwinger, T., Todd, J., Nick, F. M., Cook, S., et al. (2017). Melt-under-cutting and buoyancy-driven calving from tidewater glaciers: New insights from discrete element and continuum model simulations. Journal of Glaciology, 63(240), 691– 702.

Berghuijs, W. R., Woods, R. A., Hrachowitz, M. (2014). A precipitation shift from snow towards rain leads to a decrease in streamflow. Nature Climate Change, 4(7), 583-586.

Bernhardt M and Schulz K (2010). Snowslide: a simple routine for calculating gravitational snow transport. Geophys. Res. Lett., 37, 11.

Beven, K., Freer, J., (2001). Equifinality, data assimilation, and uncertainty estimation in mechanistic modelling of complex environmental systems using the GLUE methodology. J. Hydrol. 249 (1–4), 11–29. https://doi.org/10.1016/S0022-1694(01) 00421-8.

Beven, K. (2001). How far can we go in distributed hydrological modelling?. Hydrology and Earth System Sciences, 5(1), 1-12.

Beven, K.J., (2006). A manifesto for the equifinality thesis, Journal of Hydrology, 320 (1), 18-36. DOI: https://doi.org/10.1016/j.jhydrol.2005.07.007

Berthier, E., Y. Arnaud, R. Kumar, S. Ahmad, P. Wagnon, and P. Chevallier (2007). Remote sensing estimates of glacier mass balances in the Himachal Pradesh (Western Himalaya, India), Remote Sensing of Environment, 108(3), 327–338, doi: 10.1016/j.rse.2006.11.017.

Bhambri, R., Mehta, M., Dobhal, D. P., Gupta, A. K., Pratap, B., Kesarwani, K., and Verma, A. (2016). Devastation in the Kedarnath (Mandakini) Valley, Garhwal Himalaya, during 16–17 June 2013: a remote sensing and ground-based assessment. Natural Hazards, 80(3), 1801-1822.

Bhattacharya, T., Khare, D., and Arora, M. (2019). A case study for the assessment of the suitability of gridded reanalysis weather data for hydrological simulation in Beas river basin of North Western Himalaya. Applied Water Science, 9(4), 110.

Bhattacharya, A., Bolch, T., Mukherjee, K., King, O., Menounos, B., Kapitsa, V., ... and Yao, T. (2021). High Mountain Asian glacier response to climate revealed by multi-temporal satellite observations since the 1960s. Nature Communications, 12(1), 1-13.

Biemans, H., Siderius, C., Lutz, A. F., Nepal, S., Ahmad, B., Hassan, T., ... Immerzeel, W. W. (2019). Importance of snow and glacier meltwater for agriculture on the Indo-Gangetic Plain. Nature Sustainability, 2(7), 594-601.

Bohner, J. (2006). General climatic controls and topoclimatic variations in Central and High Asia. Boreas, 35(2), 279-295.

Bolch, T., Pieczonka, T., and Benn, D. I. (2011). Multi-decadal mass loss of glaciers in the Everest area (Nepal Himalaya) derived from stereo imagery. The Cryosphere, 5(2), 349-358.

Bolch, T., Kulkarni, A., Kaab, A., Huggel, C., Paul, F., Cogley, J. G., ... and Bajracharya, S. (2012). The state and fate of Himalayan glaciers. Science, 336(6079), 310-314.

Bonekamp PNJ, de Kok RJ,Collier E and Immerzeel WW (2019). Contrasting Meteorological Drivers of the Glacier Mass Balance Between-the Karakoram and Central Himalaya. Front. Earth Sci. 7:107.doi: 10.3389/feart.2019.00107.

Bookhagen, B., and D. W. Burbank (2006). Topography, relief, and TRMM-derived rainfall variations along the Himalaya, Geophysical Research Letters, 33, L08,405, doi: 10.1029/2006GL026037.

Bookhagen, B., Burbank, D. W. (2010). Toward a complete Himalayan hydrological budget: Spatiotemporal distribution of snowmelt and rainfall and their impact on river discharge. Journal of Geophysical Research: Earth Surface, 115(F3).

Braithwaite, R. J., and Olesen, O. B. (1989). Calculation of glacier ablation from air temperature, West Greenland. In Glacier fluctuations and climatic change (pp. 219-233). Springer, Dordrecht.

Breili, K., and Rolstad, C. (2009). Ground-based gravimetry for measuring small spatial-scale mass changes on glaciers. Annals of glaciology, 50(50), 141-147.

Brock, B. W., Mihalcea, C., Kirkbride, M. P., and three others et al.(2010). Meteorology and surface energy fluxes in the 2005-2007 ablation seasons at the Miage debris-covered glacier, Mont Blanc Massif, Italian Alps. Journal of Geophysical Research: Atmospheres, 115(D9).

Brun, F., et al. (2015). Seasonal changes in surface albedo of Himalayan glaciers from MODIS data and links with the annual mass balance. Cryosphere, 9(1), 341–355.

Brun, F., Berthier, E., Wagnon, P., Kääb, A., and Treichler, D. (2017). A spatially resolved estimate of High Mountain Asia glacier mass balances from 2000 to 2016. Nature geoscience, 10(9), 668-673.

Brun, F., Wagnon, P., Berthier, E., Shea, J. M., Immerzeel, W. W., Kraaijenbrink, P. D., ... and Arnaud, Y. (2018). Ice cliff contribution to the tongue-wide ablation of Changri Nup Glacier, Nepal, central Himalaya. The Cryosphere, 12(11), 3439-3457.

Brun, F., Wagnon, P., Berthier, E., Jomelli, V., Maharjan, S. B., Shrestha, F., et al. (2019). Heterogeneous influence of glacier morphology on the mass balance variability in High Mountain Asia. J. Geophys. Res. 124, 1331–1345. doi: 10.1029/2018JF004838

Buri, P., Miles, E. S., Steiner, J. F., Ragettli, S., and Pellicciotti, F. (2021). Supraglacial Ice Cliffs Can Substantially Increase the Mass Loss of Debris-Covered Glaciers. Geophysical Research Letters, 48(6), e2020GL092150.

Carenzo, M., Pellicciotti, F., Mabillard, J., and two others et al.(2016). An enhanced temperature index model for debris-covered glaciers accounting for thickness effect. Advances in water resources, 94, 457-469.

Carey, M., Molden, O. C., Rasmussen, M. B., Jackson, M., Nolin, A. W., and Mark, B. G. (2017). Impacts of glacier recession and declining meltwater on mountain societies. Annals of the American Association of Geographers, 107(2), 350-359.

Cauvy-Fraunié, S., Condom, T., Rabatel, A., Villacis, M., Jacobsen, D., and Dangles, O. (2013). Glacial influence in tropical mountain hydrosystems evidenced by the diurnal cycle in water levels. Hydrology and Earth System Sciences, 17(12), 4803-4816.

Chand, Mohan Bahadur, and Rijan Bhakta Kayastha (2018). Study of thermal properties of supraglacial debris and degree-day factors on Lirung Glacier, Nepal. Sciences in Cold and Arid Regions 10.5 (2018): 0357-0368.

Chandel, V. S., and Ghosh, S. (2021). Components of Himalayan River Flows in a Changing Climate. Water Resources Research, 57(2), e2020WR027589.

Chen, J. L., Wilson, C. R., and Tapley, B. D. (2013). Contribution of ice sheet and mountain glacier melt to recent sea level rise. Nature Geoscience, 6(7), 549-552.

Chen, X., Long, D., Hong, Y., Zeng, C., and Yan, D. (2017). Improved modeling of snow and glacier melting by a progressive two-stage calibration strategy with GRACE and multisource data: How snow and glacier meltwater contributes to the runoff of the U pper B rahmaputra R iver basin?. Water Resources Research, 53(3), 2431-2466.

Chen, J., and Ohmura, A. (1990). On the influence of Alpine glaciers on runoff. IAHS Publ, 193, 117-125.

Chevallier, Pierre, François Delclaux, Patrick Wagnon, Luc Neppel, Yves Arnaud, Michel Esteves, Devesh Koirala, Yves Lejeune, Frédéric Hernandez, Rémi Muller, Jean-Philippe Chazarin, Jean-François Boyer, Isabelle Sacareau. 2017. Paprika - Preshine hydrology data sets in the Everest Region (Nepal). 2010-18. Data base. 2017. https://doi.org/10.23708/000521.

Church, J. A., Clark, P. U., Cazenave, A., Gregory, J. M., Jevrejeva, S., Levermann, A., ... and Unnikrishnan, A. S. (2013). Sea-level rise by 2100. Science, 342(6165), 1445-1445.

Chylek, P., Box, J. E., and Lesins, G. (2004). Global warming and the Greenland ice sheet. Climatic Change, 63(1), 201-221.

Cogley, J. G. (2009). Geodetic and direct mass-balance measurements: comparison and joint analysis. Annals of Glaciology, 50(50), 96-100.

Cogley, J. G. (2011). Present and future states of Himalaya and Karakoram glaciers. Annals of Glaciology, 52(59), 69-73.

Cogley JG (2017), Glacier mass balance. In: Richardson D, Castree N, Goodchild MF, Kobayashi A, Liu W, and Marston RA (eds.)International Encyclopedia of Geography: People, theEarth, Environment and Technology: People, the Earth, Environment and Technology, pp. 1–10. John Wiley & Sons, Ltd.https://doi.org/10.1002/9781118786352.wbieg0470.

Colgan, W., Rajaram, H., Abdalati, W., McCutchan, C., Mottram, R., Moussavi, M. S., and Grigsby, S. (2016). Glacier crevasses: Observations, models, and mass balance implications. Reviews of Geophysics, 54(1), 119-161.

Collier, E., and Immerzeel, W. W. (2015). High-resolution modeling of atmospheric dynamics in the Nepalese Himalaya. Journal of Geophysical Research: Atmospheres, 120(19), 9882–9896.

Collier, E., Nicholson, L. I., Brock, B. W., Maussion, F., Essery, R., and Bush, A. B. G. (2014). Representing moisture fluxes and phase changes in glacier debris cover using a reservoir approach. The Cryosphere, 8(4), 1429-1444.

Comeau, L. E., Pietroniro, A., and Demuth, M. N. (2009). Glacier contribution to the North and South Saskatchewan rivers. Hydrological Processes: An International Journal, 23(18), 2640-2653.

Conway, H., and Rasmussen, L. A. (2000). Summer temperature profiles within supraglacial debris on Khunibu Glacier, Nepal. Debris covered glaciers, 89-97.

Cuffey, K. M., and Paterson, W. S. B. (2010). The physics of glaciers. Academic Press.

Dangi, M. B., Chaudhary, R. P., Rijal, K., Stahl, P. D., Belbase, S., Gerow, K. G., ... and Pyakurel, B. (2018). Impacts of environmental change on agroecosystems and livelihoods in Annapurna Conservation Area, Nepal. Environmental development, 25, 59-72.

Dooge, J. C. I., Bruen, M., Parmentier, B. (1999). A simple model for estimating the sensitivity of runoff to long-term changes in precipitation without a change in vegetation. Advances in Water Resources, 23(2), 153-163.

Dee, D. P., S. M. Uppala, A. J. Simmons, P. Berrisford, P. Poli, S. Kobayashi, U. Andrae, M. A. Balmaseda, G. Balsamo, P. Bauer, P. Bechtold, A. C. M. Beljaars, L. van de Berg, J. Bidlot, N. Bormann, C. Delsol, R. Dragani, M. Fuentes, A. J. Geer, L. Haimberger, S. B. Healy, H. Hersbach, E. V. Hólm, L. Isaksen, P. Ka allberg, M. Köhler, M. Matricardi, A. P. McNally, B. M. Monge-Sanz, J.-J. Morcrette, B.-K. Park, C. Peubey, P. de Rosnay, C. Tavolato, J.-N. Thépaut, and F. Vitart (2011), The ERA-Interim reanalysis: configuration and performance of the data assimilation system, Quarterly Journal of the Royal Meteorological Society, 137, 553–597, doi: 10.1002/qj.828.

Dey, B., and Kumar, O. S. R. U. (1983). Himalayan winter snow cover area and summer monsoon rainfall over India. Journal of Geophysical Research: Oceans, 88(C9), 5471-5474.

Dhaubanjar, S., Lutz, A. F., Gernaat, D. E., Nepal, S., Smolenaars, W., Pradhananga, S., ... and Immerzeel, W. W. (2021). A systematic framework for the assessment of sustainable hydropower potential in a river basin–The case of the upper Indus. Science of the Total Environment, 786, 147142.

Drewry, D. J. (1972), A quantitative assessment of dirt-cone dynamics, Journal of Glaciology, 11, 431–446, doi: 10.1017/S0022143000022383.

Duell Jr, L. F. W. (1994). THE SENSITWITY OF NORTHERN SIERRA NEVADA STREAMFLOW TO CLIMATE CHANGE 1. JAWRA Journal of the American Water Resources Association, 30(5), 841-859.

Duan, K., Xu, B., and Wu, G. (2015). Snow accumulation variability at altitude of 7010 m a.s.l. in Muztag Ata Mountain in Pamir Plateauduring 1958–2002. Journal of Hydrology, 531(9), 912–918.

Dyurgerov, M., Meier, M. F., and Bahr, D. B. (2009). A new index of glacier area change: a tool for glacier monitoring. J. Glaciol. 55, 710–716. doi: 10.3189/002214309789471030.

Engelhardt, M., Schuler, T. V., and Andreassen, L. M. (2015). Sensitivities of glacier mass balance and runoff to climate perturbations in Norway. Annals of Glaciology, 56(70), 79-88.

Engelhardt, M., Ramanathan, A. L., Eidhammer, T., Kumar, P., Landgren, O., Mandal, A., and Rasmussen, R.(2017). Modelling 60 years of glacier mass balance and runoff for chhota shigri glacier, western himalaya, northern india. Journal of Glaciology, 63 (240), 618–628.

Evans, S. G., and Delaney, K. B. (2015). Catastrophic mass flows in the mountain glacial environment. In Snow and ice-related hazards, risks and disasters (pp. 563-606). Academic Press.

Evatt, G. W., Abrahams, I. D., Heil, M., and five others et al.(2015). Glacial melt under a porous debris layer. Journal of Glaciology, 61(229), 825-836.

Ferguson, J., and Vieli, A. (2021). Modelling steady states and the transient response of debris-covered glaciers. The Cryosphere, 15(7), 3377-3399.

Farr, T. G., Rosen, P. A., Caro, E., Crippen, R., Duren, R., Hensley, S.,... Seal, D. (2007). The shuttle radar topography mission. Reviews of geophysics, 45(2).

Finger, D. C., Hugentobler, A., Huss, M., Voinesco, A., Wernli, H. R., Fischer, D., ... and Vennemann, T. (2013). Identification of glacial meltwater

runoff in a karstic environment and its implication for present and future water availability. Hydrology and earth system sciences, 17(8), 3261-3277.

Forsythe, N., Fowler, H. J., Li, X.-F., Blenkinsop, S., and Pritchard, D. (2017). Karakoram temperature and glacial melt driven by regional atmospheric circulation variability. Nat. Clim. Change 7:664. doi: 10.1038/nclimate3361.

Foster, L. A., Brock, B. W., Cutler, M. E. J., and one other et al.(2012). A physically based method for estimating supraglacial debris thickness from thermal band remote-sensing data. Journal of Glaciology, 58(210), 677-691.

Fountain, A. G., and Tangborn, W. V. (1985). The effect of glaciers on streamflow variations. Water Resources Research, 21(4), 579-586.

Fowler, H. J., and Archer, D. R. (2006). Conflicting signals of climatic change in the upper indus basin. J. Clim. 19, 4276–4293. doi: 10.1175/JCLI3860.1.

Frei, A., et al. (2012). A review of global satellite-derived snow products. Advances in Space Research, 50(8), 1007–1029.

Friedl, M., Sulla-Menashe, D. (2019). MCD12Q1 MODIS/Terra+Aqua Land Cover Type Yearly L3 Global 500m SIN Grid V006 [Data set]. NASA EOSDIS Land Processes DAAC. Accessed 2020-09-15 from https://doi.org/10.5067/MODIS/MCD12Q1.006.

Fujita K, Takeuchi N and Seko K (1998). Glaciological observations of Yala Glacier in Langtang Valley, Nepal Himalayas, 1994 and. Bull. Glacier Res. 16, 75–8.

Fujita K, Nakazawa F and Rana B (2001). Glaciological observations on Rikha Samba Glacier in Hidden Valley, Nepal Himalayas, 1998 and 1999. Bull. Glaciol. Res. 18, 31–35.

Fujita, K. (2008). Effect of precipitation seasonality on climatic sensitivity of glacier mass balance. Earth and Planetary Science Letters, 276(1-2), 14-19.

Fujita, K., and Nuimura, T. (2011). Spatially heterogeneous wastage of Himalayan glaciers. Proceedings of the National Academy of Sciences, 108(34), 14011-14014.

Fujita, K., and Sakai, A. (2014). Modelling runoff from a Himalayan debris-covered glacier. Hydrology and Earth System Sciences, 18(7), 2679.

Fujii, Y. (1977). Field Experiment on Glacier Ablation under a Layer of Debris Cover Glaciological Expedition of Nepal, Contribution No. 33. Journal of the Japanese Society of Snow and Ice, 39(Special), 20-21.

Fyffe, C. L., Reid, T. D., Brock, B. W., Kirkbride, M. P., Diolaiuti, G., Smiraglia, C., and Diotri, F. (2014). A distributed energy-balance melt model of an alpine debris-covered glacier. Journal of Glaciology, 60(221), 587-602.

Fyffe, C. L., Brock, B. W., Kirkbride, M. P., Mair, D. W. F., Arnold, N. S., Smiraglia, C. (2015). An investigation of the influence of supraglacial debris on glacier-hydrology. Cryosphere Discuss. 9, 5373–5411. doi: 10.5194/tcd-9-5373-2015.

Fyffe, C. L., Woodget, A. S., Kirkbride, M. P., Deline, P., Westoby, M. J., and Brock, B. W. (2020). Processes at the margins of supraglacial debris cover: Quantifying dirty ice ablation and debris redistribution. Earth Surface Processes and Landforms, 45(10), 2272-2290. DOI: https://doi.org/10.1002/esp.4879

Gao, X., Ye, B., Zhang, S., Qiao, C., and Zhang, X. (2010). Glacier runoff variation and its influence on river runoff during 1961–2006 in the Tarim River Basin, China. Science China Earth Sciences, 53(6), 880-891.

Gao, H., Li, H., Duan, Z., Ren, Z., Meng, X., and Pan, X. (2018). Modelling glacier variation and its impact on water resource in the Urumqi Glacier No. 1 in Central Asia. Science of the total environment, 644, 1160-1170.

Gardelle, J., Berthier, E., Arnaud, Y. (2012). Impact of resolution and radar penetration on glacier elevation changes computed from DEM differencing. Journal of Glaciology, 58(208), 419-422.

Gardelle, J., Berthier, E., Arnaud, Y., and Kääb, A. (2013). Region-wide glacier mass balances over the Pamir-Karakoram-Himalaya during 1999–2011. The Cryosphere, 7(4), 1263-1286.

Gardner, A. S., G. Moholdt, J. G. Cogley, B. Wouters, A. A. Arendt, J. Wahr, E. Berthier, R. Hock, W. T. Pfeffer, G. Kaser, S. R. M. Ligtenberg, T. Bolch, M. J. Sharp, J. O. Hagen, M. R. van den Broeke, and F. Paul (2013), A Reconciled Estimate of Glacier Contributions to Sea Level Rise: 2003 to 2009, Science, 340, 852–857, doi: 10.1126/science.1234532.

Gelman, A.and 5 others (2014). Bayesian data analysis. 3rd Edn. Boca Raton: Taylor and Francis, ISBN 9781439840955.

Giese, A., Boone, A. and two others et al.(2020). Incorporating moisture content in surface energy balance modeling of a debris-covered glacier. The Cryosphere, 14(5), 1555-1577.

Glen, J. W. "Experiments on the deformation of ice." Journal of Glaciology 2.12 (1952): 111-114.

Gruber S (2007) A mass-conserving fast algorithm to parameterize gravitational transport and deposition using digital elevation models. Water Resour. Res., 43(6).

Hagg, W. J., Braun, L. N., Uvarov, V. N., and Makarevich, K. G. (2004). A comparison of three methods of mass-balance determination in the Tuyuksu glacier region, Tien Shan, Central Asia. Journal of Glaciology, 50(171), 505-510.

Hagg, W., C. Mayer, A. Lambrecht, and A. Helm (2008), Sub-debris melt rates on southern Inylchek Glacier, central Tian Shan, Geografiska Annaler: Series A, Physical Geography, 90(1), 55–63, doi:10.1111/j.1468-0459.2008.00333.x.

Hagg, W., Mayr, E., Mannig, and eight others et al.(2018). Future climate change and its impact on runoff generation from the debris-covered Inylchek glaciers, Central Tian Shan, Kyrgyzstan. Water, 10(11), 1513.

Hannah, D. M., and Gurnell, A. M. (2001). A conceptual, linear reservoir runoff model to investigate melt season changes in cirque glacier hydrology. Journal of hydrology, 246(1-4), 123-141.

Haidong, H., Yongjing, D., and Shiyin, L. (2006). A simple model to estimate ice ablation under a thick debris layer. Journal of Glaciology, 52(179), 528-536.

Harrison, S., Kargel, J. S., Huggel, C., Reynolds, J., Shugar, D. H., Betts, R. A., ... and Vilímek, V. (2018). Climate change and the global pattern of moraine-dammed glacial lake outburst floods. The Cryosphere, 12(4), 1195-1209.

Haritashya, U. K., Kumar, A., Singh, P. (2010). Particle size characteristics of suspended sediment transported in meltwater from the Gangotri Glacier, central Himalaya—An indicator of subglacial sediment evacuation. Geomorphology, 122(1-2), 140-152.

Hasnain, S. I., and Thayyen, R. J. (1994). Hydrograph separation of bulk melt-waters of Dokriani Bamak glacier basin, based on electrical conductivity. Current Science, 189-193.

Hasson, S., Böhner, J., and Lucarini, V. (2017). Prevailing climatic trends and runoff response from Hindukush–Karakoram–Himalaya, upper Indus Basin. Earth System Dynamics, 8(2), 337-355.

He, R., and Pang, B. (2015). Sensitivity and uncertainty analysis of the Variable Infiltration Capacity model in the upstream of Heihe River basin. Proceedings of the International Association of Hydrological Sciences, 368, 312-316.

He, Z. (2021). Sensitivities of hydrological processes to climate changes in a Central Asian glacierized basin. Frontiers in Water, 3, 46.

Herreid, S., and Pellicciotti, F. (2020). The state of rock debris covering Earth's glaciers. Nature Geoscience, 13(9), 621-627.

Hersbach, H., Bell, B., Berrisford, P., Hirahara, S., Horányi, A., Muñoz Sabater, J., ... Simmons, A. (2020). The ERA5 global reanalysis. Quarterly Journal of the Royal Meteorological Society, 146(730), 1999-2049.

Hinkel, K. M., Paetzold, F., Nelson, F. E., and one other et al.(2001). Patterns of soil temperature and moisture in the active layer and upper permafrost at Barrow, Alaska: 1993–1999. Global and Planetary Change, 29(3), 293-309.

Hock, R. (2003). Temperature index melt modelling in mountain areas. Journal of hydrology, 282(1-4), 104-115.

Hock, R., Jansson, P., and Braun, L. N. (2005). Modelling the response of mountain glacier discharge to climate warming. In Global change and mountain regions (pp. 243-252). Springer, Dordrecht.

Hock R, Rasul G, Adler C, Cáceres B, Gruber S, Hirabayashi Y, Jackson M, Kääb A, Kang S, Kutuzov S, Milner A, Molau U, Morin S, Orlove B, and Steltzer H (2019). High mountainareas. In: Pörtner H-O, Roberts DC, Masson-Delmotte V, Zhai P, Tignor M, Poloczanska E, Mintenbeck K, Alegría A, Nicolai M, Okem A, Petzold J, Rama B, and Weyer NM (eds.)IPCC Special Report on the Ocean and Cryosphere in a Changing Climate. In press [seehttps://www.ipcc.ch/srocc/cite-report/, Chapter 2].

Huang, L., Z. Li, H. Han, B. Tian, and J. Zhou (2018). Analysis of thickness changes and the associated driving factors on a debris-covered glacier in the Tienshan Mountain, Remote Sensing of Environment, 206, 63 – 71, doi: https://doi.org/10.1016/j.rse.2017.12.028.

Hubbard, B., & Glasser, N. F. (2005). Field techniques in glaciology and glacial geomorphology. John Wiley & Sons.

Hughes P (2008). Response of a Montenegro glacier to extreme summer heatwaves in 2003 and 2007. Geogr. Ann.: Ser. A, Phys. Geogr., 90(4), 259–267.

Hugonnet, R., McNabb, R., Berthier, E., Menounos, B., Nuth, C., Girod, L., ... and Kääb, A. (2021). Accelerated global glacier mass loss in the early twenty-first century. Nature, 592(7856), 726-731.

Huss, M., Hock, R. (2018). Global-scale hydrological response to future glacier mass loss. Nature Climate Change, 8(2), 135-140.

Huss, M. (2013). Density assumptions for converting geodetic glacier volume change to mass change. The Cryosphere, 7(3), 877-887.

Huss, M., and Hock, R. (2015). A new model for global glacier change and sea-level rise. Frontiers in Earth Science, 3, 54.

Huybrechts, P., H. Goelzer, I. Janssens, E. Driesschaert, T. Fichefet, H. Goosse and M.-F. Loutre, (2011). Response of the Greenland and Antarctic ice sheets to multi-millennial greenhouse warming in the Earth system model of intermediate complexity LOVECLIM, Surv. Geophy., 1–20, published online, doi: 10.1007/s10712-011-9131-5.

Immerzeel, W. W., Droogers, P., De Jong, S. M., and Bierkens, M. F. P. (2009). Large-scale monitoring of snow cover and runoff simulation in Himalayan river basins using remote sensing. Remote sensing of Environment, 113(1), 40-49.

Immerzeel, W. W., Van Beek, L. P., and Bierkens, M. F. (2010). Climate change will affect the Asian water towers. Science, 328(5984), 1382-1385.

Immerzeel, W. W., Pellicciotti, F., and Shrestha, A. B. (2012). Glaciers as a proxy to quantify the spatial distribution of precipitation in the Hunza basin. Mountain research and development, 32(1), 30-38.

Immerzeel WW, Pellicciotti F and Bierkens MFP (2013). Rising river flows throughout the twenty-first century in two Himalayan glacierized watersheds. Nature Geosci., 6(9), 742–745.

Immerzeel, W. W., Lutz, A. F., Andrade, M., Bahl, A., Biemans, H., Bolch, T., ... Emmer, A. (2020). Importance and vulnerability of the world's water towers. Nature, 577(7790), 364-369.

Irvine-Fynn, Tristram and Hubbard, Bryn. (2017). Glacier Hydrology and Runoff. DOI:10.1002/9781118786352.wbieg0709.

Isenstein, E. M., Wi, S., Ethan Yang, Y. C. (2015). Calibration of a distributed hydrologic model using streamflow and remote sensing snow data. In World Environmental and Water Resources Congress 2015 (pp. 973-982).

Jacob, T., J. Wahr, W. T. Pfeffer, and S. Swenson (2012), Recent contributions of glaciers and ice caps to sea level rise, Nature, 482(7386), 514–518, doi: 10.1038/nature10847.

Jansson, P., Hock, R., and Schneider, T. (2003). The concept of glacier storage: a review. Journal of Hydrology, 282(1-4), 116-129.

Jennings, K. S., Winchell, T. S., Livneh, B., & Molotch, N. P. (2018). Spatial variation of the rain–snow temperature threshold across the Northern Hemisphere. Nature communications, 9(1), 1-9.

Jóhannesson, T., O. Sigurdsson, T. Laumann and M. Kennett, 1995. Degree-day glacier mass-balance modelling with applications to glaciers in Iceland, Norway and Greenland, J. Glaciol., 41(138), 345–358.

Johnson, E., and Rupper, S. (2020). An examination of physical processes that trigger the albedo-feedback on glacier surfaces and implications for regional glacier mass balance across High Mountain Asia. Frontiers in Earth Science, 8, 129.

Joseph, J., Ghosh, S., Pathak, A., Sahai, A. K. (2018). Hydrologic impacts of climate change: Comparisons between hydrological parameter uncertainty and climate model uncertainty. Journal of Hydrology, 566, 1-22.

Jost, G., Moore, R. D., Menounos, B., and Wheate, R. (2012). Quantifying the contribution of glacier runoff to streamflow in the upper Columbia River Basin, Canada. Hydrology and Earth System Sciences, 16(3), 849-860. DOI: https://doi.org/10.5194/hess-16-849-2012.

Juen, M., Mayer, C., Lambrecht, and two others et al.(2014). Impact of varying debris cover thickness on ablation: a case study for Koxkar Glacier in the Tien Shan. The Cryosphere, 8(2), 377.

Kääb, A., Berthier, E., Nuth, C., Gardelle, J., and Arnaud, Y. (2012). Contrasting patterns of early twenty-first-century glacier mass change in the Himalayas. Nature, 488(7412), 495-498.

Kääb, A., D. Treichler, C. Nuth, and E. Berthier (2015), Brief Communication: Contending estimates of 2003-2008 glacier mass balance over the Pamir–Karakoram–Himalaya, The Cryosphere, 9(2),557–564, doi: 10.5194/tc-9-557-2015.

Kanda, N., Negi, H. S., Rishi, M., and Kumar, A. (2020). Performance of various gridded temperature and precipitation datasets over Northwest Himalayan Region. Environ. Res. Commun. 2 085002.

Kaser, G., and Osmaston, H. A. (2002). Tropical Glaciers. Oxford: Cambridge University Press.

Kaser, G., Fountain, A., and Jansson, P. (2003). A manual for monitoring the mass balance of mountain glaciers (p. 137). Paris: Unesco.

Kaser, G., Großhauser, M., and Marzeion, B. (2010). Contribution potential of glaciers to water availability in different climate regimes. Proceedings of the National Academy of Sciences, 107(47), 20223-20227.

Kaspari, S., Hooke, R. L., Mayewski, P. A., Kang, S., Hou, S., and Qin, D. (2008). Snow accumulation rate on Qomolangma (Mount Everest), Himalaya: synchroneity with sites across the Tibetan Plateau on 50–100 year timescales. Journal of Glaciology, 54(185), 343-352.

Kayastha RB, Ohata T and Ageta Y (1999) Application of a mass-balance model to a Himalayan glacier. J. Glaciol. 45(151), 559–567.

Kehrwald, N. M., Thompson, L. G., Tandong, Y., Mosley-Thompson, E., Schotterer, U., Alfimov, V., ... and Davis, M. E. (2008). Mass loss on Hi-

malayan glacier endangers water resources. Geophysical Research Letters, 35(22).

Khadka, D., Babel, M. S., Shrestha, S., Tripathi, N. K. (2014). Climate change impact on glacier and snow melt and runoff in Tamakoshi basin in the Hindu Kush Himalayan (HKKH) region. Journal of Hydrology, 511, 49-60.

Khan, A. A., Pant, N. C., Sarkar, A., Tandon, S. K., Thamban, M., and Mahalinganathan, K. (2017). The Himalayan cryosphere: a critical assessment and evaluation of glacial melt fraction in the Bhagirathi basin. Geoscience Frontiers, 8(1), 107-115.

King, O., Quincey, D. J., Carrivick, J. L., and Rowan, A. V.: Spatial variability in mass loss of glaciers in the Everest region, central Himalayas, between 2000 and 2015, The Cryosphere, 11, 407–426, https://doi.org/10.5194/tc-11-407-2017, 2017.

Kayastha, R. B., Takeuchi, Y., Nakawo, M., and Ageta, Y. (2000). Practical prediction of ice melting beneath various thickness of debris cover on Khumbu Glacier. Nepal, using a positive degree-day factor, IAHS-AISH P, 264, 71-81.

Kayastha, R. B., Steiner, N., Kayastha, R., Mishra, S. K., McDonald, K. (2020). Comparative study of hydrology and icemelt in three Nepal river basins using the Glacio-Hydrological Degree-Day Model (GDM) and observations from the Advanced Scatterometer (ASCAT). Frontiers in Earth Science, 7, 354.

King, O., D. J. Quincey, J. L. Carrivick, and A. V. Rowan (2017), Spatial variability in mass loss of glaciers in the Everest region, central Himalayas, between 2000 and 2015, The Cryosphere, 11(1), 407–426, doi: 10.5194/tc-11-407-2017.

Kirkbride, M. P. (2000). Ice-marginal geomorphology and Holocene expan-

sion of debris-covered Tasman Glacier. New Zealand, IAHSAISH P, 264, 211-217.

Kirkbride MP (2011). Debris-covered glaciers. In: Singh VP, Singh P, and Haritashya UK (eds.)Encyclopedia of Snow, Ice and Glaciers.Encyclopedia of Earth Sciences Series.Dordrecht: Springer.https://doi.org/10.1007/978-90-481-2642-2.

Kirkbride, M. P., and Deline, P. (2013). The formation of supraglacial debris covers by primary dispersal from transverse englacial debris bands. Earth Surface Processes and Landforms, 38(15), 1779-1792.

Klein, A. and Isacks, B., (1998). Alpine glacier geomorphological studies in the central Andesusing Landsat Thematic Mapper images.Glacial Geology and Geomorphology, rp01/1998.

Konz, M., Uhlenbrook, S., Braun, L., Shrestha, A., and Demuth, S. (2007). Implementation of a process-based catchment model in a poorly gauged, highly glacierized Himalayan headwater. Hydrology and Earth System Sciences Discussions, 11(4), 1323-1339.

Koppes, M., Rupper, S., Asay, M., and Winter-Billington, A. (2015). Sensitivity of glacier runoff projections to baseline climate data in the Indus River basin. Frontiers in Earth Science, 3, 59.

Koskinen, J. T., Pulliainen, J. T., and Hallikainen, M. T. (1997). The use of ERS-1 SAR data in snow melt monitoring. IEEE Transactions on Geoscience and Remote Sensing, 35(3), 601–610.

Kraaijenbrink, P. D. A., Bierkens, M. F. P., Lutz, A. F., Immerzeel, W. W. (2017). Impact of a global temperature rise of 1.5 degrees. Nature, 549(7671), 257-260.

Krakauer, N. Y., Lakhankar, T., and Dars, G. H. (2019). Precipitation trends over the Indus basin. Climate, 7(10), 116. DOI: https://doi.org/10.3390/cli7100116.

Kraaijenbrink, P. D., Shea, J. M., five others (2018). Mapping surface temperatures on a debris-covered glacier with an unmanned aerial vehicle. Frontiers in Earth Science, 6, 64.

Krakauer, N. Y., Lakhankar, T., and Dars, G. H. (2019). Precipitation trends over the Indus basin. Climate, 7(10), 116.

Kulkarni, A. V. (1992). Mass balance of Himalayan Glaciers using AAR and ELA methods. J. Glaciol. 38, 101–104. doi: 10.1017/s0022143000009631.

Kulkarni, A. V., Rathore, B. P., and Alex, S. (2004). Monitoring of glacial mass balance in the Baspa basin using accumulation area ratio method. Curr. Sci. 86, 185–190.

Kulkarni, A., Patwardhan, S., Kumar, K. K., Ashok, K., and Krishnan, R. (2013). Projected climate change in the Hindu Kush–Himalayan region by using the high-resolution regional climate model PRECIS. Mountain Research and Development, 33(2), 142-151.

Kulkarni, Anil V. Tejal S. Shirsat, Ashutosh Kulkarni, H.S. Negi, I.M. Bahuguna, Meloth Thamban, (2021). State of Himalayan cryosphere and implications for water security. Water Security, Volume 14, 100101, ISSN 2468-3124, https://doi.org/10.1016/j.wasec.2021.100101.

Kulp, S. A. and Strauss, B. H. New elevation data triple estimates of global vulnerability to sea-level rise and coastal flooding. Nat. Commun. 10, 4844 (2019); author correction 10, 5752 (2019).

Kumar, V., Singh, P., and Singh, V. (2007). Snow and glacier melt contribution in the Beas river at Pandoh dam, Himachal Pradesh, India. Hydrological sciences journal, 52(2), 376-388.

Kumar, A., Gokhale, A. A., Shukla, T., Dobhal, D. P. (2016). Hydroclimatic influence on particle size distribution of suspended sediments evacuated from debris-covered Chorabari Glacier, upper Mandakini catchment, central Himalaya. Geomorphology, 265, 45-67.

Kumar, V., Mehta, M., Mishra, A., and Trivedi, A. (2017). Temporal fluctuations and frontal area change of Bangni and Dunagiri glaciers from 1962 to 2013, Dhauliganga Basin, central Himalaya, India. Geomorphology, 284, 88-98.

Kumar, P., Saharwardi, M. S., Banerjee, A., Azam, M. F., Dubey, A.K., Murtugudde, R. (2019). Snowfall Variability Dictates Glacier Mass Balance Variability in Himalaya-Karakoram. Scientific reports, 9(1), 1-9.

Laha, S., Kumari, R., Singh, S., Mishra, A., Sharma, T., Banerjee, A., ... and Shankar, R. (2017). Evaluating the contribution of avalanching to the mass balance of Himalayan glaciers. Annals of Glaciology, 58(75pt2), 110-118.

Lang, H. (1986). Forecasting meltwater runoff from snow-covered areas and from glacier basins. In River flow modelling and forecasting (pp. 99-127). Springer, Dordrecht.

Laskar, A. H., Bhattacharya, S. K., Rao, D. K., Jani, R. A., and Gandhi, N. (2018). Seasonal variation in stable isotope compositions of waters from a Himalayan river: Estimation of glacier melt contribution. Hydrological Processes, 32(26), 3866-3880.

Leclercq, P. W., and Oerlemans, J. (2012). Global and hemispheric temperature reconstruction from glacier length fluctuations. Climate Dynamics, 38(5), 1065-1079.

Lejeune, Y., Bertrand, J. M., Wagnon, P., and one other et al.(2013). A physically based model of the year-round surface energy and mass balance of debris-covered glaciers. Journal of Glaciology, 59(214), 327-344.

Lemke, P., J. Ren, R.B. Alley, I. Allison, J. Carrasco, G. Flato, Y. Fujii, G. Kaser,P. Mote, R.H. Thomas and T. Zhang, 2007. Observations: Changes in Snow, Ice and Frozen Ground, In Solomon, S. and 7 others, eds., Climate Change 2007: The Physical Science Basis. Contribution of WGI to the Fourth Assessment Report of the IPCC , Cambridge Univ. Press, Cambridge, 337–383.

Li, H., Xu, C. Y., Beldring, S., Tallaksen, L. M., Jain, S. K. (2016). Water resources under climate change in Himalayan basins. Water Resources Management, 30(2), 843-859.

Liang, X., Lettenmaier, D. P., Wood, E. F., and Burges, S. J. (1994). A simple hydrologically based model of land surface water and energy fluxes for general circulation models. Journal of Geophysical Research: Atmospheres, 99(D7), 14415-14428.

Liang, X., Wood, E. F., Lettenmaier, D. P. (1996). Surface soil moisture parameterization of the VIC-2L model: Evaluation and modification. Global and Planetary Change, 13(1-4), 195-206.

Llibutry, L. (1998). "Glaciers of the dry Andes," in Satellite Image Atlas of Glaciers of the World: South America, eds R. S. J. Williams and J. G. Ferrigno (Reston, VA: United States Geological Survey).

Longuevergne, L., C. R. Wilson, B. R. Scanlon, and J. F. Crétaux (2013), GRACE water storage estimates for the Middle East and other regions with significant reservoir and lake storage, Hydrologyand Earth System Sciences, 17(12), 4817–4830, doi: 10.5194/hess-17-4817-2013.

Lohmann, D., Raschke, E., Nijssen, B., Lettenmaier, D. P. (1998). Regional scale hydrology: I. Formulation of the VIC-2L model coupled to a routing model. Hydrological sciences journal, 43(1), 131-141.

Luo, Y., Wang, X., Piao, S., Sun, L., Ciais, P., Zhang, Y., ... and He, C. (2018). Contrasting streamflow regimes induced by melting glaciers across the Tien Shan–Pamir–North Karakoram. Scientific reports, 8(1), 1-9.

Lutz, A. F., Immerzeel, W. W., Shrestha, A. B., and Bierkens, M. F. P. (2014). Consistent increase in High Asia's runoff due to increasing glacier melt and precipitation. Nature Climate Change, 4(7), 587-592.

Lutz, A. F., Immerzeel, W. W., Kraaijenbrink, P. D., Shrestha, A. B., and Bierkens, M. F. (2016). Climate change impacts on the upper Indus hydrology: sources, shifts and extremes. PloS one, 11(11), e0165630.

Lythe, M.B., D.G. Vaughan and the BEDMAP Group, (2001). BEDMAP: a new ice thickness and subglacial topographic model of Antarctica, J. Geophys. Res., 106(B6),11335–11351.

MacDonald, M. K., Pomeroy, J. W., and Pietroniro, A. (2010). On the importance of sublimation to an alpine snow mass balance in the Canadian Rocky Mountains. Hydrology and Earth System Sciences, 14(7), 1401-1415.

MacDougall, A. H., Wheler, B. A., and Flowers, G. E. (2011). A preliminary assessment of glacier melt-model parameter sensitivity and transferability in a dry subarctic environment. The Cryosphere, 5(4), 1011.

Mark, B. G., and Seltzer, G. O. (2003). Tropical glacier meltwater contribution to stream discharge: a case study in the Cordillera Blanca, Peru. Journal of Glaciology, 49(165), 271-281.

Mark, B. G., McKenzie, J. M., and Gomez, J. (2005). Hydrochemical evaluation of changing glacier meltwater contribution to stream discharge: Callejon de Huaylas, Peru/Evaluation hydrochimique de la contribution évolutive de la fonte glaciaire à l'écoulement fluvial: Callejon de Huaylas, Pérou. Hydrological Sciences Journal, 50(6).

Marzeion, B., Cogley, J. G., Richter, K. and Parkes, D. Attribution of global glacier mass loss to anthropogenic and natural causes. Science 345, 919–921 (2014).

Matsuo, K., and K. Heki (2010), Time-variable ice loss in Asian high mountains from satellite gravimetry, Earth and Planetary Science Letters, 290, 30–36, doi: 10.1016/j.epsl.2009.11.053.

Maskey, S., Uhlenbrook, S., and Ojha, S. (2011). An analysis of snow cover changes in the Himalayan region using MODIS snow products and in-situ temperature data. Climatic Change, 108(1-2), 391.

Mattson, L. E., Gardner, J. S., and Young, G. J. (1993). Ablation on debris covered glaciers: An example from the Rakhiot Glacier, Punjab, Himalaya,

Snow and Glacier Hydrology. International Association of Hydrological Sciences Publication, 218, 289–296.

Maurer, J. M., Schaefer, J. M., Rupper, S., Corley, A. (2019). Acceleration of ice loss across the Himalayas over the past 40 years. Science advances, 5(6), eaav7266.

Maussion, F., D. Scherer, T. Mölg, E. Collier, J. Curio, and R. Finkelnburg (2014), Precipitation Seasonality and Variability over the Tibetan Plateau as Resolved by the High Asia Reanalysis, Journal of Climate, 27(5), 1910–1927, doi: 10.1175/JCLI-D-13-00282.1.

Meier, M. F., Dyurgerov, M. B., Rick, U. K., O'neel, S., Pfeffer, W. T., Anderson, R. S., ... and Glazovsky, A. F. (2007). Glaciers dominate eustatic sea-level rise in the 21st century. Science, 317(5841), 1064-1067.

Ménégoz, M., H. Gallée, and H. W. Jacobi (2013), Precipitation and snow cover in the Himalaya: from reanalysis to regional climate simulations, Hydrology and Earth System Sciences, 17, 3921–3936, doi: 10.5194/hess-17-3921-2013.

McFadden, E. M., Ramage, J., and Rodbell, D. T. (2011). Landsat TM and ETM+ derived snowline altitudes in the Cordillera Huayhuash and Cordillera Raura, Peru, 1986–2005. The Cryosphere, 5(2), 419-430.

Meier, M.F. and Post, A.S., (1962). Recent variations in mass net budgets of glaciers in westernNorth America. International Association of Scientific Hydrology Publication, 58 (Symposium at Obergurgl 1962 - Variations of Glaciers), 63–77.

Mihalcea, C., Mayer, C., Diolaiuti, G., and three others at al.(2006). Ice ablation and meteorological conditions on the debris-covered area of Baltoro glacier, Karakoram, Pakistan. Annals of Glaciology, 43(1), 292-300.

Mihalcea, C., Mayer, C., Diolaiuti, G., and five others et al.(2008). Spatial distribution of debris thickness and melting from remote-sensing and me-

teorological data, at debris-covered Baltoro glacier, Karakoram, Pakistan. Annals of Glaciology, 48, 49-57.

Miles, E. S., Willis, I., Buri, P., Steiner, J. F., Arnold, N. S., and Pellicciotti, F. (2018). Surface pond energy absorption across four Himalayan glaciers accounts for 1/8 of total catchment ice loss. Geophysical research letters, 45(19), 10-464.

Miles, K. E., Hubbard, B., Quincey, D. J., Miles, E. S., Irvine-Fynn, T. D., and Rowan, A. V. (2019). Surface and subsurface hydrology of debris-covered Khumbu Glacier, Nepal, revealed by dye tracing. Earth and Planetary Science Letters, 513, 176-186.

Miller, J. D., Immerzeel, W. W., and Rees, G. (2012). Climate change impacts on glacier hydrology and river discharge in the Hindu Kush–Himalayas. Mountain Research and Development, 32(4), 461-468.

Mimeau, L., Esteves, M., Zin, I., Jacobi, H. W., Brun, F., Wagnon, P., and Arnaud, Y. (2018). Quantification of different flow components in a high-altitude glacierized catchment (Dudh Koshi, Nepalese Himalaya). Hydrol. Earth Syst. Sci. Discuss.

Mölg, T., Maussion, F., Yang, W., Scherer, D. (2012). The footprint of Asian monsoon dynamics in the mass and energy balance of a Tibetan glacier. The Cryosphere, 6(6), 1445.

Mukherjee, K., Bhattacharya, A., Pieczonka, T., Ghosh, S., Bolch, T. (2018). Glacier mass budget and climate reanalysis data indicate a climatic shift around 2000 in Lahaul-Spiti, western Himalaya. Climatic change, 148(1-2), 219-233.

Mukhopadhyay, B. & Khan, A. Rising river flows and glacial mass balance in central Karakoram. J. Hydrol. 513, 192-203 (2014).

Nagai, H., Fujita, K., Nuimura, T., and Sakai, A. (2013). Southwest-facing slopes control the formation of debris-covered glaciers in the Bhutan Himalaya. The Cryosphere, 7(4), 1303-1314.

Nachtergaele, F., van Velthuizen, H., Verelst, L., Batjes, N. H., Dijkshoorn, K., van Engelen, V. W. P., ... Montanarela, L. (2010). The harmonized world soil database. In Proceedings of the 19th World Congress of Soil Science, Soil Solutions for a Changing World, Brisbane, Australia, 1-6 August 2010 (pp. 34-37).

Nainwal, H. C., Negi, B. D. S., Chaudhary, M., Sajwan, K. S., and Gaurav, A. (2008). Temporal changes in rate of recession: Evidences from Satopanth and Bhagirath Kharak glaciers, Uttarakhand, using Total Station Survey. Current Science, 653-660.

Nainwal, H. C., Banerjee, A., Shankar, R., Semwal, P., and Sharma, T. (2016). Shrinkage of Satopanth and Bhagirath Kharak glaciers, India, from 1936 to 2013. Annals of glaciology, 57(71), 131-139.

Naito, N., Nakawo, M., Kadota, T., and one other et al.(2000). Numerical simulation of recent shrinkage of Khumbu Glacier, Nepal Himalayas. In Debris-covered Glaciers: Proceedings of an International Workshop Held at the University of Washington in Seattle, Washington, USA, 13-15 September 2000 (No. 264, p. 245). IAHS.

Nakawo, M., and G. J. Young (1981), Field experiments to determine the effect of a debris layer on ablation of glacier ice, Annals of Glaciology, 2, 85–91, doi: 10.3189/172756481794352432.

Nakawo, M., and Young, G. J. (1982). Estimate of glacier ablation under a debris layer from surface temperature and meteorological variables. Journal of Glaciology, 28(98), 29-34.

Nakawo, M., and Rana, B. (1999). Estimate of ablation rate of glacier ice under a supraglacial debris layer. Geografiska Annaler: Series A, Physical Geography, 81(4), 695-701.

Nepal, S. (2016). Impacts of climate change on the hydrological regime of the Koshi river basin in the Himalayan region. Journal of Hydro-Environment Research, 10, 76-89.

Neckel, N., J. Kropáček, T. Bolch, and V. Hochschild (2014), Glacier mass changes on the Tibetan Plateau 2003–2009 derived from ICESat laser altimetry measurements, Environmental Research Letters, 9(1), 014,009.

Nicholson, L., and Benn, D. I. (2006). Calculating ice melt beneath a debris layer using meteorological data. Journal of Glaciology, 52(178), 463-470.

Nicholson, L., and Benn, D. I. (2013). Properties of natural supraglacial debris in relation to modelling sub-debris ice ablation. Earth Surface Processes and Landforms, 38(5), 490-501.

Nicholson, L. I., McCarthy, M., Pritchard, H. D., and one other et al.(2018). Supraglacial debris thickness variability: impact on ablation and relation to terrain properties.

Nie, Y., Sheng, Y., Liu, Q., Liu, L., Liu, S., Zhang, Y., and Song, C. (2017). A regional-scale assessment of Himalayan glacial lake changes using satellite observations from 1990 to 2015. Remote Sensing of Environment, 189, 1-13.

Nie, Y., Pritchard, H. D., Liu, Q., Hennig, T., Wang, W., Wang, X., ... and Chen, X. (2021). Glacial change and hydrological implications in the Himalaya and Karakoram. Nature Reviews Earth & Environment, 2(2), 91-106.

Nuimura, T., Fujita, K., Yamaguchi, S., Sharma, R. R. (2012). Elevation changes of glaciers revealed by multitemporal digital elevation models calibrated by GPS survey in the Khumbu region, Nepal Himalaya, 1992-2008. Journal of Glaciology, 58(210), 648-656.

Oerlemans, J., and Hoogendoorn, N. C. (1989). Mass-balance gradients and climatic change. Journal of Glaciology, 35(121), 399-405.

Oerlemans, J. (2001). Glaciers and climate change. CRC Press.

Oerlemans, J. (2005). Extracting a climate signal from 169 glacier records. science, 308(5722), 675-677.

Oerlemans, J. (2010). The microclimate of valley glaciers (pp. 1-138). Igitur, Utrecht Publishing & Archiving Services.

Ohmura, A. (2001). Physical basis for the temperature-based melt-index method. Journal of applied Meteorology, 40(4), 753-761.

Ohmura, A., 2004. Cryosphere during the twentieth century, In Sparks, R.S.J. and C.J. Hawkesworth, eds., The state of the planet: Frontiers and challenges in geophysics, Geophysical monograph 150, 239–257.

Oke, T. R. (2002). Boundary layer climates. Routledge.

Osmaston, H. A. (2005). Estimates of glacier equilibrium line altitudes by the area×altitude, the area×altitude balance ratio and the area×altitude balance index methods and their validation. Quat. Int. 138-139, 22–31. doi: 10.1016/j.quaint.2005.02.004.

Östrem, G. (1959). Ice melting under a thin layer of moraine, and the existence of ice cores in moraine ridges. Geografiska Annaler, 41(4), 228-230.

Ostrem, G., 1975. ERTS data in glaciology – an effort to monitor glacier mass balance forsatellite imagery.Journal of Glaciology, 15 (73), 403–415.

Østrem, G. and Brugman, M.: Glacier mass-balance measurements: A manual for field and office work, NHRI Science Report, Saskatoon, Canada, 224 pp., 1991.

Pandey, P., Venkataraman, G., and Shukla, S. P. (2011, July). Study of retreat of Hamtah glacier, Indian Himalaya, using remote sensing technique. In 2011 IEEE International Geoscience and Remote Sensing Symposium (pp. 3194-3197). IEEE.

Pandey, P., Venkataraman, G. (2013). Changes in the glaciers of Chandra–Bhaga basin, Himachal Himalaya, India, between 1980 and 2010 measured using remote sensing. International Journal of Remote Sensing, 34(15), 5584-5597.

Pandey, P., Kulkarni, A. V., and Venkataraman, G. (2013). Remote sensing study of snowline altitude at the end of melting season, Chandra-Bhaga basin, Himachal Pradesh, 1980–2007. Geocarto International, 28(4), 311-322.

Parkes, D., and Marzeion, B. (2018). Twentieth-century contribution to sea-level rise from uncharted glaciers. Nature, 563(7732), 551-554.

Pellicciotti, F., Brock, B., Strasser, and three others et al.(2005). An enhanced temperature-index glacier melt model including the shortwave radiation balance: development and testing for Haut Glacier d'Arolla, Switzerland. Journal of Glaciology, 51(175), 573-587.

Pellicciotti, F., Buergi, C., Immerzeel, W. W., Konz, M., Shrestha,A. B. (2012). Challenges and uncertainties in hydrological modeling of remote Hindu Kush–Karakoram–Himalayan (HKKH) basins: suggestions for calibration strategies. Mountain Research and Development, 32(1), 39-50.

Pfeffer, W. T., Meier, M. F., and Illangasekare, T. H. (1991). Retention of Greenland runoff by refreezing: implications for projected future sea level change. Journal of Geophysical Research: Oceans, 96(C12), 22117-22124.

Pfeffer, W. T., Tad Pfeffer, W., Arendt, A. A., Bliss, A., Bolch, T., Graham Cogley,J., et al. (2014). The randolph glacier inventory: a globally complete inventoryof glaciers.J. Glaciol.60, 537–552. doi: 10.3189/2014JoG13J176.

Pokhrel, B. K., Chevallier, P., Andreassian, V., Tahir, A. A., Arnaud, Y., Neppel, L., ... Budhathoki, K. P. (2014). Comparison of two snowmelt modelling approaches in the Dudh Koshi basin (eastern Himalayas, Nepal). Hydrological sciences journal, 59(8), 1507-1518.

Porter, S.C., (1975). Equilibrium-line altitudes of late Quaternary glaciers in the Southern Alps,New Zealand.Quaternary Research, 5, 27–47.

Pramanik, A., Van Pelt, W., Kohler, J., and Schuler, T. V. (2018). Simulating climatic mass balance, seasonal snow development and associated

freshwater runoff in the Kongsfjord basin, Svalbard (1980–2016). Journal of Glaciology, 64(248), 943-956.

Pratap, B., Sharma, P., Patel, L., Singh, A. T., Gaddam, V. K., Oulkar, S.,Thamban, M. (2019). Reconciling High Glacier Surface Melting in Summer with Air Temperature in the Semi-Arid Zone of Western Himalaya. Water, 813 11(8), 1561.

Pritchard, H. D. (2019). Asia's shrinking glaciers protect large populations from drought stress. Nature, 569(7758), 649-654.

Qiu, J., 2008. The Third Pole. Nature 454, 393–396.

Quincey, D. J., A. Luckman, and D. Benn (2009), Quantification of Everest region glacier velocities between 1992 and 2002, using satellite radar interferometry and feature tracking, Journal of Glaciology, 55, 596–606, doi: 10.3189/002214309789470987.

Quincey, D. J., Copland, L., Mayer, C., Bishop, M., Luckman, A., and Belò, M. (2009). Ice velocity and climate variations for Baltoro Glacier, Pakistan. Journal of Glaciology, 55(194), 1061-1071.

Racoviteanu, A. E., Armstrong, R., and Williams, M. W. (2013). Evaluation of an ice ablation model to estimate the contribution of melting glacier ice to annual discharge in the nepal himalaya. Water Resources Research, 49 (9), 5117–5133.

Racoviteanu, A. E., Rittger, K., and Armstrong, R. (2019). An automated approach for estimating snowline altitudes in the Karakoram and eastern Himalaya from remote sensing. Frontiers in Earth Science, 7, 220.

Radić, V. and R. Hock, (2010). Regional and global volumes of glaciers derived from statistical upscaling of glacier inventory data, J. Geophys. Res., 155, F01010.

Radić, V. & Hock, R. Glaciers in the Earth's hydrological cycle: assessments of glacier mass and runoff changes on global and regional scales. Surv. Geophys. 35, 813–837 (2014).

Raina VK, Kaul MK and Singh S (1977) Mass-balance studies of Gara Glacier. J. Glaciol. 18(80), 415–423.

Rankl, M., and Braun, M. (2016). Glacier elevation and mass changes over the central Karakoram region estimated from TanDEM-X and SRTM/X-SAR digital elevation models. Ann. Glaciol. 57, 273–281. doi: 10.3189/2016AoG71A024.

Ramillien, G., J. S. Famiglietti, and J. Wahr (2008), Detection of Continental Hydrology and Glaciology Signals from GRACE: A Review, Surveys in Geophysics, 29(4), 361–374, doi: 10.1007/ s10712-008-9048-9.

Ramanathan, A. L. (2011). Status Report on Chhota Shigri Glacier (Himachal Pradesh) Status Report on Chhota Shigri Glacier (Himachal Pradesh). Sci. Eng. Res. Counc. Dep. Sci. Technol. Gov. India, 1-89.

Rasul, G. (2014). Food, water, and energy security in South Asia: A nexus perspective from the Hindu Kush Himalayan region. Environmental Science & Policy, 39, 35-48.

Rasul, G., and Molden, D. (2019). The global social and economic consequences of mountain cryospheric change. Frontiers in Environmental Science, 7, 91.

Ragettli, S., Immerzeel, W. W., Pellicciotti, F. (2016). Contrasting climate change impact on river flows from high-altitude catchments in the Himalayan and Andes Mountains. Proceedings of the National Academy of Sciences, 113(33), 9222-9227.

Rai, S. P., Singh, D., Jacob, N., Rawat, Y. S., and Arora, M. (2019). Identifying contribution of snowmelt and glacier melt to the Bhagirathi River (Upper Ganga) near snout of the Gangotri Glacier using environmental isotopes. Catena, 173, 339-351.

Rango, A., Salomonson, V. V., and Foster, J. L. (1977). Seasonal streamflow estimation in the Himalayan region employing meteorological satellite snow cover observations. Water Resources Research, 13(1), 109-112.

Rees, H. G., and Collins, D. N. (2006). Regional differences in response of flow in glacier-fed Himalayan rivers to climatic warming. Hydrological Processes: An International Journal, 20(10), 2157-2169.

Reid, T. D., Carenzo, M., Pellicciotti, F., and one other et al.(2012). Including debris cover effects in a distributed model of glacier ablation. Journal of Geophysical Research: Atmospheres, 117(D18).

Reid, T. D., and Brock, B. W. (2014). Assessing ice-cliff backwasting and its contribution to total ablation of debris-covered Miage glacier, Mont Blanc massif, Italy. Journal of Glaciology, 60(219), 3-13.

Reynolds, J. M. (1992). The identification and mitigation of glacier-related hazards: examples from the Cordillera Blanca, Peru. In Geohazards (pp. 143-157). Springer, Dordrecht.

Reynolds, J. M. (2000). On the formation of supraglacial lakes on debris-covered glaciers. IAHS publication, 153-164.

RGI Consortium (2017), Randolph glacier inventory—A dataset of global glacier outlines: Version 6.0: Technical Report, Global Land Ice Measurements from Space, Colorado, USA:Digital Media.https://doi.org/10.7265/N5-RGI-60.

Richardson, S. D., and Reynolds, J. M. (2000). An overview of glacial hazards in the Himalayas. Quaternary International, 65, 31-47.

Roberts, M. J. (2005). Jökulhlaups: a reassessment of floodwater flow through glaciers. Reviews of Geophysics, 43(1).

Rodell, M., P.R. Houser, U. Jambor, J. Gottschalck, K. Mitchell, C.-J. Meng, K. Arsenault, B. Cosgrove, J. Radakovich, M. Bosilovich, J.K. Entin, J.P. Walker, D. Lohmann, and D. Toll, (2004). The Global Land Data Assimilation System, Bull. Amer. Meteor. Soc., 85(3), 381-394.

Roe, G. H., Baker, M. B., and Herla, F. (2017). Centennial glacier retreat as categorical evidence of regional climate change. Nature Geoscience, 10(2), 95-99.

Rohrer, M., Salzmann, N., Stoffel, M., and Kulkarni, A. V. (2013). Missing (in-situ) snow cover data hampers climate change and runoff studies in the Greater Himalayas. Science of the Total Environment, 468, S60-S70.

Rounce, D. R., and McKinney, D. C. (2014). Debris thickness of glaciers in the Everest area (Nepal Himalaya) derived from satellite imagery using a nonlinear energy balance model. The Cryosphere, 8(4), 1317-1329.

Rounce, D. R., Quincey, D. J., and McKinney, D. C. (2015). Debris-covered energy balance model for Imja-Lhotse Shar Glacier in the Everest region of Nepal. Cryosph, 9, 3503-3540.

Rounce, D. R., McKinney, D. C., Lala, J. M., Byers, A. C., and Watson, C. S. (2016). A new remote hazard and risk assessment framework for glacial lakes in the Nepal Himalaya. Hydrology and Earth System Sciences, 20(9), 3455-3475.

Rounce, D. R., Hock, R., and Shean, D. E. (2020). Glacier mass change in High Mountain Asia through 2100 using the open-source python glacier evolution model (PyGEM). Frontiers in Earth Science, 7, 331.

Rounce, D. R., Hock, R., McNabb, R. W., Millan, R., Sommer, C., Braun, M. H., ... and Shean, D. E. (2021). Distributed global debris thickness estimates reveal debris significantly impacts glacier mass balance. Geophysical research letters, 48(8), e2020GL091311.

Rowan, A. V., Egholm, D. L., Quincey, D. J., and one other et al.(2015). Modelling the feedbacks between mass balance, ice flow and debris transport to predict the response to climate change of debris-covered glaciers in the Himalaya. Earth and Planetary Science Letters, 430, 427-438.

Roberts, G. O., Gelman, A., and Gilks, W. R. (1997). Weak convergence and optimal scaling of random walk Metropolis algorithms. The annals of applied probability, 7(1), 110-120.

Rott, H., Müller, F., Nagler, T., and Floricioiu, D. (2011). The imbalance of glaciers after disintegration of Larsen-B ice shelf, Antarctic Peninsula. The Cryosphere, 5(1), 125-134.

Rowan, A. V. (2017), The 'Little Ice Age' in the Himalaya: A review of glacier advance driven by Northern Hemisphere temperature change, The Holocene, 27, 292–308, doi: 10.1177/0959683616658530.

Rowan, A. V., Nicholson, L. I., Quincey, D. J., Gibson, M. J., Irvine-Fynn, T. D., Watson, C. S., ... and Glasser, N. F. (2021). Seasonally stable temperature gradients through supraglacial debris in the Everest region of Nepal, Central Himalaya. Journal of Glaciology, 67(261), 170-181.

Rupper, S., and Roe, G. (2008). Glacier changes and regional climate: a mass and energy balance approach. Journal of Climate, 21(20), 5384-5401.

Sabin T.P. et al. (2020) Climate Change Over the Himalayas. In: Krishnan R., Sanjay J., Gnanaseelan C., Mujumdar M., Kulkarni A., Chakraborty S. (eds) Assessment of Climate Change over the Indian Region. Springer, Singapore. https://doi.org/10.1007/978-981-15-4327-2.

Salerno, F., N. Guyennon, S. Thakuri, G. Viviano, E. Romano, E. Vuillermoz, P. Cristofanelli, P. Stocchi, G. Agrillo, Y. Ma, and G. Tartari (2015), Weak precipitation, warm winters and springs impact glaciers of south slopes of Mt. Everest (central Himalaya) in the last 2 decades (1994-2013), The Cryosphere, 9, 1229–1247, doi: 10.5194/tc-9-1229-2015.

Sanjay J, Krishnan R, Shrestha AB, Rajbhandari R, Ren GY, (2017). Downscaled climate change projections for the Hindu Kush Himalayan region using CORDEX South Asia regional climate models. Adv Clim Change Res 8(3):185–198. https://doi.org/10.1016/j.accre.2017.08.003.

Savéan, M., Delclaux, F., Chevallier, P., Wagnon, P., Gonga-Saholiariliva, N., Sharma, R., . . . Arnaud, Y. (2015). Water budget on the dudh koshi river (nepal): uncertainties on precipitation. Journal of Hydrology, 531 , 850–862.

Sakai, A., Takeuchi, N., Fujita, K., and Nakawo, M. (2000). Role of supraglacial ponds in the ablation process of a debris-covered glacier in the Nepal Himalayas. IAHS PUBLICATION, 119-132.

Sakai, A., Nakawo, M., and Fujita, K. (2002). Distribution characteristics and energy balance of ice cliffs on debris-covered glaciers, Nepal Himalaya. Arctic, Antarctic, and Alpine Research, 34(1), 12-19.

Sakai, A., and Fujita, K. (2010). Formation conditions of supraglacial lakes on debris-covered glaciers in the Himalaya. Journal of Glaciology, 56(195), 177-181.

Sakai, A., et al. (2015). Climate regime of Asian glaciers revealed by GAMDAM glacier inventory. The Cryosphere, 9(3), 865–880.

Sakai, A., and Fujita, K. (2017). Contrasting glacier responses to recent climate change in high-mountain Asia. Scientific reports, 7(1), 1-8.

Schaffer, N., MacDonell, S., Réveillet, M., Yáñez, E., and Valois, R. (2019). Rock glaciers as a water resource in a changing climate in the semiarid Chilean Andes. Regional Environmental Change, 1-17.

Schellnhuber, H.J., 1999. 'Earth system' analysis and the second Copernican revolution,Nature, 402, C19–C23.

Schaner, N., Voisin, N., Nijssen, B., and Lettenmaier, D. P. (2012). The contribution of glacier melt to streamflow. Environmental Research Letters, 7(3), 034029.

Scherler, D., Leprince, S., and Strecker, M. R. (2008). Glacier-surface velocities in alpine terrain from optical satellite imagery—Accuracy improvement and quality assessment. Remote Sensing of Environment, 112(10), 3806-3819.

Scherler, Dirk, Hendrik Wulf, and Noel Gorelick (2018). Global Assessment of Supraglacial Debris-Cover Extents. Geophysical Research Letters 45.21 (2018): 11-798.

Schauwecker, S., Rohrer, M., Huggel, C., and five others et al.(2015). Remotely sensed debris thickness mapping of Bara Shigri glacier, Indian Himalaya. Journal of Glaciology, 61(228), 675-688.

Spatially variable response of Himalayan glaciers to climate change affected by debris cover. Nature Geosci.,4(3), 156159(doi:10.1038/ngeo1068).

Scherler, D., Bookhagen, B., and Strecker, M. R. (2011). Hillslope-glacier coupling: The interplay of topography and glacial dynamics in High Asia. Journal of Geophysical Research: Earth Surface, 116(F2).

Schmittner, A., M. Yoshimori and A.J. Weaver, (2002). Instability of glacial climate in a model of the Ocean-Atmosphere-Cryosphere system, Science, 295(5559), 1489–1493.

Schweizer, J. (1999). Review of dry snow slab avalanche release. Cold Regions Science and Technology, 30(1-3), 43-57.

Schweizer, J., Bruce Jamieson, J., and Schneebeli, M. (2003). Snow avalanche formation. Reviews of Geophysics, 41(4).

Selley, H. L., Hogg, A. E., Cornford, S., Dutrieux, P., Shepherd, A., Wuite, J., ... and Kim, T. W. (2021). Widespread increase in dynamic imbalance in the Getz region of Antarctica from 1994 to 2018. Nature communications, 12(1), 1-10.

Shea, J. M., and Immerzeel, W. W. (2016). An assessment of basin-scale glaciological and hydrological sensitivities in the Hindu Kush–Himalaya. Annals of Glaciology, 57(71), 308-318.

Shean, D. E., Bhushan, S., Montesano, P., Rounce, D. R., Arendt, A., and Osmanoglu, B. (2020). A systematic, regional assessment of high mountain Asia glacier mass balance. Frontiers in Earth Science, 7, 363.

Sherpa, S. F., Wagnon, P., Brun, F., Berthier, E., Vincent, C., Lejeune, Y., ... Sinisalo, A. (2017). Contrasted surface mass balances of debris-free

glaciers observed between the southern and the inner parts of the Everest region (2007–15). Journal of Glaciology, 63(240), 637-651.

Shepherd, A., and Wingham, D. (2007). Recent sea-level contributions of the Antarctic and Greenland ice sheets. science, 315(5818), 1529-1532.

Shukla, S. P., Mishra, R., and Chitranshi, A. (2015). Dynamics of Hamtah Glacier, Lahaul & Spiti district, Himachal Pradesh. J. Ind. Geophys. Union, 19(4), 414-421.

Simons, G. W. H., Bastiaanssen, W. G. M., Cheema, M. J. M., Ahmad, B., Immerzeel, W. W. (2020). A novel method to quantify consumed fractions and non-consumptive use of irrigation water: Application to the Indus Basin Irrigation System of Pakistan. Agricultural Water Management, 236, 106174.

Shah, S. S., Banerjee, A., Nainwal, H. C., and one other et al.(2019). Estimation of the total sub-debris ablation from point-scale ablation data on a debris-covered glacier. Journal of Glaciology, 65(253), 759-769.

Shrestha AB, Wake CP, Mayewski PA and Dibb JE (1999) Maximumtemperature trends in the Himalaya and its vicinity: an analysisbased on temperature records from Nepal for the period 1971–94.J. Clim.,12(9), 2775–2786.

Shugar, D. H., Jacquemart, M., Shean, D., Bhushan, S., Upadhyay, K., Sattar, A., ... and Westoby, M. J. (2021). A massive rock and ice avalanche caused the 2021 disaster at Chamoli, Indian Himalaya. Science.

Singh, P., and Kumar, N. (1997). Effect of orography on precipitation in the western Himalayan region. Journal of Hydrology, 199(1-2), 183-206.

Singh, P., Kumar, N., Arora, M. (2000). Degree–day factors for snow and ice for Dokriani Glacier, Garhwal Himalayas. Journal of Hydrology, 235(1-2), 1-11.

Singh, P., and Bengtsson, L. (2005). Impact of warmer climate on melt and evaporation for the rainfed, snowfed and glacierfed basins in the Himalayan region. Journal of Hydrology, 300(1-4), 140-154.

Singh, P., and Jain, S. K. (2002). Snow and glacier melt in the Satluj River at Bhakra Dam in the western Himalayan region. Hydrological sciences journal, 47(1), 93-106.

Singh, P., and Jain, S. K. (2003). Modelling of streamflow and its components for a large Himalayan basin with predominant snowmelt yields. Hydrological sciences journal, 48(2), 257-276.

Singh, P., Kumar, N., Arora, M. (2000). Degree–day factors for snow and ice for Dokriani Glacier, Garhwal Himalayas. Journal of Hydrology, 235(1-2), 1-11.

Singh, P., Haritashya, U. K., Ramasastri, K. S., and Kumar, N. (2005). Diurnal variations in discharge and suspended sediment concentration, including runoff-delaying characteristics, of the Gangotri Glacier in the Garhwal Himalayas. Hydrological Processes: An International Journal, 19(7), 1445-1457

Singh, A. T., Rahaman, W., Sharma, P., Laluraj, C., Patel, L. K., Pratap, B., . . .Thamban, M. (2019). Moisture sources for precipitation and hydrograph components of the sutri dhaka glacier basin, western himalayas. Water , 11 (11), 2242.

Singh, A. T., Sharma, P., Sharma, C., Laluraj, C. M., Patel, L., Pratap, B., ...Thamban, M. (2020). Water discharge and suspended sediment dynamics in the Chandra River, Western Himalaya. Journal of Earth System Science, 832 129(1), 1-15.

Slingerland, Rudy, and Lee Kump (2011). Mathematical Modeling of Earth's Dynamical Systems: A Primer. Princeton University Press, 2011.

Small, R. J., M. J. Clark, and T. J. P. Cawse (1979), The formation of medial moraines on Alpine glaciers, Journal of Glaciology, 22, 43–52, doi: 10.1017/S0022143000014040.

Smith, T., Bookhagen, B. (2018). Changes in seasonal snow water equivalent distribution in High Mountain Asia (1987 to 2009). Science advances, 4(1), e1701550.

Soncini, A., Bocchiola, D., Confortola, G., Minora, U., Vuillermoz, E., Salerno, F., ... Diolaiuti, G. (2016). Future hydrological regimes and glacier cover in the Everest region: The case study of the upper Dudh Koshi basin. Science of the Total Environment, 565, 1084-1101.

Sorg A, Bolch T, Stoffel M, Solomina O and Beniston M (2012), Climate change impacts on glaciers and runoff in Tien Shan (Central Asia). Nature Climate Change, 2(10), 725–731.

Steiner, J. F., Pellicciotti, F., Buri, P., Miles, E. S., Immerzeel, W. W., and Reid, T. D. (2015). Modelling ice-cliff backwasting on a debris-covered glacier in the Nepalese Himalaya. Journal of Glaciology, 61(229), 889-907.

Steiner, J. F., Kraaijenbrink, P. D., and Immerzeel, W. W. (2021). Distributed melt on a debris-covered glacier: field observations and melt modelling on the Lirung Glacier in the Himalaya. Frontiers in Earth Science, 9, 567. DOI: https://doi.org/10.3389/feart.2021.678375

Stigter, E. E., Litt, M., Steiner, J. F., Bonekamp, P. N., Shea, J. M., Bierkens, M. F., and Immerzeel, W. W. (2018). The importance of snow sublimation on a Himalayan glacier. Frontiers in Earth Science, 6, 108.

Stenborg, T. (1970). Delay of run-off from a glacier basin. Geografiska Annaler: Series A, Physical Geography, 52(1), 1-30.

Srivastava, D., and Swaroop, S. (1992). Glaciological studies on Dunagiri glacier, district, Chamoli, UP–Final Report. Rep. Geol. Surv. India.

Srivastava, D., Kumar, A., Verma, A., Swaroop, S. (2014). Characterization of suspended sediment in meltwater from glaciers of Garhwal Himalaya. Hydrological Processes, 28(3), 969-979.

Sunako, S., Fujita, K., Sakai, A., and Kayastha, R. B. (2019). Mass balance of Trambau Glacier, Rolwaling region, Nepal Himalaya: in-situ observations, long-term reconstruction and mass-balance sensitivity. Journal of Glaciology, 65(252), 605-616.

Soruco, A., Vincent, C., Rabatel, A., Francou, B., Thibert, E., Sicart, J. E., and Condom, T. (2015). Contribution of glacier runoff to water resources of La Paz city, Bolivia (16 S). Annals of Glaciology, 56(70), 147-154.

Suzuki, R., Fujita, K., and one other (2007). Spatial distribution of thermal properties on debris-covered glaciers in the Himalayas derived from ADTER data. Bulletin of Glaciological Research, 24, 13-22.

Swithinbank, C. (1950), The Origin of Dirt Cones on Glaciers, Journal of Glaciology, 1, 461–465, doi: 10.1017/S0022143000012880.

Tapley, B. D., S. Bettadpur, M. Watkins, and C. Reigber (2004), The gravity recovery and climate experiment: Mission overview and early results, Geophysical Research Letters, 31, L09,607, doi:10.1029/2004GL019920.

Tarantola, A. (2005). Inverse problem theory and methods for model parameter estimation. Society for Industrial and Applied Mathematics.

Tawde, S., Kulkarni, A., and Bala, G. (2017). An estimate of glacier mass balance for the Chandra basin, western Himalaya, for the period 19842012. Annals of Glaciology, 58(75pt2), 99-109.

Tedesco, M., and Miller, J. (2007). Observations and statistical analysis of combined active–passive microwave space-borne data and snow depth at large spatial scales. Remote Sensing of Environment, 111 (2–3), 382–397.

Thakuri, S., Salerno, F., Smiraglia, C., Bolch, T., D'Agata, C., Viviano, G., and Tartari, G. (2014). Tracing glacier changes since the 1960s on the south slope of Mt. Everest (central Southern Himalaya) using optical satellite imagery. The Cryosphere, 8(4), 1297-1315.

Thakuri, S., Salerno, F., Bolch, T., Guyennon, N., and Tartari, G. (2016). Factors controlling the accelerated expansion of Imja Lake, Mount Everest region, Nepal. Annals of Glaciology, 57(71), 245-257.

Thibert, E., Blanc, R., Vincent, C. and Eckert, N., (2008). Glaciological and volumetric mass-balance measurements: error analysis over 51 years for Glacier de Sarennes, French Alps. J. Glaciol.,54(186), 522–532.

Thompson, L. G., et al. (2000). A high-resolution millennial record of the South asian monsoon from himalayan ice cores. Science, 289 (5486), 1916–1920.

Thompson, S., D. I. Benn, J. Mertes, and A. Luckman (2016), Stagnation and mass loss on a Himalayan debris-covered glacier: processes, patterns and rates, Journal of Glaciology, 62(233), 467–485, doi: 10.1017/jog.2016.37.

van Tiel, M., Kohn, I., Van Loon, A. F., and Stahl, K. (2020). The compensating effect of glaciers: Characterizing the relation between interannual streamflow variability and glacier cover. Hydrological Processes, 34(3), 553-568.

Treichler, D., and A. Kääb (2016), ICESat laser altimetry over small mountain glaciers, The Cryosphere, 10(5), 2129–2146, doi: 10.5194/tc-10-2129-2016.

Turetsky, M. R., Abbott, B. W., Jones, M. C., Walter Anthony, K., Olefeldt, D., Schuur, E. A., ... and Sannel, A. B. K. (2019). Permafrost collapse is accelerating carbon release.

Vano, J. A., Das, T., Lettenmaier, D. P. (2012). Hydrologic sensitivities of Colorado River runoff to changes in precipitation and temperature. Journal of Hydrometeorology, 13(3), 932-949.

Vano, J. A., Lettenmaier, D. P. (2014). A sensitivity-based approach to evaluating future changes in Colorado River discharge. Climatic Change, 122(4), 621-634.

Valdiya, K. S., Paul, S. K., Chandra, T., and two others et al.(1999). Tectonic and lithological characterization of Himadri (Great Himalaya) between Kali and Yamuna rivers, central Himalaya. Himalayan Geol, 20(2), 1-17.

Veh, G., Korup, O., and Walz, A. (2020). Hazard from Himalayan glacier lake outburst floods. Proceedings of the National Academy of Sciences, 117(2), 907-912.

Venkatesh, T. N., Kulkarni, A. V., and Srinivasan, J. (2012). Relative effect of slope and equilibrium line altitude on the retreat of Himalayan glaciers. The cryosphere, 6(2), 301-311.

Vijay, S., and Braun, M. (2016). Elevation change rates of glaciers in the Lahaul-Spiti (Western Himalaya, India) during 2000–2012 and 2012–2013. Remote Sensing, 8(12), 1038.

Vincent, C., Ramanathan, Al., Wagnon, P., Dobhal, D. P., Linda, A., Berthier, E., Sharma, P., Arnaud, Y., Azam, M. F., Jose, P. G., and Gardelle, J.: Balanced conditions or slight mass gain of glaciers in the Lahaul and Spiti region (northern India, Himalaya) during the nineties preceded recent mass loss, The Cryosphere, 7, 569–582, https://doi.org/10.5194/tc-7-569-2013, 2013.

Vincent, C., Ramanathan, A., Wagnon, P., Dobhal, D. P., Linda, A., Berthier, E., ... and Gardelle, J. (2013). Balanced conditions or slight mass gain of glaciers in the Lahaul and Spiti region (northern India, Himalaya) during the nineties preceded recent mass loss. The Cryosphere, 7(2), 569-582.

Vincent, C., and Six, D. (2013). Relative contribution of solar radiation and temperature in enhanced temperature-index melt models from a case study at Glacier de Saint-Sorlin, France. Annals of Glaciology, 54(63), 11-17.

Viviroli, D., Archer, D. R., Buytaert, W., Fowler, H. J., Greenwood, G., Hamlet, A. F., ... and Lorentz, S. (2011). Climate change and mountain

water resources: overview and recommendations for research, management and policy. Hydrology and Earth System Sciences, 15(2), 471-504.

Viste E and Sorteberg A (2015) Snowfall in the Himalayas: an uncertain future from a little-known past. Cryosphere, 9, 1147–1167.

Vorren, T.O., 1973. Glacial geology in the area between Jostedalsbreen and Jotunheimen,South Norway.Norges geologiskeunderskelse, 291, 1–46.

Wang Z, Deng Y, Zeng X, (1982). Water-heat conditions for maritime glaciers developing in Guxiang, Tibetan Region. In Memoirs of Lanzhou Institute of Glaciology and Geocryology, CAS, No. 3. Science Press, Beijing, 82–90.

Wang, R., Liu, S., Shangguan, D., Radic, V., Zhang, Y. (2019). Spatial heterogeneity in glacier mass-balance sensitivity across High Mountain Asia. Water, 11(4), 776.

Wang, X., Liu, S. W., and Zhang, J. L. (2019). A new look at roles of the cryosphere in sustainable development. Advances in Climate Change Research, 10(2), 124-131.

Wagnon, P., Kumar, R., Arnaud, Y., Linda, A., Sharma, P., Vincent, C., et al. (2007). Four years of mass balance on Chhota Shigri Glacier, Himachal Pradesh, India, a new benchmark glacier in the western Himalaya. J. Glaciol. 53, 603–611. doi: 10.3189/002214307784409306.

Wagnon, P., Vincent, C., Arnaud, Y., Berthier, E., Vuillermoz, E., Gruber, S., et al. (2013). Seasonal and annual mass balances of Mera and Pokalde glaciers (Nepal Himalaya) since 2007. Cryosphere 7, 1769–1786. doi: 10.5194/tc-7-1769-2013.

Weertman, J. (1957). On the sliding of glaciers. Journal of glaciology, 3(21), 33-38.

Wei, Y., Tandong, Y., Baiqing, X., and Hang, Z. (2010). Influence of supraglacial debris on summer ablation and mass balance in the 24K

Glacier, southeast Tibetan Plateau. Geografiska Annaler: Series A, Physical Geography, 92(3), 353-360.

Wijngaard, R. R., Lutz, A. F., Nepal, S., Khanal, S., Pradhananga, S., Shrestha, A. B., and Immerzeel, W. W. (2017). Future changes in hydroclimatic extremes in the Upper Indus, Ganges, and Brahmaputra River basins. PloS one, 12(12), e0190224.

Wilson, A. M., Williams, M. W., Kayastha, R. B., and Racoviteanu, A. (2016). Use of a hydrologic mixing model to examine the roles of meltwater, precipitation and groundwater in the Langtang River basin, Nepal. Annals of Glaciology, 57(71), 155-168.

Winkler, M., Juen, I., Mölg, T., Wagnon, P., Gómez, J., and Kaser, G. (2009). Measured and modelled sublimation on the tropical Glaciar Artesonraju, Perú. The Cryosphere, 3(1), 21-30.

Wirbel, A., A. H. Jarosch, and L. Nicholson (2018), Modelling debris transport within glaciers by advection in a full-Stokes ice flow model, The Cryosphere, 12(1), 189–204, doi: 10.5194/tc-12-189-2018.

Winter-Billington, A., Moore, R. D., and Dadic, R. (2020). Evaluating the transferability of empirical models of debris-covered glacier melt. J. Glaciol., 66(260), 978-995.

Wortmann, M., Bolch, T., Menz, C., Tong, J. & Krysanova, V. Comparison and correction of high-mountain precipitation data based on glacio-hydrological modeling in the Tarim River headwaters (High Asia). J. Hydrometeorol. 19, 777–801 (2018).

Wu, L., Li, H., and Wang, L. (2011). Application of a degree-day model for determination of mass balance of Urumqi Glacier No. 1, eastern Tianshan, China. Journal of Earth Science, 22(4), 470-481.

Wu, Y., He, J., Guo, Z., and Chen, A. (2014). Limitations in identifying the equilibrium-line altitude from the optical remote-sensing de-

rived snowline in the Tien Shan, China. J. Glaciol. 60, 1093–1100. doi: 10.3189/2014jog13j221.

Xu, J., Grumbine, R. E., Shrestha, A., Eriksson, M., Yang, X., Wang, Y. U. N., Wilkes, A. (2009). The melting Himalayas: cascading effects of climate change on water, biodiversity, and livelihoods. Conservation Biology, 23(3), 520-530.

Yang, K., H. Lu, S. Yue, G. Zhang, Y. Lei, Z. La, and W. Wang (2018), Quantifying recent precipitation change and predicting lake expansion in the Inner Tibetan Plateau, Climatic Change, 147(1), 149–163, doi: 10.1007/s10584-017-2127-5.

Yao, T., L. Thompson, W. Yang, W. Yu, Y. Gao, X. Guo, X. Yang, K. Duan, H. Zhao, B. Xu, J. Pu, A. Lu, Y. Xiang, D. B. Kattel, and D. Joswiak (2012), Different glacier status with atmospheric circulations in Tibetan Plateau and surroundings, Nature Clim. Change, 2(9), 663–667, doi: 10.1038/nclimate1580.

Yao, T., Pu, J., Lu, A., Wang, Y., and Yu, W. (2007). Recent glacial retreat and its impact on hydrological processes on the Tibetan Plateau, China, and surrounding regions. Arctic, Antarctic, and Alpine Research, 39(4), 642-650.

Yatagai, A., K. Kamiguchi, O. Arakawa, A. Hamada, N. Yasutomi, and A. Kitoh (2012). APHRODITE: Constructing a Long-Term Daily Gridded Precipitation Dataset for Asia Based on a Dense Network of Rain Gauges, Bulletin of the American Meteorological Society, 93(9), 1401–1415, doi: 10.1175/BAMS-D-11-00122.1.

Yi, S., and W. Sun (2014), Evaluation of glacier changes in high-mountain Asia based on 10 year GRACE RL05 models, Journal of Geophysical Research: Solid Earth, 119(3), 2504–2517, doi: 10.1002/2013JB010860.

Yin, Z.-Y., X. Zhang, X. Liu, M. Colella, and X. Chen (2008). An Assessment of the Biases of Satellite Rainfall Estimates over the Tibetan Plateau and

Correction Methods Based on Topographic Analysis, Journal of Hydrometeorology, 9, 301–326, doi: 10.1175/2007JHM903.1.

You, Q., Fraedrich, K., Ren, G., Ye, B., Meng, X., and Kang, S. (2012). Inconsistencies of precipitation in the eastern and central Tibetan Plateau between surface adjusted data and reanalysis. Theoretical and applied climatology, 109(3-4), 485-496.

Zaz, S. N., Romshoo, S. A., Krishnamoorthy, R. T., and Viswanadhapalli, Y. (2019). Analyses of temperature and precipitation in the Indian Jammu and Kashmir region for the 1980–2016 period: implications for remote influence and extreme events. Atmospheric Chemistry & Physics, 19(1).

Zemp, M., E. Thibert, M. Huss, D. Stumm, C. Rolstad Denby, C. Nuth, S. U. Nussbaumer, G. Moholdt, A. Mercer, C. Mayer, P. C. Joerg, P. Jansson, B. Hynek, A. Fischer, H. Escher-Vetter, H. Elvehøy, and L. M. Andreassen (2013). Reanalysing glacier mass balance measurement series, The Cryosphere, 7(4), 1227–1245, doi: 10.5194/tc-7-1227-2013.

Zhang, Y., Fujita, K., Liu, S., Liu, Q., and Nuimura, T. (2011). Distribution of debris thickness and its effect on ice melt at Hailuogou glacier, southeastern Tibetan Plateau, using in situ surveys and ASTER imagery. Journal of Glaciology, 57(206), 1147-1157.

Zhang, T., and Osterkamp, T. E. (1995). Considerations in determining thermal diffusivity from temperature time series using finite difference methods. Cold Regions Science and Technology, 23(4), 333-341.

Zhang, Y., Liu, S., Ding, Y. (2006). Observed degree-day factors and their spatial variation on glaciers in western China. Annals of Glaciology, 43, 301-306.

Zhang, Y., Hirabayashi, Y., Fujita, K., Liu, S., and Liu, Q. (2016). Heterogeneity in supraglacial debris thickness and its role in glacier mass changes of the Mount Gongga. Science China Earth Sciences, 59(1), 170-184.

Zhang, Y., Liu, S., Liu, Q., and three others et al.(2019). The Role of Debris Cover in Catchment Runoff: A Case Study of the Hailuogou Catchment, South-Eastern Tibetan Plateau. Water, 11(12), 2601.

Zhao, Q., Zhang, S., Ding, Y. J., Wang, J., Han, H., Xu, J., ... Shangguan, D. (2015). Modeling hydrologic response to climate change and shrinking glaciers in the highly glacierized Kunma Like River Catchment, Central Tian Shan. Journal of Hydrometeorology, 16(6), 2383-2402.

Zhao, Q., Ding, Y., Wang, J., Gao, H., Zhang, S., Zhao, C., ... Shangguan, D. (2019). Projecting climate change impacts on hydrological processes on the Tibetan Plateau with model calibration against the glacier inventory data and observed streamflow. Journal of Hydrology, 573, 60-81.

Zhang, Y., Li, T., and Wang, B. (2004). Decadal change of the spring snow depth over the Tibetan Plateau: The associated circulation and influence on the East Asian summer monsoon. Journal of Climate, 17(14), 2780-2793.

Zhang, L., Su, F., Yang, D., Hao, Z., and Tong, K. (2013). Discharge regime and simulation for the upstream of major rivers over Tibetan Plateau. Journal of Geophysical Research: Atmospheres, 118(15), 8500-8518.

Zhang, G., T. Yao, C. K. Shum, S. Yi, K. Yang, H. Xie, W. Feng, T. Bolch, L. Wang, A. Behrangi,H. Zhang, W. Wang, Y. Xiang, and J. Yu (2017), Lake volume and groundwater storage variations in Tibetan Plateau's endorheic basin, Geophysical Research Letters, 44(11), 5550–5560, doi: 10.1002/2017GL073773.

Zheng, H., Zhang, L., Zhu, R., Liu, C., Sato, Y., Fukushima, Y. (2009). Responses of streamflow to climate and land surface change in the headwaters of the Yellow River Basin. Water Re- sources Research, 45(7).

Zhu M, Yao T, Yang W, Maussion F, Huintjes E, Li S. Energy- and mass-balance comparison between Zhadang and Parlung No. 4 glaciers

on the Tibetan Plateau. Journal of Glaciology. 2015;61(227):595-607. doi:10.3189/2015JoG14J206.

Zingg, T. (1951). IUGG/IAHS Gen. Ass. Bruxelles, Publ. No. 32, Vol. 1, 266-269. 'Beziehungen zwischen Temperatur und Schmelzwasser' ('Relations between temperature and meltwater').